

USAAMRDL-TR-76-1



ADVANCED V/STOL PROPELLER CRITICAL COMPONENTS INVESTIGATION

AD A 024663

Hamilton Standard Division
United Technologies Corporation
Windsor Locks, Conn. 06096

April 1976

Final Report for Period February 1973 - June 1975

Approved for public release;
distribution unlimited.

U D C
RECEIVED
OFFICE OF THE
DIRECTOR
A

Prepared for

EUSTIS DIRECTORATE
U. S. ARMY AIR MOBILITY RESEARCH AND DEVELOPMENT LABORATORY
Fort Eustis, Va. 23604

EUSTIS DIRECTORATE POSITION STATEMENT

This report presents the results of an experimental test program involving critical components for a 2000-SHP advanced technology V/STOL propeller system. Work involved fatigue testing of advanced materials in the propeller hub and blade spar retention, and endurance testing of a high-contact-angle, tapered roller main bearing used for the hub-to-gearbox mount.

Blade stub spar fatigue testing demonstrated that the manufacturing process requires additional research to eliminate the boron fiber degradation. Additional redesign and test work is required to achieve a more optimum blade retention concept. The tapered roller bearing configuration produced successful test results that indicated that this design can be used on future propeller systems.

James Gomez, Jr., Propulsion Technical Area, Technology Applications Division, served as technical monitor for this contract.

DISCLAIMERS

The findings in this report are not to be construed as an official Department of the Army position unless so designated by other authorized documents.

When Government drawings, specifications, or other data are used for any purpose other than in connection with a definitely related Government procurement operation, the United States Government thereby incurs no responsibility nor any obligation whatsoever; and the fact that the Government may have formulated, furnished, or in any way supplied the said drawings, specifications, or other data is not to be regarded by implication or otherwise as in any manner licensing the holder or any other person or corporation, or conveying any rights or permission, to manufacture, use, or sell any patented invention that may in any way be related thereto.

Trade names cited in this report do not constitute an official endorsement or approval of the use of such commercial hardware or software.

DISPOSITION INSTRUCTIONS

Destroy this report when no longer needed. Do not return it to the originator.

Unclassified

SECURITY CLASSIFICATION OF THIS PAGE (When Data Entered)

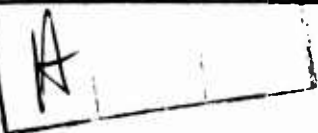
REPORT DOCUMENTATION PAGE		READ INSTRUCTIONS BEFORE COMPLETING FORM
1. REPORT NUMBER USAAMRDL/TR-76-1	2. JOINT ACCESSION NO.	3. RECIPIENT'S CATALOG NUMBER
4. TITLE (and Subtitle) ADVANCED V/STOL PROPELLER CRITICAL COMPONENTS INVESTIGATION.		5. TYPE OF REPORT & PERIOD COVERED Final Report. February 1973 - June 1975.
7. AUTHOR E. H. Walz	8. CONTRACT OR GRANT NUMBER(s) DAAJ92-72-C-0012	9. PERFORMING ORG. REPORT NUMBER
9. PERFORMING ORGANIZATION NAME AND ADDRESS Hamilton Standard Division of United Technologies Corporation Windsor Locks, Connecticut, 06096	10. PROGRAM ELEMENT, PROJECT, TASK AREA & WORK UNIT NUMBERS 62807A IG1 62297AA72 03	
11. CONTROLLING OFFICE NAME AND ADDRESS Eustis Directorate U. S. Army Air Mobility Research and Development Fort Eustis, Virginia, 23604 Laboratory	12. REPORT DATE April 1976	13. NUMBER OF PAGES 229
14. MONITORING AGENCY NAME & ADDRESS (if different from Controlling Office) 234p.	15. SECURITY CLASS. (of this report) Unclassified	16. DECLASSIFICATION/DOWNGRADING SCHEDULE
16. DISTRIBUTION STATEMENT (of this Report) Approved for public release; distribution unlimited.		
17. DISTRIBUTION STATEMENT (of the abstract entered in Block 20, if different from Report) 16 DA-1-1-1612A1-AA-12		
18. SUPPLEMENTARY NOTES		
19. KEY WORDS (Continue on reverse side if necessary and identify by block number) Borsic® Aluminum Composite Ballistic Fatigue Bearing Forging V/STOL Propeller System Barrel Titanium B-10 Life Spar		
20. ABSTRACT (Continue on reverse side if necessary and identify by block number) This report presents the results of an experimental program to evaluate a full-scale Borsic aluminum composite structure spar/titanium propeller barrel retention system and a high-contact-angle duplex tapered roller bearing for an advanced technology 2000-SHP propeller system.		

Unclassified

SECURITY CLASSIFICATION OF THIS PAGE(When Data Entered)

This was accomplished by the design and fabrication of six composite spars, two propeller barrels, three duplex tapered roller bearings, and three ballistic spar specimens. The Hamilton Standard effort involved an experimental stress analysis and a fatigue strength investigation of the spar/barrel retention system, accelerated life test of the bearing, and the analysis of the ballistic specimens tested by the U. S. Army Air Mobility Research and Development Laboratory.

The basic design concepts for the advanced technology propeller barrel and bearing were confirmed by test. The spar test results indicate that the fabrication technology associated with low-pressure bonding of thick wall sections does not produce the anticipated strength to weight benefit.



Unclassified

SECURITY CLASSIFICATION OF THIS PAGE(When Data Entered)

PREFACE

This final report concludes a 34-month program for the design, fabrication, test, and evaluation of selected critical propeller components. The program was conducted by Hamilton Standard for the Eustis Directorate, U. S. Army Air Mobility Research and Development Laboratory under Contract DAAJ02-72-C-0012. This program was an outgrowth of the experience and data generated in the performance of three earlier USAAMRDL contracts: Contract DAAJ02-67-C-0073, involving a feasibility study of advanced V/STOL propeller technology; Contract DAAJ02-68-C-0079, which was a detailed design study of an advanced technology propeller system; and Contract DAAJ02-70-C-0030, which involved the design, test and evaluation of a one-half scale composite material propeller system.

U. S. Army Air Mobility Research and Development Laboratory technical direction was provided by the Contracting Officer's Technical Representative, Mr. J. Gomez, of the Technology Applications Division.

This program was conducted under the management of W. H. Habicht, Program Manager, and directed by D. E. Karpe, Assistant Project Engineer, and by E. H. Walz, Senior Experimental Engineer. Significant contributions were made by the following Hamilton Standard technical personnel:

Design	N. A. Neffinger	Assistant Design Project Engineer
	W. Mandelbaum	Assistant Design Project Engineer
Spar and Ballistic Specimen Manufacture	L. Stoltze	Assistant Project Engineer
	R. A. Walters	Senior Experimental Engineer
Barrel and Bearing Manufacture	D. E. Karpe	Assistant Project Engineer
Spar and Barrel Test	J. L. Mattavi	Senior Analytical Engineer
	S. H. Cohen	Analytical Engineer

TABLE OF CONTENTS

	<u>Page</u>
PREFACE	3
LIST OF ILLUSTRATIONS	6
LIST OF TABLES	14
INTRODUCTION	16
DISCUSSION	17
Propeller System Design Criteria	17
Spar Design	20
Spar Fabrication	21
Spar Test	30
Barrel Design	30
Barrel Fabrication	34
Barrel Test	34
Bearing Design	142
Bearing Test	143
Ballistic Specimen Design	174
Ballistic Specimen Test	174
CONCLUSIONS	225
RECOMMENDATIONS	227
LITERATURE CITED	228
LIST OF SYMBOLS	229

LIST OF ILLUSTRATIONS

<u>Figure</u>		<u>Page</u>
1	Spar Retention Components	22
2	Tape Manufacture Setup	24
3	Schematic of Tape Cutting Operation	25
4	Tape Layup Operation	25
5	Spar Braze Facility	27
6	Schematic of Spar Braze Fixturing	28
7	Electric Heaters on Outer Die	29
8	Schematic of Retention Braze Fixturing	31
9	Retention Braze Rig	32
10	Borsic Aluminum Fatigue Test Spar	33
11	Barrel and Gothic-Arch Bearing Race Inserts	35
12	Titanium Propeller Barrel Detail Drawing	36
13	Gothic-Arch Inner Bearing Race Insert Detail Drawing	37
14	Cothic-Arch Outer Bearing Race Insert Detail Drawing	38
15	Microstructure of Barrel Forging Tensile Test Specimens	40
16	Microstructure of Barrel Forging Tensile Test Specimens	41
17	Barrel Forging Fatigue Test Specimen Locations	42
18	Krouse Machine Fatigue Test Setup, Mean Load Evaluation	44
19	Titanium Barrel Design Fatigue Strength.....	45
20	Centrifugal Load Test Setup	48

LIST OF ILLUSTRATIONS (Continued)

<u>Figure</u>		<u>Page</u>
21	Experimental Stress Analysis Test Setup, 1P In-Plane Evaluation.....	49
22	Centrifugal Load Brittle Lacquer Patterns (46,000 pounds), Arms 5 and 6	50
23	Centrifugal Load Brittle Lacquer Patterns (46,000 pounds), Arms 5 and 7	51
24	Centrifugal Load Brittle Lacquer Patterns (46,000 pounds), Arms 6 and 7	52
25	1P Out-of-Plane Brittle Lacquer Patterns (62,500 inch-pounds), Arm 3.....	53
26	1P Out-of-Plane Brittle Lacquer Patterns (62,500 inch-pounds), Arm 3.....	54
27	1P In-Plane Brittle Lacquer Pattern (59,200 inch-pounds), Arm 1.....	55
28	Strain-Gage Installation, Locations 1 through 6	59
29	Strain-Gage Installation, Locations 7 through 11	60
30	Strain-Gage Installation, Locations 13 through 18	61
31	Strain-Gage Installation, Locations 25 through 29	62
32	Strain-Gage Installation, Locations 30 and 32 through 35	63
33	Strain-Gage Installation, Locations 30 through 33 and 35	64
34	Strain-Gage Installation, Locations 36 and 37	65
35	Borsic Aluminum Spar ESA Test Results	66
36	Titanium Barrel Design Fatigue Strength	68

LIST OF ILLUSTRATIONS (Continued)

<u>Figure</u>		<u>Page</u>
37	Gothic-Arch Inner Bearing Race Insert Loading Pattern	72
38	Gothic-Arch Outer Bearing Race Insert Loading Pattern	73
39	3P Out-of-Plane Fatigue Test Setup	75
40	Spar Number 5 After Fracture, 3P Out-of-Plane Fatigue Test	76
41	Outboard Section of Spar Number 5 After Fracture	77
42	Retention Section of Spar Number 5 After Fracture	78
43	Overall Exploded View of Spar Number 5	79
44	Retention Section of Spar Number 5 at Titanium Outer Support	81
45	Borsic Aluminum Spar - Titanium Outer Support Separation of Spar Number 5	83
46	Radial Fractures in Borsic Aluminum Spar Outboard of Titanium Outer Support in Spar Number 5	84
47	Scanning Electron Microscope Fractographs of Spar Number 5	85
48	Microsections at Fracture of Spar Number 5	87
49	Borsic Aluminum Spar Compaction Thermal Cycle of Spar Number 5	92
50	Borsic Aluminum Spar to Retention Braze Thermal Cycle of Spar Number 5	93
51	Ultrasonic Inspection of Outboard Section of Spar Number 5	95
52	Ultrasonic Inspection of Retention Section of Spar Number 5	96
53	Microstructure of Retention Section of Spar Number 5	97
54	Microstructure of Spar Number 5 Hot Spot	98

LIST OF ILLUSTRATIONS (Continued)

<u>Figure</u>		<u>Page</u>
55	Microstructure of Spar Number 5 Retention Section Fibers	99
56	Borsic Aluminum Spar Fatigue Test Results	101
57	Bending Moment Distribution	102
58	Borsic Aluminum Spar Fatigue Test Results	104
59	Inner-Race Insert of Spar Number 6	105
60	Reconstructed Inner-Race Insert of Spar Number 6	106
61	Inner-Race Insert of Spar Number 6	109
62	Outer-Race Insert of Barrel Arm Number 2.....	110
63	Reconstructed Outer-Race Insert of Barrel Arm Number 2	111
64	Outer-Race Insert of Barrel Arm Number 2	113
65	Outer-Race Insert of Barrel Arm Number 1 and Inner-Race Insert of Spar Number 8	115
66	Reconstructed Outer-Race Insert of Barrel Arm Number 1.....	116
67	Reconstructed Inner-Race Insert of Spar Number 8	118
68	Outer-Race Insert of Barrel Arm Number 3 and Inner-Race Insert of Spar Number 7	120
69	Reconstructed Inner-Race Insert of Spar Number 7	121
70	Reconstructed Outer-Race Insert of Barrel Arm Number 3	123

LIST OF ILLUSTRATIONS (Continued)

<u>Figure</u>		<u>Page</u>
71	Schematic of Gothic-Arch Construction	126
72	Inner-Race Insert Rework Drawing	128
73	Outer-Race Insert Rework Drawing	129
74	Test Bar Detail Drawing	130
75	1P Out-of-Plane Fatigue Test Setup	131
76	Titanium Barrel Fatigue Test Results	133
77	Outer-Race Insert of Barrel Arm 1 and Inner-Race Insert of Test Bar 1	134
78	Inner-Race Insert of Barrel Arm 1	135
79	Outer-Race Insert of Barrel Arm 2 and Inner-Race Insert of Test Bar 2	137
80	Outer-Race Insert of Barrel Arm 3 and Inner-Race Insert of Test Bar 3	139
81A	Inner-Race Insert of Barrel Arm 3	140
81B	Typical Microstructure of Barrel Arm 3 Inserts	141
82	Angular Contact Duplex Tapered Roller Bearing Detail Drawing	144
83	Exploded View of Bearing Assembly	145
84	Exploded View of Bearing Test Configuration	146
85	Bearing Endurance Test Setup	149
86	Inner Race and Roller Assembly of Bearing Number 1	152
87	Inner Race and Roller Assembly of Bearing Number 1, Side 1A	155
88	Inner Race and Roller Assembly of Bearing Number 1, Side 1B	156

LIST OF ILLUSTRATIONS (Continued)

<u>Figure</u>		<u>Page</u>
89	Rollers of Bearing Number 1, Side 1A	157
90	Inner Race of Bearing Number 1, Side 1A	159
91	Inner Race and Roller Assembly of Bearing Number 3, Side 3A ...	163
92	Inner Race and Roller Assembly of Bearing Number 3, Side 3B ...	164
93	Inner Race and Roller Assembly of Bearing Number 3, Side 3A ...	165
94	Inner Race and Roller Assembly of Bearing Number 3, Side 3B ...	166
95	Outer Race of Bearing Number 3, Side 3A	167
96	Outer Race of Bearing Number 3, Side 3B	168
97	Inner Race and Roller Assembly of Bearing Number 2, Side 2A ...	172
98	Inner Race and Roller Assembly of Bearing Number 2, Side 2B ...	173
99	Outer Race of Bearing Number 2, Sides 2A and 2B	175
100	Typical Microstructure of Inner Race and Rollers	176
101	Ballistic Specimen Detail Drawing	177
102	Ballistic Test Specimens	179
103	Entrance Damage to Ballistic Specimen Number 4, 0.50 Caliber Projectile	182
104	Exit Damage to Ballistic Specimen Number 4, 0.50 Caliber Projectile	183
105	Tensile Loading Machine With Specimen Number 1 Following Impact by 14.5 MM Projectile	184
106	Ballistic Specimen Number 2 Fatigue Test Fracture, 0° to 120° of Revolution	185

LIST OF ILLUSTRATIONS (Continued)

<u>Figure</u>		<u>Page</u>
107	Ballistic Specimen Number 2 Fatigue Test Fracture, 90° to 210° of Revolution	186
108	Ballistic Specimen Number 2 Fatigue Test Fracture, 100° to 220° of Revolution	187
109	Ballistic Specimen Number 2 Fatigue Test Fracture, 160° to 210° of Revolution	188
110	Ballistic Specimen Number 2 Fatigue Test Fracture, 180° to 300° of Revolution	189
111	Ballistic Specimen Number 2 Fatigue Test Fracture, 280° to 45° of Revolution	190
112	Borsic Aluminum Fatigue Test Results	191
113	Retention Section of Ballistic Specimen Number 4	192
114	Exit Damage to Ballistic Specimen Number 4	193
115	Outboard Section of Ballistic Specimen Number 1	195
116	Exit Damage to Ballistic Specimen Number 1	196
117	Retention Section of Ballistic Specimen Number 2	197
118	Entrance Damage to Ballistic Specimen Number 2	198
119	Scanning Electron Microscope Fractographs of Ballistic Specimen Number 1	200
120	Metallographic Sections of Ballistic Specimens Numbers 1 and 4 ...	204
121	Ultrasonic Inspection of Retention Section of Ballistic Specimen Number 4	216
122	Ultrasonic Inspection of Outboard Section of Ballistic Specimen Number 1	217

LIST OF ILLUSTRATIONS (Continued)

<u>Figure</u>		<u>Page</u>
123	Ultrasonic Inspection of Retention Section of Ballistic Specimen Number 2	219
124	In-Process Ultrasonic Inspection of Ballistic Specimen Number 4	220
125	In-Process Ultrasonic Inspection of Ballistic Specimen Number 1	221
126	In-Process Ultrasonic Inspection of Ballistic Specimen Number 2	222

LIST OF TABLES

<u>Table</u>		<u>Page</u>
1	Aircraft Mission	17
2	Propeller Characteristics	17
3	Aircraft Maneuver Cyclic Spectrum - Shank and Barrel	18
4	Blade Shank and Barrel Flight Loading	19
5	Aircraft Maneuver Cyclic Spectrum - Bearing	19
6	Flight Thrust Loads - Bearing	20
7	Bearing Life	20
8	Forging Mechanical Properties	39
9	Forging Fatigue Strengths	43
10	Forging Critical Stress Intensity Factor	46
11	Borsic Aluminum Spar Load Spectrum and Stress Summary	57
12	Titanium Barrel Load Spectrum and Stress Summary	67
13	Load Spectrum, Weight Reduction	69
14	Margin-of-Safety Analysis	71
15	3P Out-of-Plane Fatigue Test Loading and Stressing	80
16	Tensile Strengths of Fibers Outboard of Fracture	90
17	Tensile Strengths of Fibers Inboard of Fracture	91
18	Bearing Characteristics	143
19	Endurance Test Spectrum	150
20	Endurance Test - Cycle No. 5	151

LIST OF TABLES (Continued)

<u>Table</u>		<u>Page</u>
21	Endurance Test - Cycle No. 15	151
22	Endurance Test - Cycle No. 24	153
23	Accelerated Endurance Test Spectrum - First	153
24	Accelerated Endurance Test Results - First	154
25	Hardness Traverses	160
26	Accelerated Endurance Test Spectrum and Results - Second.....	161
27	Ballistic Specimen Test Spectrum and Results	181
28	Tensile Strengths of Fibers from Bonded Area of Specimen Number 1	209
29	Tensile Strengths of Fibers from Outboard of Brazed Area of Specimen Number 1	210
30	Tensile Strengths of Fibers from Brazed Area of Specimen Number 2.....	211
31	Tensile Strengths of Fibers from Outboard of Brazed Area of Specimen Number 2	212
32	Tensile Strengths of Fibers from Brazed Area of Specimen Number 4	213
33	Tensile Strengths of Fibers from Outboard of Brazed Area of Specimen Number 4	214
34	Tensile Strengths of Extracted Fibers from All Spars and Specimens	215
35	Extracted Fiber Tensile Strengths	223

INTRODUCTION

For some time, Hamilton Standard has been exploring the application of advanced materials and processes and new design concepts to V/STOL propeller systems. The primary focus of these efforts has been significant weight reduction. The step-by-step progression of the overall technology program, which began with feasibility concepts, has now progressed to full-scale detail design, fabrication, and experimental test of three key structural components specifically sized for a 2000-SHP installation. The three components are the composite blade spar, the titanium propeller barrel with Gothic arch blade retention, and the propeller barrel tail shaft duplex tapered roller support bearing.

DISCUSSION

PROPELLER SYSTEM DESIGN CRITERIA

It is essential that aircraft configuration and mission profile be defined to properly execute the design of advanced technology propeller system components. As this contract did not involve a specific application, it was necessary to make reasonable assumptions. In this regard these assumptions were based on previous studies and, where experience existed, from aircraft operating experiences. Table 1, which follows, indicates the mission spectrum that was established.

TABLE 1. AIRCRAFT MISSION			
Condition	Altitude (ft)	Speed (kn)	Duration (%)
Climb	to 10,000	150	8
Cruise	10,000	300	72
High-Speed Cruise	10,000	350	9
Descent	to 2,500	150	2
Maneuver	2,500	-	9

Table 2 summarizes the predicted propeller design and aerodynamic characteristics to accomplish the defined mission.

TABLE 2. PROPELLER CHARACTERISTICS	
Characteristic	Dimension
Diameter	14.8 ft
Number of Blades	3
Blade Activity Factor	120 per blade
Blade Integrated Lift Coefficient	0.4
Maximum Speed	1160 rpm
Cruise Speed	985 rpm

From the aircraft mission and the propeller characteristics, the magnitude of component loadings was established.

Angularity of propeller inflow as a function of aircraft forward speed was determined on the basis of wing loading, wing lift curve slope, and the geometric relationship between the propeller axis and the wing zero lift line. Military specifications MIL-A-8861, Airplane Strength and Rigidity-Flight Loads, and MIL-A-8866, Airplane Strength and Rigidity-Reliability Requirement, Repeated Loads and Fatigue were employed to establish maneuver duration as a function of load factor and airspeed. Excitation levels were established on the basis of propeller inflow and equivalent forward airspeed. Table 3 summarizes the predicted cycle effects of the maneuver spectrum on the infinite-life components; i.e., blade spar and propeller barrel, which were designed for an assumed aircraft life of 7500 hours.

TABLE 3. AIRCRAFT MANEUVER CYCLE SPECTRUM - SHANK AND BARREL					
Airspeed (kn)	Load Factor	Excitation Factor	Bending Moment		Cycles (10 ⁶)
			Shank (in.-lb)	Barrel (in.-lb)	
150	1.5	3.92	49,000	81,000	11.920
	2.0	5.51	69,000	114,000	0.593
	2.5	7.06	88,400	147,000	0.031
250	1.5	2.53	32,900	39,000	11.850
	2.0	4.12	53,500	63,400	0.593
	2.5	5.67	73,800	87,750	0.030
	3.0	7.26	94,500	112,000	0.018
	3.5	8.82	114,000	136,000	0.002
350	1.5	0.45	6,300	45,400	11.100
	2.0	2.04	28,600	20,600	0.555
	2.5	3.59	50,300	35,600	0.030
	3.0	5.18	72,500	52,500	0.018
	3.5	6.74	94,500	68,250	0.002

The complete loading of the blade shank and barrel must, in addition to cyclic moments, include the effects of centrifugal force and steady bending moment. At the maximum propeller design speed of 1160 rpm, the Borsic[®] aluminum spar/fiber-glass shell blade assumed for this program is estimated to have a centrifugal

force of 45,000 lb. The predicted vibratory bending moments of Table 3 and propeller blade data generated under one of the earlier USAAMRDL contracts were used to calculate steady bending moments. Table 4 records the results of the overall assessment.

TABLE 4. BLADE SHANK AND BARREL FLIGHT LOADING				
Condition	Centrifugal Load (lb)	Steady Bending Moment (in. -lb)	Shank (in. -lb)	Barrel (in. -lb)
Continuous (Infinite Life)	45,000	35,000	65,000	97,450
Maximum (Finite Life)	45,000	18,000	114,000	136,000

The barrel-to-gearbox mount main bearing was designed to a reduced cycle requirement; i. e., a life of 3000 hours vs. the aircraft's life of 7,500 hours. It is normal practice to size bearings on the basis of several overhauls during the life of the aircraft. Based on this life, the cycle effects of the maneuver spectrum on the bearing are shown in Table 5.

TABLE 5. AIRCRAFT MANEUVER CYCLIC SPECTRUM - BEARING			
Airspeed (kn)	Load Factor	Shaft Moment (in. -lb)	Cycles (10 ⁶)
150	1.5	80,600	4.768
	2.0	114,000	0.237
	2.5	147,000	0.012
250	1.5	39,000	4.740
	2.0	63,400	0.237
	2.5	87,750	0.012
	3.0	112,000	0.007
	3.5	136,000	0.001
350	1.5	45,400	4.440
	2.0	20,600	0.222
	2.5	35,600	0.012
	3.0	52,500	0.007
	3.5	68,250	0.001

In addition to the maneuver moment loading, the bearing must react the thrust loads of Table 6.

TABLE 6. FLIGHT THRUST LOADS - BEARING	
Condition	Thrust (lb)
Continuous (Mean Effective)	3260
Maximum (Take Off)	6440

Accordingly, the parameters of Tables 5 and 6 became the basis for the experimental endurance test schedules. Table 7 summarizes the bearing lives for the pertinent loads.

TABLE 7. BEARING LIFE			
Case	Vibratory Bending Moment (in. -lb)	Thrust (lb)	B-10 Life
Continuous	44,000	3,260	3,250
Maximum	147,000	3,260	65
500-hr Test	32,300-114,000	3,260	3,125
370-hr Test	80,6000-130,000	3,260-8,000	368.2
75-hr Test	130,000	3,260	67.7

SPAR DESIGN

The typical Hamilton Standard propeller blade currently utilizes a central structural metal, either aluminum or steel, spar with the shank retention an integral part of the spar, and a composite material, usually fiberglass, airfoil shell. Contrasting the normal design, the advanced technology blade concept consists of a Borsic aluminum blade spar extending the full length of the blade and with a titanium shank retention having a shell, which forms the blade airfoil section, attached along its axial length. The blade shank or inboard end is mounted to the barrel by the bearing retention. In this design the spar is a tapered Borsic aluminum tube. The outer end of the tube is attached to a steel moment arm simulation,

while the inner end is sandwiched between an outer brazed bonded titanium collar and an inner adhesively bonded collar. Figure 1 illustrates this configuration. Proper transfer of load from the spar to the outer titanium collar is the prime objective of this configuration. Theoretically, the more uniform the load transfer, the shorter the spar/collar interface and the lighter the joint. The tapered joint most closely approaches this ideal. The inner aluminum collar prevents hoopwise distortion of the retention in the direction in which the Borsic aluminum composite material is weakest. A split-hardened steel insert is positioned over the titanium collar and is used for the inner ball raceway of the retention.

SPAR FABRICATION

Tape

The composite portion of the retention assembly was composed of 47 layers of a metal matrix foil tape reinforced with a silicon-coated boron fiber, designated Borsic. The individual tape layer, employed as the basic building block in composite structures, was considered the best form for manufacturing operation. The single-ply tape was a mechanically stable structure by virtue of the fixed fiber position uniformly spaced within the tape. The tape form permitted ease of handling and could be readily positioned on dies without disturbing the integrity of the fiber spacing. In addition, the single-ply tape could be easily cut or punched.

The incorporation of the fiber and metal matrix material into a monolayer tape was accomplished in three basic operations:

1. Mandrel preparation and substrate layup.
2. Filament winding of the fiber.
3. Plasma spraying of the AA 6061 aluminum onto the fiber and substrate.

The equipment employed during these operations consisted of large winding drums, approximately 40 inches in diameter. The surface of each drum was cut longitudinally at one location and the ends held in place by tension springs. This spring loaded joint served as an expansion joint and an area for fiber splicing and tape cutting for removal of the finished tape from the drum. Tapes 10 feet long by 15 inches wide were prepared.

The aluminum braze substrate, Alcoa 703 with a nominal thickness of 0.001 inch, was placed around the drum with care to prevent the foil from wrinkling. The foil was held in place by tape at the expansion joint of the drum. The drum was then

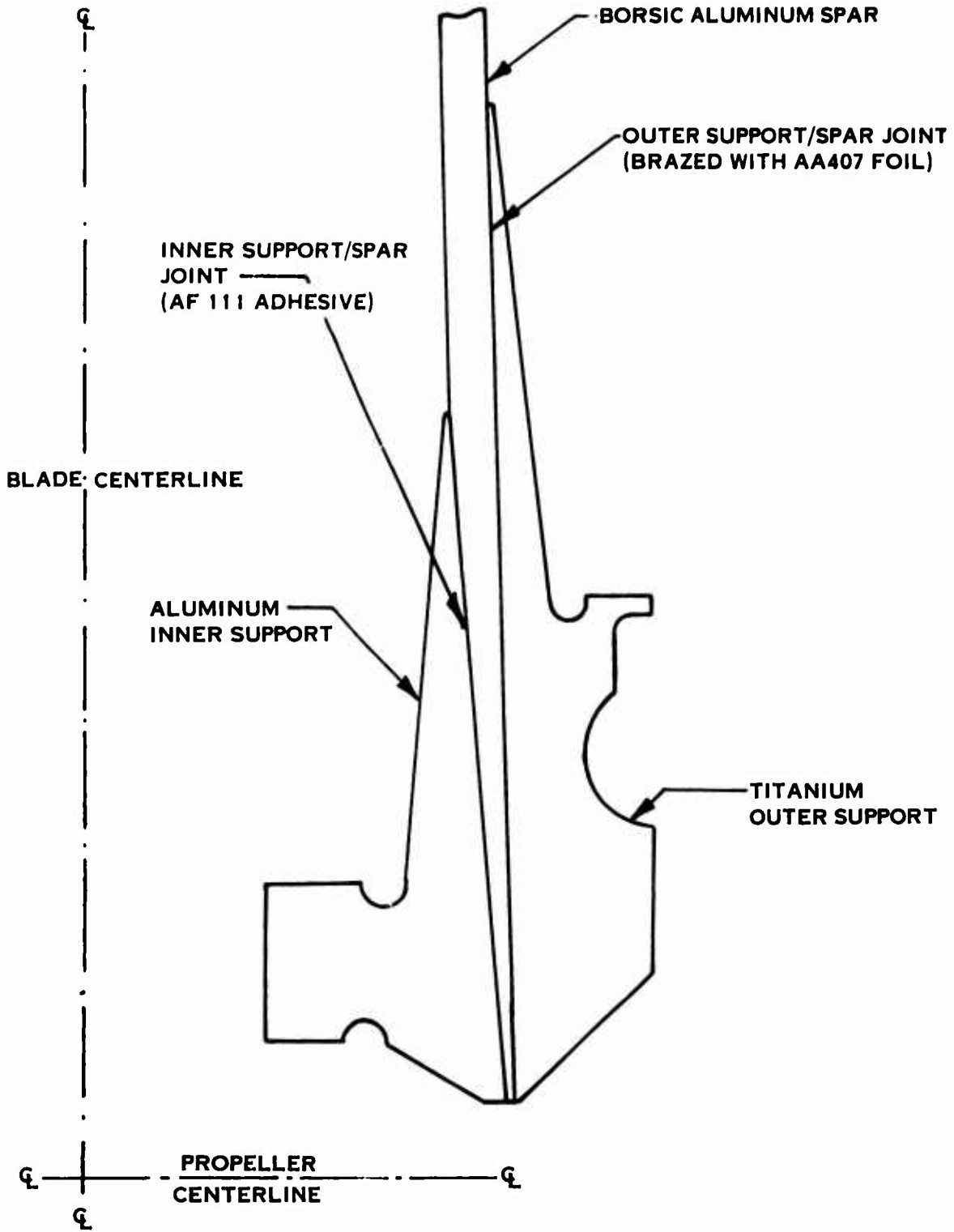


FIGURE 1. SPAR RETENTION COMPONENTS

placed in the lathe-like winder and the filament winding initiated. See Figure 2. The fibers were wound at 175 turns/inch. The drum was then placed on the plasma spray equipment. The matrix material, AA6061, was applied by injecting the aluminum powder into the plasma gun. The powder united with the hot argon gas of the plasma arc, liquifying in the exothermic or recombination zone of the gun, and was impacted and quickly solidified on the fiber and substrate. The fiber represented approximately 50% of the tape weight.

Spar

Fabrication of a composite spar section was essentially a manual operation except for the consolidation phase. Care was exercised throughout these operations to minimize contamination of the part. Clean white gloves were utilized during the initial preparation and layup phases, with consolidation of the part being performed in a vacuum.

The tape was initially cut into rectangular pieces; then each rectangle was cut into two pieces, with the length of the rectangle being 27 inches (allowing a 2-inch overlap on each end of the 23-inch test piece) and one width equal to one-fourth the circumference of the base of the conical specimen and the other one-fourth that of the tip circumference. See Figure 3. These sections were precompact to a thickness of 0.0085 inch by cold rolling the tape in a rolling mill. Both sections were then placed on a wooden mandrel. One section was rotated and tack brazed into position as illustrated in Figure 4. This operation eliminated the possibility of the part being misoriented during the successive buildup of layers. The entire procedure was then repeated by butting successive pieces and forming them tightly to the surface of the mandrel. Each tape layer was wiped with gauze and an acetone cleaning solvent prior to the layup operation. The pieces were changed dimensionally, as required, to compensate for the diameter increases that resulted as each layer was added. The direction of rotation of each section was reversed and the butt joints were staggered relative to the location of the joint in the preceding layers to maintain a balanced fiber alignment. Each layer was formed to the surface of the preceding layer using a deadweighted elastic strap to pull the layer as tightly as possible.

Forty-seven layers of composite tape were assembled for each conical section, which, after consolidation, yielded a specimen with a 5.000-inch internal diameter at the base and a 4.147-inch internal diameter at the tip. The average wall thickness was 0.300 inch and the fiber volume was approximately 57.5%.

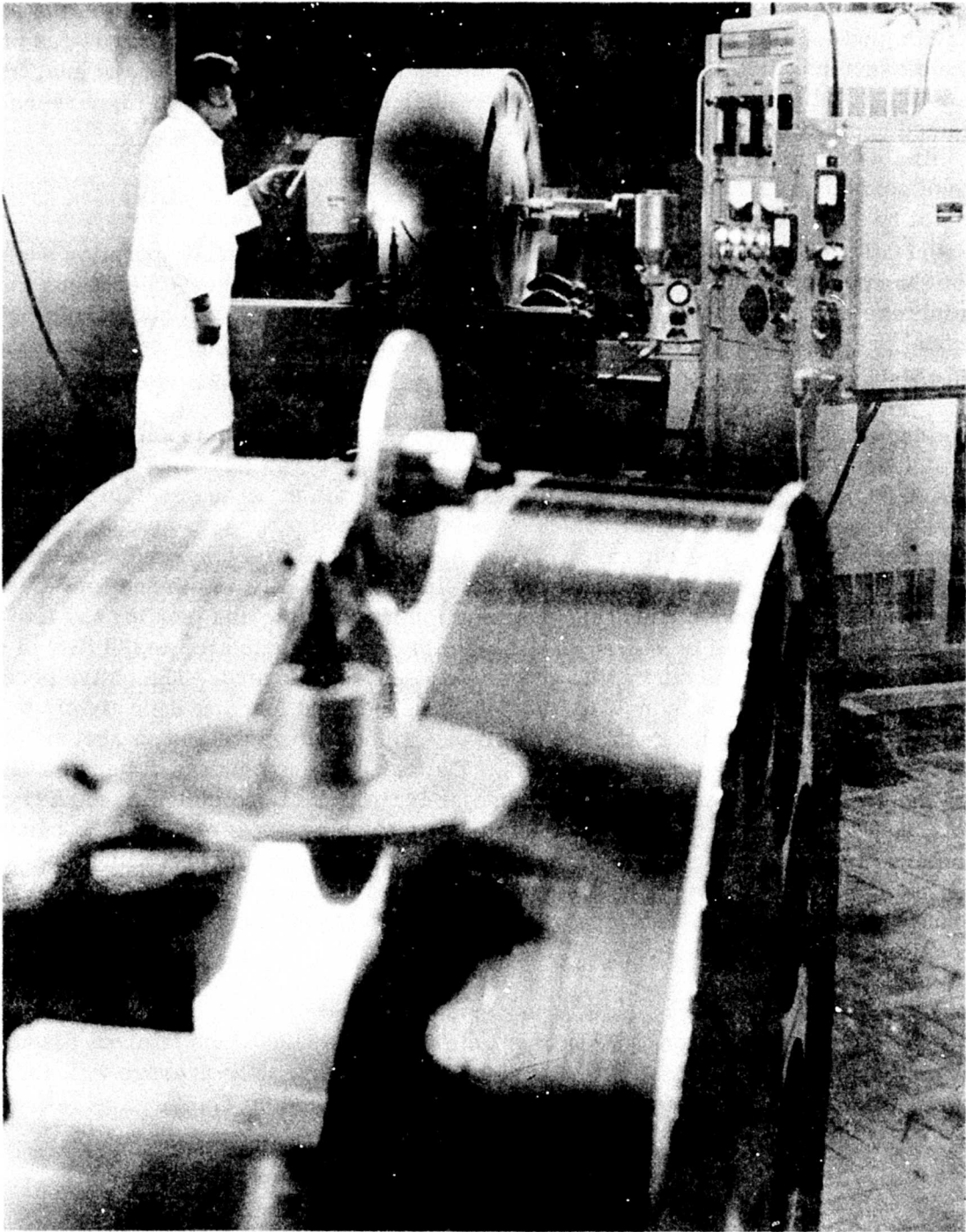
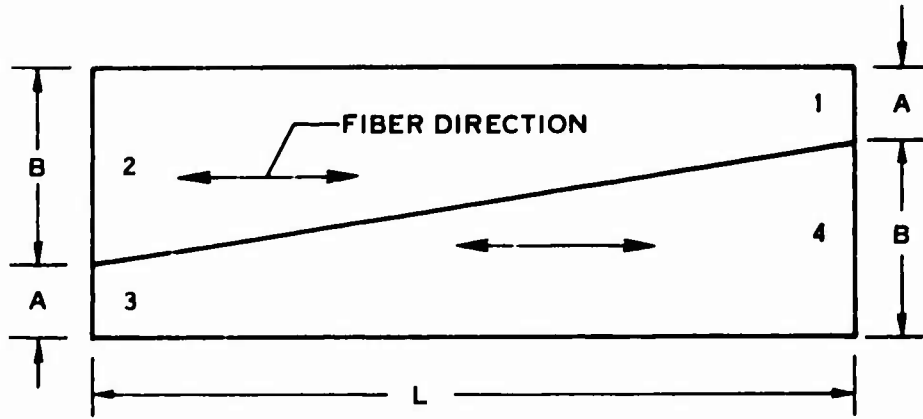


FIGURE 2. TAPE MANUFACTURING SETUP



A = 1/4 CIRCUMFERENCE OF SPECIMEN TIP DIAMETER
 L = LENGTH OF TEST SPECIMEN CONE
 B = 1/4 CIRCUMFERENCE OF SPECIMEN BASE DIAMETER

FIGURE 3. SCHEMATIC OF TAPE CUTTING OPERATION

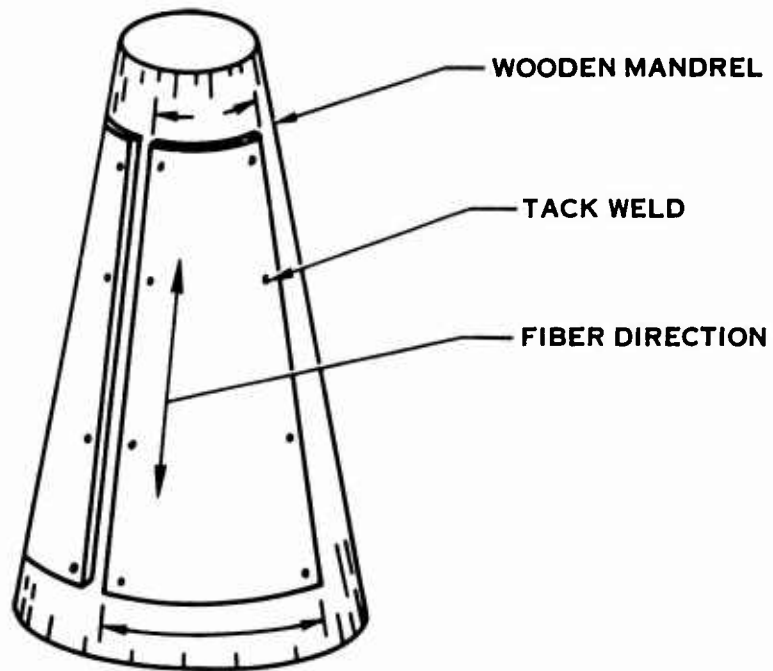


FIGURE 4. TAPE LAYUP OPERATION

The unconsolidated tape assembly was then placed in the spar rig for the bond and compaction operations. See Figure 5. This was accomplished by removing the assembly from the wooden mandrel and placing it over the metallic inner mandrel. Prior to placing the assembly on the mandrel, an aluminum dam was positioned on the mandrel to prevent excessive runout of aluminum from the specimen during the compaction process. The metallic inner mandrel was coated with a milk of magnesia solution and sprayed with a dry graphite film to prevent the specimen from adhering to the mandrel. A steel cap was placed on the inner mandrel, just above the specimen. Three 0.003-inch stainless steel strips, 1.0 inch wide at the top and 1.5 inches wide at the base, were tack welded to the cap. These strips allowed the conical specimen to slide on the outer die as the inner mandrel was raised, thereby compacting the composite inward. See Figure 6 for a schematic illustration of the spar rig.

The outer die was set in place over the conical specimen and bolted to a 10-inch spacer, which in turn was bolted to the base of the spar rig. Integral with the outer die was a series of electrical band heaters to obtain the required 1100°F to 1140°F temperature for braze bonding. See Figure 7.

The vacuum chamber was then installed and a vacuum of 3×10^{-4} torr minimum was drawn. The composite material was finally compacted when the specimen reached the designated temperature and pressure was applied. The pressure was generated by activating the hydraulic ram, located below the inner mandrel, until the inner mandrel was aligned with the outer die, the mandrel and die having been designed to produce the final wall thickness when this condition was reached.

Retention

Attachment of the titanium and aluminum components to the large end of the composite spar completed the retention. These components enveloped the spar at the external and internal surfaces. The outer titanium member was finished internally prior to assembly, while the inner aluminum member was completely finished. The outer surface of the former component was completed after braze bonding.

The titanium outer component was carefully fitted to the composite spar; then both surfaces were sand blasted using #80 grit sand and a pressure of 20 to 40 psi. All surfaces were cleaned with an acetone solvent and then hydrogen air dried. The titanium component and composite spar were then reassembled with AA4047 braze foil sandwiched between. This assembly was positioned over a steel inner mandrel. A steel outer shield, incorporating electric band heaters, was then lowered into place. The vacuum chamber was then installed and a vacuum of 3×10^{-4} torr minimum drawn. The electric heaters were energized and the hydraulic ram was

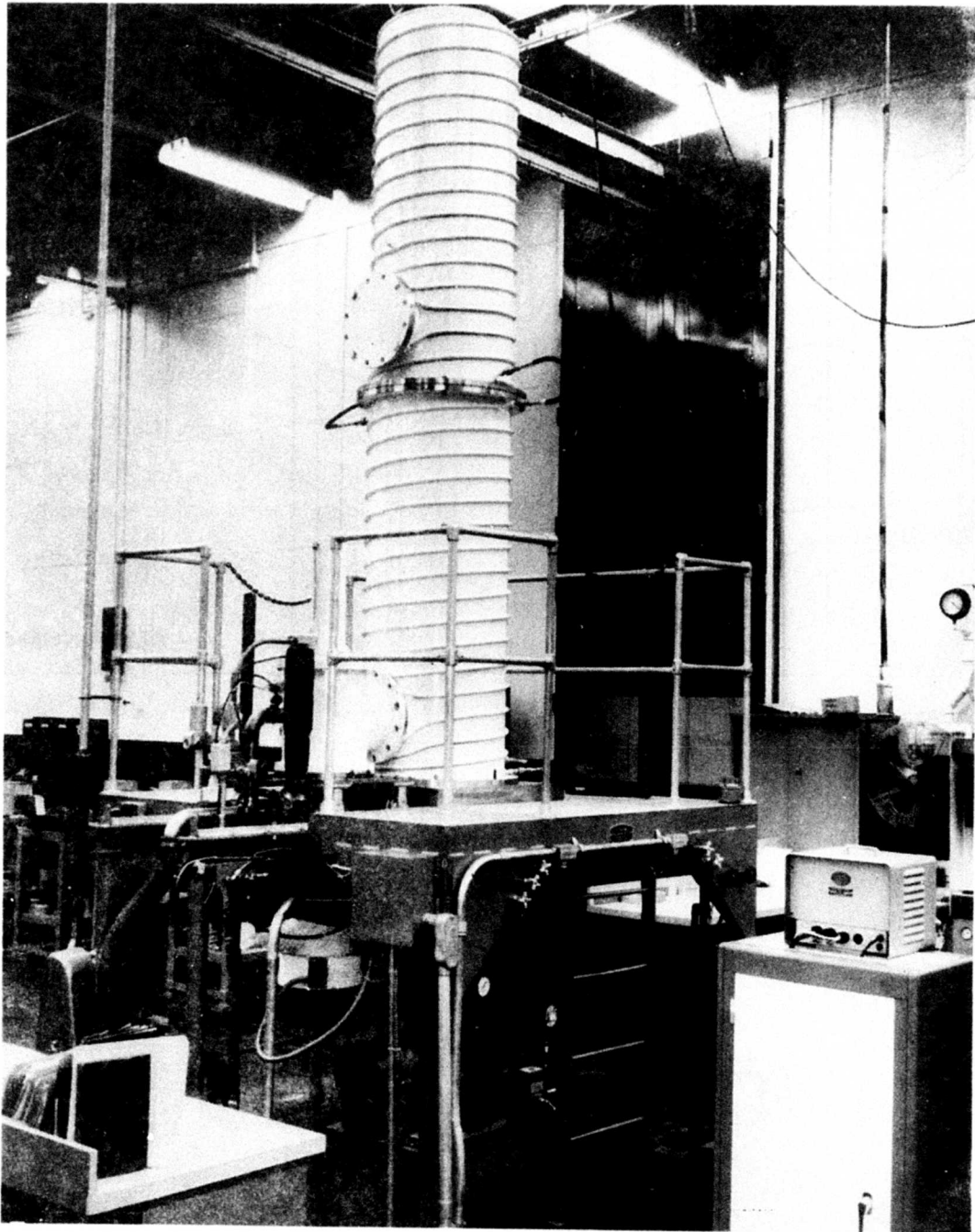


FIGURE 5. SPAR BRAZE FACILITY

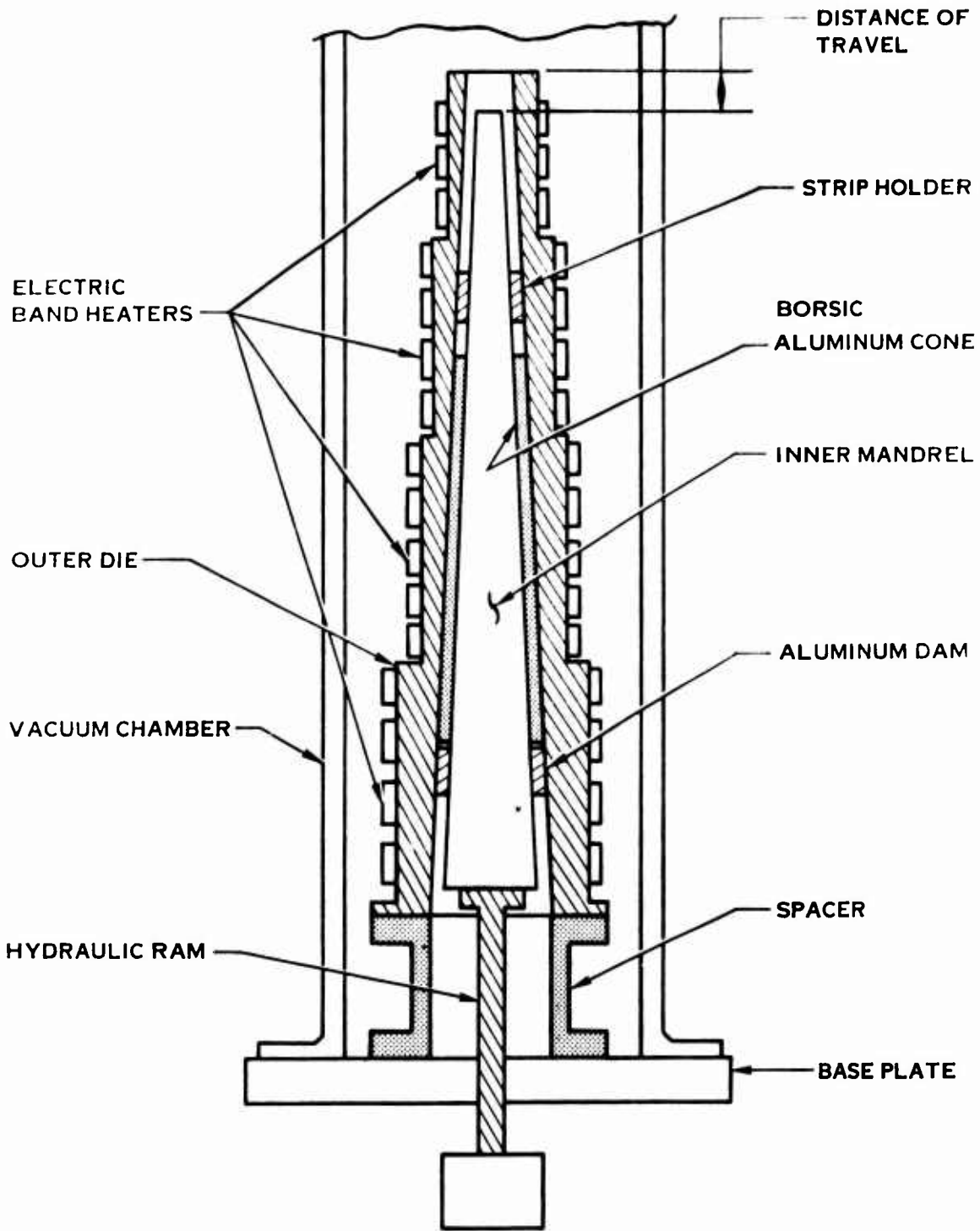


FIGURE 6. SCHEMATIC OF SPAR BRAZE FIXTURING



FIGURE 7. ELECTRIC HEATERS ON OUTER DIE

activated to impart preload. Selection of this particular braze foil was based on its melting point, 1085° F to 1100° F, which is below the melting range of the consolidated spar. See Figure 8 for a schematic illustration of the retention braze rig and Figure 9 for a photograph of the rig with the vacuum chamber removed.

The aluminum inner component was carefully prefitted to the composite spar, following which both surfaces were sand blasted using #80 grit sand and a pressure of 20 to 40 psi. All surfaces were cleaned with an acetone solvent and then hydrogen air dried. The aluminum component was then reassembled with AF 111 adhesive between the mating surfaces. The assembly was then placed in an oven and the temperature was raised to 250° F and held for one hour to affix the aluminum component to the composite spar.

The entire assembly was then heat treated to establish a T6 condition in the aluminum component. The assembly was heated to 980° F to 990° F for 65 minutes, U-CON A quenched, aged at 345° F to 355° F for 9 hours, and slow cooled to room temperature.

Final machining of the outer titanium component was completed after the steel moment arm was adhesively bonded in place. The raceway surfaces were cold worked by means of shot peening. A photograph of a finished spar is shown in Figure 10.

SPAR TEST

The spar test program was conducted in conjunction with the barrel test program in order to more realistically simulate an actual propeller system. See BARREL TEST section later in this report.

BARREL DESIGN

The propeller barrel typically is either a one-piece or a two-piece, vacuum-melted, fully-machined steel forging incorporating an integral bearing race blade retention. Historically, retentions are plain angular contact bearings preloaded against moment loading by the centrifugal load of the blades.

In this design the barrel is a one-piece pressed and pierced, fully-worked titanium forging. The forgings used for barrel manufacture were worked both in the billet form and in the press die. Working was controlled by a process which pierces

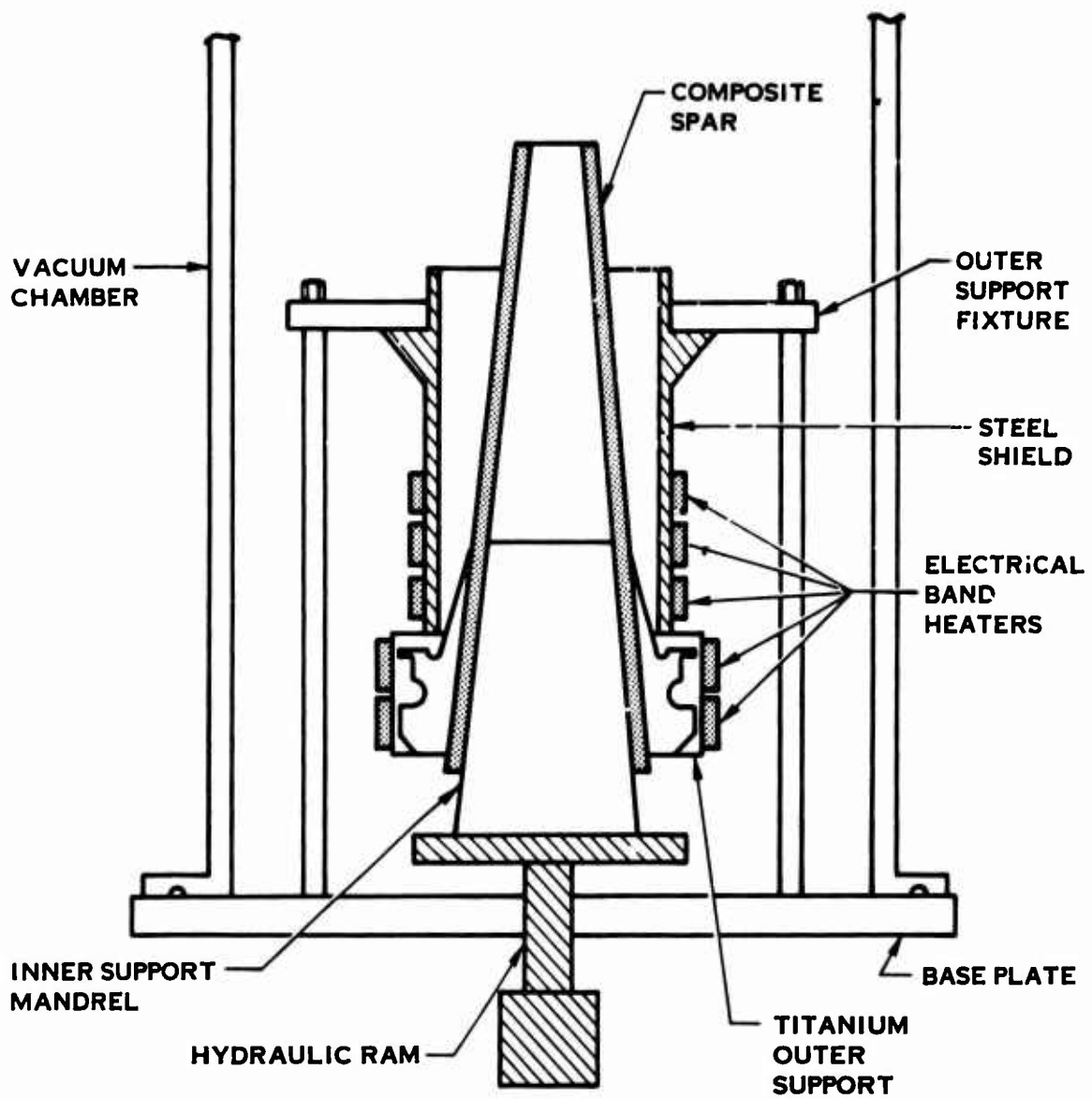


FIGURE 8. SCHEMATIC OF RETENTION BRAZE FIXTURING

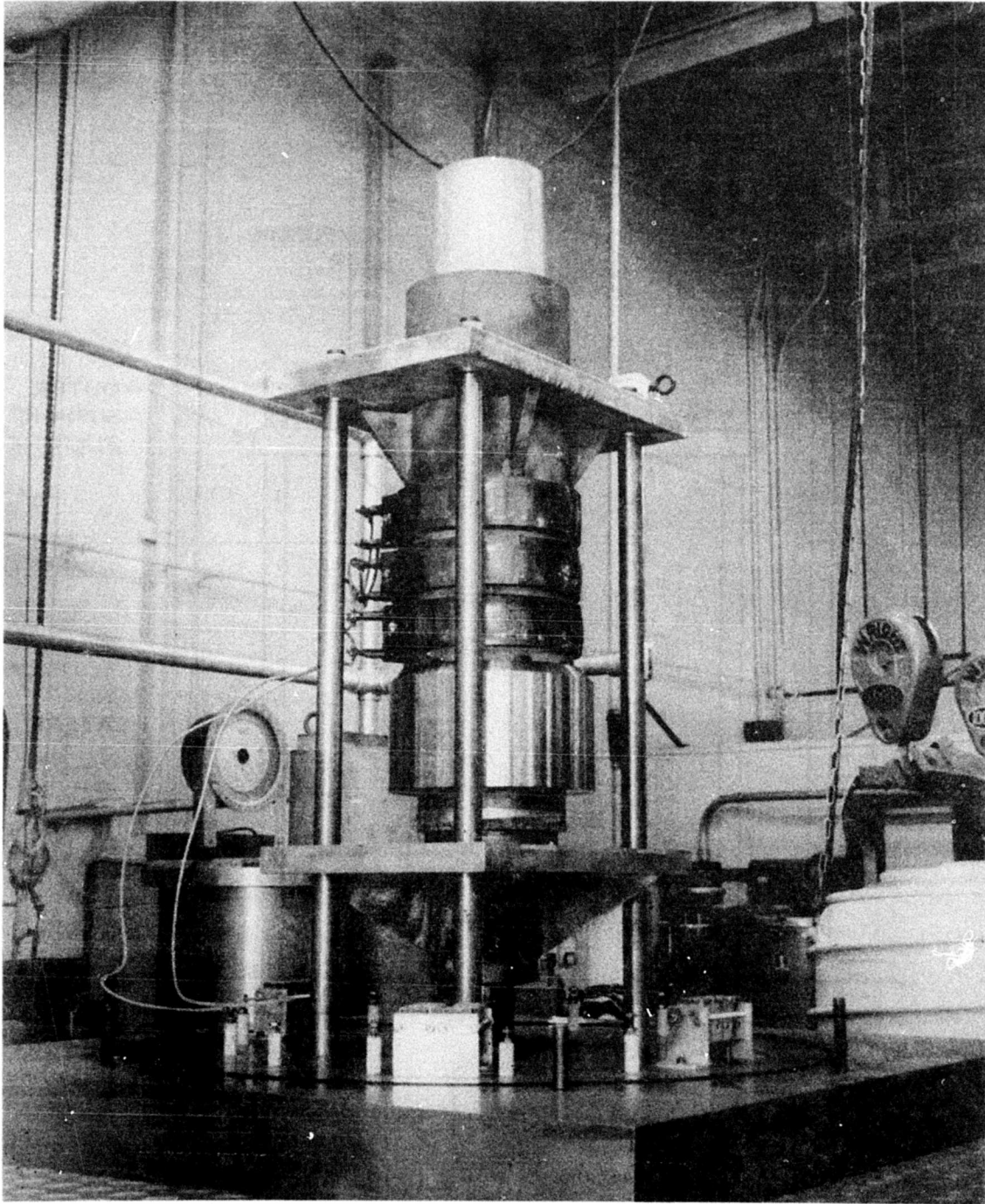


FIGURE 9. RETENTION BRAZE RIG

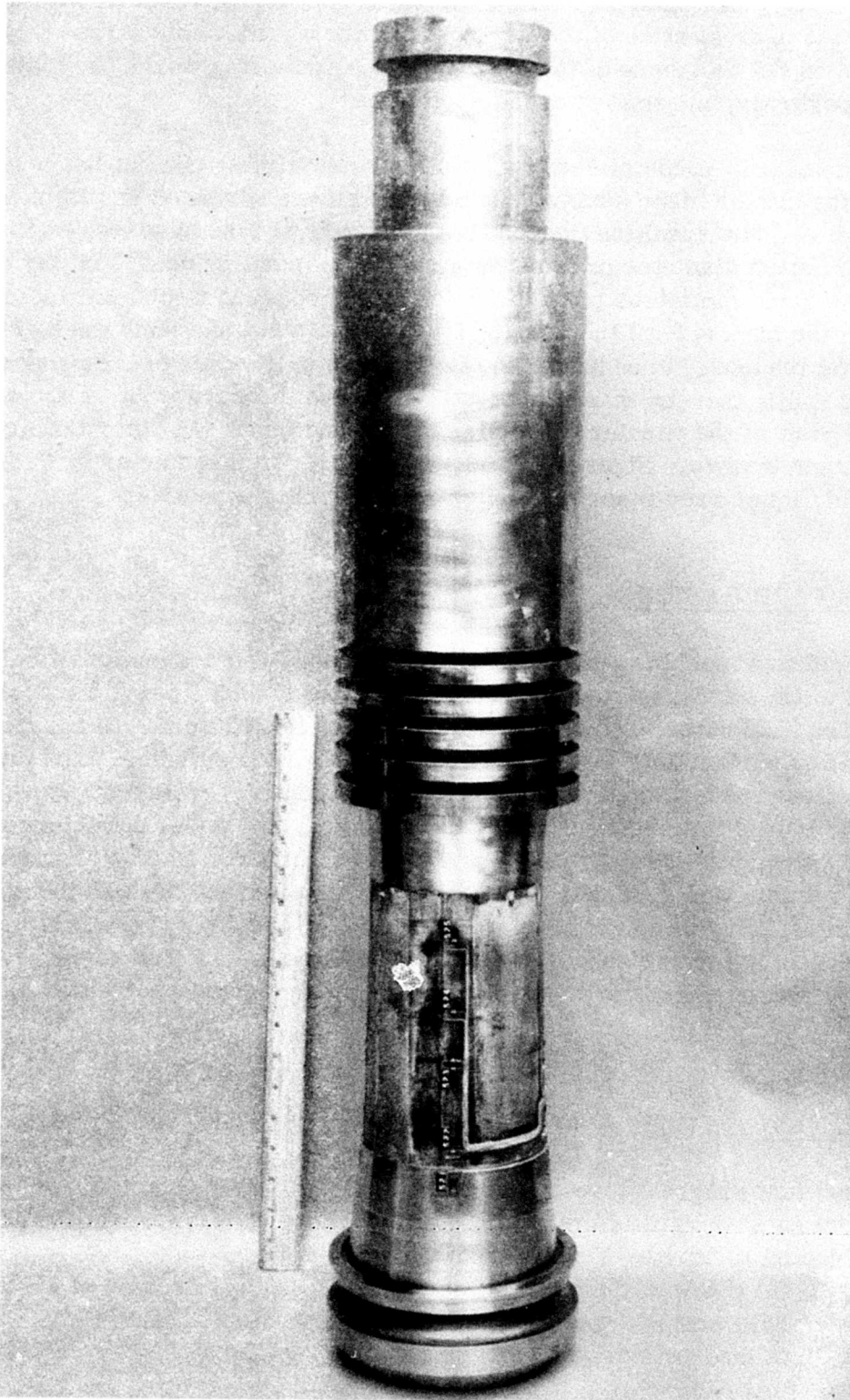


FIGURE 10. BORSIC ALUMINUM FATIGUE TEST SPAR

the centerbody, tail shaft and arms, all while the forging remains within the closed die. As the present state of the art for determining allowable stress depends heavily upon the thickness of the forged section, pressing works the metal and, most importantly, minimizes cross section.

Blade retention is accomplished by a Gothic-arch angular contact bearing. As the state of the art for blade designs has produced more advanced and lighter weight constructions, the resulting decreases in centrifugal load have caused large increases in pitch diameter in order to maintain moment preload. In this design the Gothic arch minimizes pitch diameter by introducing a split-hardened steel insert on the back side of the bearing balls that resists moments greater than centrifugal preload. In addition, the Gothic arch allows for overlapping of ball matching radii, thereby minimizing axial and radial clearances. Figure 11 is an exploded view of the titanium propeller barrel and inner and outer Gothic-arch bearing race inserts. Figures 12, 13, and 14 are the manufacturing drawings for the barrel, inner-race insert and outer-race insert, respectively.

BARREL FABRICATION

This barrel was machined using traditional methods and conventional tools. Outer surfaces of the barrel were machined on a milling machine using a tracer attachment. The final outer surface operation involved hand grinding to change the rough milled surface into a smooth surface. Following grinding, the barrel was stress relieved to eliminate the possibility of entrapped residual stresses. Outside and inside barrel tail-shaft surfaces, together with the inside diameters of the front and rear rings, were turned about the barrel centerline. The inner surface of each barrel arm was generated by turning and/or grinding, as was the case for the bearing race, about the arm bore centerline. The inside of the barrel centerbody was produced by turning about the barrel centerline. Selective surfaces were cold worked by rolling and/or shot peening and all surfaces were subjected to glass bead peening.

BARREL TEST

The barrel test program involved a number of distinct efforts. Specimens were taken from an as-forged barrel and metallurgically analyzed. Additional specimens were subjected to tensile, fatigue and fracture toughness tests. An experimental stress analysis (ESA) of the barrel/Borsic aluminum spar retention system was conducted. This was followed by a fatigue strength investigation (FSI). These tests are discussed in detail in succeeding paragraphs.

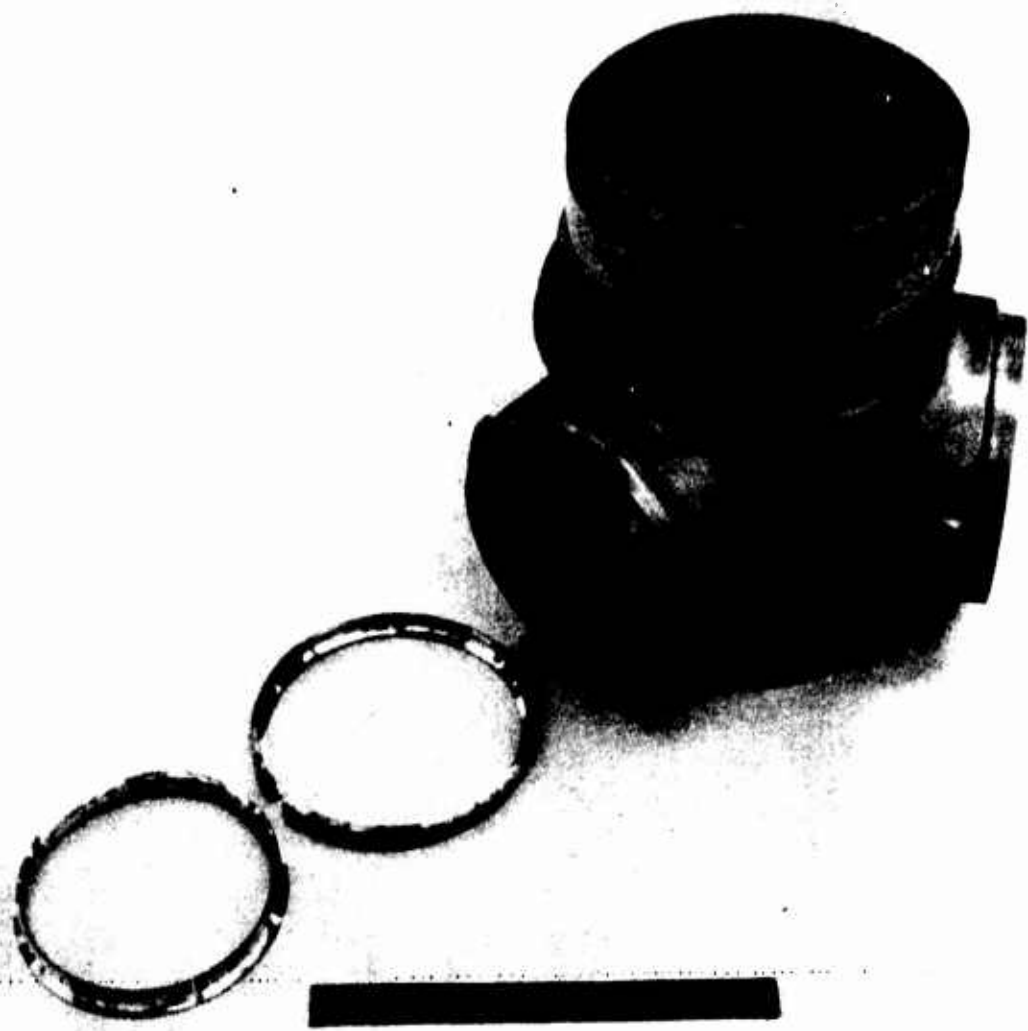


FIGURE 11. BARREL AND GOTHIC-ARCH BEARING RACE INSERTS

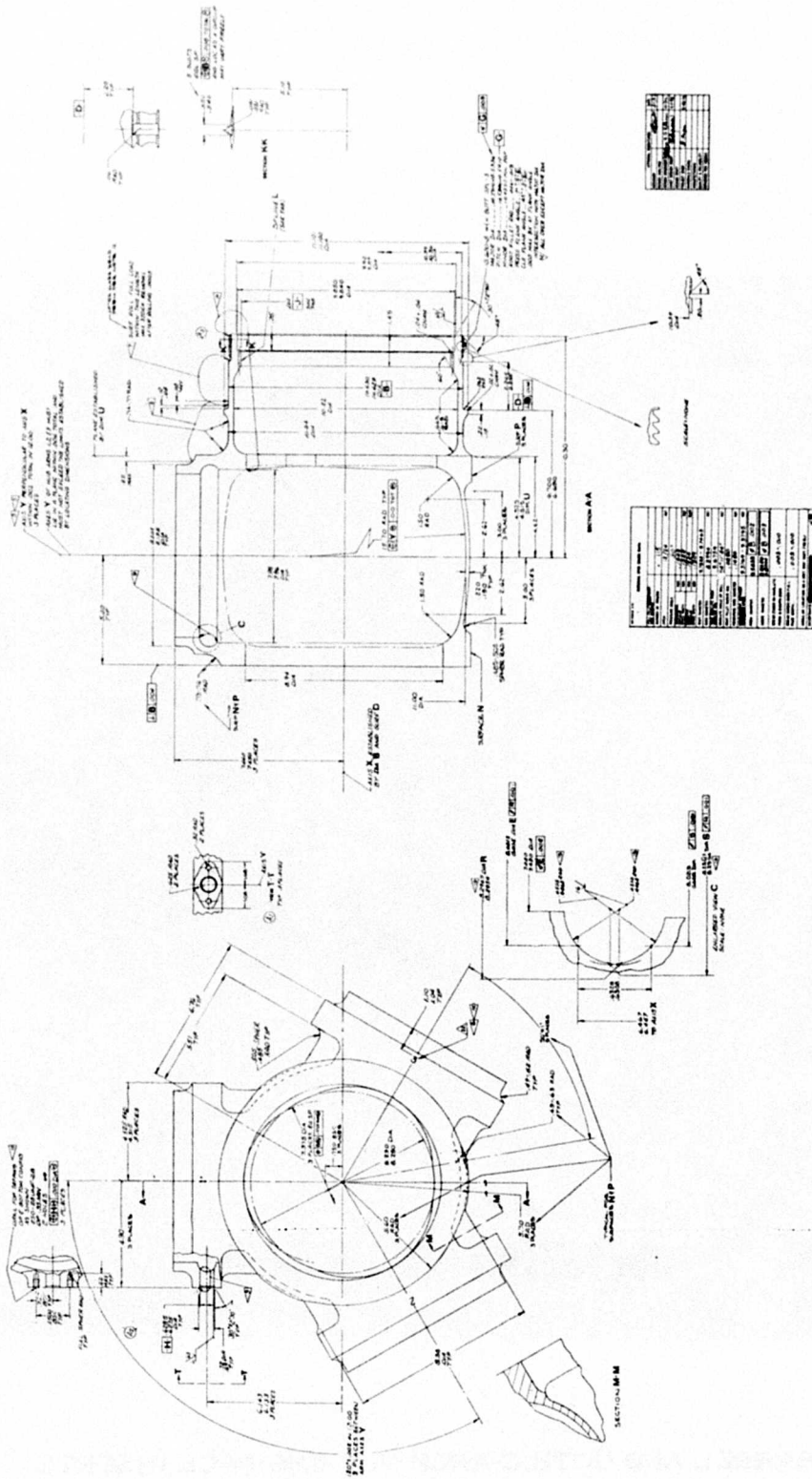


FIGURE 12. TITANIUM PROPELLER BARREL DETAIL DRAWING

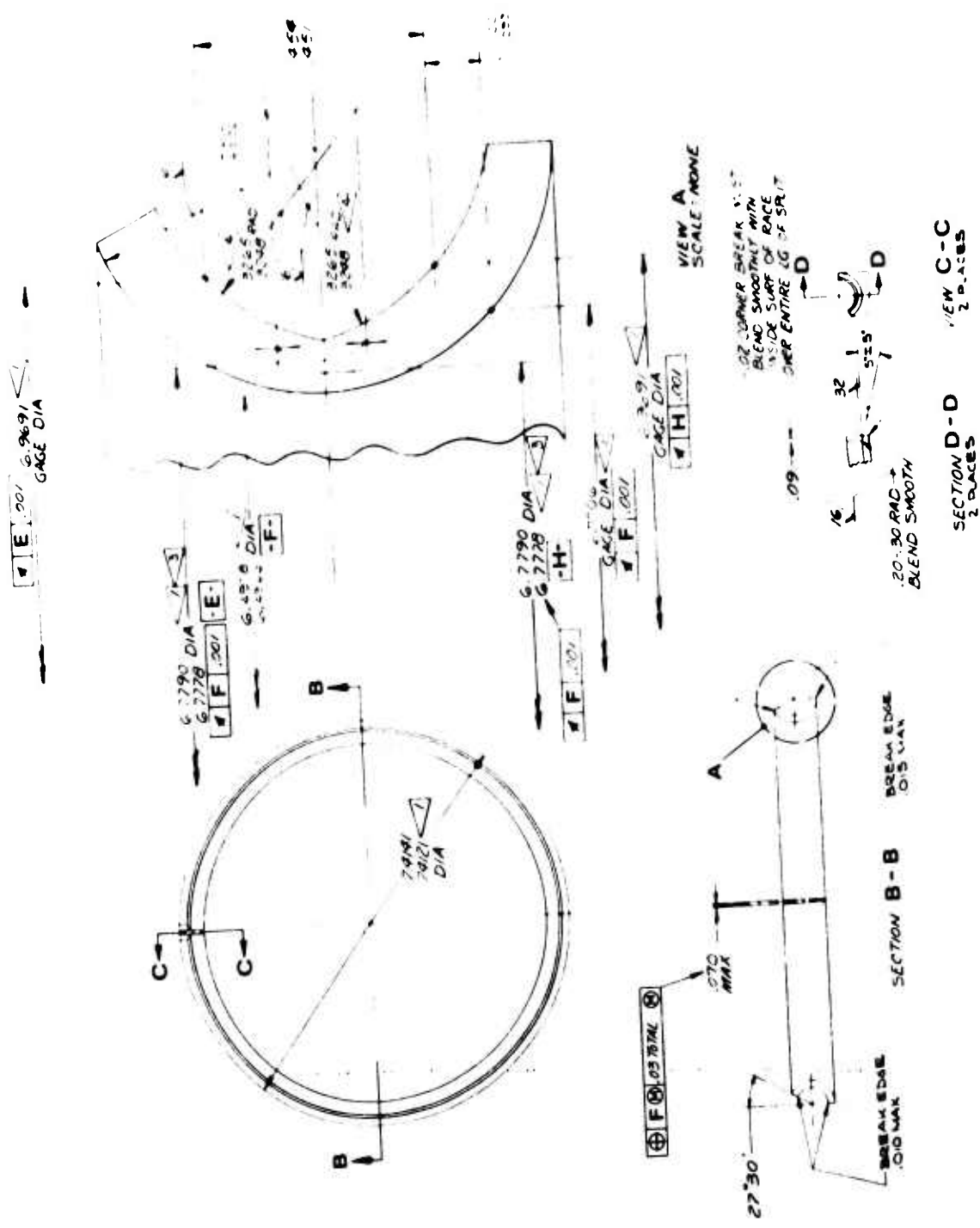


FIGURE 13. GOTHIC-ARCH INNER BEARING RACE INSERT DETAIL DRAWING

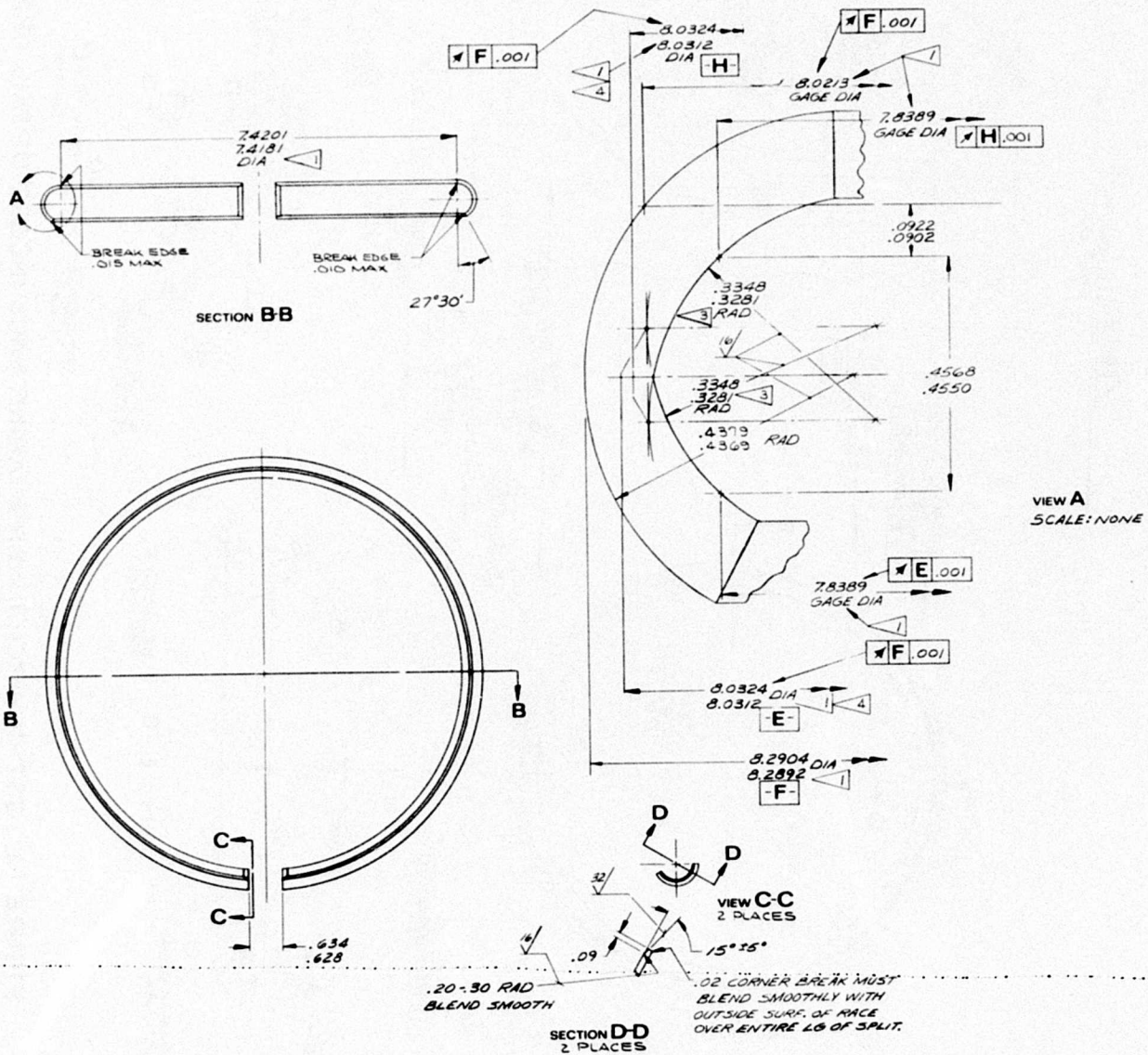


FIGURE 14. GOTHIC-ARCH OUTER BEARING RACE INSERT DETAIL DRAWING

Specimen Tensile Test

The barrel forging was HS 463 Type I annealed 5A1-4V titanium (Reference AMS 4928). It was annealed at 1325°F for three hours, followed by air cooling. A review of the resulting microstructure revealed the necessity for improving the fine-grain structure. Consequently, the forging was reheated at 1775°F for one hour, water quenched, and reannealed at 1300°F for three hours, followed by air cooling. The resulting grain structure, which did not exceed 25% primary alpha, was considered satisfactory. The average mechanical properties obtained from eight tensile specimens, removed from the locations shown in Figure 17A, were 147,850 psi yield strength, 156,700 psi tensile strength, 13.2% elongation, and 36.4% reduction in area. The actual results for these eight specimens are recorded in Table 8.

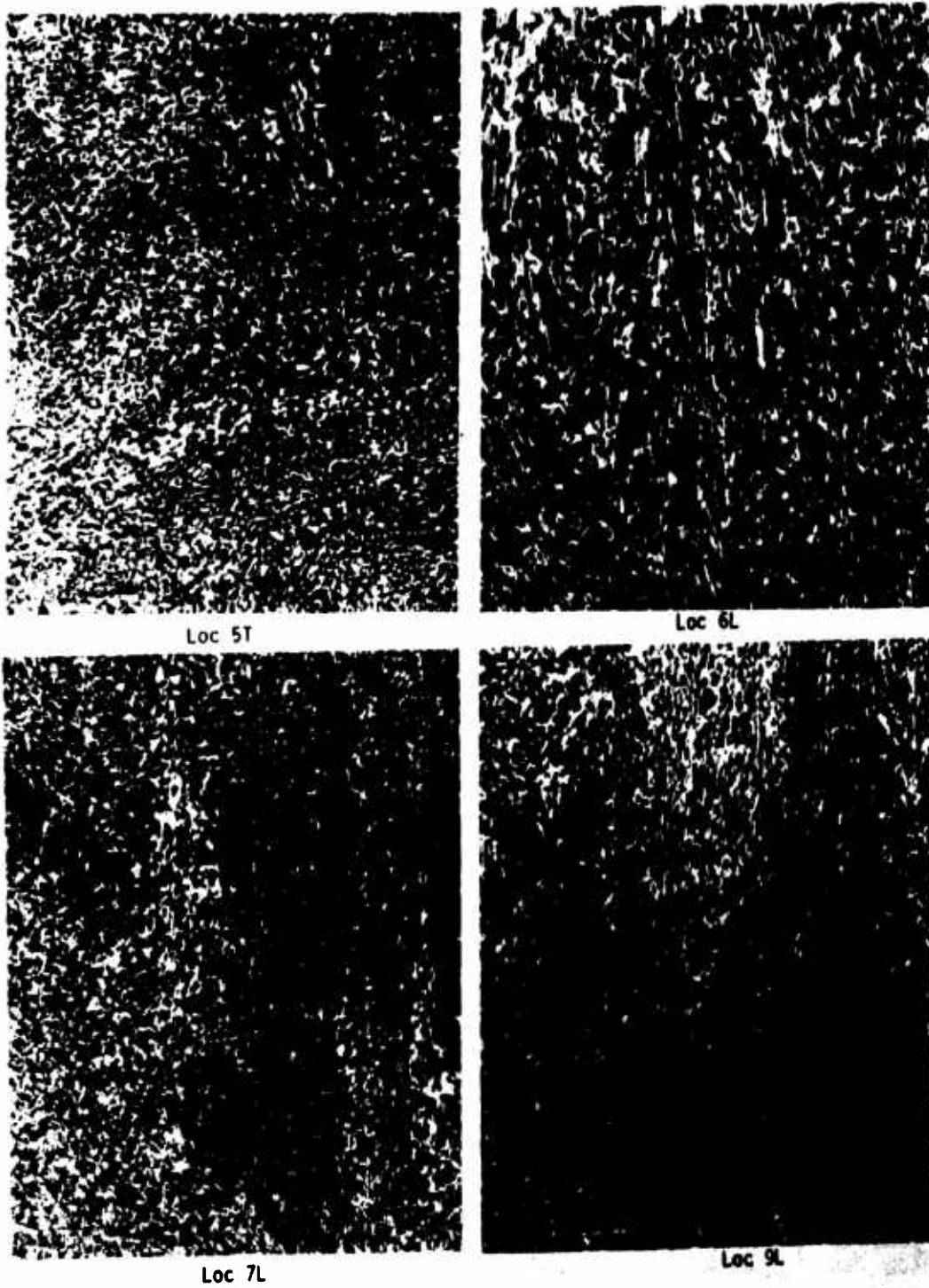
TABLE 8. FORGING MECHANICAL PROPERTIES				
Specimen Number	Yield Strength (psi)	Tensile Strength (psi)	Elongation (%)	Reduction (%)
1L	149,000	156,000	10.0	21.7
2L	147,600	154,800	11.5	33.8
3T	147,000	152,800	16.5	43.2
4L	148,800	157,600	13.5	37.0
5T	149,600	160,800	13.6	41.3
6L	144,400	155,600	14.0	40.1
7L	143,200	151,600	13.5	35.7
9L	153,200	164,400	12.5	38.3

Figures 15 and 16 are typical photomicrographs of the specimens.

Specimen Fatigue Test

The effectiveness of the pressing and piercing of the forging to obtain minimum sections while maximizing allowable stress was evaluated by investigating the fatigue strength of specimens taken from the analytically determined points of highest stress.

Figure 17B indicates the circumferential and longitudinal locations from which specimens were selected. Four types of specimens were taken; i.e., smooth-round-rotating bending, notched-round-rotating bending, flat-constant stress-completely reversed, and flat-constant stress-reversed.



100X

FIGURE 15. MICROSTRUCTURE OF BARREL FORGING TENSILE TEST SPECIMENS

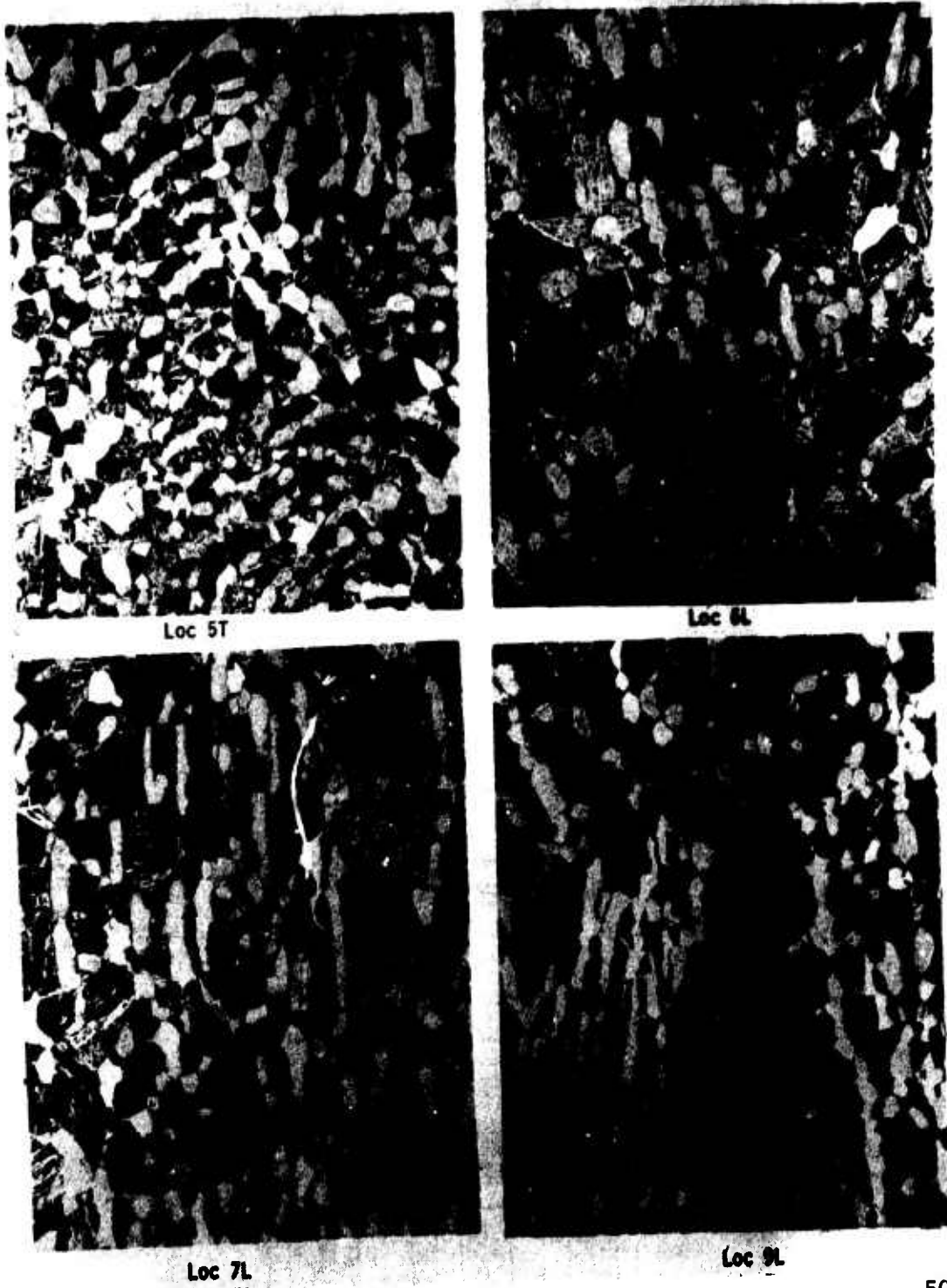


FIGURE 16. MICROSTRUCTURE OF BARREL FORGING TENSILE TEST SPECIMENS

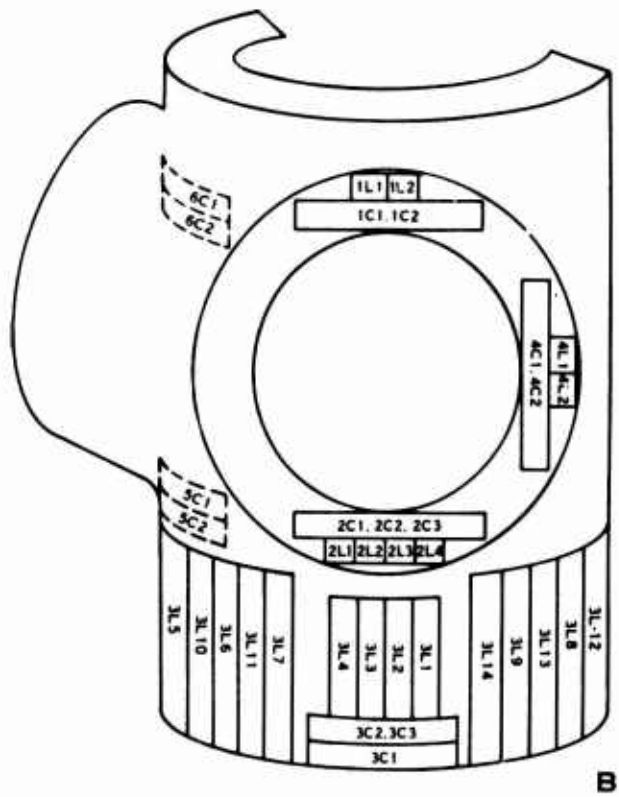
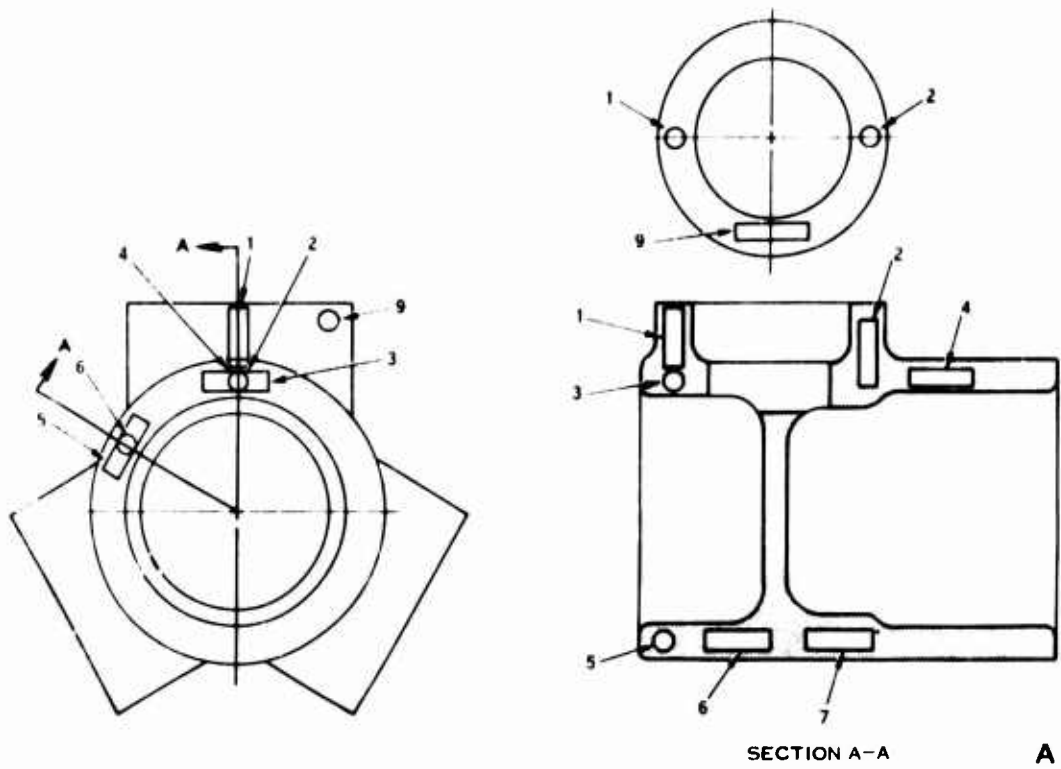


FIGURE 17. BARREL FORGING FATIGUE TEST SPECIMEN LOCATIONS

The test procedure employed for the R. R. Moore smooth-round specimens was to initiate stressing at $\pm 50,000$ psi and to increase, in 10,000 psi increments, until fracture or ten million cycles was achieved. The notched-round specimens were started $\pm 20,000$ psi with subsequent levels incremented by 5,000 psi. Testing of the completely reversed Krouse flat specimens was initiated at $\pm 40,000$ psi since a reduction in strength was anticipated due to the edge effect associated with flat specimens. The reverse-bending Krouse specimens were chosen for the mean stress evaluation and, based on the anticipated maximum stress of 70,000 psi, were initiated at 52,000 psi $\pm 17,500$ psi and increased by 15,000 psi. Figure 18 shows the latter test setup.

Table 9 summarizes the room-temperature results in terms of \bar{X} fatigue strengths.

TABLE 9. FORGING FATIGUE STRENGTHS				
Specimen Type	Sample Size	Stress Concentration (K_t)	Stress Ratio (R)	\bar{X} (psi)
R. R. Moore	20	1.0	-1	67,100
R. R. Moore	5	2.75	-1	27,600
Krouse	5	1.0	-1	55,850
Drouse	5	1.0	.5	18,675*

* Based on maximum stress of 74,900 psi

Negligible strength differences were detected in the various areas of the barrel. That the Krouse specimen results were approximately 17% lower than the R. R. Moore specimens is probably due to the edge effects of the flat Krouse specimen. Although reasonable completely reversed bending fatigue was realized in this forging, a higher than anticipated degree of sensitivity to mean stress was evidenced. The fatigue test specimens indicated a droop, in the linear predicted curve used for this design, at the typically required mean stress levels. Figure 19 illustrates, in the form of a modified Goodman diagram, the design fatigue strength derived from the test data.

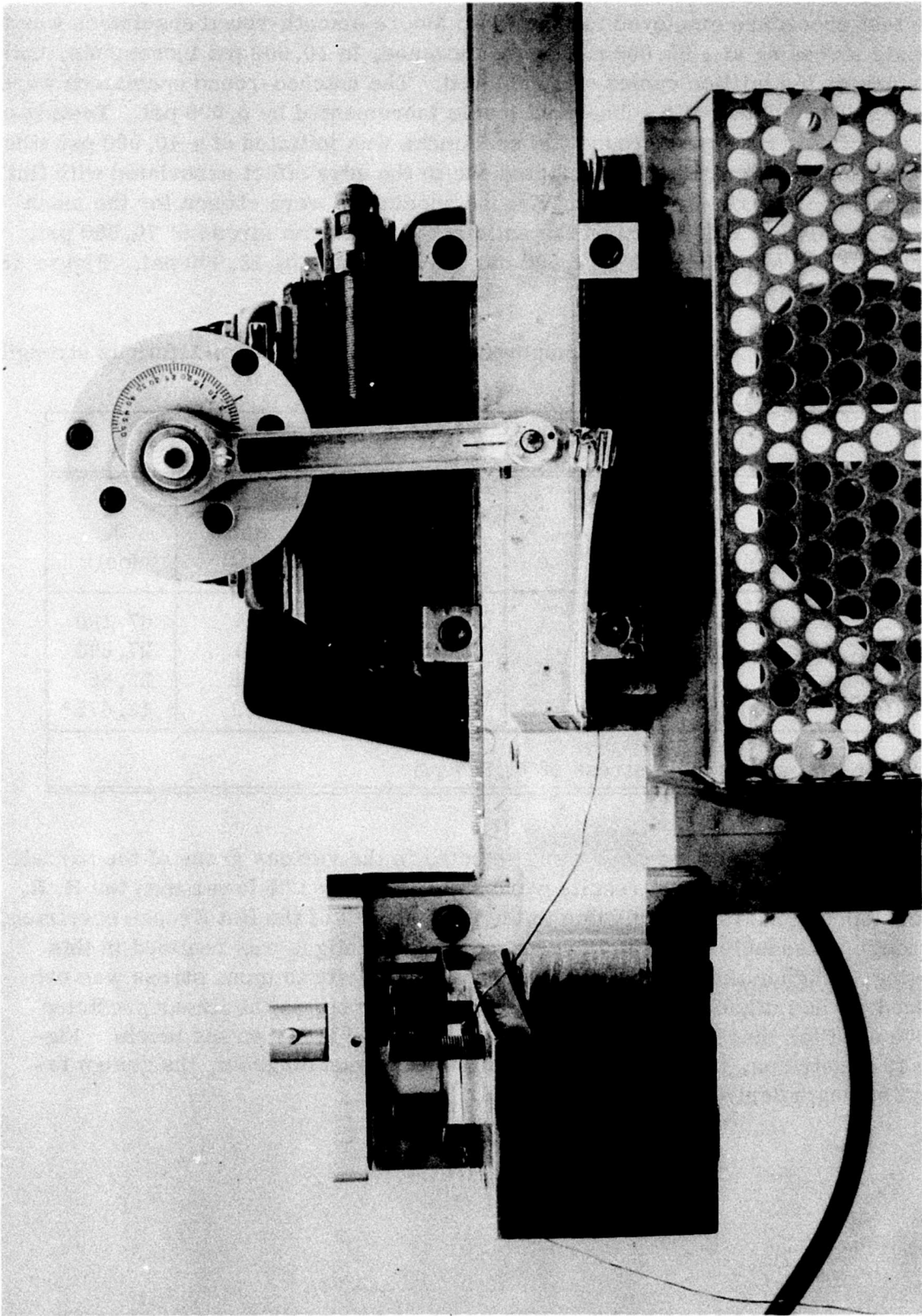


FIGURE 18. KROUSE MACHINE TEST SETUP - MEAN LOAD EVALUATION

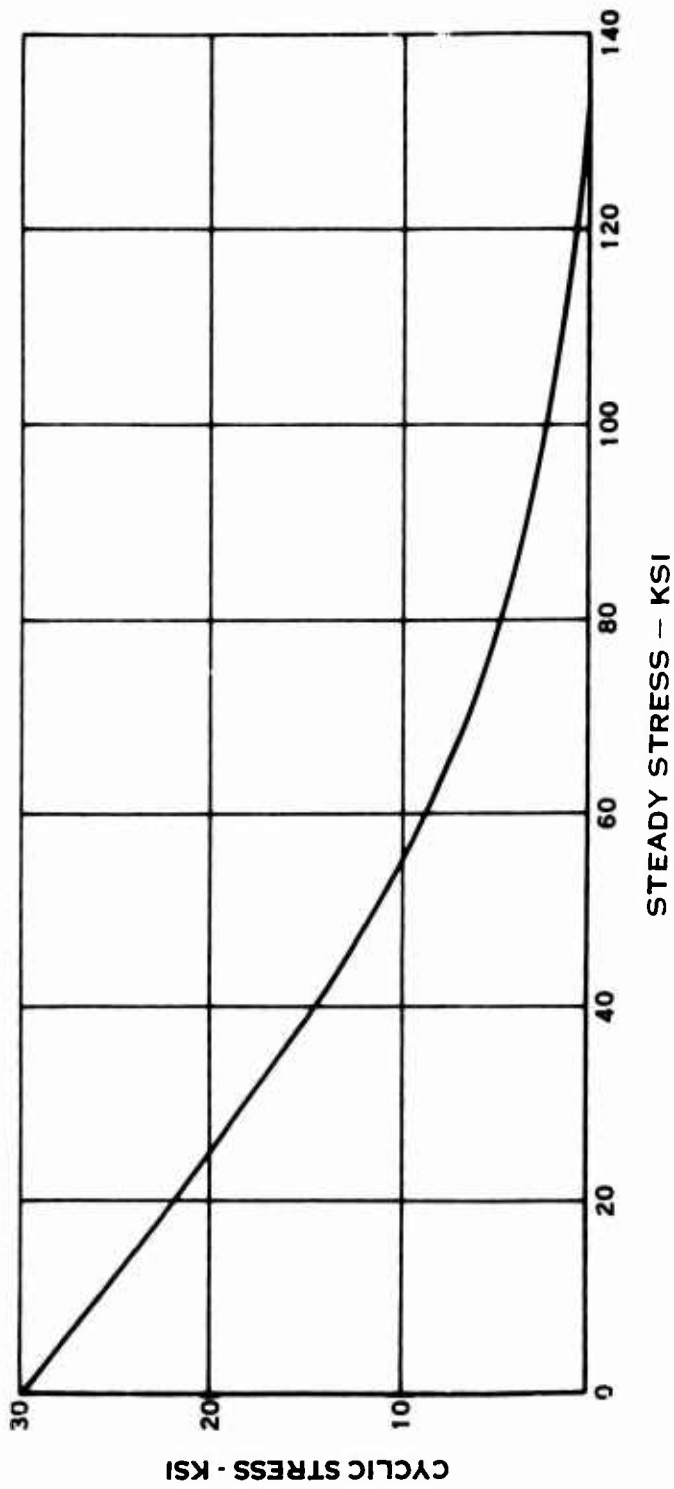


FIGURE 19. TITANIUM BARREL DESIGN FATIGUE STRENGTH

Specimen Fracture Toughness Test

The plane strain fracture toughness behavior of the actual forging was evaluated statically in the form of critical stress intensity factor, K_{IC} , and dynamically in the form of crack propagation rate, da/dN . Specimen numbers FAAC-1 and -2 were removed from the barrel arm region, FATL-1 from the barrel tail shaft, and FBAC-1 from between arms.

The test was conducted in a Budd tension-tension machine at a frequency of 25 Hz. Crack length was monitored via electrical resistance gages which permitted detection in 0.010-inch increments. The first specimen was subjected to a conventional fracture toughness test per ASTM E399. The remaining specimens were tested cyclically to evaluate the crack propagation behavior of the material. The three crack propagation specimens were tested at R values of 0.1, 0.4, and 0.7, respectively, where R is the ratio of minimum to maximum stress. Cracking was initiated and extended to a minimum of 0.50 inch on a side at an R value of 0.1. At this point the load ratio was changed to effect the desired R test value under investigation. This required from 17,400 cycles to 37,200 cycles for the group. The crack propagation specimens were tested beyond the subcritical crack growth stage to the onset of rapid fracture. The crack length at fracture was utilized to calculate a dynamic K_{IC} for each of the fatigue specimens.

Table 10 summarized the room-temperature results, which indicate the average critical stress intensity factor to be 51.1 ksi $\sqrt{in.}$. This compares favorably with 6Al-4V titanium plate stock heat treated to the same level.

TABLE 10. FORGING CRITICAL STRESS INTENSITY FACTOR		
Specimen	Type Test	K_{IC} ksi $\sqrt{in.}$
FAAC-1	Static Fracture Toughness	52.8
FAAC-2	Cyclic Crack Propagation	53.0
FATL-1	Cyclic Crack Propagation	44.3
FBAC-1	Cyclic Crack Propagation	54.3

Fracture toughness testing also established the maximum size material flaw that would be permitted in barrel forgings produced in production quantities. Standard practice at Hamilton Standard defines flaws in three classes as a function of size;

namely, class A 0.03 inch, class B 0.06 inch and class C 0.09 inch. Assuming a circular flaw as the most severe shape detectable by an orthogonal ultrasonic inspection scan, and using the minimum and maximum K_{IC} and yield strength values obtained in this program, results in minimum and maximum critical flaw sizes of 0.107 and 0.160, respectively. As these values are within the minimum barrel wall thickness of 0.190 inch, critical crack growth is possible. Consequently, a class B maximum flaw size requirement is desired to prevent crack growth in barrels manufactured for this program.

Experimental Stress Analysis (ESA)

The experimental stress analysis of the titanium barrel/Borsic aluminum spar retention system employed first a brittle lacquer and then strain gaging. The purpose of this test was to determine the actual barrel and blade spar retention stresses, under controlled loading conditions, and to correlate these results with computer theoretical stress analysis. Propeller barrel number one and spars numbers five, six, and seven were employed. One of the three sets of Gothic-arch bearing race inserts was superficially plated with gold to provide a record of Hertzian load impressions. The plating, as applied, is rather lackluster but upon loading, polishes quite readily to a highly discernible pattern.

Stresscoat, the brittle lacquer, was applied to the outside of the barrel and the test spars. Strain gages were also installed at selected locations inside the barrel and spars in those areas considered to be high-stress locations, but could not be viewed. The test configuration was incrementally loaded, by means of a preload internal wedge system that applied axial loading through the spars and into the barrel. Load levels of 25,000 pounds, 35,000 pounds and 45,000 pounds were explored to insure that the behavior of the retention was linear with load. Figure 20 shows the test configuration under centrifugal loading. Bending moment was applied by pushing and/or pulling on the spars either in the in-plane or the out-of-plane direction, as referenced to the propeller plane of rotation, while the barrel remained fixed. Bending moments of 20,000 inch-pounds, 40,000 inch-pounds and 60,000 inch-pounds were applied. Figure 21 shows the typical test setup, in this instance the 1P in-plane mode. Centrifugal loading was measured via strain gaging on the internal preload system. Moment was measured by spar gaging and extrapolated to the midpoint of the retention; i.e., 6 1/4-inch blade station.

No stresscoat crack patterns were observed on the test spars due to centrifugal loading. As the sensitivity of the brittle lacquer was 0.00072 inch/inch, the equivalent of 27,600 psi, any stressing less than this value could not be detected. Crack patterns were recorded on the barrel. They are shown in Figures 22 through 27. The arrows indicate the direction of cracking, which is perpendicular to the direction of principal stress.

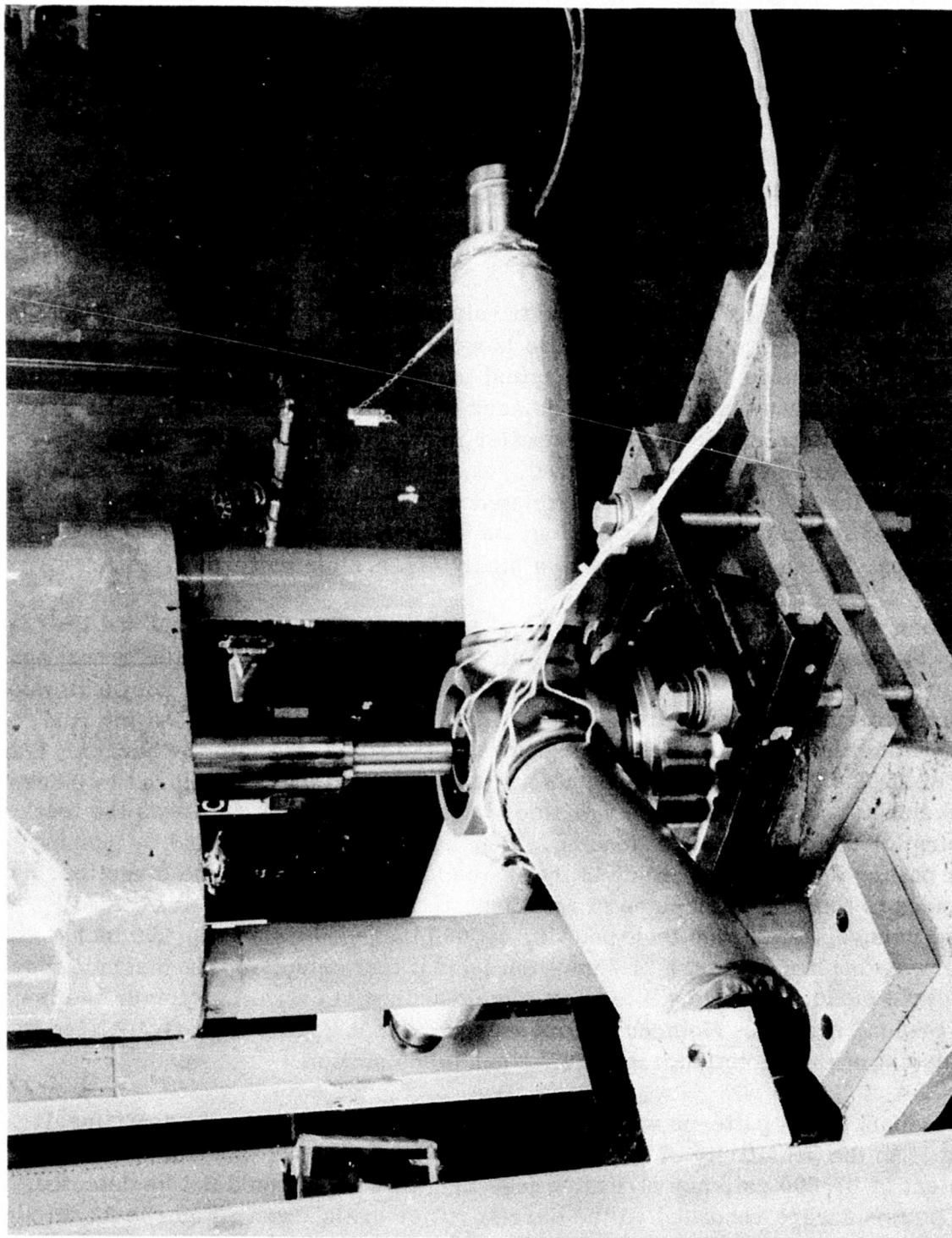
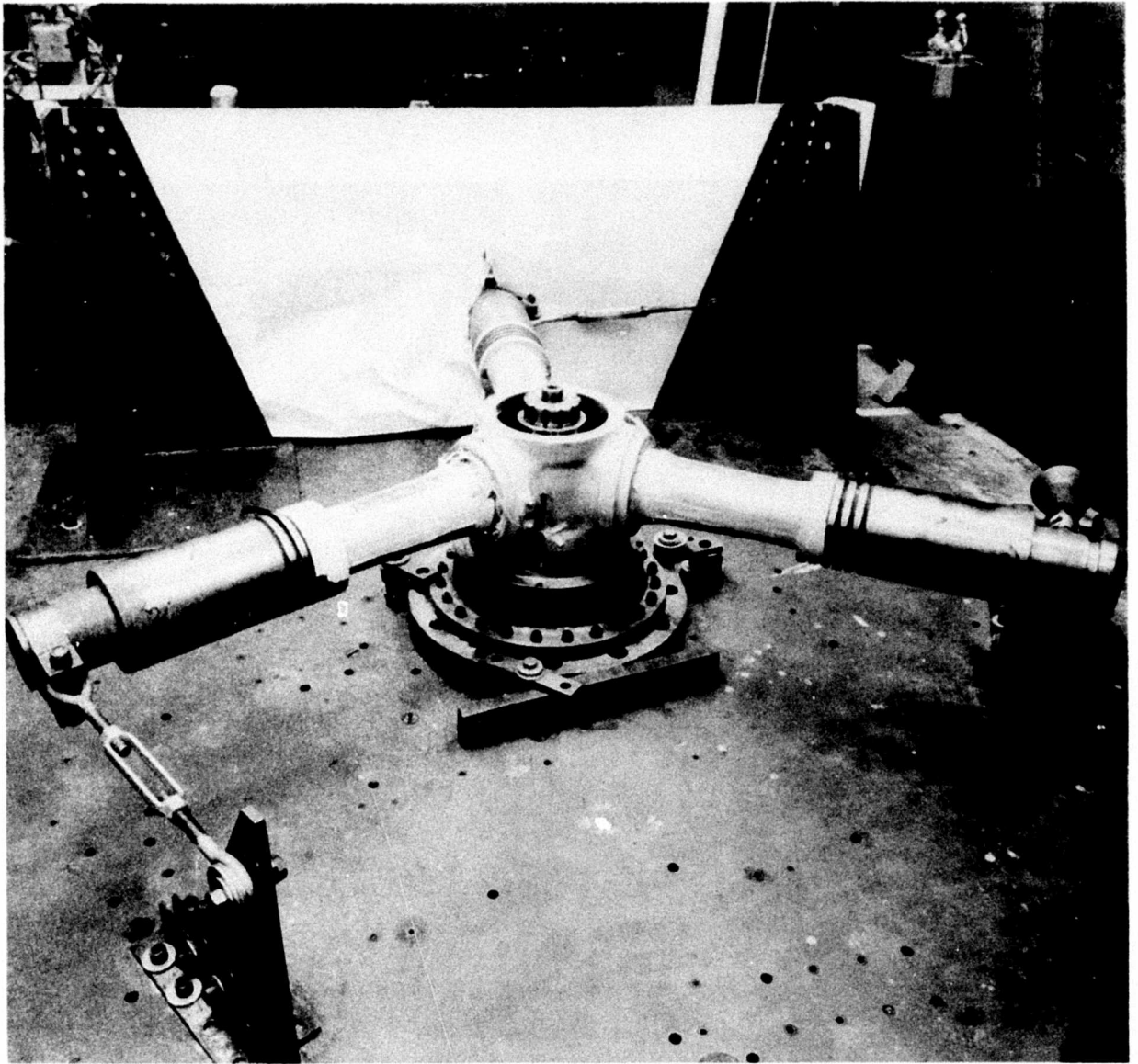


FIGURE 20. CENTRIFUGAL LOAD TEST SETUP



**FIGURE 21. EXPERIMENTAL STRESS ANALYSIS TEST SETUP,
IP-IN PLANE EVALUATION**

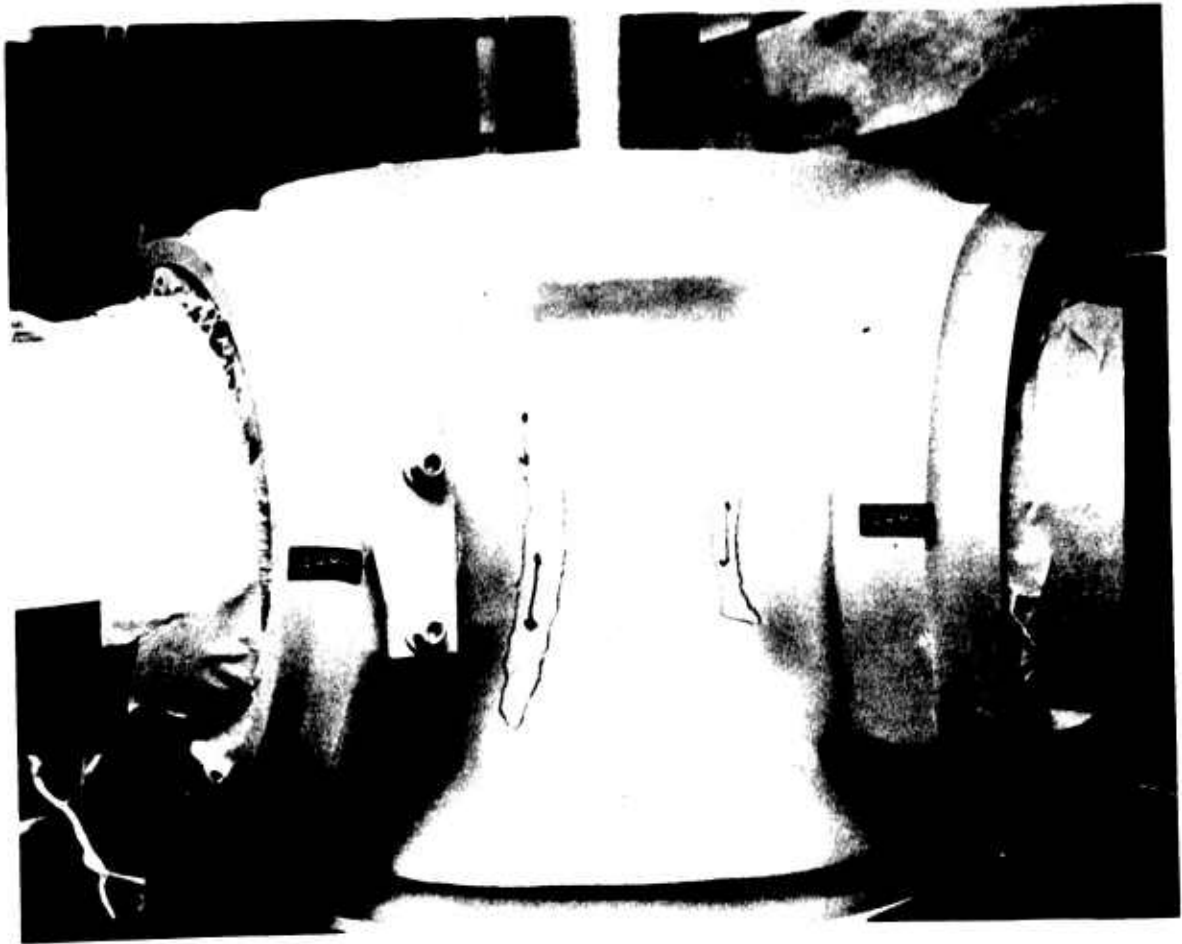


FIGURE 22. CENTRIFUGAL LOAD BRITTLE LACQUER PATTERNS
(046,000 POUNDS), ARMS 5 AND 6

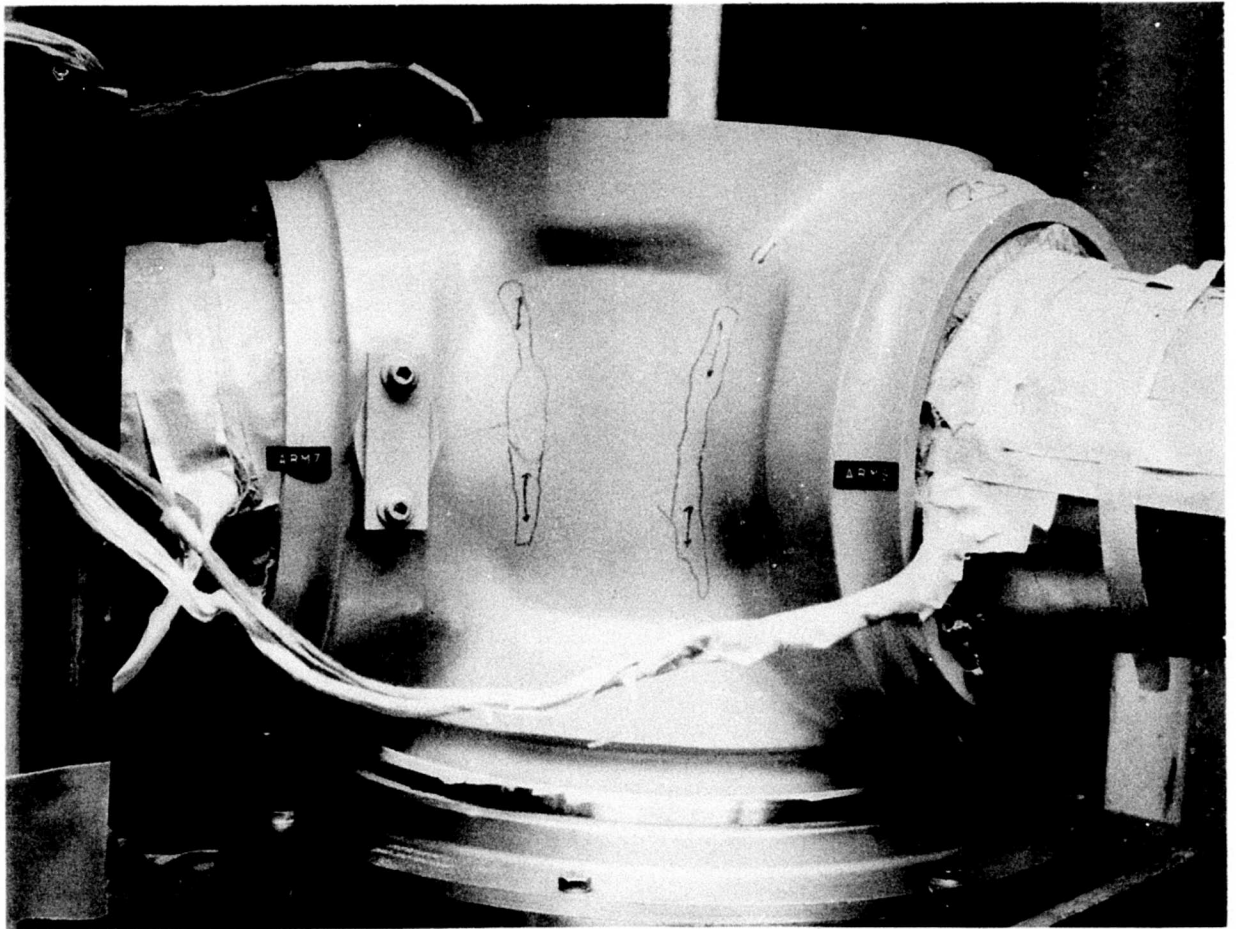
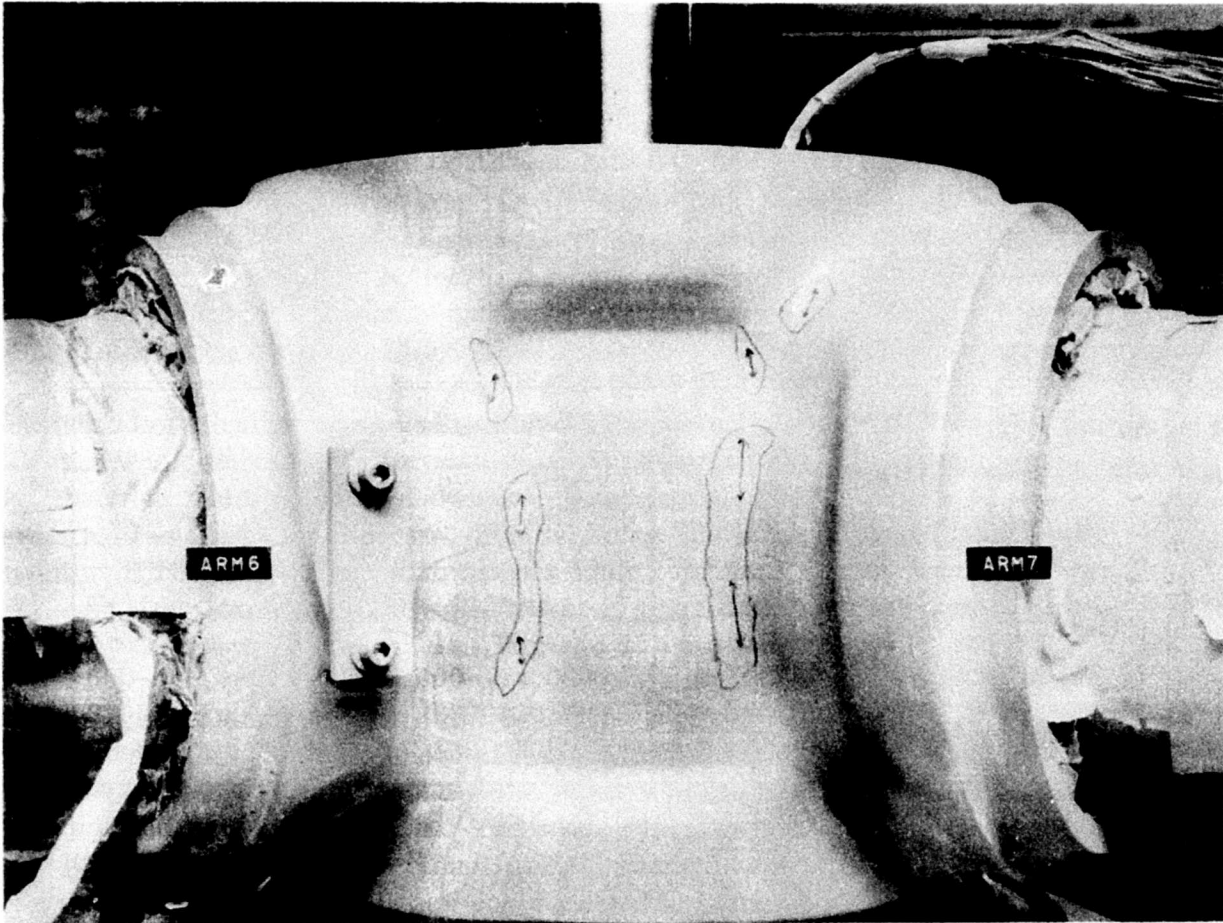


FIGURE 23. CENTRIFUGAL LOAD BRITTLE LACQUER PATTERNS
(46,000 POUNDS), ARMS 5 AND 7



**FIGURE 24. CENTRIFUGAL LOAD BRITTLE LACQUER PATTERNS
(46,000 POUNDS), ARMS 6 AND 7**



FIGURE 25. 1P OUT-OF-PLANE BRITTLE LACQUER PATTERNS
(62,500 INCH-POUNDS), ARM 3

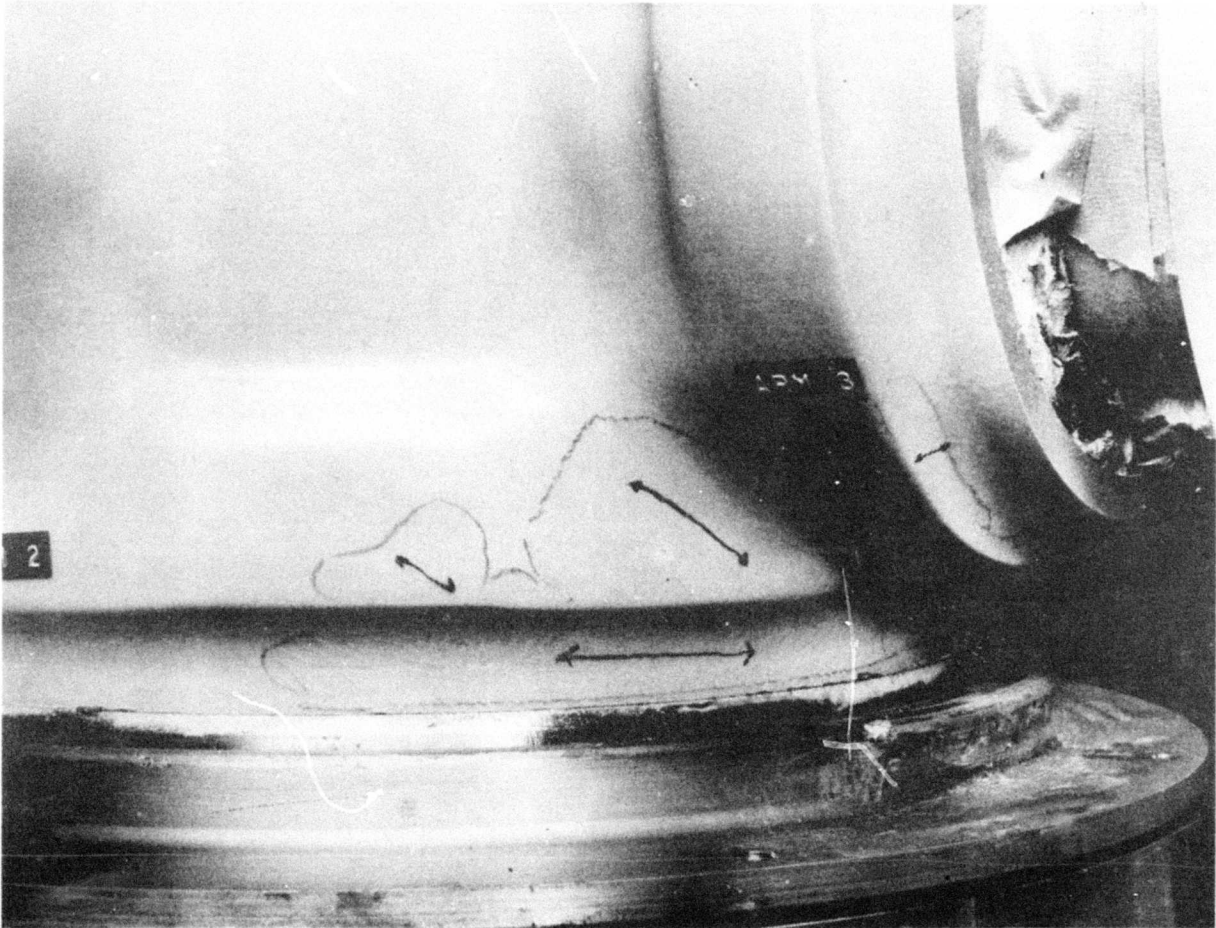


FIGURE 26. 1P OUT-OF-PLANE BRITTLE LACQUER PATTERNS
(62,500 INCH-POUNDS), ARM 3

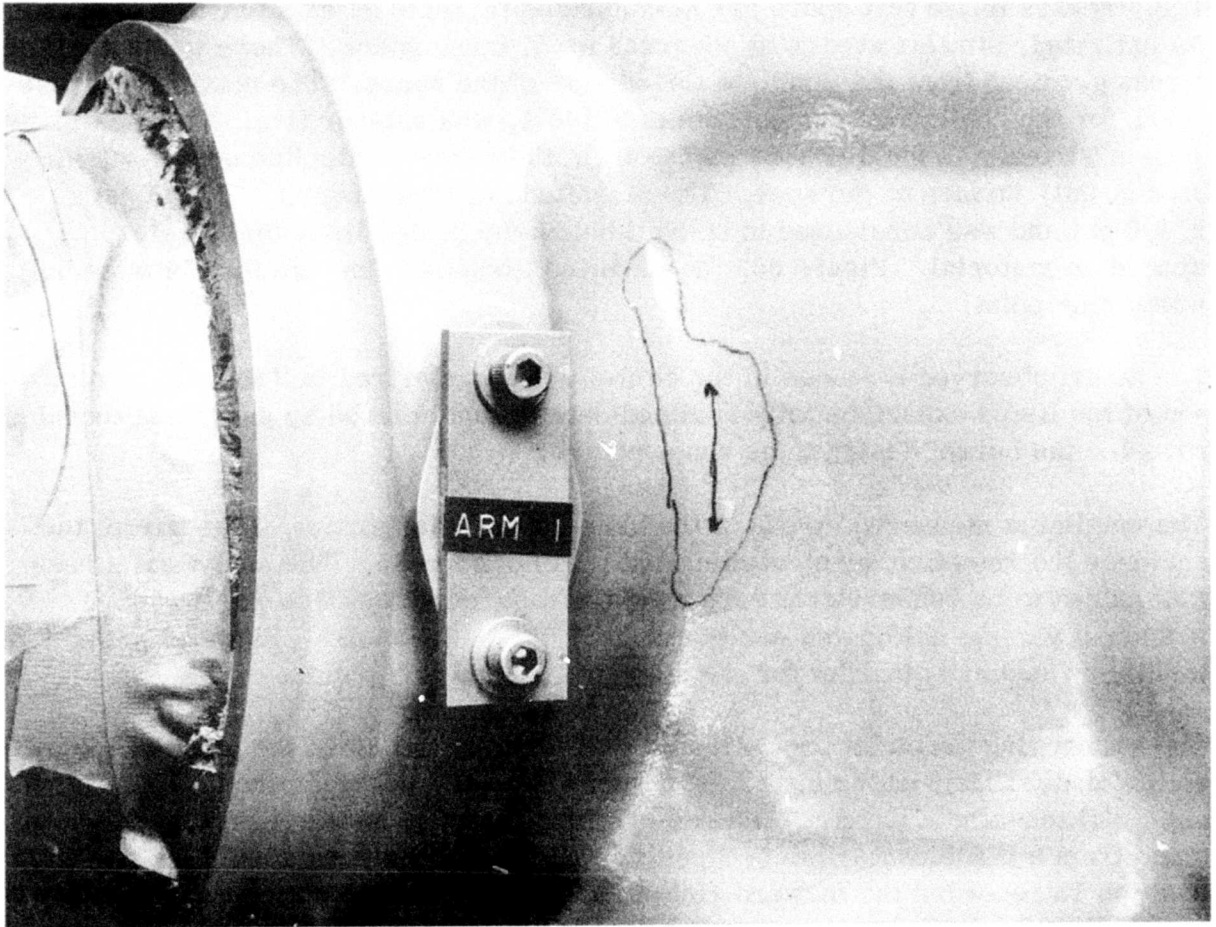


FIGURE 27. 1P IN-PLANE BRITTLE LACQUER PATTERN
(59, 200 INCH-POUNDS), ARM 1

As a consequence of the brittle lacquer evaluation, strain gages were mounted in those locations showing highest stress. The test spar gage installation involved 57 gages at the locations shown in Table 11. The barrel gage installation involved 37 gages, as illustrated in Figures 28 through 34.

The loading modes performed for the brittle lacquer evaluation were repeated during the strain gage evaluation. An additional 3P-00P test mode was also repeated.

The stresses in the test spars are summarized in Table 11 as a function of load. As indicated, similar stressing occurred in all three spars. There was a negligible stress gradient from the inside to the outside of the spars. The maximum stressed spar, for the continuous design case of Table 4, was number five. The maximum area of stress was located 9.19 inches from the barrel centerline on the outside bottom (aft) surface of the spar. The magnitude of stressing was $11,295 \text{ psi} \pm 9,480 \text{ psi}$ and was considered to be well below the design limit for Borsic aluminum material. Figure 35, the modified Goodman diagram for the material, shows this point.

The actual observed stresses in the barrel are summarized in Table 12. Comparison of the listed experimentally obtained data to that derived by analytical techniques revealed the barrel design to be conservative.

The maximum measured stress in the barrel arm, that portion of the barrel that encloses the retention area, occurred at gage location 35. The analytical stress was judged to be conservative because the measured stress was $13,760 \text{ psi} \pm 9,820 \text{ psi}$ vs. the calculated value of $25,187 \text{ psi} \pm 13,838 \text{ psi}$. Figure 36, the modified Goodman diagram for the material, shows this point.

The barrel rings are that part of the barrel forward and aft of the plane of the propeller blades. For each ring, a section of symmetry is determined. With this design, a three-bladed barrel, the section of symmetry is 60 degrees; i.e., the distance from a blade centerline to a position midway between adjacent blades. Gage location 12 recorded the forward ring stress at the 60-degree station. The analytical stress was again conservative because the measured stress was $13,760 \text{ psi} \pm 9,820 \text{ psi}$ vs. $22,290 \text{ psi} \pm 20,970 \text{ psi}$. Gage location 7 recorded an aft ring stress, at the 60-degree station, of $16,530 \text{ psi} \pm 6,920 \text{ psi}$. This was also conservative, as the calculated value was $26,050 \text{ psi} \pm 19,970 \text{ psi}$.

At the blade centerline the fibers in the forward and aft rings and in the barrel arm are identical and are strained by the hoop action of each other. Maximum hoop stress is therefore a combination of both analyses. Gage location 18 recorded the combined barrel arm/forward ring hoop stress as $9,740 \text{ psi} \pm 5,660 \text{ psi}$. The actual stress was conservative as the calculated value was $14,990 \text{ psi} \pm 10,970 \text{ psi}$.

TABLE 11. BORSIC ALUMINUM SPAR LOAD SPECTRUM AND STRESS SUMMARY (SHEET 1 of 2)

Test Bar	From Blade Butt Face Station	Gage Data			Coordinate	Number	Centrifugal Load			Bending Moment		
		Direction	Surface	Direction			25,000 lb.	35,000 lb.	45,000 lb.	20,000 in.-lb.	40,000 in.-lb.	60,000 in.-lb.
5	6.05	Longitudinal	Outside	0°	501	4700	6540	460	2600	5200	7000	
	6.05	Longitudinal	Outside	90°	511	3440	4970	6390	--	--	--	
	6.05	Longitudinal	Outside	180°	521	4775	6685	5395	2400	5200	7000	
	6.05	Longitudinal	Outside	270°	531	925	1295	1665	--	--	--	
	6.05	Longitudinal	Inside	180°	521A	5550	7770	9990	2660	5320	7900	
	7.14	Longitudinal	Outside	0°	502	5825	8155	10485	3160	6320	9400	
	7.14	Longitudinal	Outside	90°	512	4675	6545	4415	--	--	--	
	7.14	Longitudinal	Outside	180°	522	6000	8400	10800	3180	6360	9540	
	7.14	Longitudinal	Outside	270°	532	5075	7105	9135	--	--	--	
	7.14	Hoop	Outside	0°	502H	-950	-1330	-1710	--	--	--	
	7.14	Hoop	Outside	90°	512H	-1200	-1680	-2160	--	--	--	
	7.14	Longitudinal	Inside	0°	502A	5550	7770	9990	2720	5440	8160	
	7.14	Longitudinal	Inside	180°	522A	5900	8260	10620	2800	5600	8400	
	7.14	Hoop	Inside	0°	502HA	-1325	-1855	-2385	--	--	--	
	6	9.19	Longitudinal	Outside	0°	503	5900	8260	10620	3160	6320	9400
9.19		Longitudinal	Outside	90°	513	5150	7210	9270	--	--	--	
9.19		Longitudinal	Outside	180°	523	6275	8755	11295	3160	6320	9400	
9.19		Longitudinal	Outside	270°	533	5675	7945	10215	--	--	--	
9.19		Longitudinal	Inside	180°	523A	6175	8645	11115	2720	5440	8160	
9.19		Hoop	Outside	0°	504H	-1275	-1785	-2295	--	--	--	
9.19		Hoop	Outside	90°	513H	-1675	-2345	-3015	--	--	--	
11.15		Longitudinal	Outside	0°	504	5750	8050	10350	3000	6000	9000	
11.15		Longitudinal	Outside	180°	524	6325	8855	11385	3060	6120	9100	
13.15		Longitudinal	Outside	0°	505	5650	7910	10170	2880	5760	8640	
13.15		Longitudinal	Outside	180°	525	6425	8995	11565	2880	5760	8640	
6		6.18	Longitudinal	Outside	0°	601	5050	7070	9090	2700	5100	7100
		6.18	Longitudinal	Outside	90°	611	4000	5600	7200	--	--	--
		6.18	Longitudinal	Outside	180°	621	4975	6965	9555	2680	5360	7540
		6.18	Longitudinal	Outside	270°	631	4125	5775	7425	--	--	--
	7.28	Longitudinal	Outside	0°	602	5075	7105	9135	2880	5760	8640	
	7.28	Longitudinal	Outside	90°	612	4325	6055	7785	--	--	--	
	7.28	Longitudinal	Outside	180°	622	5550	7770	9990	3060	6120	9100	
	7.28	Longitudinal	Outside	270°	632	4525	6335	8145	--	--	--	
	9.28	Longitudinal	Outside	0°	603	5350	7490	9630	3000	6000	9000	
	9.28	Longitudinal	Outside	90°	613	5250	7350	9450	--	--	--	
	9.28	Longitudinal	Outside	180°	623	5975	8365	10755	3160	6320	9400	
	9.28	Longitudinal	Outside	270°	633	6450	7630	9910	--	--	--	
	11.30	Longitudinal	Outside	0°	604	5350	7490	9630	2880	5760	8640	
	13.30	Longitudinal	Outside	180°	624	5875	8225	10575	2960	5920	8400	
	13.30	Longitudinal	Outside	0°	605	5125	7175	9225	2780	5560	8340	
13.30	Longitudinal	Outside	180°	625	6375	8925	11475	2980	5960	8940		

TABLE 11. BORSIC ALUMINUM SPAR LOAD SPECTRUM AND STRESS SUMMARY (SHEET 2 of 2)

Test Bar	From Blade Butt Face Station	Cage Data			Centrifugal Load			Bending Moment			
		Direction	Surface	Coordinate	Number	25,000 lb.	35,000 lb.	45,000 lb.	20,000 in.-lb.	40,000 in.-lb.	60,000 in.-lb.
7	6.23	Longitudinal	Ca' side	0°	701	4700	6580	~160	2680	5360	~040
	6.23	Longitudinal	Outside	90°	711	3800	5320	~440	--	--	--
	6.23	Longitudinal	Outside	180°	721	4325	6055	7785	2480	4960	7440
	7.33	Longitudinal	Outside	270°	731	3950	5530	7110	--	--	--
	7.33	Longitudinal	Outside	0°	702	5775	8085	10395	3180	6360	9540
	7.33	Longitudinal	Outside	90°	712	5075	7105	9135	--	--	--
	7.33	Longitudinal	Outside	180°	722	5775	8085	10395	3160	6320	9480
	7.33	Longitudinal	Outside	270°	732	4675	6545	~115	--	--	--
	9.33	Longitudinal	Outside	0°	703	5625	7875	10125	3000	6000	9000
	9.33	Longitudinal	Outside	90°	713	5200	7280	9360	--	--	--
	9.33	Longitudinal	Outside	180°	723	5825	8155	10485	3040	6080	9120
	9.33	Longitudinal	Outside	270°	733	5220	7280	9360	--	--	--
	11.33	Longitudinal	Outside	0°	704	5700	7980	10260	2940	5880	8820
	11.33	Longitudinal	Outside	90°	724	5875	8225	10575	2920	5840	8760
	13.33	Longitudinal	Outside	0°	705	5925	8295	10665	2880	5760	8640
	13.33	Longitudinal	Outside	180°	725	6150	8610	11070	2920	5840	8760

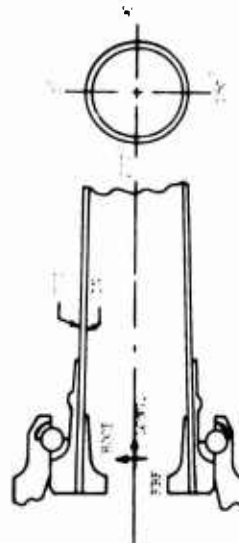




FIGURE 28. STRAIN-GAGE INSTALLATION. LOCATIONS 1 THROUGH 6

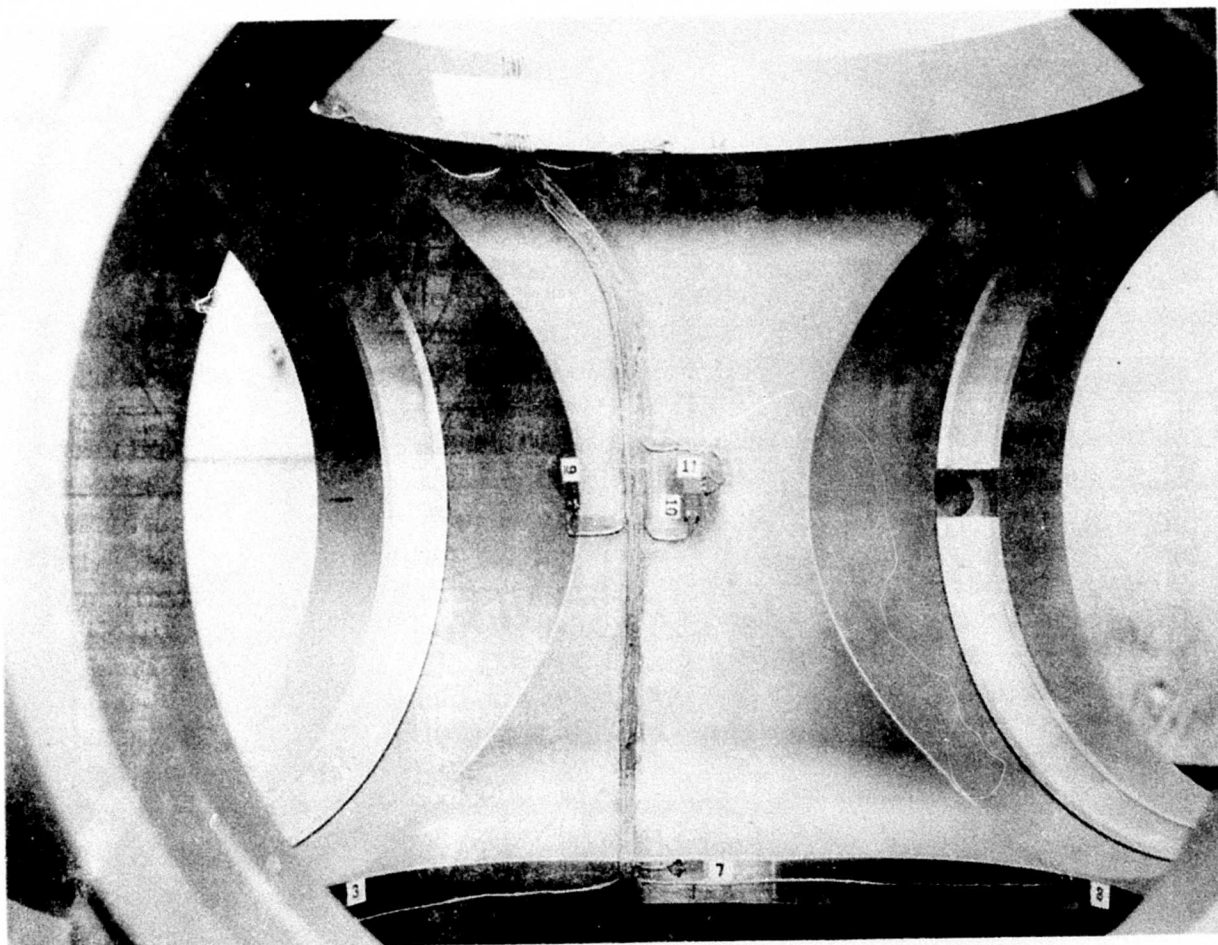


FIGURE 29. STRAIN-GAGE INSTALLATION, LOCATIONS 7 THROUGH 11

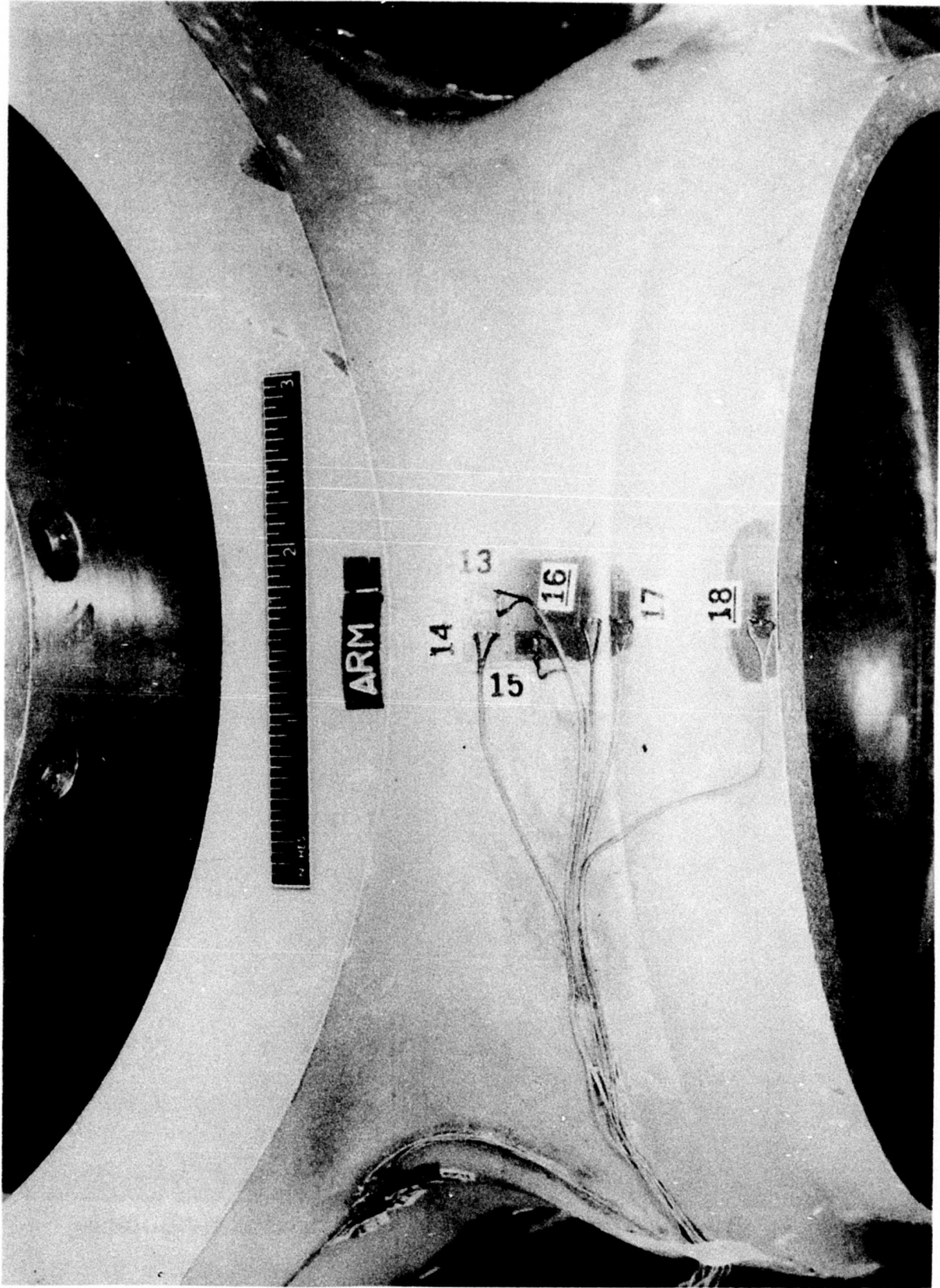


FIGURE 30. STRAIN-GAGE INSTALLATION, LOCATIONS 13 THROUGH 18

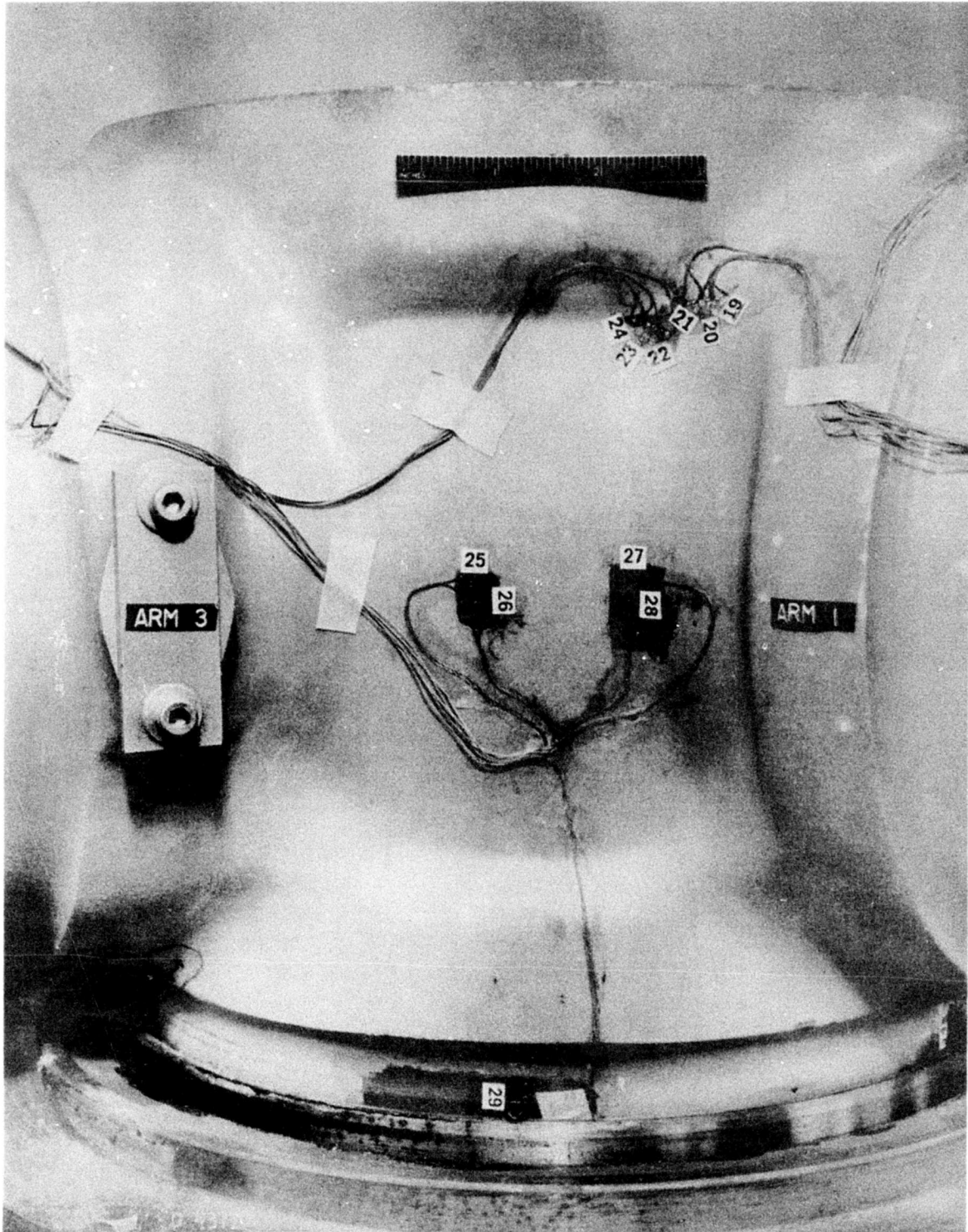


FIGURE 31. STRAIN-GAGE INSTALLATION, LOCATIONS 25 THROUGH 29

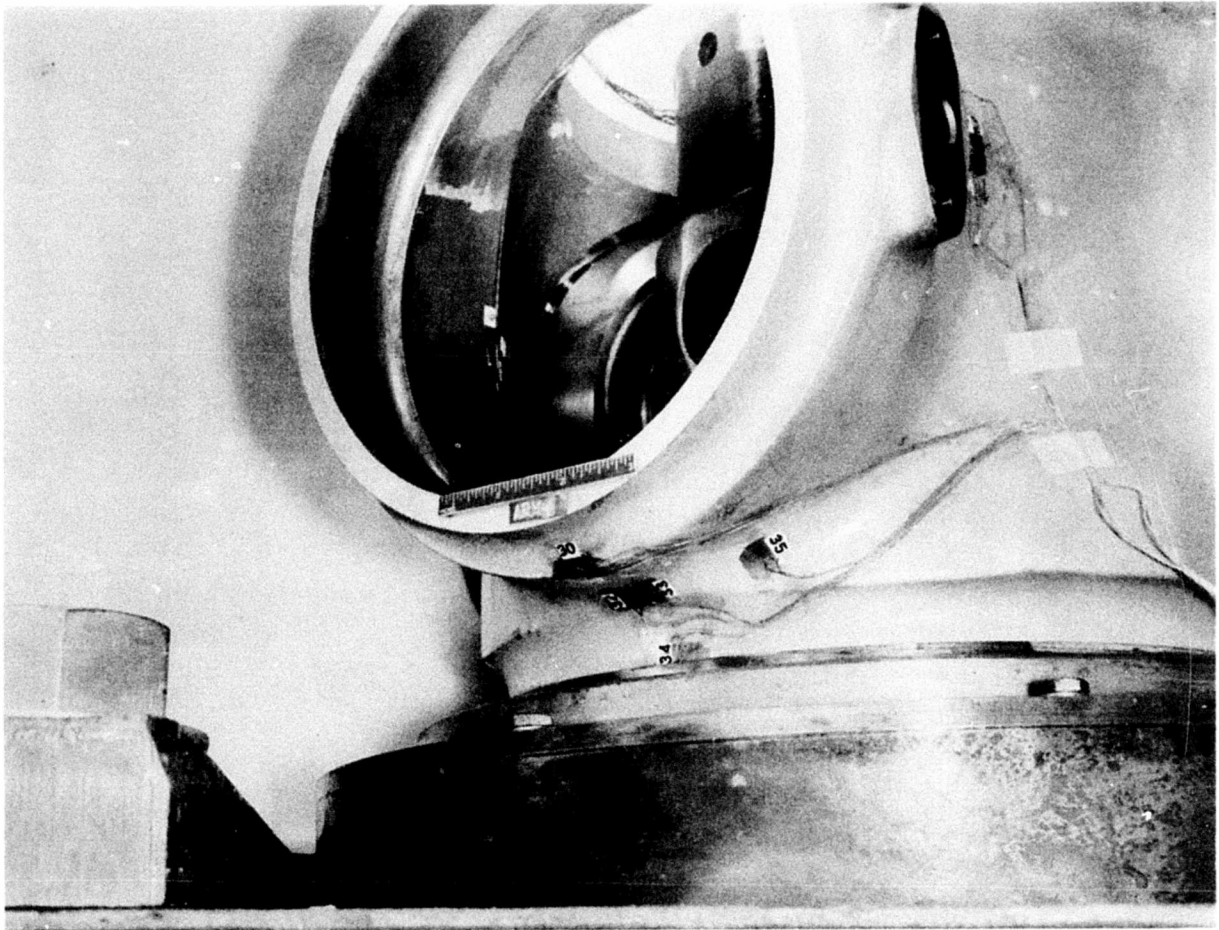


FIGURE 32. STRAIN-GAGE INSTALLATION, LOCATIONS 30 AND 32 THROUGH 35

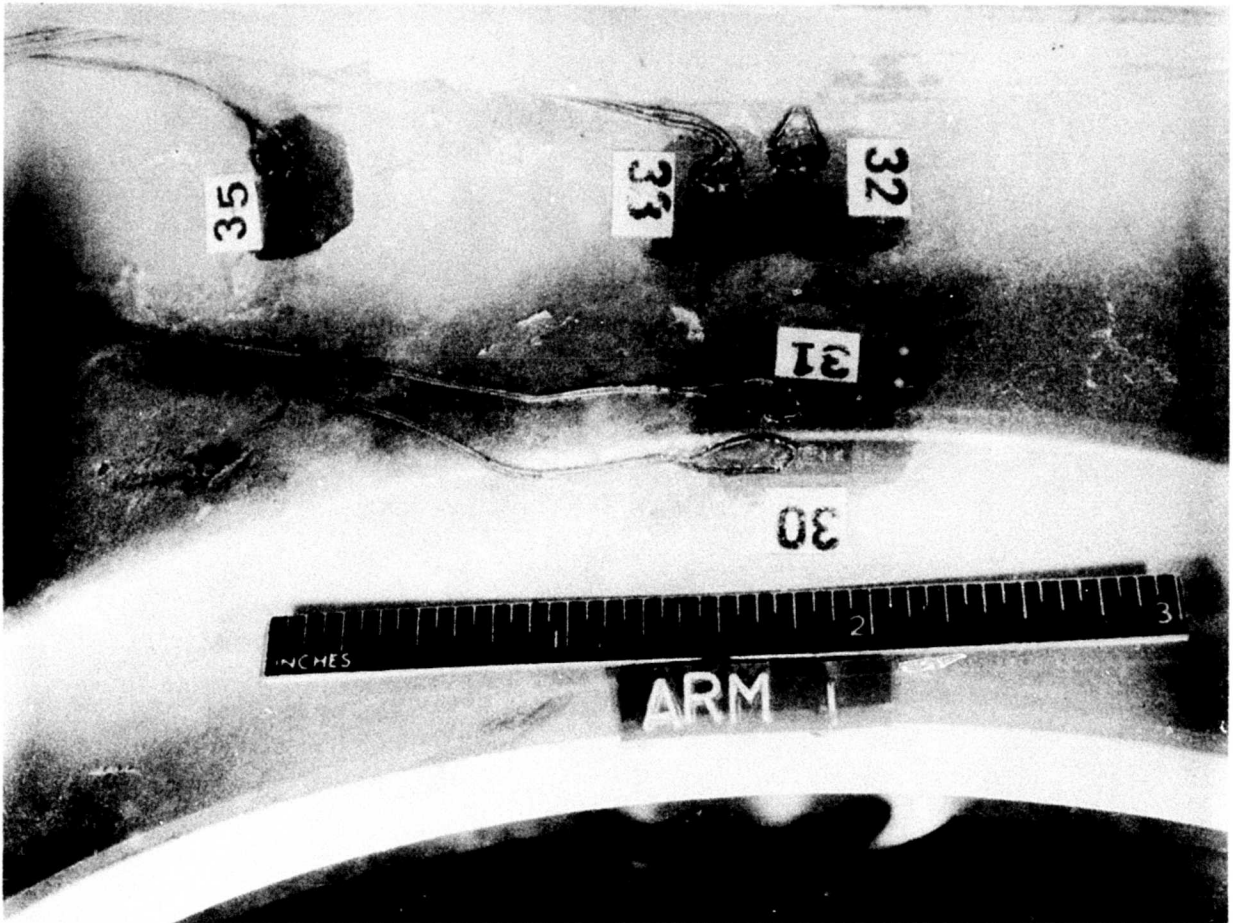


FIGURE 33. STRAIN GAGE-INSTALLATION, LOCATIONS 30 THROUGH 33 AND 35

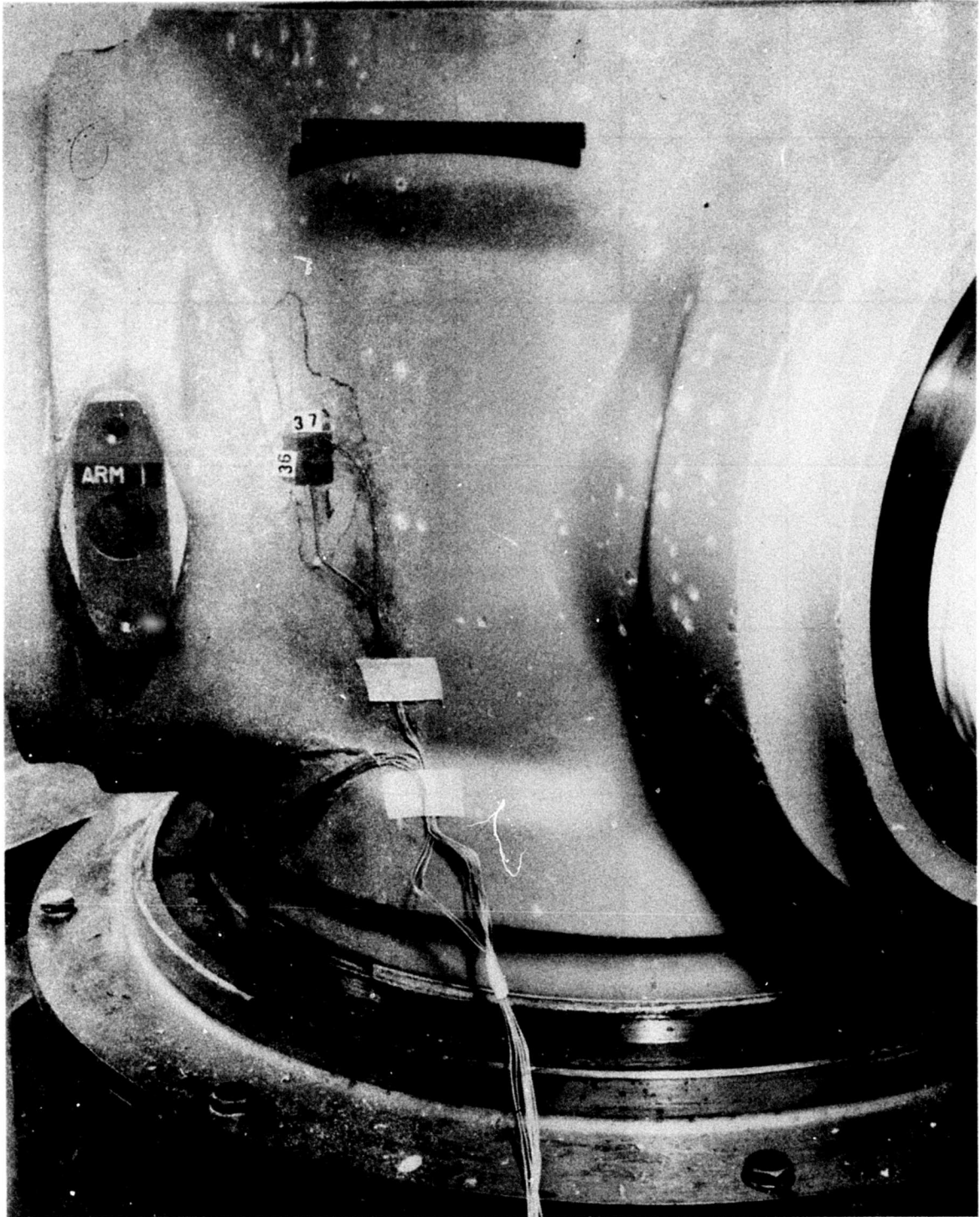


FIGURE 34. STRAIN-GAGE INSTALLATION, LOCATIONS 36 AND 37

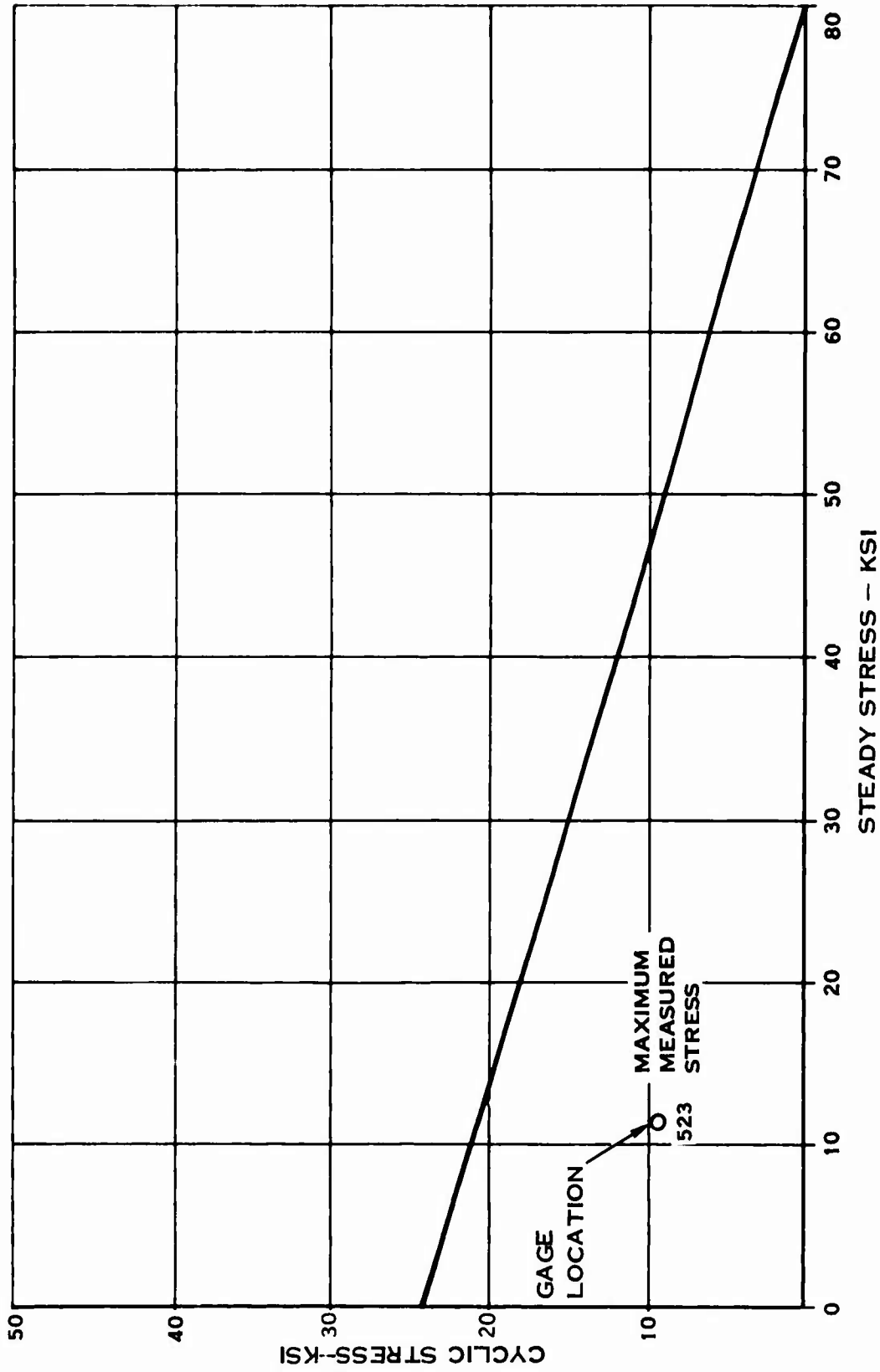
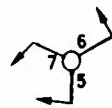


FIGURE 35. BORSIC ALUMINUM SPAR ESA TEST RESULTS

TABLE 12. TITANIUM BARREL LOAD SPECTRUM AND STRESS SUMMARY

Gage Location	Centrifugal Load (lb)	1P-1P (psi)	1P-1P (psi)	1P-(X)P (psi)	1P-(O)P (psi)	1P-(O)P (psi)	3P-(O)P (psi)
1	5552	1712	1424	-5392	4288	2048	240
2	8512	2000	1712	-4740	3392	1600	-704
3	5984	1600	944	2960	-3680	-3120	-2624
4	10544	720	976	4080	-6160	-2144	-1728
5	480	680	752	-6608	6752	3872	1408
6	10512	480	400	-2672	1232	1568	1712
7	12064	3008	-1568	-1920	2832	6832	6400
8	6176	-2928	-4112	-2720	1360	-2304	-1552
9	-7760	-1200	-2160	-1920	3952	4032	1552
10	-1487	-316	-949	-749	1633	2794	658
11	18081	-6495	4995	63	2778	2166	1445
12	13376	6960	-5072	4752	-4608	-9072	-6432
13	-5458	-114	564	-2119	4274	1495	5670
14	2395	46	-39	1204	914	-192	2101
15	2432	960	400	-4320	2624	1328	4720
16	7440	-128	-208	3504	-1440	-1168	-720
17	8592	-80	-112	4256	-2192	-1680	-1360
18	7680	-240	-288	6864	-3360	-1920	-3312
19	P = 19612	P = -2375	P = 11906	P = 5388	P = -635	P = -875	P = -1004
20	Q = 3931 = 18°	Q = -11797 = 16.6°	Q = 2448 = 18.8°	Q = 1355 = 27.5°	Q = -4736 = 31.1°	Q = -4428 = 6.2°	Q = -4367 = 17.2°
21	P = 17612	P = -2454	P = 9343	P = 4752	P = 649	P = 869	P = 512
22	Q = -1978	Q = -9546	Q = 1286	Q = 139	Q = -3575	Q = -1760	Q = -2450
23	P = -11.7°	= -21.2°	= -18.8°	= 1.8°	= -2.3°	= 23.2°	= -18.8°
24	3246	-1783	2008	-16	269	-589	-141
25	6926	-2743	3066	-53°	417	-97	-42
26	19130	-12070	10764	2416	-795	1106	1164
27	10859	-6741	6173	1013	178	1500	1053
28	-7568	-1840	-480	-1296	2400	3056°	-992
29	9152	-368	-320	-2256	3696	1760	3808
30	8000	-144	-304	-1648	3472	1520	2768
31	-6560	288	400	-3120	4240	2640	480
32	-6400	0	848	-1920	4000	2448	128
33	-2240	720	528	-6208	1128	4000	1040
34	-2544	720	-272	-6544	6400	2224	3200
35	10367	6785	-6585	1336	60	-719	566
36	19782	13284	-12615	3281	-2094	-1543	-86
37							



1P-1P



1P-1P



1P-(O)P



1P-(O)P



1P-(O)P



3P-(O)P

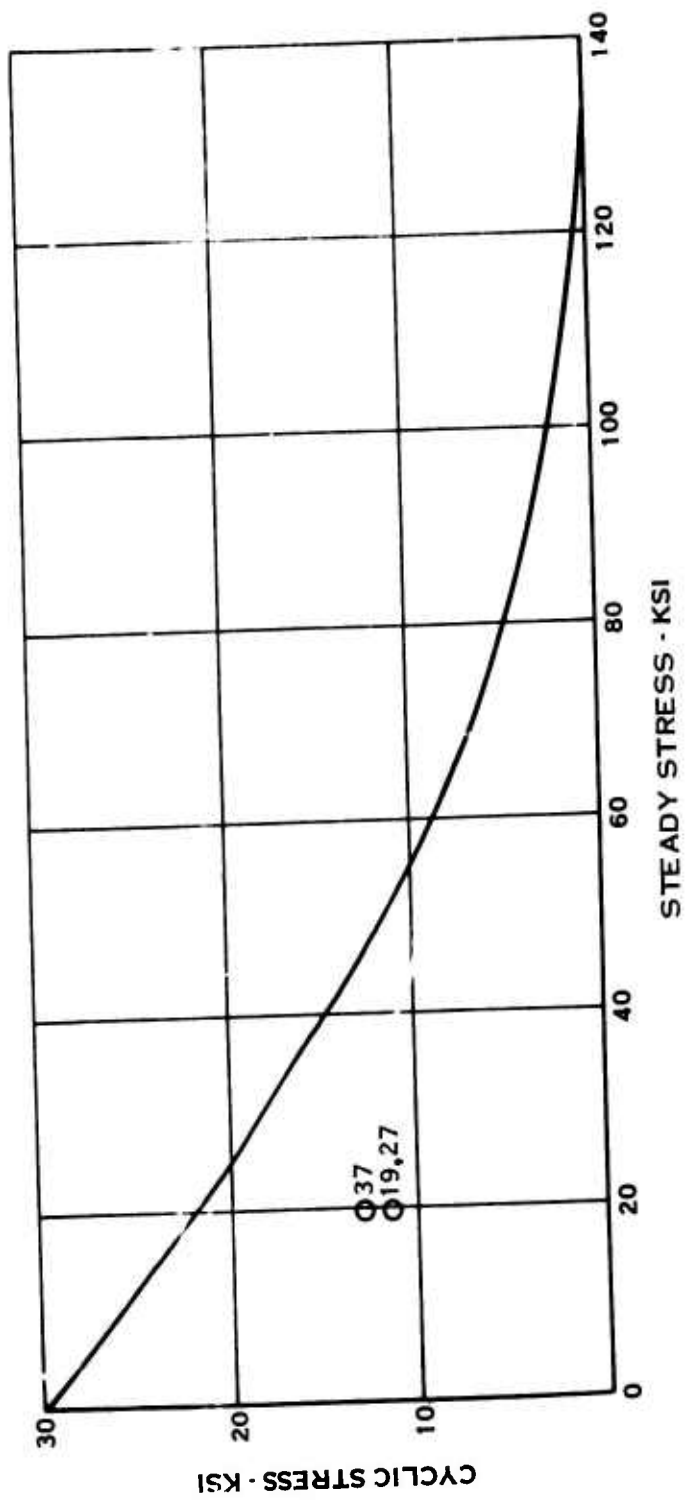


FIGURE 36. TITANIUM BARREL DESIGN FATIGUE STRENGTH

The tail-shaft blend area of the barrel is subjected to complex loading. The blend region transfers 1P bending moment and thrust from the barrel hub into the tail shaft. Loadings such as centrifugal force and steady bending moment, which are reacted elastically in the hub and not transferred to the tail shaft, cause distortion and stressing of the blend region. Similarly, bearing reaction loading on the tail shaft also causes distortion and stressing of the blend region. The analytical stress again was conservative; i. e. , 10,250 psi \pm 10,090 psi vs. 9,760 psi \pm 5,790 psi.

The tail shaft, that portion of the barrel beyond the blend, supports the angular contact tapered roller bearing. The most significant tail shaft stresses arise from 1P vibratory bending moment and bearing reaction loads. Gage location 5 recorded the stress at the inside of the tail shaft, again, conservative. The actual stress was 1,380 psi \pm 7,200 psi. The calculated stress was 1,320 psi \pm 13,230 psi.

An additional comparison was made at the inside of the barrel midway between the \pm forward and aft rings. Analysis indicated a stress of -26,580 psi \pm 3,200 psi, while the actual recorded stress was -670 psi \pm 2,530 psi.

The ESA results were further analyzed to establish the margins of safety and to identify the potential weight reduction resulting from these margins. This analysis considered four distinct loading conditions. Case 1 was the 1P-OOP fatigue test condition. Case 2 was the continuous design condition of Table 4. test results indicated that some of the gage locations were more sensitive to in-plane than to out-of-plane loading, two additional cases were studied. Cases 3 and 4 orientate the 1P moment loading midway between the in-plane and out-of-plane directions. The resultant IP moment thus becomes equal in-plane and out-of-plane components of 46,000 inch-pounds. This orientation is consistent with typical aircraft loading and thus allows a realistic assessment of the effects of in-plane 1P moment loading. The load spectrum for each case is shown in Table 13.

TABLE 13. LOAD SPECTRUM, WEIGHT REDUCTION					
Case	Centrifugal Force (lb)	Steady Bending Moment		1P Bending Moment	
		Out-of-Plane (in. -lb)	In-Plane (in. -lb)	Out-of-Plane (in. -lb)	In-Plane (in. -lb)
1	45,000	0	0	65,000	0
2	45,000	35,000	0	65,000	0
3	45,000	0	0	46,000	46,000
4	45,000	35,000	0	46,000	46,000

All gage locations were analyzed for the most severe of the four loading conditions shown above. The resultant stressing and margins of safety are presented in Table 14.

Inspection of Table 14 reveals the minimum margin of safety to be 53% at gage location 37. The measured stress at the location was 20,650 psi \pm 11,410 psi for case 3. The actual weights of the two barrels manufactured during this program were 46.9 pounds and 47.2 pounds. The potential for weight reduction was explored on the basis of the stressing at location 37. In order to achieve a reduction in weight, it is necessary to reduce the wall thickness throughout the barrel. The most severe increase in stress, for a given wall thickness change, can be found by the ratio $(t_0/t)^2$. At location 37 this amounts to a ratio of 1.24. If all barrel wall thicknesses were reduced by this ratio, a 19% weight reduction could be attained and the design objective of 38 pounds realized.

As it may not be practical to reduce all the walls by 19%, greater reductions could be accomplished in the lower stressed areas and lesser reductions in the higher stressed areas, thereby maintaining adequate margins of safety. Rework and re-test to demonstrate compliance with the design objective was not conducted, as this effort was outside the scope of the program.

Visual inspection of the two sets of bearing race inserts, to assess load distribution of the retention system, was quite satisfactory. Figures 37 and 38 show the inner and outer Gothic-arch bearing race insert Hertzian impression patterns, respectively. The lengths of the patterns were not excessive, and there was no "roll-off" over the edges of the inserts.

Fatigue Strength Investigation (FSI) 3P-OOP (First Test)

The purpose of the FSI was to determine the structural characteristics and fatigue load capacity of the titanium barrel/Borsic aluminum spar retention system. The 3P phase of the FSI was specifically concerned with subjecting the barrel arm region to the complex loadings arising from out-of-plane vibratory bending moment.

Following the ESA, the same test hardware was reassembled, the maximum centrifugal load locked in, the assembly mounted on an electromagnetic vibration motor for the FSI, and the barrel cavity filled with MIL-L-7808 lubricating oil. The vibration motor excited the assembly in a 3P-OOP mode; i.e., each test spar vibrated out-of-plane of normal propeller rotation at a simulated frequency of three times the speed of propeller rotation. 3P indicates zero-degree bending moment phasing between barrel arms, and OOP indicates the loading to be in the direction out-of-plane of rotation. The actual test frequency was set at the natural frequency of the system because of the low power required to drive the system and because of the rapid accumulation of cycles at this frequency as opposed to the actual frequency of 3P vibration in an aircraft. The actual natural frequency of the system was 45 Hz. Each arm of the barrel was tuned by adjusting the position of tip weights located at the end of each spar in order to insure that all arms vibrated at the same resonant frequency. The bending moment was applied by powering the vibration

TABLE 14. MARGIN-OF-SAFETY ANALYSIS

Gage Location	Load Condition	Stress (psi)		Margin of Safety
1	2	5220	± 5200	3.10
2	1	8000	± 4360	2.99
3	1	5730	± 3820	3.79
4	1	9670	± 5790	2.07
5	2	1300	± 7200	2.85
6	2	10970	± 2640	3.51
7	2	16530	± 6930	1.22
8	3	5840	± 5510	2.85
9	2	-5950	± 3690	7.14
10	2	-670	± 2530	10.85
11	4	80330	± 5560	1.27
12	1	13760	± 9820	0.94
13	2	-1140	± 3730	7.05
14	2	4800	± 1470	5.33
15	2	4310	± 3770	4.36
16	1	8720	± 2910	4.11
17	1	8900	± 3720	2.98
18	1	9740	± 5660	2.09
19	3	21740	± 10990	0.52
20	3	2820	± 10721	1.30
21				
22	4	20220	± 8210	0.07
23	3	-3240	± 8260	2.63
24				
25	3	3410	± 2070	7.75
26	3	7212	± 2530	4.54
27	4	20810	± 9990	0.64
28	4	12140	± 5730	1.86
29	1	-7150	± 2790	9.75
30	2	12340	± 3240	2.86
31	2	10760	± 2870	3.15
32	1	-5830	± 3960	6.58
33	2	-5350	± 3180	8.44
34	2	-1730	± 6730	3.45
35	2	-830	± 7050	3.25
36	4	11420	± 5810	1.84
37	3	20650	± 11410	0.53

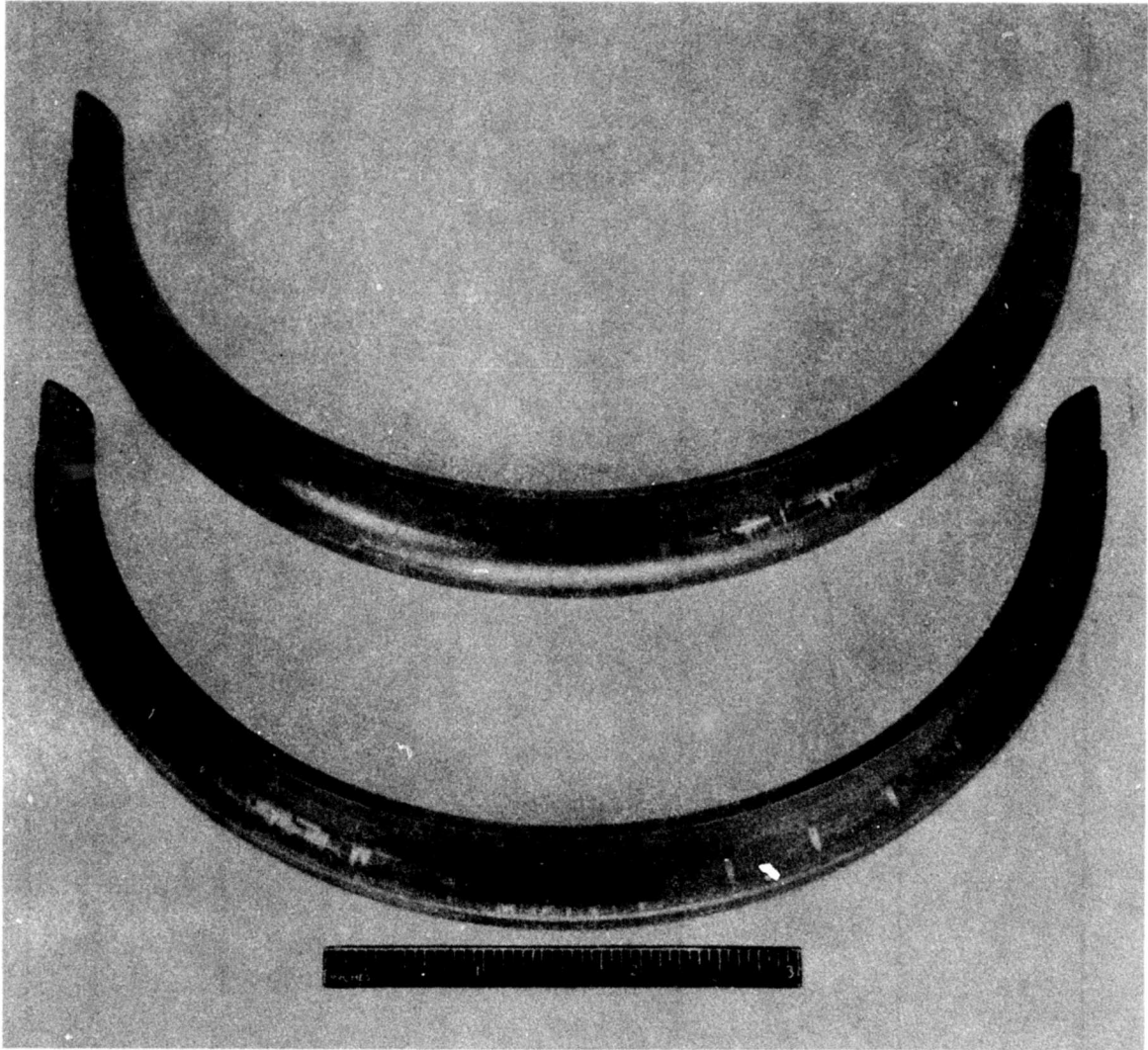


FIGURE 37. GOTHIC-ARCH INNER BEARING RACE INSERT LOADING PATTERN

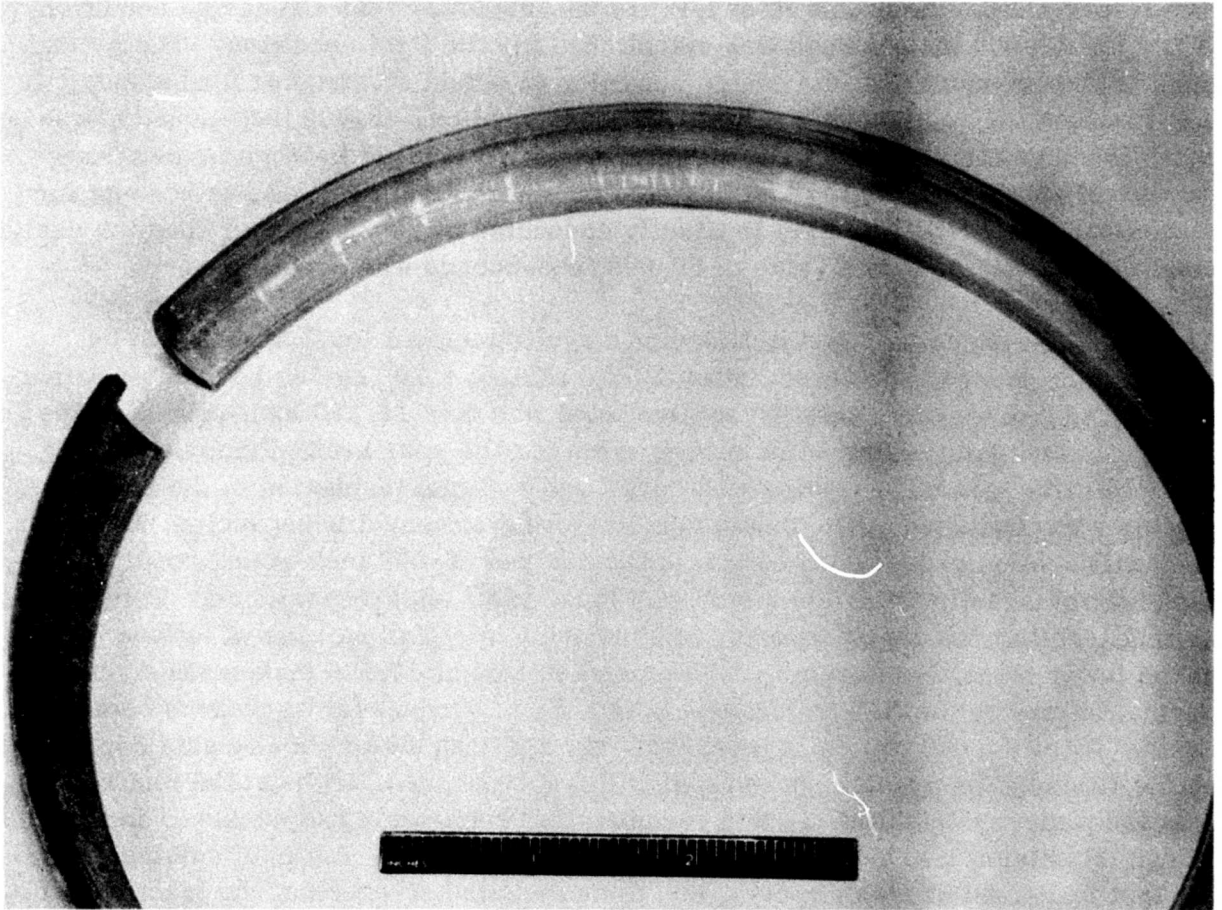


FIGURE 38. GOTHIC-ARCH OUTER BEARING RACE INSERT LOADING PATTERN

motor to a level which caused the strain gages to match readings taken during the ESA at a particular bending moment. During testing, the frequency and the strain gages were checked periodically as fracture of a component in the system would be indicated by a marked difference in readings. Frequency was monitored with a Strobocom frequency meter, reading to three decimal places, which allowed close control and acted as an indicator of small frequency changes which might be caused by the first stages of a fracture. Figure 39 shows the 3P-OOP test setup.

In order to establish confidence in a new design, testing is initiated at a conservative level. Customarily this first level is 20-30% lower than the design condition. A level of 50,000 inch-pounds was established for the first condition. The second level is then conducted at the design condition to establish structural adequacy. In this instance the continuous condition shown in Table 4, 65,000 inch-pounds, was established as the second level. Finally, the third level is used to demonstrate margin of safety and, as the test is based on a sample size of one, to account for statistical scatter. This level is usually conducted at 20-30% higher than the design condition. For this test a value of 80,000 inch-pounds was established.

The 3P-OOP fatigue test was initiated at a cyclic moment level assumed to be 50,000 inch-pounds. However, after a total of 6.85×10^6 cycles had been accumulated, it was discovered that the applied level was only 19,250 inch-pounds. The error resulted from using an incorrect value for the spar section modulus during the calibration period. Testing was halted and a visual inspection of the test assembly was conducted. The inspection did not reveal any discrepancies. During the recalibration process, to establish the desired 50,000 inch-pound condition, the electromagnetic vibration motor was found to be undercapacitated. Tempered by this inability and the successful accumulation of a high number of fatigue cycles at the lower level, the assembly was placed on test at 43,500 inch-pounds. The normal tolerance for fatigue test levels is $\pm 5\%$ to account for variations between arms. After 44,000 cycles at this level, the test was automatically shut down by the feedback loop which sensed a significant transgression from the test resonant frequency. Visual inspection revealed that separation had occurred in the Borsic aluminum test section of spar serial number five. Table 15 summarizes the test loads, numbers of cycles, and the calculated stresses at the fractured section of spar. The stressing was calculated from the measured moment distribution and the nominal section modulus at the fracture location.

Figure 40 shows the undisturbed overall test condition following the incident. Figure 41 is a close-up view of the outboard section of the spar, while Figure 42 shows the inboard or retention section. Fracture had occurred at approximately the 10-inch chordal section, separating the spar into two major sections and three smaller pieces, as shown in Figure 43.

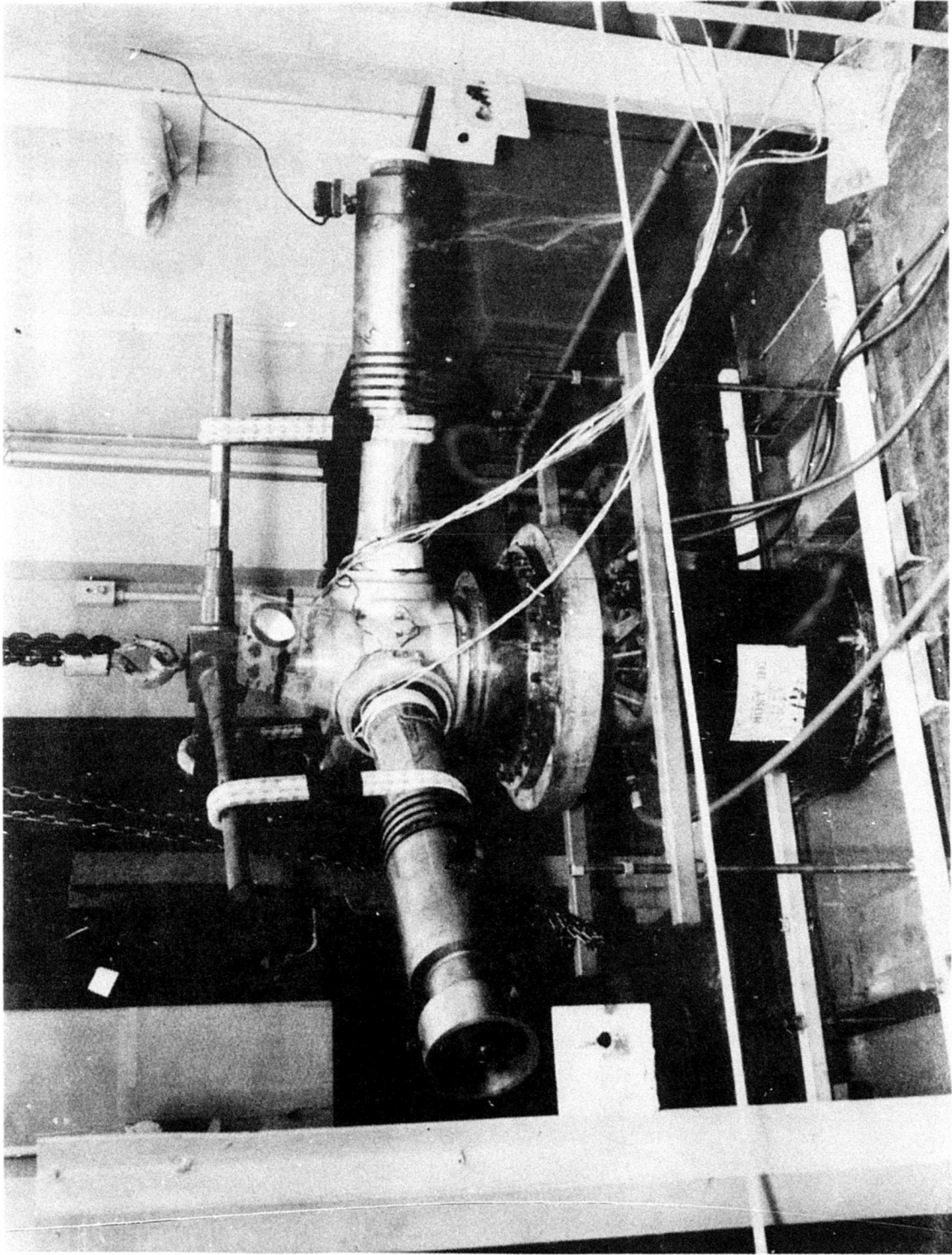


FIGURE 39. 3P OUT-OF-PLANE FATIGUE TEST SETUP

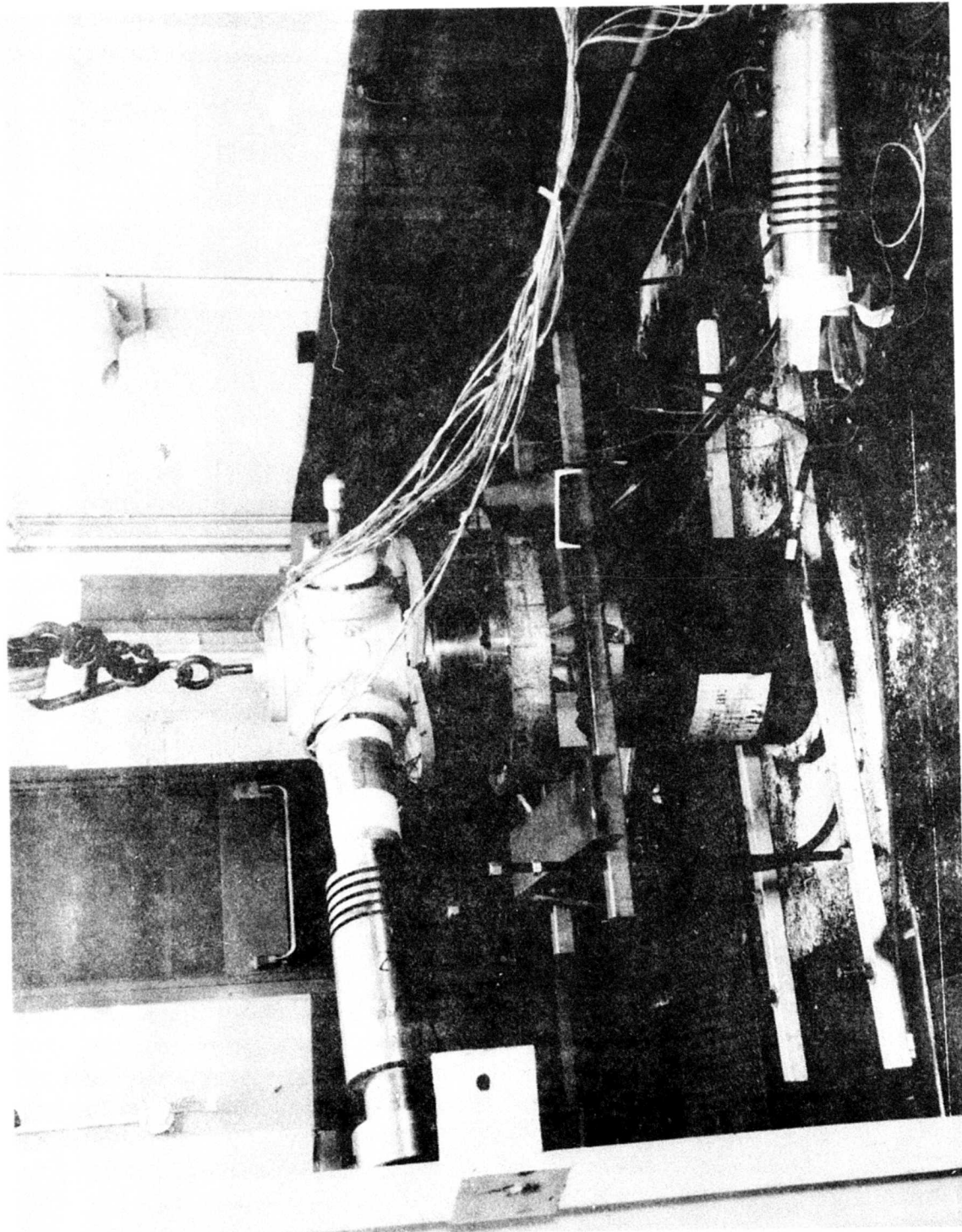


FIGURE 40. SPAR NUMBER 5 AFTER FRACTURE, 3P OUT-OF-PLANE FATIGUE TEST

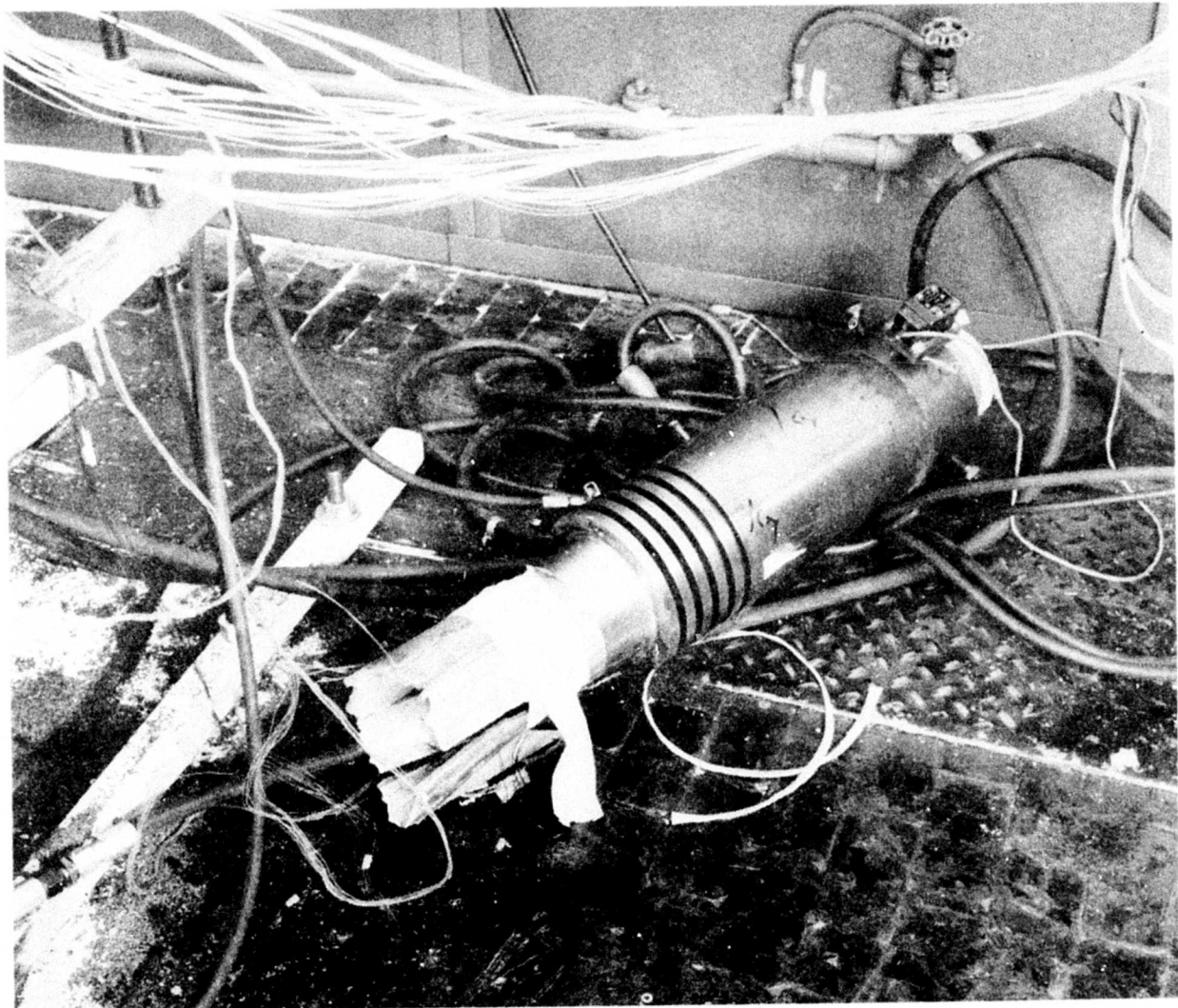


FIGURE 41. OUTBOARD SECTION OF SPAR NUMBER 5 AFTER FRACTURE

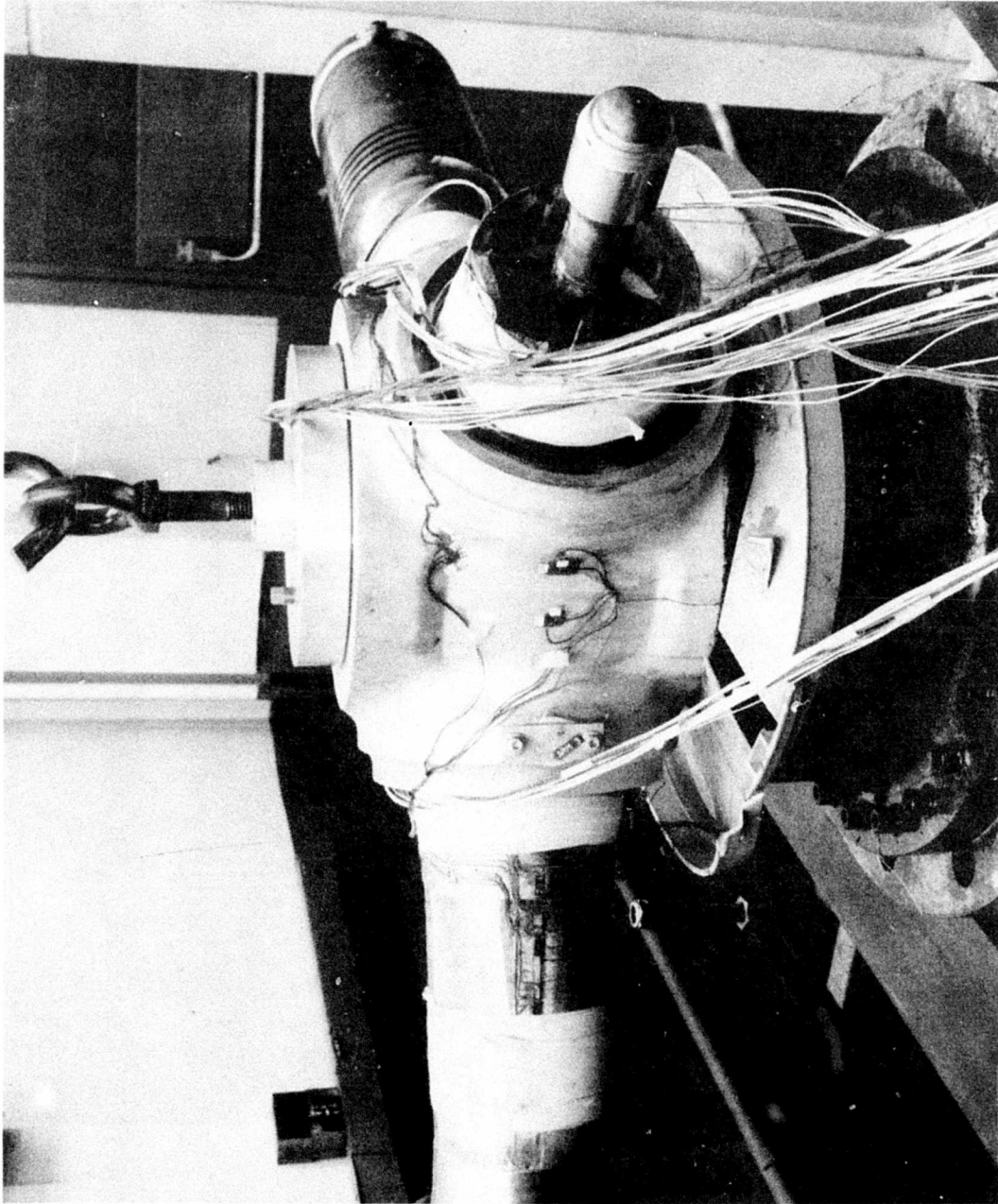


FIGURE 42. RETENTION SECTION OF SPAR NUMBER 5 AFTER FRACTURE

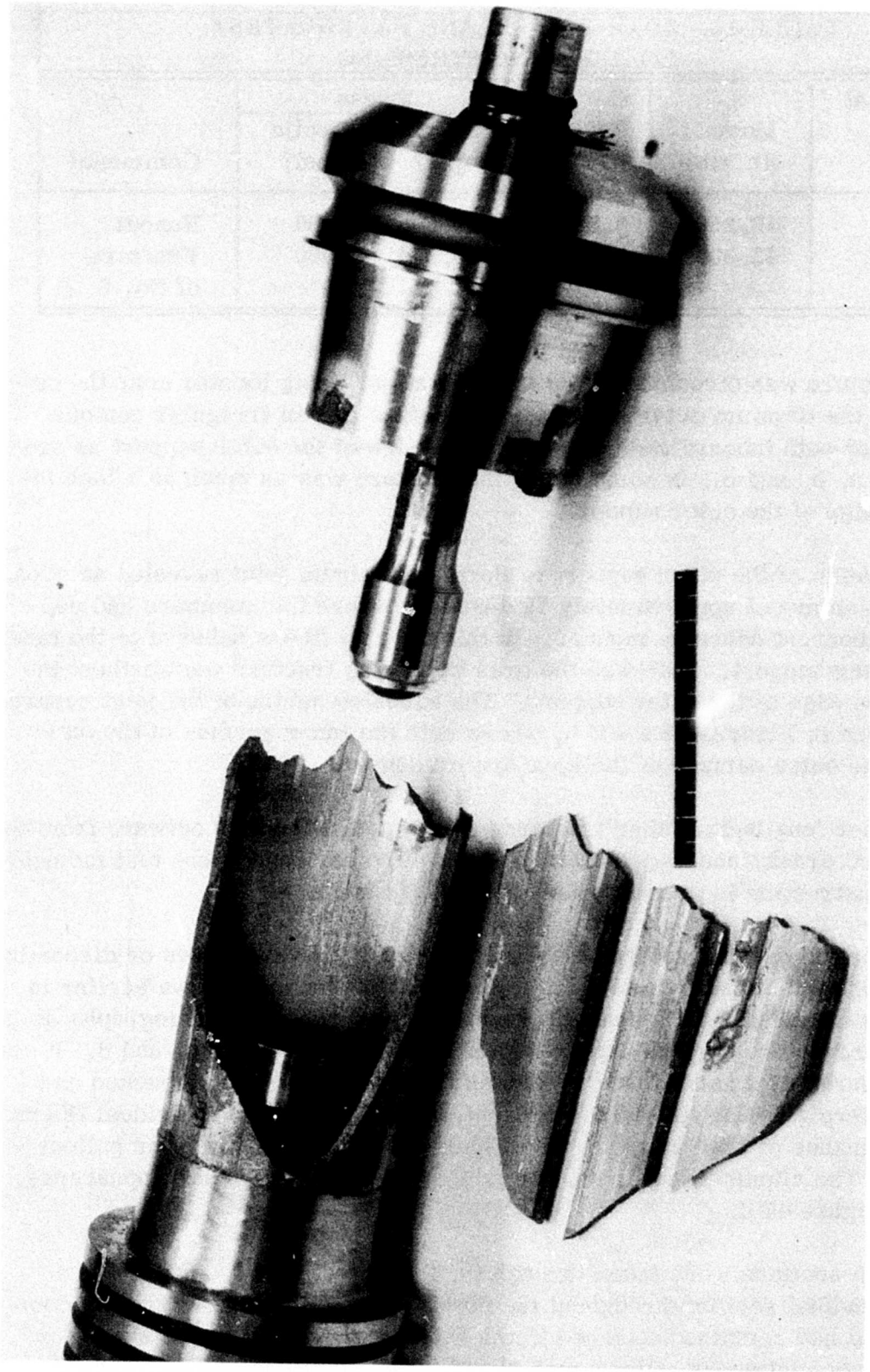


FIGURE 43. OVERALL EXPLODED VIEW OF SPAR NUMBER 5

TABLE 15. 3P OUT-OF-PLANE FATIGUE TEST LOADING AND STRESSING					
Centrifugal Load (lb)	Moment (in. -lb)	Cycles (10 ⁶)	Stress		Comments
			Steady (psi)	Cyclic (psi)	
45,000	19,250	6.850	10,500	3080	Runout Fracture of No. 5
45,000	43,500	0.044	10,500	6950	

The basic fracture was circumferential in orientation, being located near the out-board edge of the titanium outer support. Its surface had an irregular contour which projected both inboard and outboard of the edge of the outer support as seen in Figures 44 a, b, and c. In some areas the fracture was as much as 1 inch in-board of the edge of the outer support.

Close examination of the outer support to Borsic aluminum joint revealed an area, encompassing an arc of approximately 70 degrees, where the members had separated in an apparent adhesive manner. In this area no fibers adhered to the inner wall of the outer support. This was the area where the fracture was furthest in-board from the edge of the outer support. The adhesive nature of the joint separation can be seen in Figures 45 a and b, where both the inner surface of the outer support and the outer surface of the spar are presented.

There were four longitudinal spar fractures that traveled radially outward from the circumferential crack, and they converged near the inner edge of the test moment arm. A reconstruction is presented in Figures 46 a and b.

Visual examination of the fracture surfaces revealed no obvious flaws or discontinuities in the Borsic aluminum material. The section of the spar shown earlier in Figure 45 was examined with a scanning electron microscope. Fractographs of sections of the fracture surface are presented in Figures 47 a, b, c, and d. It can be seen in Figures 47 a and b that the composite material is closely packed and only minor interply radial splitting is present. The fractures of individual fibers had a predominance of edge origins. See Figure 47 c. Very little fiber pullout was evident. The aluminum alloy matrix exhibited a flaky, granular appearance, as shown in Figure 47 d.

Metallographic sections were taken through the fracture surface. Figure 48 a shows a longitudinal section throughout the portion of the fracture where the composite material had remained attached to the outer support. It can be seen that there is a nearly continuous silicon-rich phase in the aluminum approximately

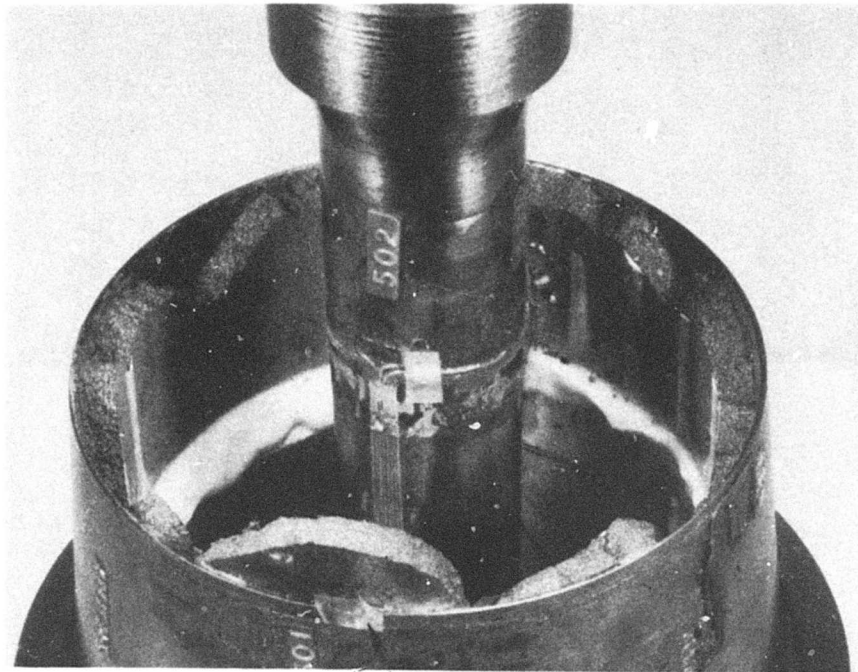
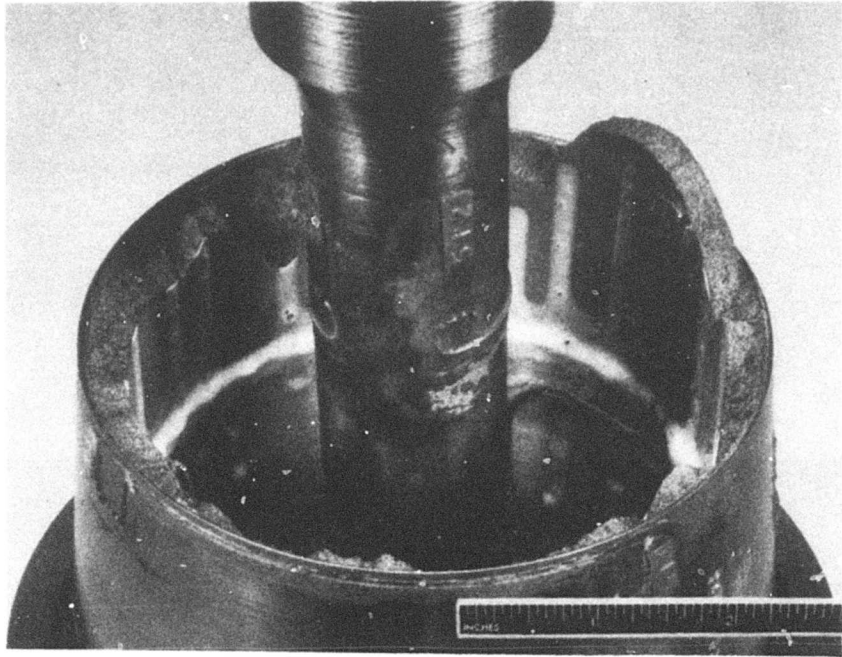
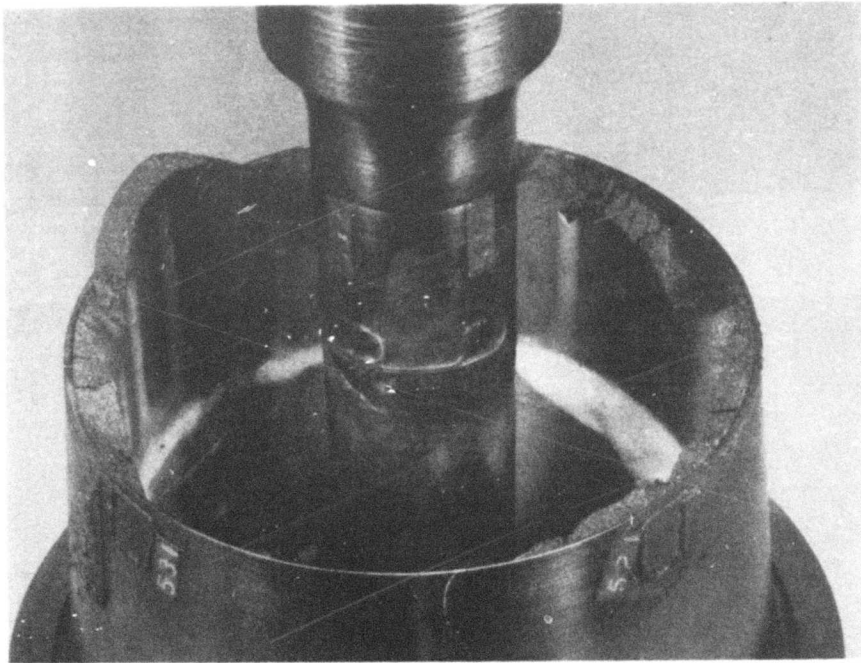
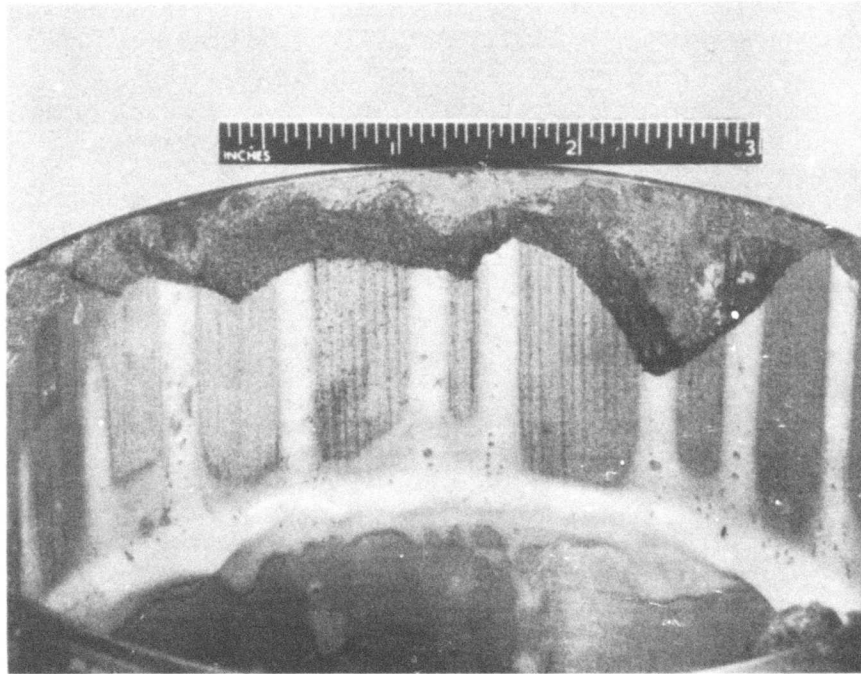


FIGURE 44. RETENTION SECTION OF SPAR NUMBER 5
AT TITANIUM OUTER SUPPORT

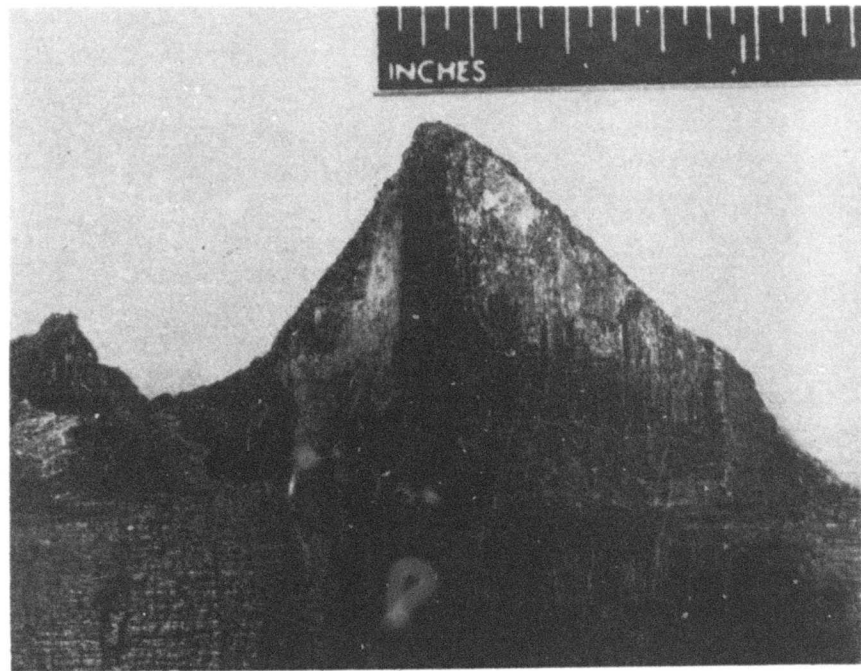


C

FIGURE 44. CONTINUED

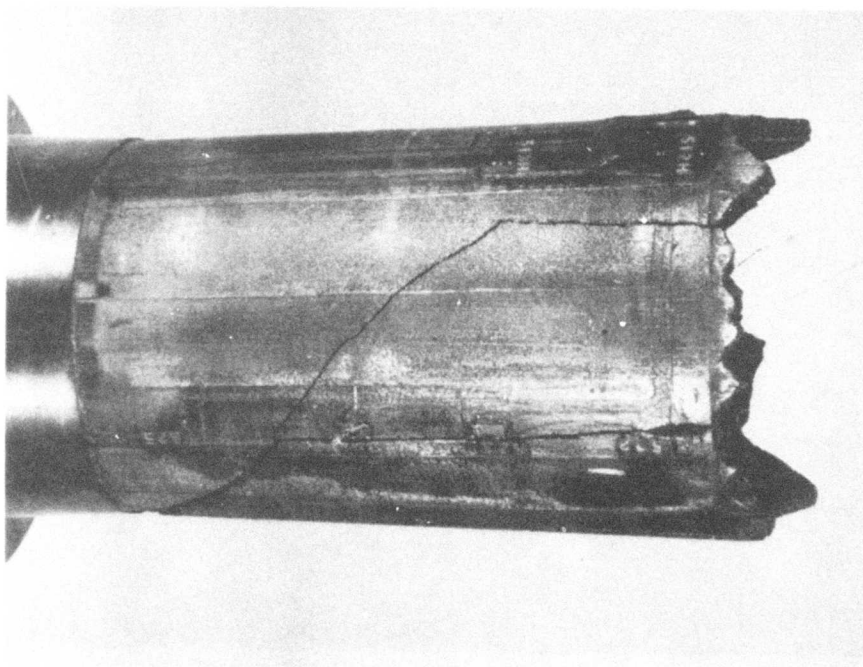


A

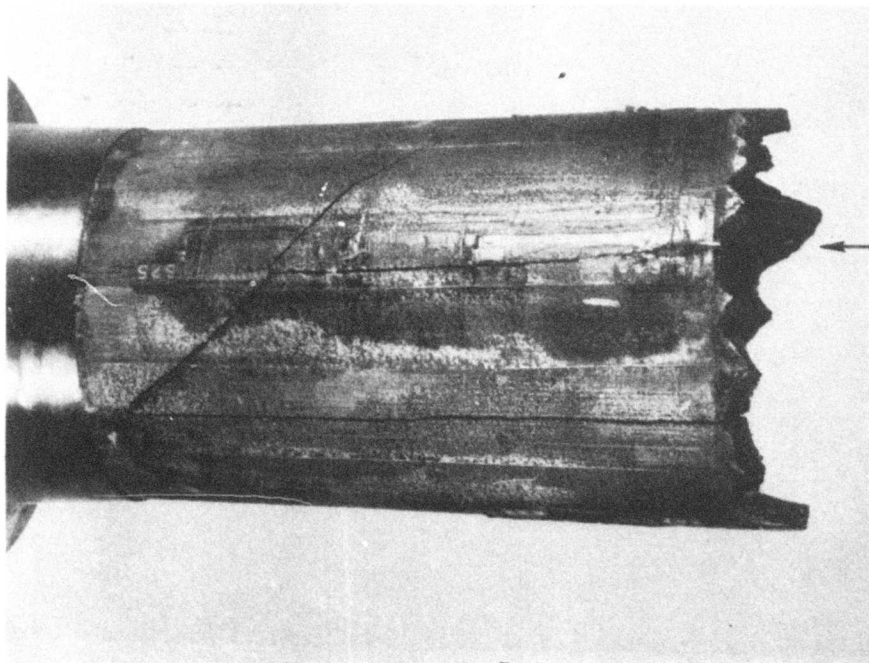


B

FIGURE 45. BORSIC ALUMINUM SPAR - TITANIUM OUTER SUPPORT
SEPARATION OF SPAR NUMBER 5

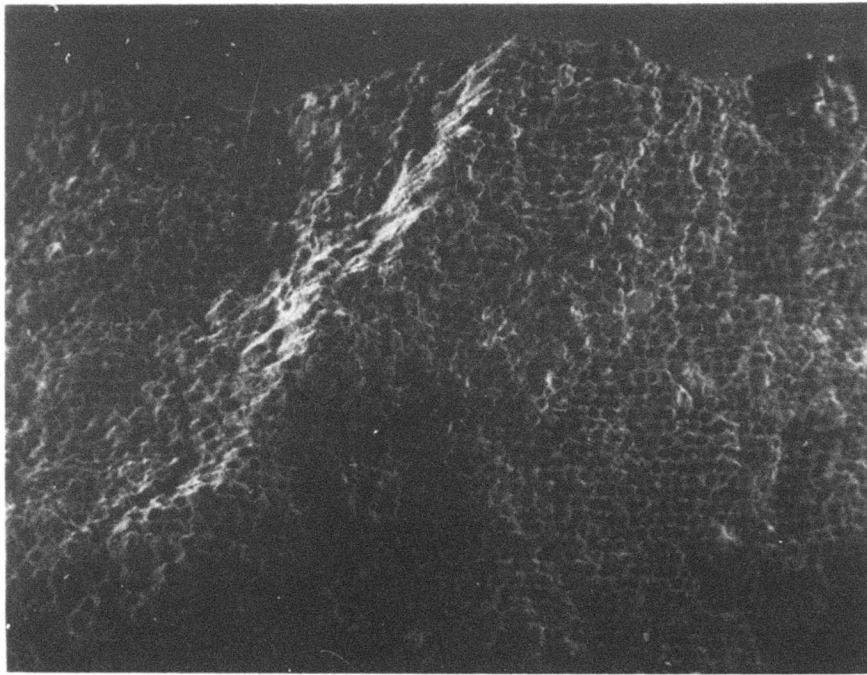


A



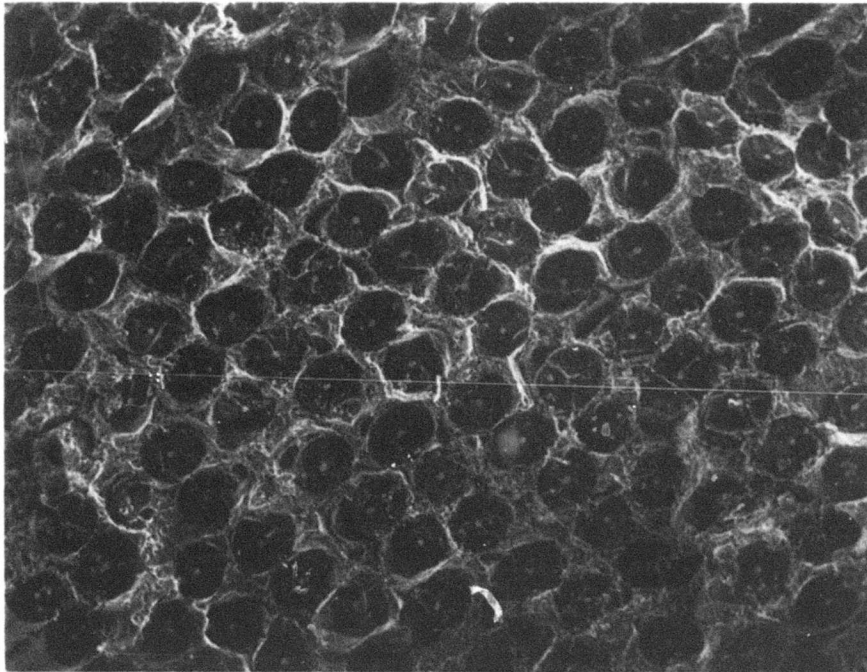
B

FIGURE 46. RADIAL FRACTURES IN BORSIC ALUMINUM SPAR OUTBOARD OF TITANIUM OUTER SUPPORT IN SPAR NUMBER 5



A

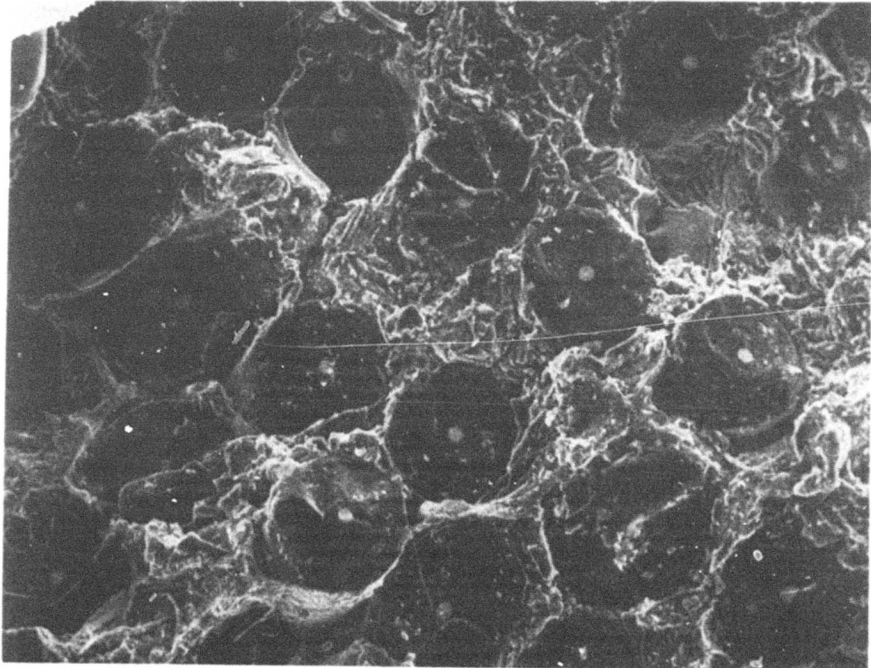
X12



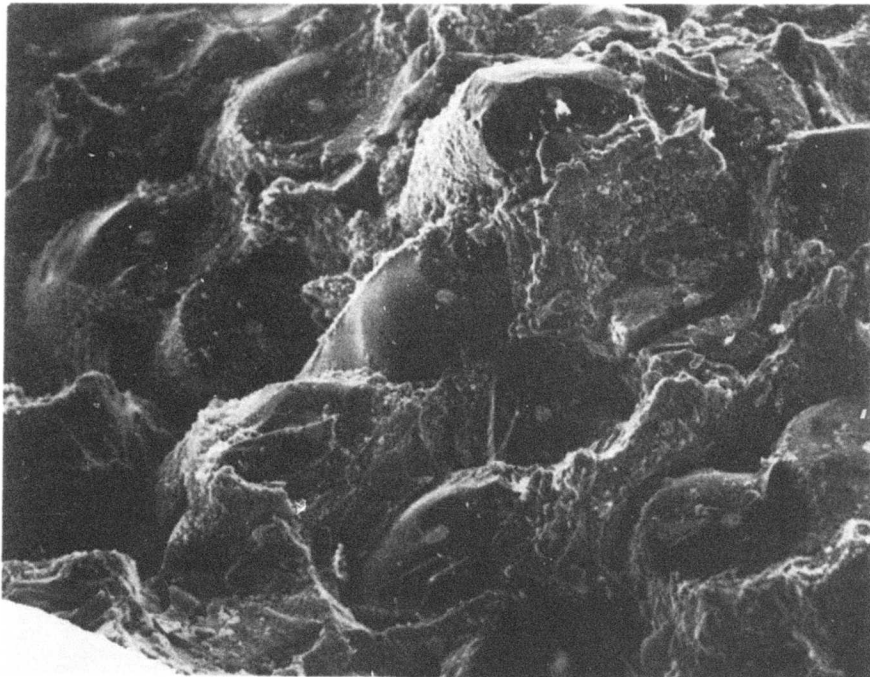
B

X50

FIGURE 47. SCANNING ELECTRON MICROSCOPE FRACTOGRAPHS OF SPAR NUMBER 5

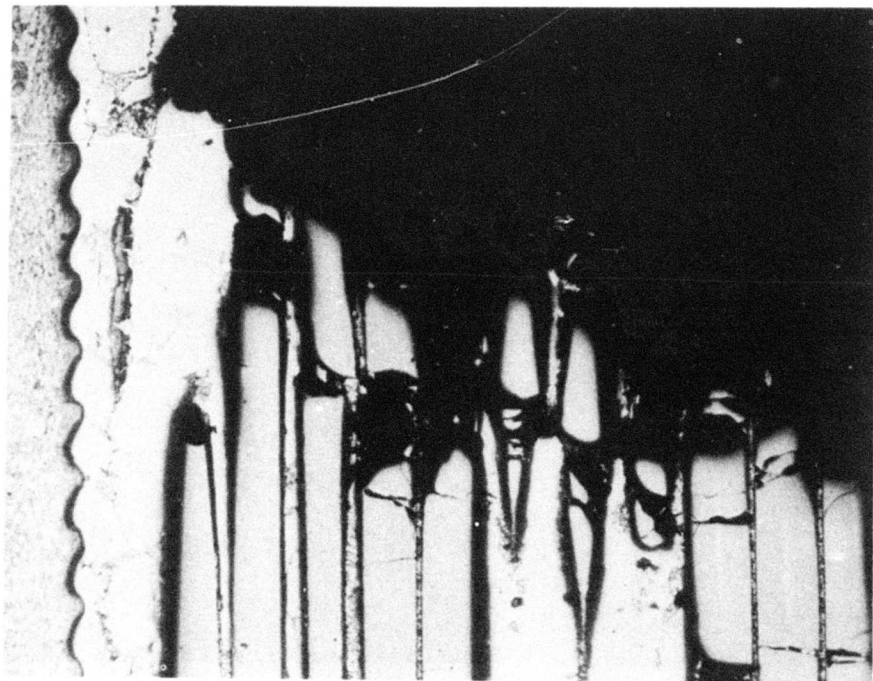


C
X100



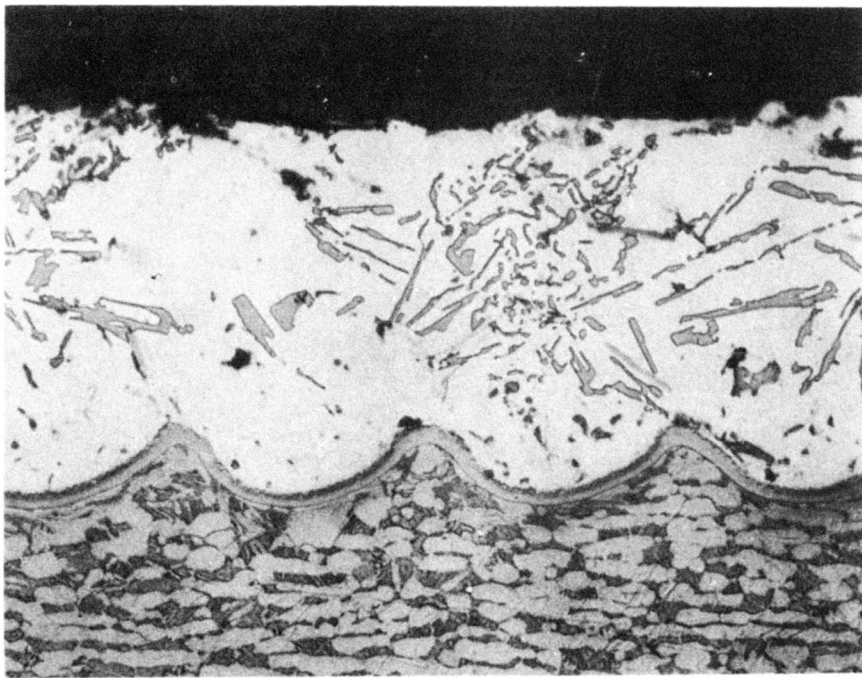
D
X140

FIGURE 47. CONTINUED



A

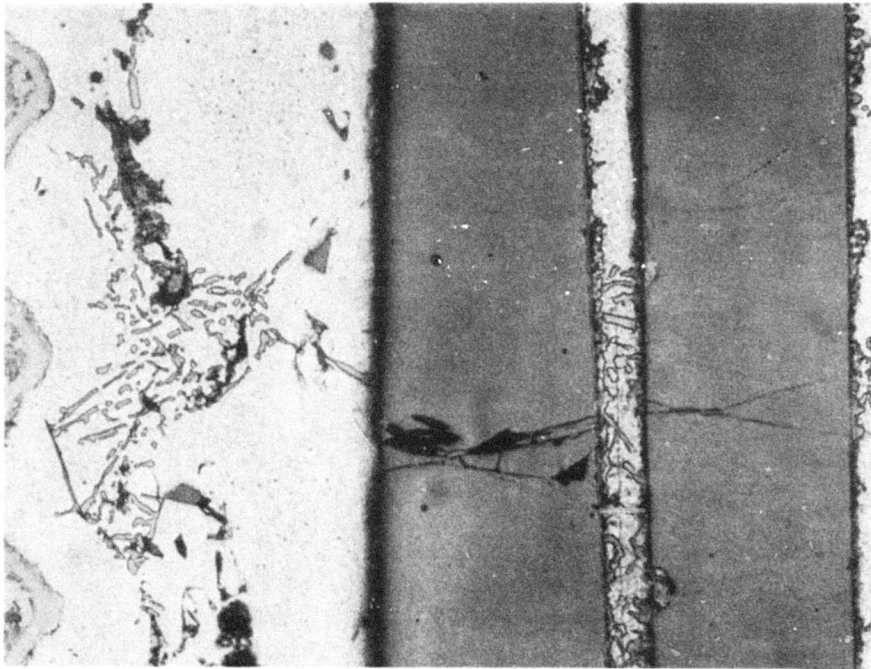
X50



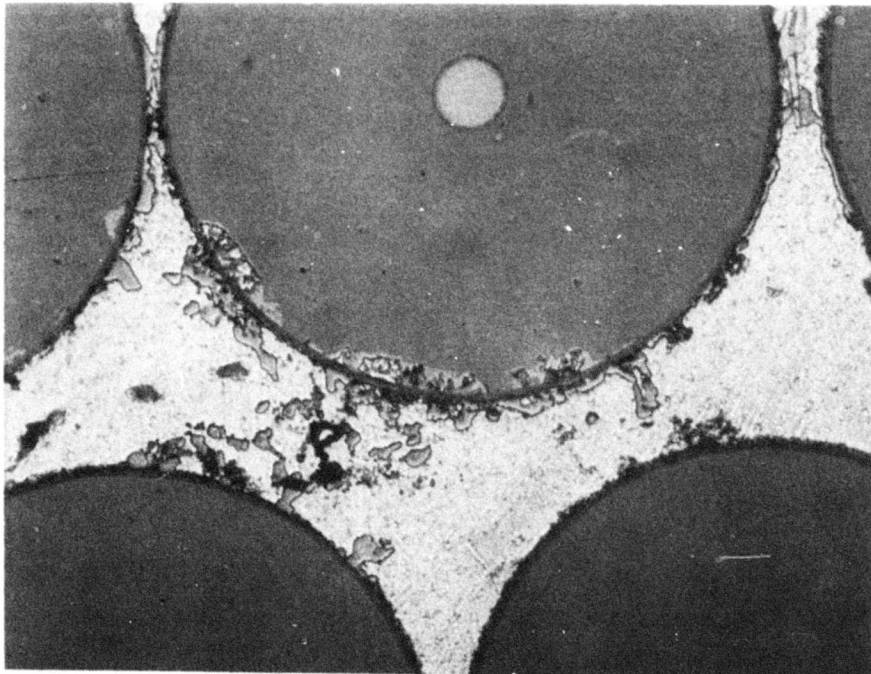
B

X200

FIGURE 48. MICROSECTIONS AT FRACTURE OF SPAR NUMBER 5



C
X200



D
X500

FIGURE 48. CONTINUED

midway between the outer support and the outermost fiber; in some areas a relatively large reaction zone existed. In those areas where the spar had become separated from the outer support, the fracture had occurred at the AA 407 braze foil to Borsic aluminum interface. In all areas examined, the titanium outer support to Borsic aluminum braze joint appeared satisfactory, as shown in Figure 48 b.

A close view of the fiber cracks that ran parallel to the principal fracture surface is shown in Figure 48 c. It can be seen that the cracks start on one side of the fibers and progress through, but not across, the aluminum matrix. Some fiber to matrix reaction can also be observed. Further evidence of fiber-to-matrix reaction is presented in the chordal section shown in Figure 48 d.

Numerous fibers were extracted from sections both outboard and inboard of the fracture, the latter being from within the braze bonded retention joint. The results are presented in Tables 16 and 17. They show the average ultimate tensile strength of fibers extracted from the outboard region to be 226,000 psi, with a standard deviation of 37 psi, while for those from the retention region it was 294,000 psi, with a standard deviation of 66 psi. These strengths reflected greater than anticipated degradation in mechanical properties. As this degradation could have resulted from over tempering, i.e., an excessive length of time at elevated temperature to assure a satisfactory composite structure and retention braze joint, the manufacturing records for spar number five as well as the records for all spars were reviewed.

Sensitivity to the effects of temperature is reflected in the process technique in which temperature is gradually increased to a point just below critical, 1000° F, and stabilized. As discussed earlier in the section devoted to spar fabrication, a temperature of 1100° F to 1140° F was cited for compaction of the composite material. Figure 49 graphically records the actual time at temperature cycle for the compaction process. It can be seen that the actual time above 1100° F was held to a minimum, being approximately 45 minutes of the nearly 7 hours involved in the cycle. Figure 50 is a similar presentation of the time at temperature for the brazing operation. The temperature required for brazing, 1085° F to 1100° F, was held for 30 minutes of the 6 hours involved in the cycle. This total of 1 1/2 hours was representative of all the spars manufactured and therefore was not unique to number five.

Dye penetrant inspection of spars numbers six and seven revealed the absence of any surface cracks, and they were concluded to be in satisfactory condition for further test.

**TABLE 16. TENSILE STRANGTHS OF FIBERS
OUTBOARD OF FRACTURE**

Strength Distribution (ksi)	Number of Samples	Cumulative (%)	Residual Composite Strength (ksi)
under 101	0	0.0	
101-120	11	1.0	119
121-140	2	3.0	136
141-160	4	7.0	149
161-180	4	11.0	160
181-200	8	19.0	162
201-220	21	44.0	132
221-240	19	59.0	99
241-260	27	86.0	37
261-280	9	95.0	14
281-300	4	99.0	3
300-320	1	100.0	0

Average strength,	X = 226,000 psi
Standard deviation,	σ = 37,000 psi
Sample size,	n = 100

**TABLE 17. TENSILE STRENGTHS OF FIBERS INBOARD
OF FRACTURE**

Strength Distribution (ksi)	Number of Samples	Cumulative (%)	Residual Composite Strength (ksi)
under 101	3	3.0	
101-120	2	5.0	114
121-140	2	7.0	130
141-160	0	7.0	149
161-180	1	8.0	166
181-200	3	11.0	178
201-220	2	13.0	192
221-240	1	14.0	206
241-260	0	14.0	224
261-280	10	24.0	213
281-300	15	39.0	183
301/320	25	64.0	115
321-340	18	82.0	61
341-360	11	93.0	25
361-380	5	98.0	8
381-400	2	100.0	0
Average strength,	X = 294,000 psi		
Standard deviation,	$\sigma = 66,000$ psi		
Sample size,	n = 100		

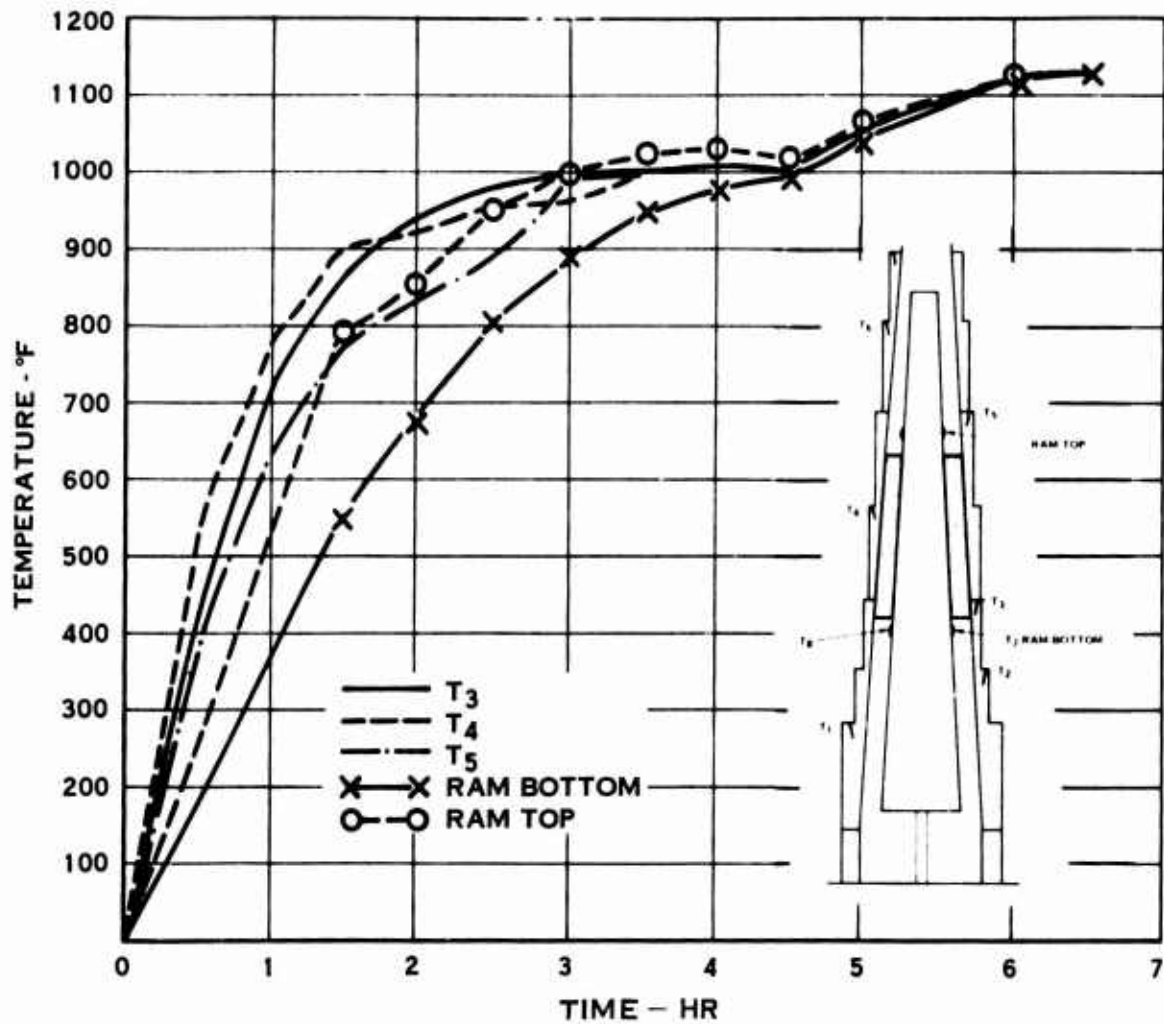


FIGURE 49. BORSIC ALUMINUM SPAR COMPACTION
THERMAL CYCLE OF SPAR NUMBER 5

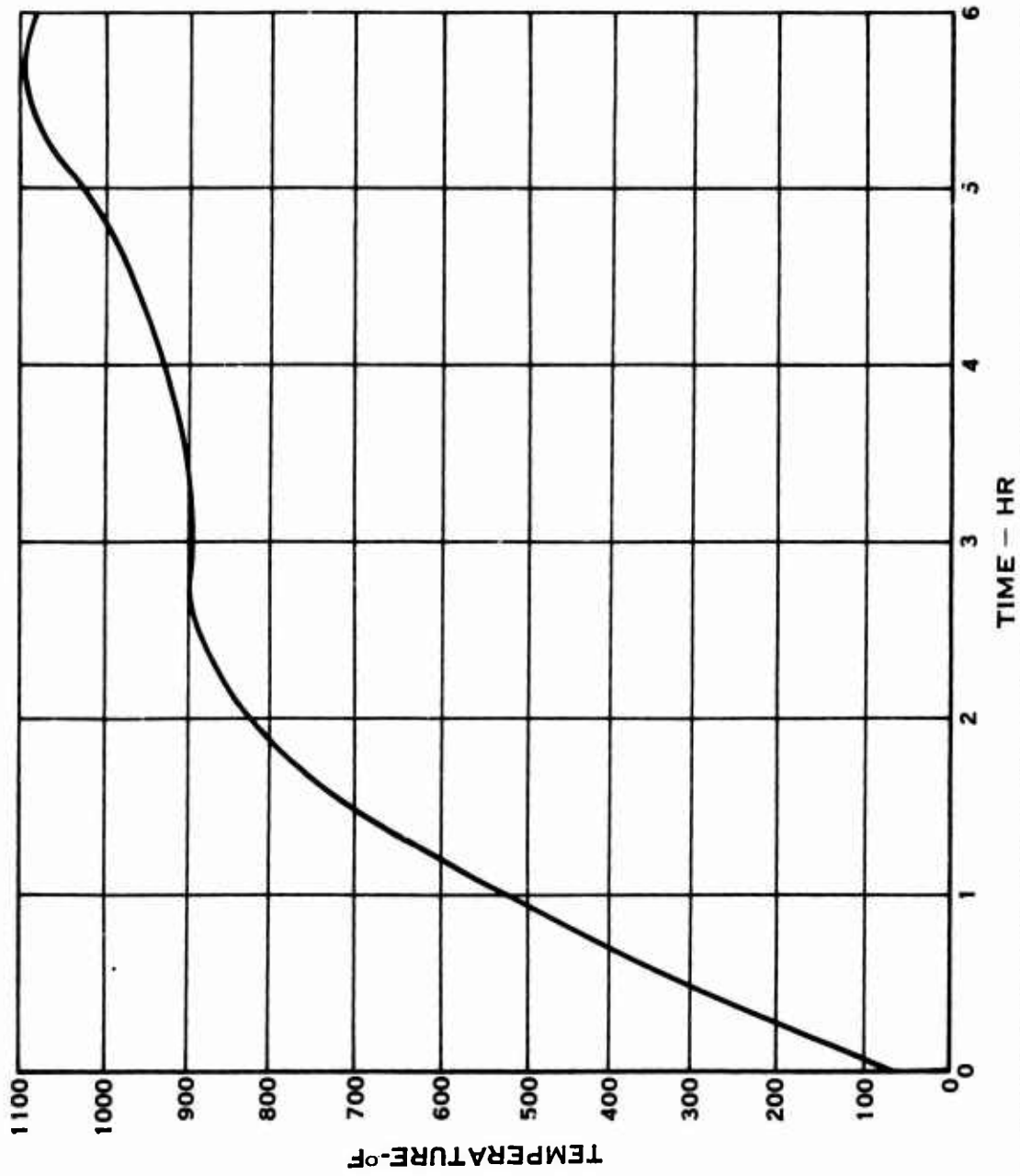


FIGURE 50. BORSIC ALUMINUM SPAR TO RETENTION BRAZE THERMAL CYCLE OF SPAR NUMBER 5

Ultrasonic inspection scans of the outboard section of spar number five are shown in Figure 51. The dark areas indicate dense Borsic aluminum material that is relatively free of voids or inclusions, while the light areas indicate defective material. From past experience, 4Db scans are usually representative of the true condition of the material. On this basis, Figure 51 reveals that 75 to 80% of the outboard cross section contains no defects.

Ultrasonic inspection scans of the Borsic aluminum spar to titanium outer support braze joint within the retention section are shown in Figure 52. In these scans the light areas indicate sound bonding while the black areas indicate separation. With this in mind, Figure 52 reveals the top or outer section of the retention to be 45% sound, while the bottom or inner section of the retention is 50% sound.

Microstructures of the retention section were studied. Figure 53a shows a cross section of the spar in an area where a crack had developed, probably at the time of fracture during fatigue testing. With the exception of this crack, the spar appeared to be well consolidated and to possess generally good fiber distribution. As evidenced by a long void in the braze area, only partial bonding of the composite material to the titanium outer support had occurred during the braze cycle. Figure 53b shows the formation of a continuous intermetallic, of approximately 0.0002 inch in thickness, between the braze and the titanium. This view, also indicates the presence of extraneous elongated material in the center of the braze. This material was not identified but probably was decomposed fiber. Figure 54 reveals a "hot spot" where extensive reactions had occurred between the composite and the aluminum inner support. A long void also existed in the braze between the composite material and the titanium outer support. This was the most severe case of fiber attack, but it generally occurred elsewhere. Figure 55 shows a typical area away from the braze joint. Figure 55a is a transverse view of a fiber, while Figure 55b is a longitudinal view of several fibers. Noticeable attack can be seen near the outside diameter of the fibers, as indicated by the light areas just inside of the dark-appearing silicon carbide coating. Fibers with this type of attack were also seen in the outboard region of the spar.

The classical sequence of events associated with metal matrix composite fatigue fracture is as follows:

1. Initial filament fracture arises at point of high stress and/or weakness during fatigue loading.
2. Stress concentrations in the adjoining matrix, resulting from the filament break, grow in magnitude under cyclic loading. Matrix work hardening accelerates this growth of the stress concentration zone.



SETTINGS:
FREQUENCY: 2 1/4 MHZ.
SENSITIVITY: 3
TRANSDUCER: 3/4"
PULSE LENGTH: MINIMUM

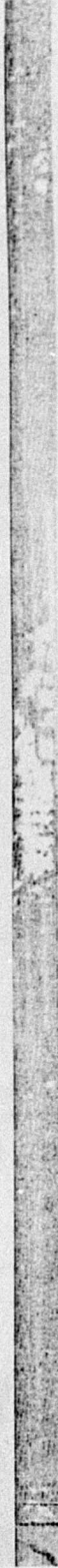
REJECT: 9 O'CLOCK
CLIPPER: 5
STONE: 9
PRINT: POSITIVE
DATE: 5/9/74

FIGURE 51. ULTRASONIC INSPECTION OF OUTBOARD SECTION OF SPAR NUMBER 5

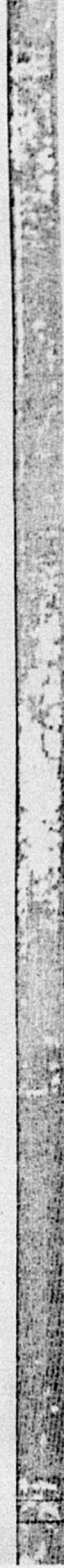
A. TOP (Ti-6 AL-4V TAPE RED)
SENSITIVITY: 0 * 10



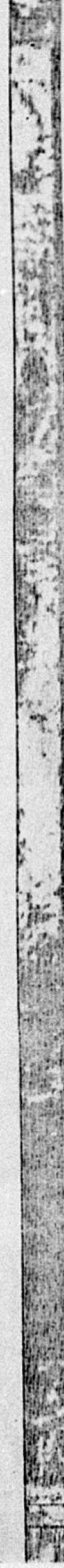
B. BOTTOM
(1) SENSITIVITY: 1.2 * 10



(2) SENSITIVITY: 1.4 * 10



(3) SENSITIVITY: 1.6 * 10



OTHER SETTINGS:
FREQUENCY: 10 MHZ
TRANSDUCER: 3/8"
PULSE LENGTH: MINIMUM
REJECT: 0 CLOCK

CLIPPER: 8
TRIGGER: 4
PRINT: NEGATIVE
DATES: 4/22/73, 4/23/73

FIGURE 52. ULTRASONIC INSPECTION OF RETENTION SECTION OF SPAR NUMBER 5

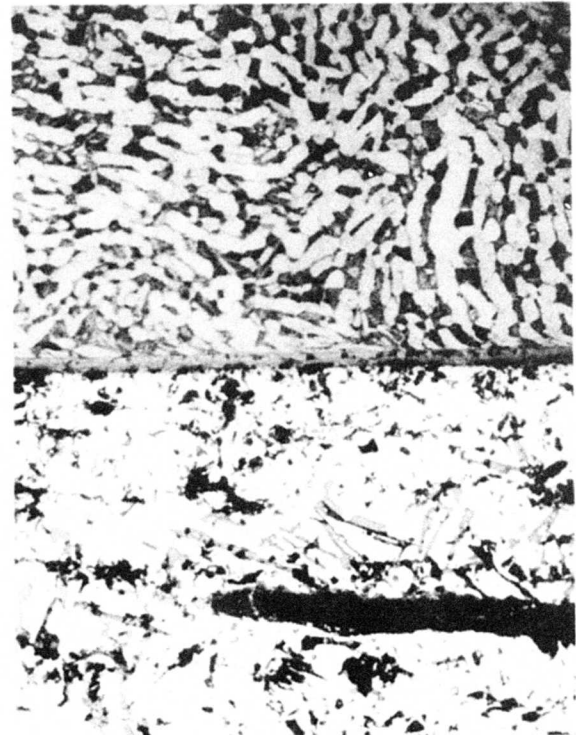
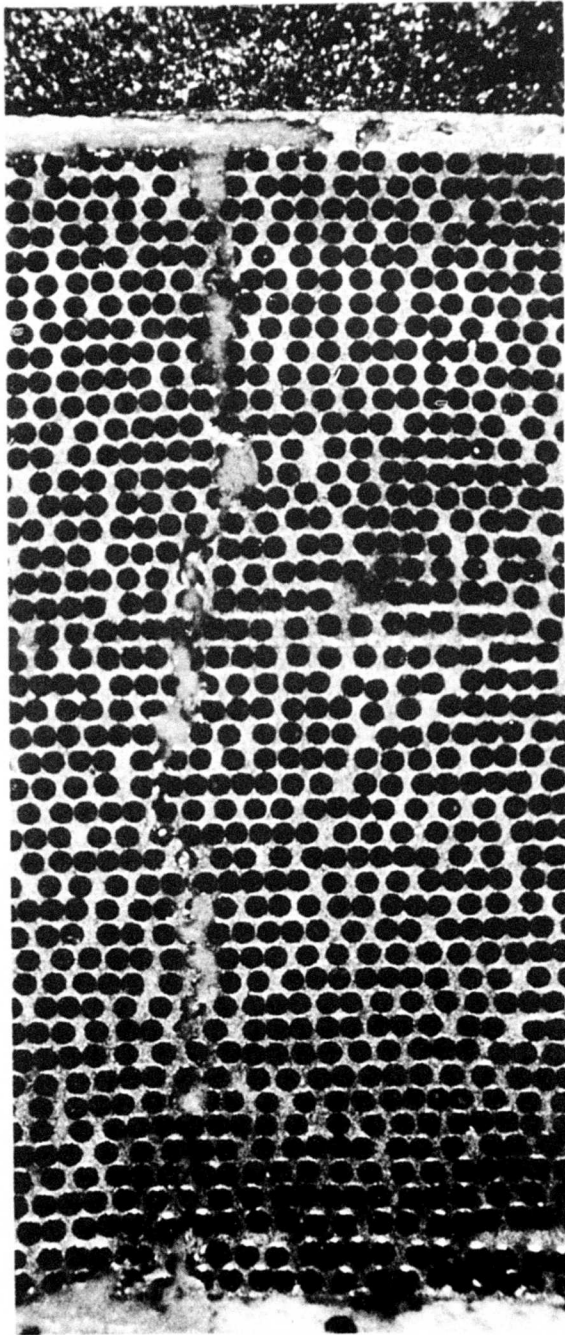


FIGURE 53. MICROSTRUCTURE OF RETENTION SECTION OF SPAR NUMBER 5

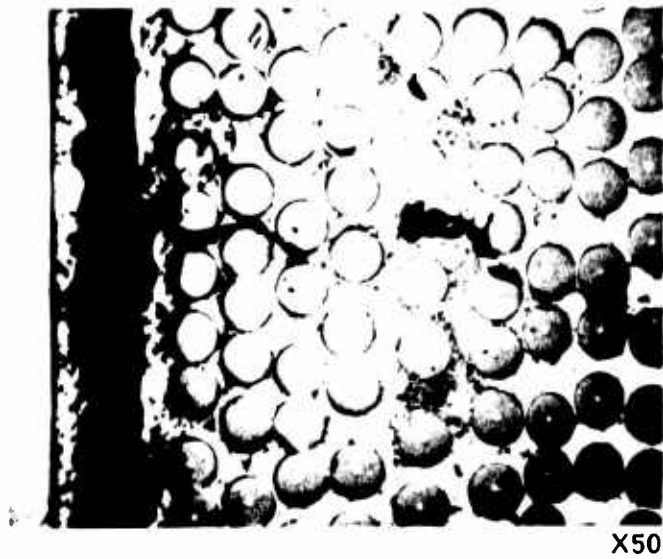


FIGURE 54. MICROSTRUCTURE OF SPAR NUMBER 5 HOT SPOT



A

X500



B

X500

FIGURE 55. MICROSTRUCTURE OF SPAR NUMBER 5
RETENTION SECTION FIBERS

3. Cracks initiate at the matrix-filament interface of proximate filaments when the magnitude of the stress concentration becomes large.
4. Newly nucleated cracks propagated by a shear mechanism along the matrix filament interface to a point where the existing stress level exceeds the filament tensile fracture stress and results in filament fracture.

This failure mode of fracturing proximate filaments continues in a localized plane until the effective component area in that plane is reduced enough for composite tensile fracture to occur. Consequently, in areas adjoining the fracture area, cracks are found in the filaments only. This was observed in spar number five. Cracks along the fiber to matrix interfaces, representing longitudinal splitting, were not evidenced, indicating a multiplicity of crack nucleation sites. The scanning electron microscope examination confirmed that rapid propagation had occurred, as evidenced by the brittle fracture appearance of the matrix. Microstructural studies confirmed the existence of severely damaged fibers. Hence, fracture originated at the edges of the Borsic fibers, which exhibited severe surface attack resulting from reaction between the Borsic filaments and the aluminum matrix. Boride formations were seen to occur well below the surface of the filaments.

Figure 56 is a presentation of the above observations in terms of engineering stress. This illustration shows the curves for nondegraded and degraded material at 44,000 cycles superimposed on the infinite-life fatigue strength shown in Figure 35. A stress concentration value of 2.17 is included to reflect a stepped tube in tension. The number of cycles accumulated by each of the three spars, numbers five, six and seven, are listed next to the fracture and/or runout point. Spar number five is seen to fall 50% below its strength line. This is attributed to a lesser degree to material scatter but more importantly to the severe subsurface damage to the Borsic filaments. An effective additional stress concentration of approximately 1.5 to 2.0 is apparently in order to reflect the damage.

Fatigue Strength Investigation (FSI) 3P-OOP (Second Test)

As a result of the untimely Borsic aluminum spar fracture just discussed, a second fatigue test was undertaken. A replacement spar, serial number eight, was brought forward from the three assigned to 1P-OOP test to replace number five and, together with numbers six and seven, was strain gaged. Additional gages were placed at the section corresponding to the earlier fracture location to experimentally define stressing at this location. Simulated centrifugal load was applied in the previous manner, and the test unit was reinstalled on the same electromagnetic vibrator. Once tuning was accomplished, the test unit was calibrated for moment distribution. Figure 57 has been included to show the resultant distribution and consistency between spars.

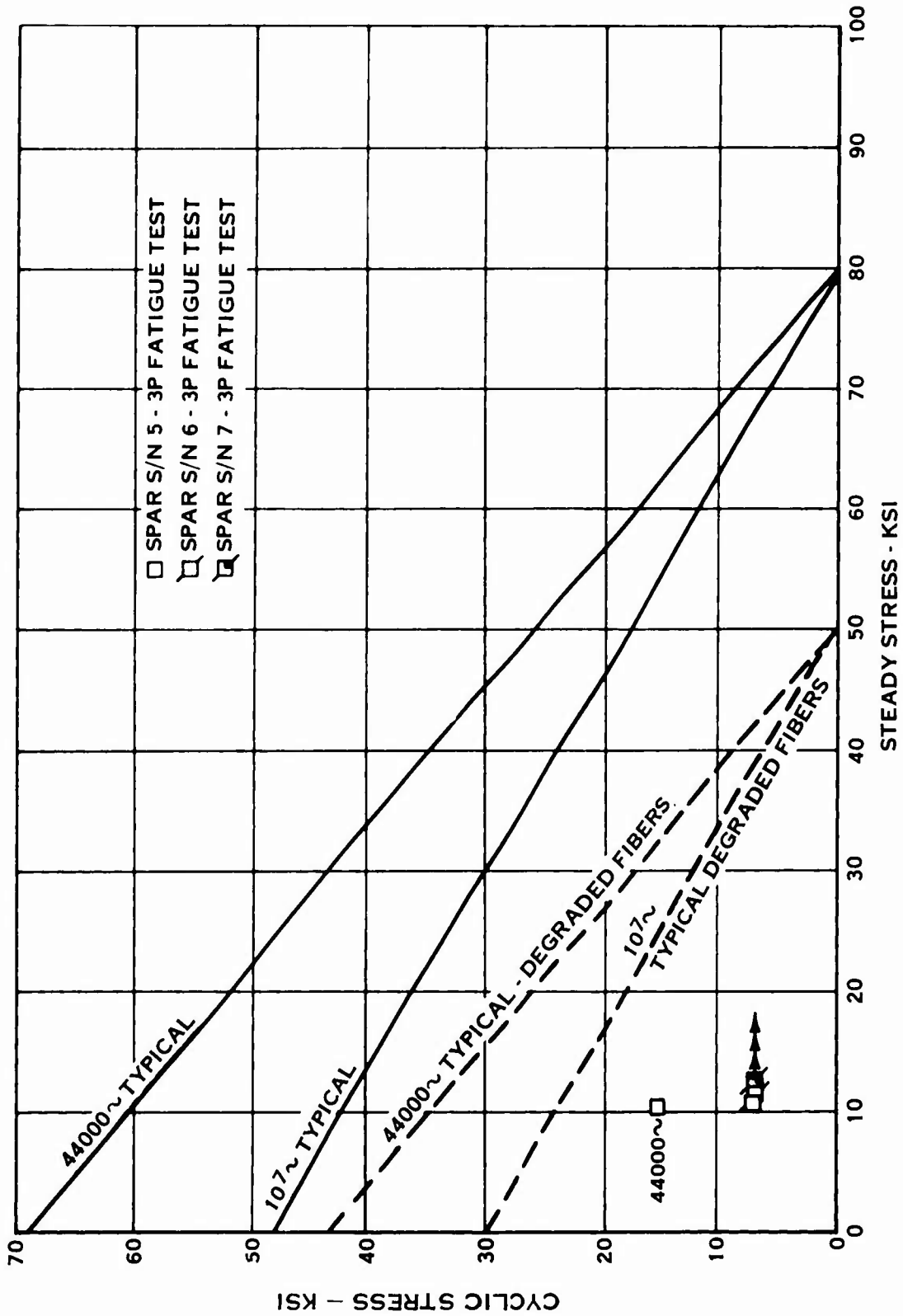


FIGURE 56. BORSIC ALUMINUM SPAR FATIGUE TEST RESULTS

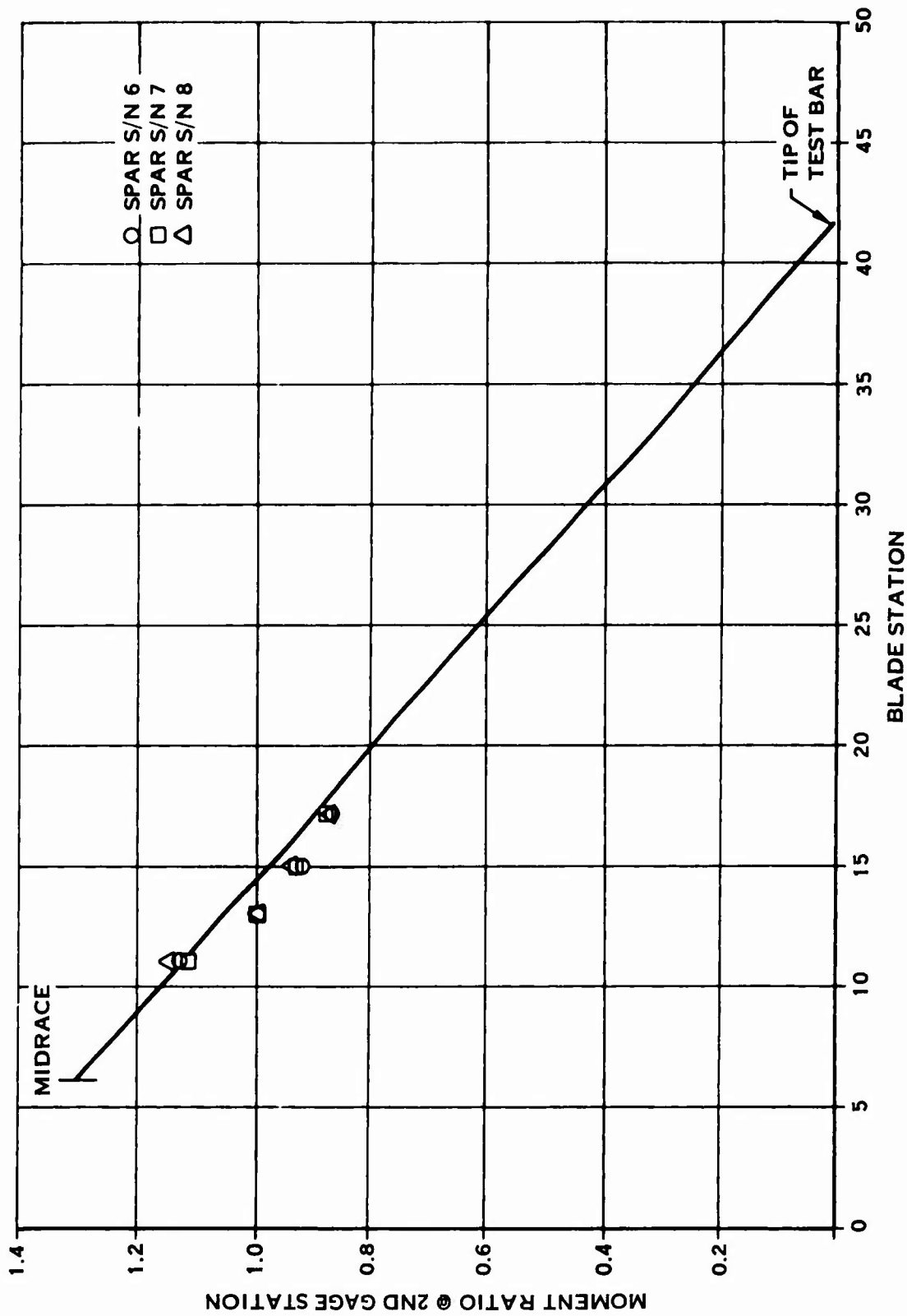


FIGURE 57. BENDING MOMENT DISTRIBUTION

The assembly was placed on test at the previously imposed 45,000 pounds centrifugal load and a slightly higher bending moment, 45,000 inch-pounds. The bending moment increase of 1500 inch-pounds resulted from the spar exchange, as the identical electro-magnetic vibration motor was employed.

The measured stressing corresponding to the fracture location of spar number five, when linearly corrected to the prior 43,500 inch-pounds level, was 10,800 psi steady stress and 7,300 psi cyclic stress. This stressing was in good agreement with the values shown earlier in Table XV. Following the accumulation of ten million cycles, without incident, the unit was disassembled for routine nondestructive surface inspection.

Figure 58 is a presentation of the cumulative results of all 3P-OOP fatigue tests in terms of the engineering stress. Superimposed on the diagram are the typical infinite-life strength curves for sound and degraded material, based on the tensile strength data generated in this program. The number of cycles accumulated by each of the four spars is listed next to the fracture and/or run out points.

Visual inspection of the disassembled unit revealed all three spars and the barrel to be free of surface distress. This was later confirmed by dye penetrant inspection. However, visual inspection of the bearing race inserts revealed numerous fractures.

The metallurgical examination that followed showed that the most extensive damage had been sustained by the race inserts installed in the number two arm of the barrel where number six spar was assembled, spar number six having been reinstalled in its original number two barrel arm, spar seven in arm three, and replacement spar eight in arm one. An overall view of the sections of the inner race insert is presented as Figure 59. One of the sections had a circumferential fracture separating it into two pieces. The fracture was located at the apex of the Gothic arch. The fracture profile was slightly scalloped, with the loops running from ball impressions to ball impressions. A reconstruction of the section showing the fracture profile and the ball impression pattern is shown in Figure 60. From these photos, it can be seen that the ball contact patterns were heaviest midway between the machined splits. The spar contact surface was fretted, with the heaviest fretting also located midway between the splits. Figure 60a is a view at a split and shows a fractured segment on the left. Figure 60b is a view 90 degrees to Figure 60a and shows a crack within an intact segment. Figure 60c is a view 180 degrees from Figure 60a and shows a fractured segment on the right. Finally, Figure 60d is a view 270 degrees from Figure 60a and shows a reconstruction of the fracture. The fracture surfaces were rubbed, but the visible fracture markings indicated that the origins were located on

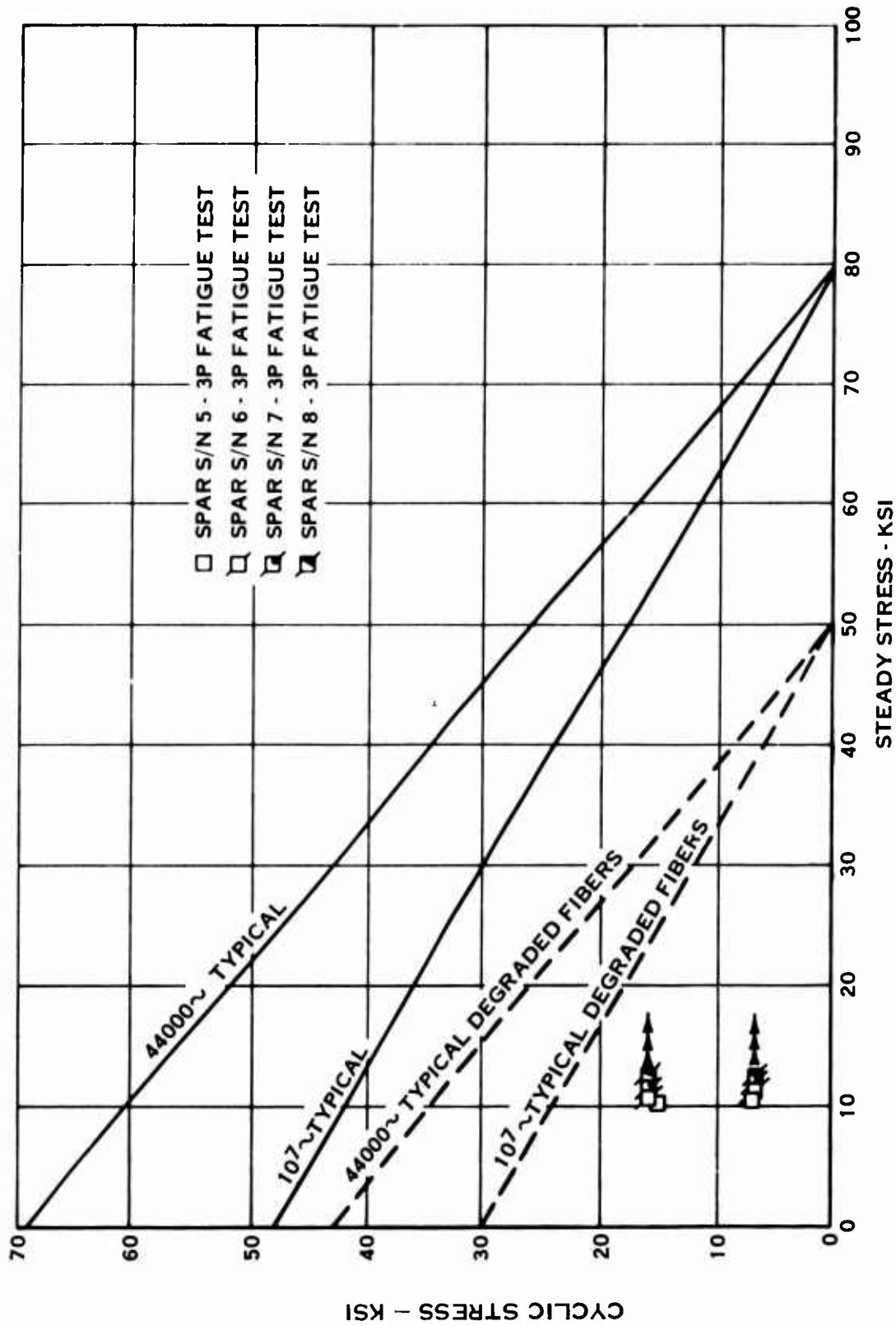


FIGURE 58. BORSIC ALUMINUM SPAR FATIGUE TEST RESULTS

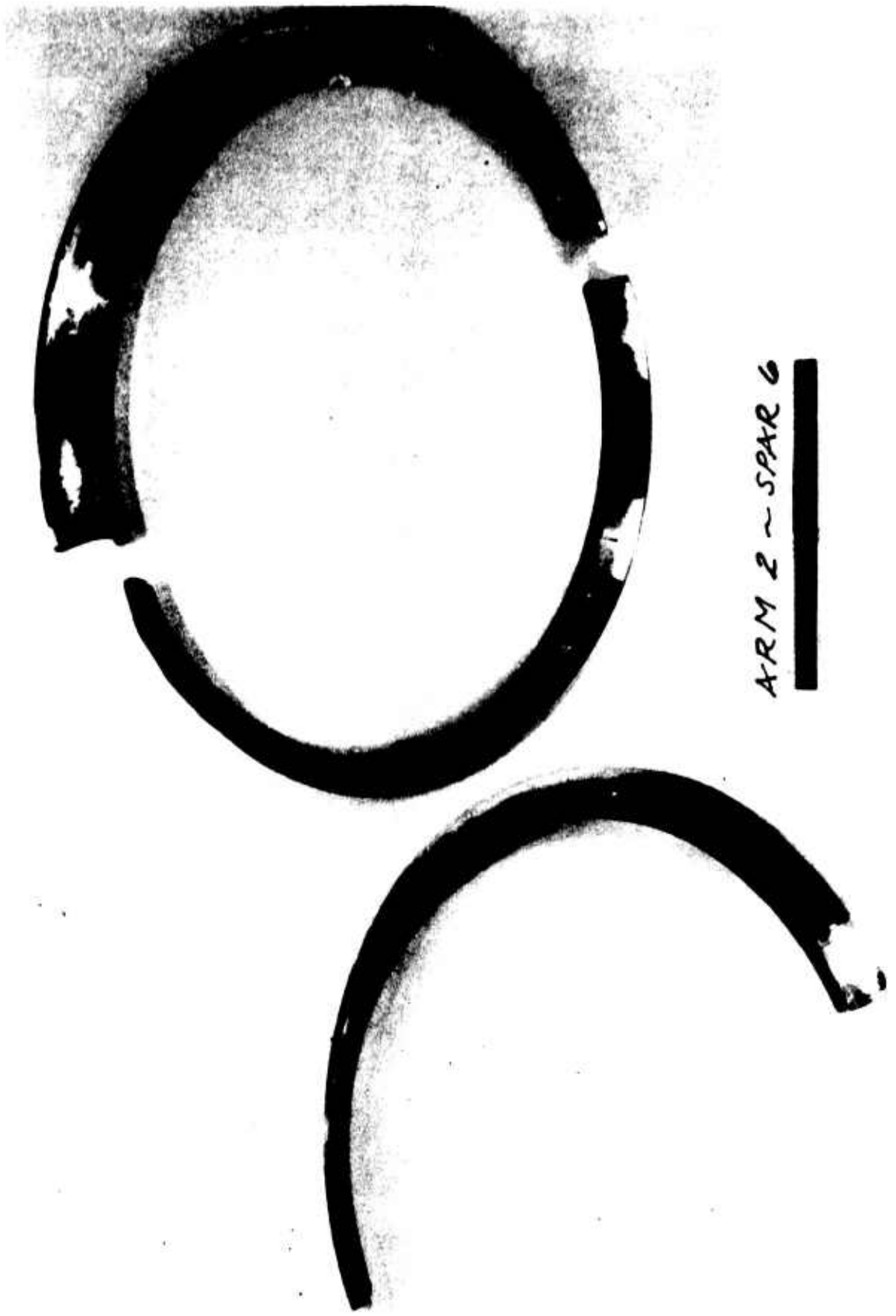
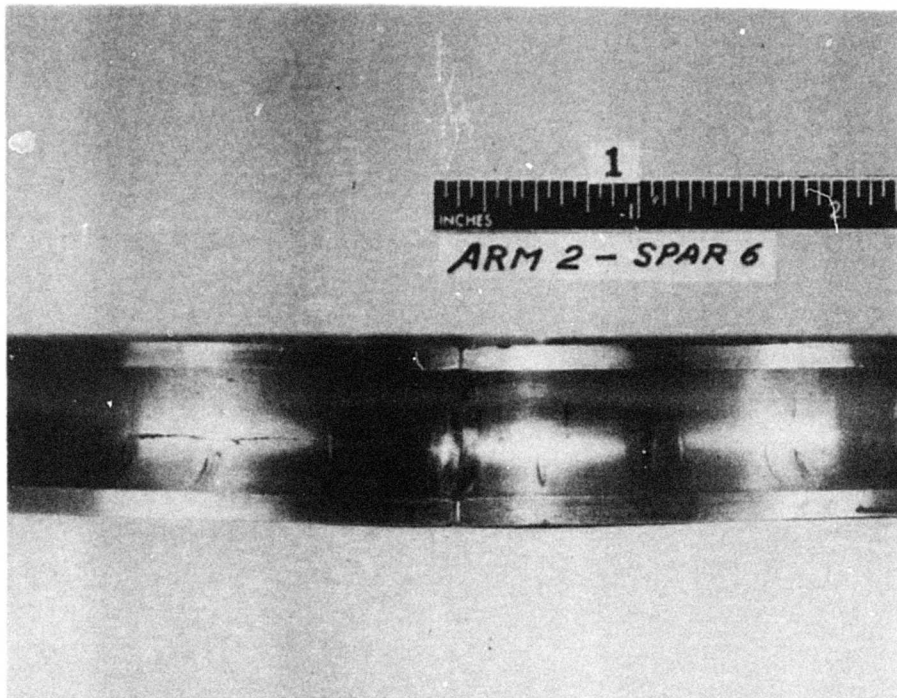
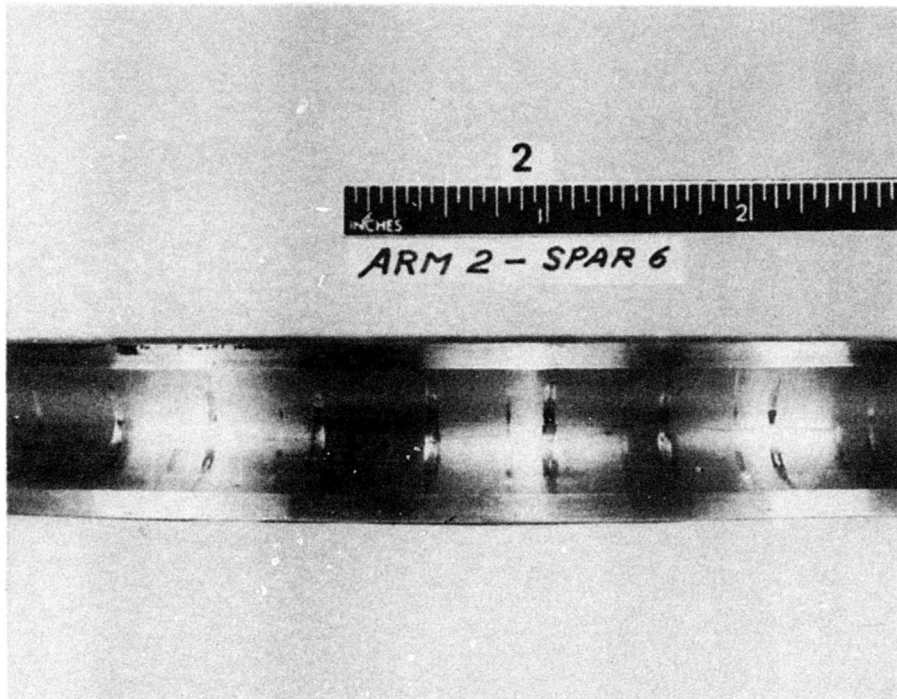


FIGURE 59. INNER-RACE INSERT OF SPAR NUMBER 6

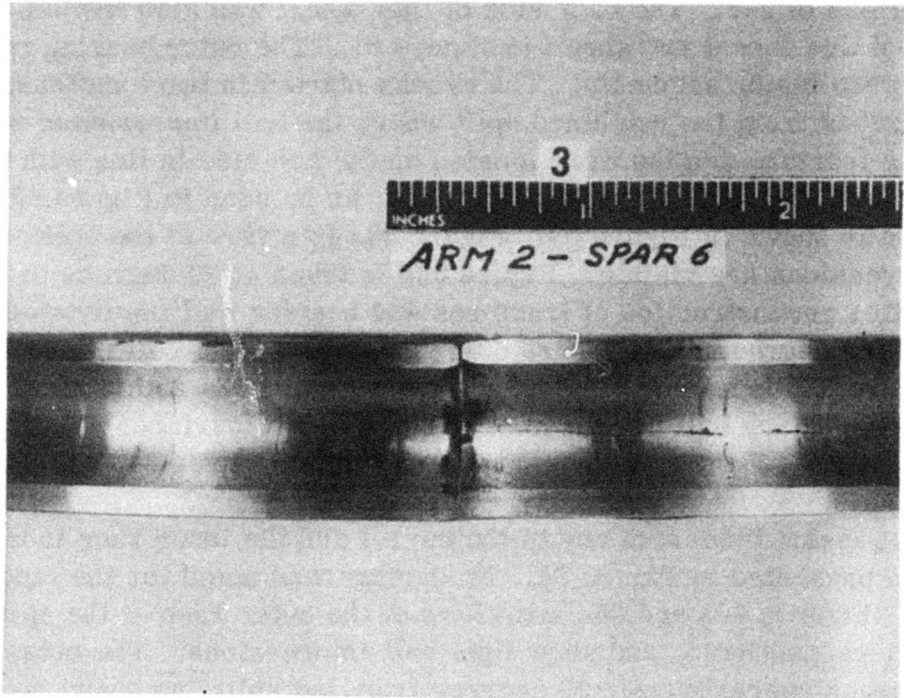


A

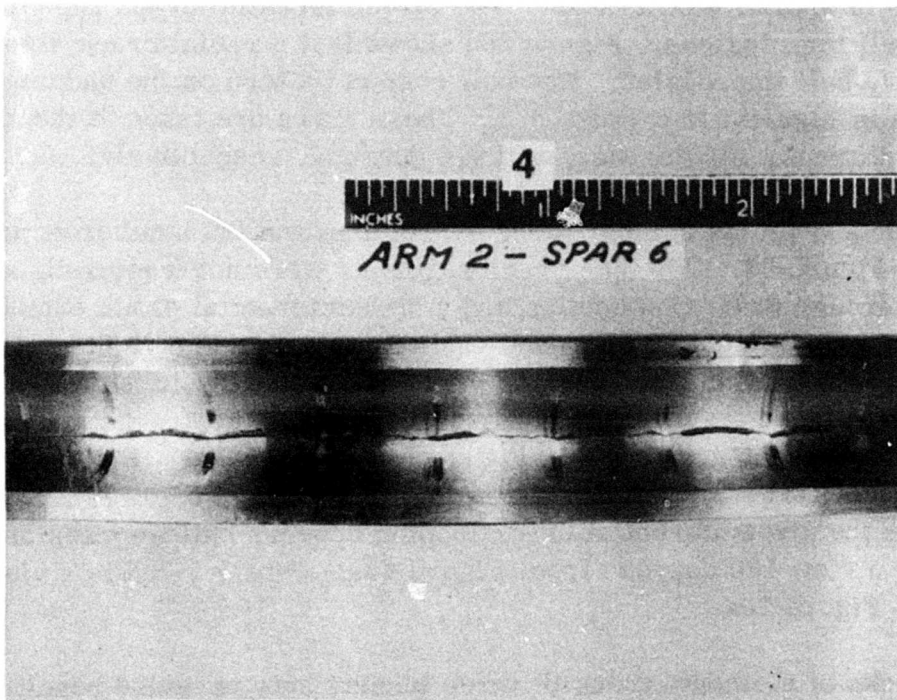


B

FIGURE 60. RECONSTRUCTED INNER-RACE INSERT OF SPAR NUMBER 6



C



D

FIGURE 60, CONTINUED.

the circular arc spar contact side of the insert. The second half of the insert was cracked at the center of the semicircular section. This crack ran for approximately 90 degrees of arc. The back side of this insert was also fretted. Views of both sides of this insert are shown in Figure 61. The outer bearing race was fractured into two major segments. The cracks started in two locations, each located 90 degrees from the machined split where the ball impressions were the greatest. The fracture origins were located on the hub side in line with the apex of the Gothic arch. An overall view of the race can be seen in Figure 62, and a reconstruction is shown in Figure 63. Figure 63a is a view at the split, and only light ball impressions are visible. Figure 63b is taken at 90 degrees to Figure 63a and shows both a reconstruction of fractures and heavier ball impressions. Figure 63c is a view 180 degrees from Figure 63a; again, only light ball impressions are present. Figure 63d is a view 270 degrees from Figure 63a and is similar to Figure 63b; i. e., heavy ball impressions. The fracture surfaces are illustrated in Figure 64a and 64c, while the origins are shown in Figures 64b and 64d.

The outer race insert from arm one of the barrel and the inner race insert from spar eight are presented in Figure 65. No damage was noted for the inner race at this position. Figures 66a and 66c are views of the outer race at the split and 180 degrees away, respectively, and show light ball impressions. The outer race also had a radial crack approximately 90 degrees from the split, as shown in Figure 66b, and a 4-inch-long circumferential crack. This crack was in the base of the groove where the Gothic arches met. A section of the race had also separated from the ring by means of short radial cracks. The circumferential crack appeared to loop between the ball impressions. Figure 66d shows that a radial crack also passed through a heavy ball impression. The ball contact pattern on the undamaged inner race is shown in Figure 67a through 67d. These views are taken at the split (zero degrees), 90 degrees, 180 degrees, and 270 degrees, respectively.

The race inserts from the number three barrel arm and the number seven spar are illustrated in Figure 68. The inner race segments were not fractured, as shown in Figures 69a through 69d. One section had a circumferential crack extending from a split end for approximately 90 degrees. This is shown in Figure 69c. The outer race insert had two radial fractures and circumferential fractures which permitted the separation of three small segments from the ring. The cracks and ball contact pattern for this element are shown in Figure 70a through 70d. Figure 70a shows the split and light ball impressions. Figure 70b is a view 90 degrees from Figure 70a and shows the circumferential crack looping between ball impressions. Figure 70c is a view 180 degrees from Figure 70a. Finally, 70d is a view 270 degrees from Figure 70a.

Hardness checks of elements from all three inserts sets revealed results at or just below the drawing specification of Rc 58-62.

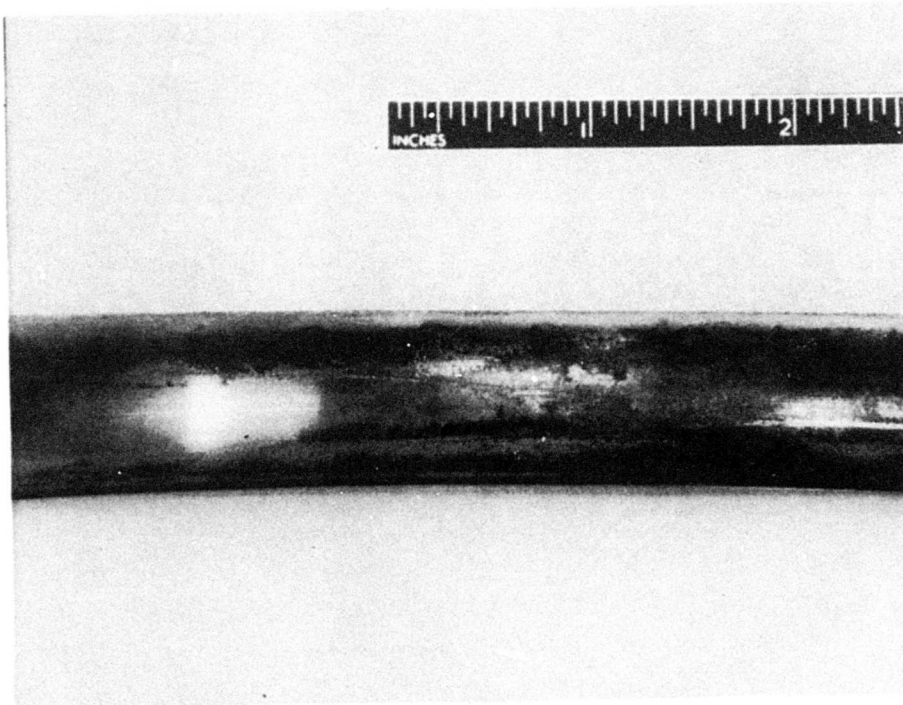
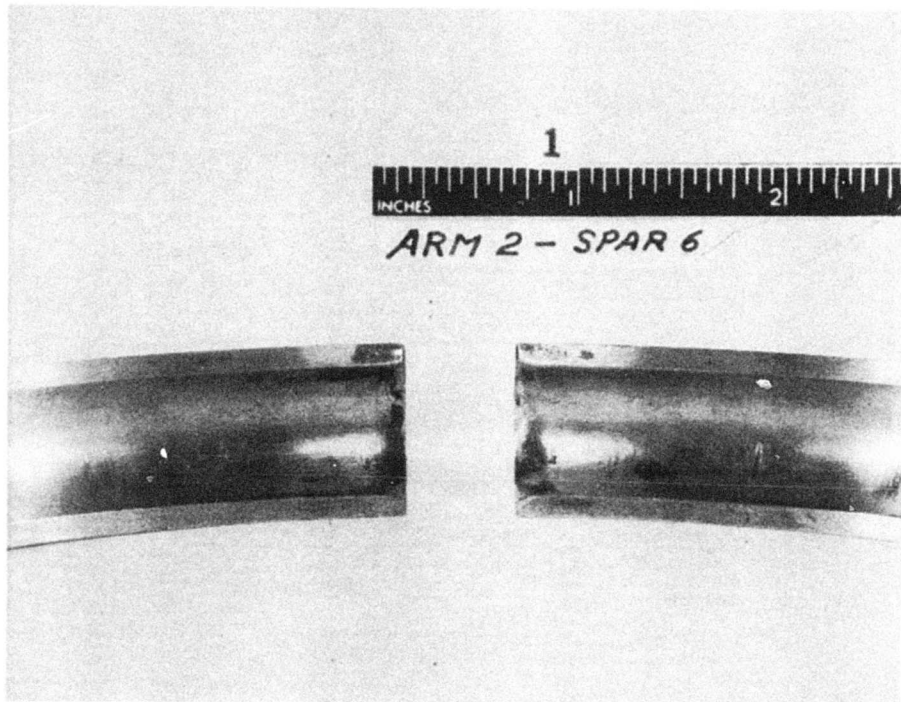


FIGURE 61. INNER-RACE INSERT OF SPAR NUMBER 6

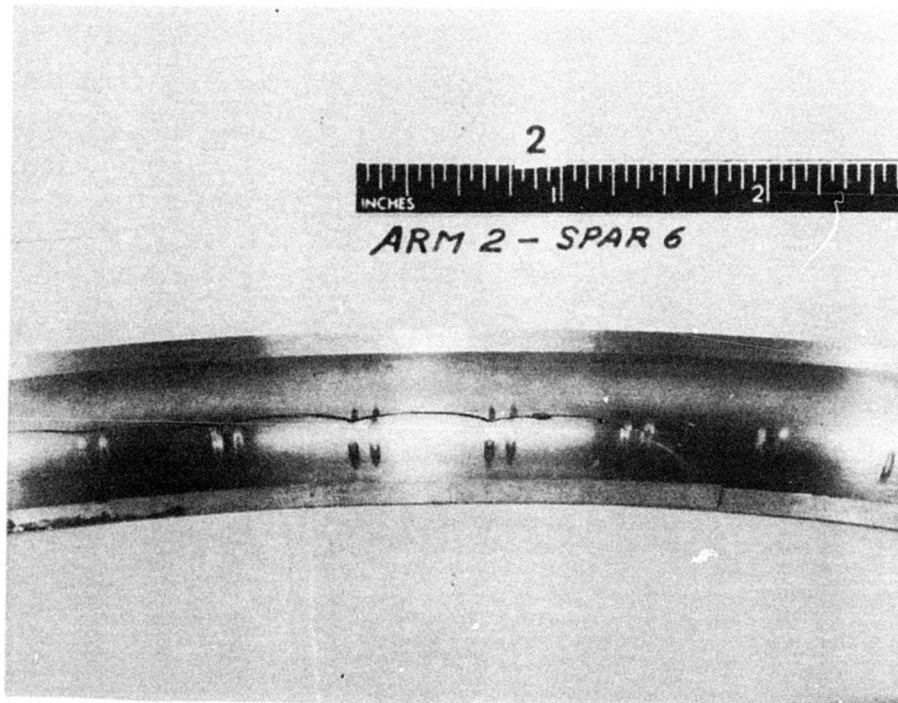


ARM 2 ~ SPAR 6

FIGURE 62. OUTER-RACE INSERT OF BARREL ARM NUMBER 2

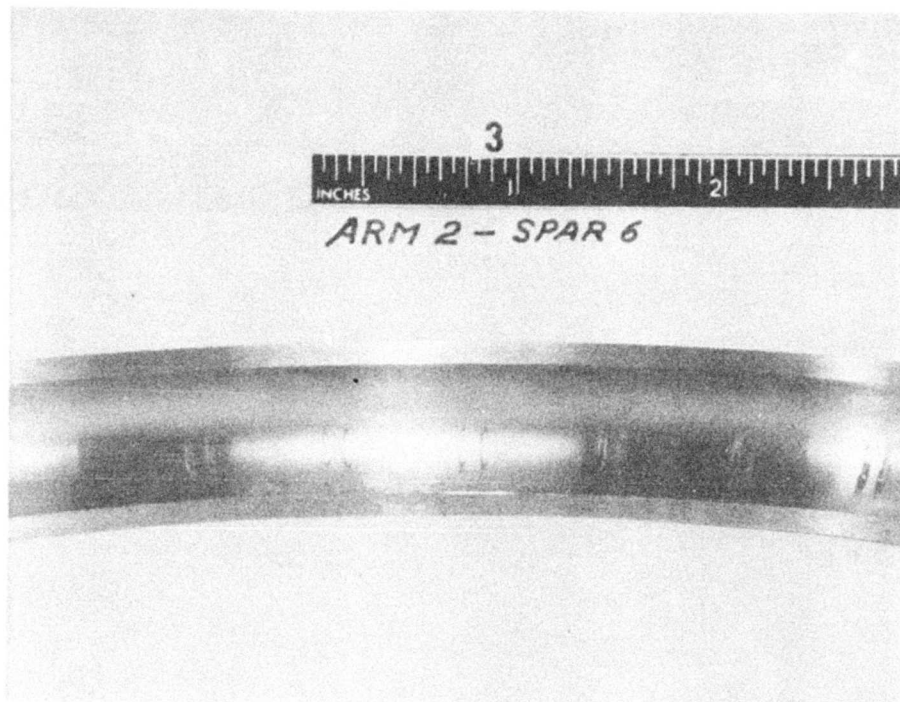


A

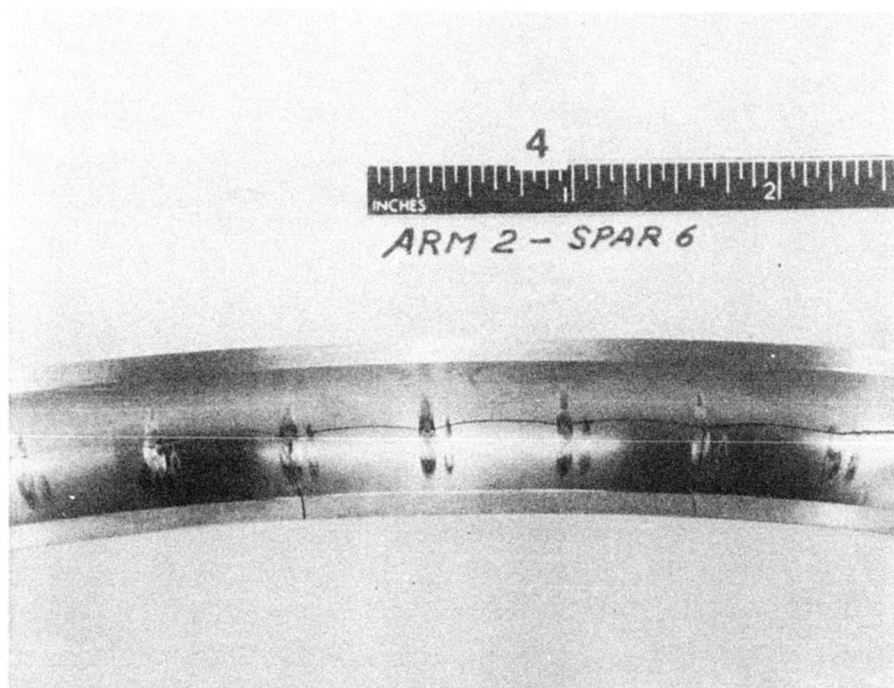


B

FIGURE 63. RECONSTRUCTED OUTER RACE INSERT OF BARREL ARM NUMBER 2

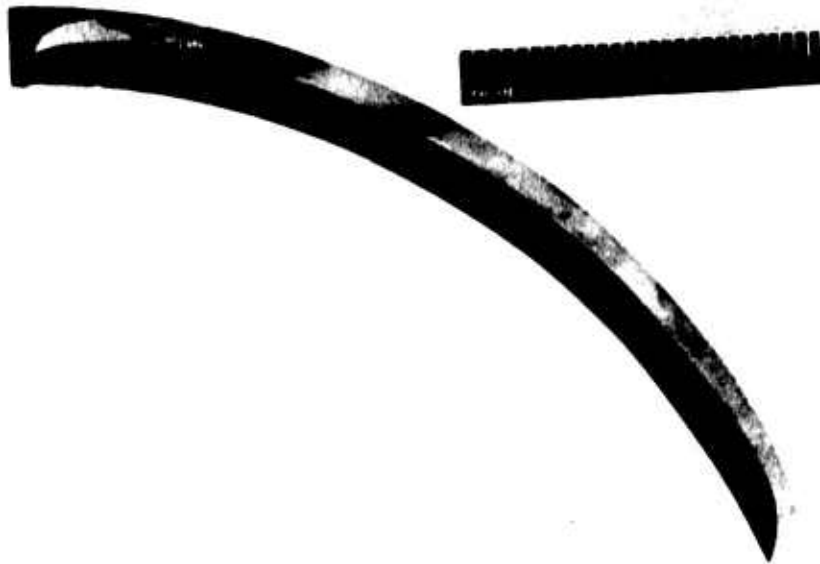


C

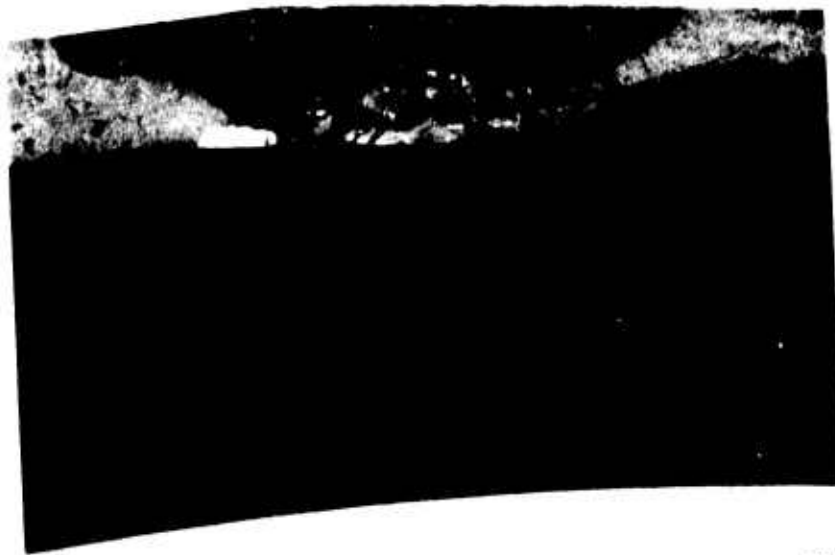


D

FIGURE 63. CONTINUED



A



B

X5

FIGURE 64. OUTER-RACE INSERT OF BARREL ARM NUMBER 2



C



D
X5

FIGURE 64. CONTINUED

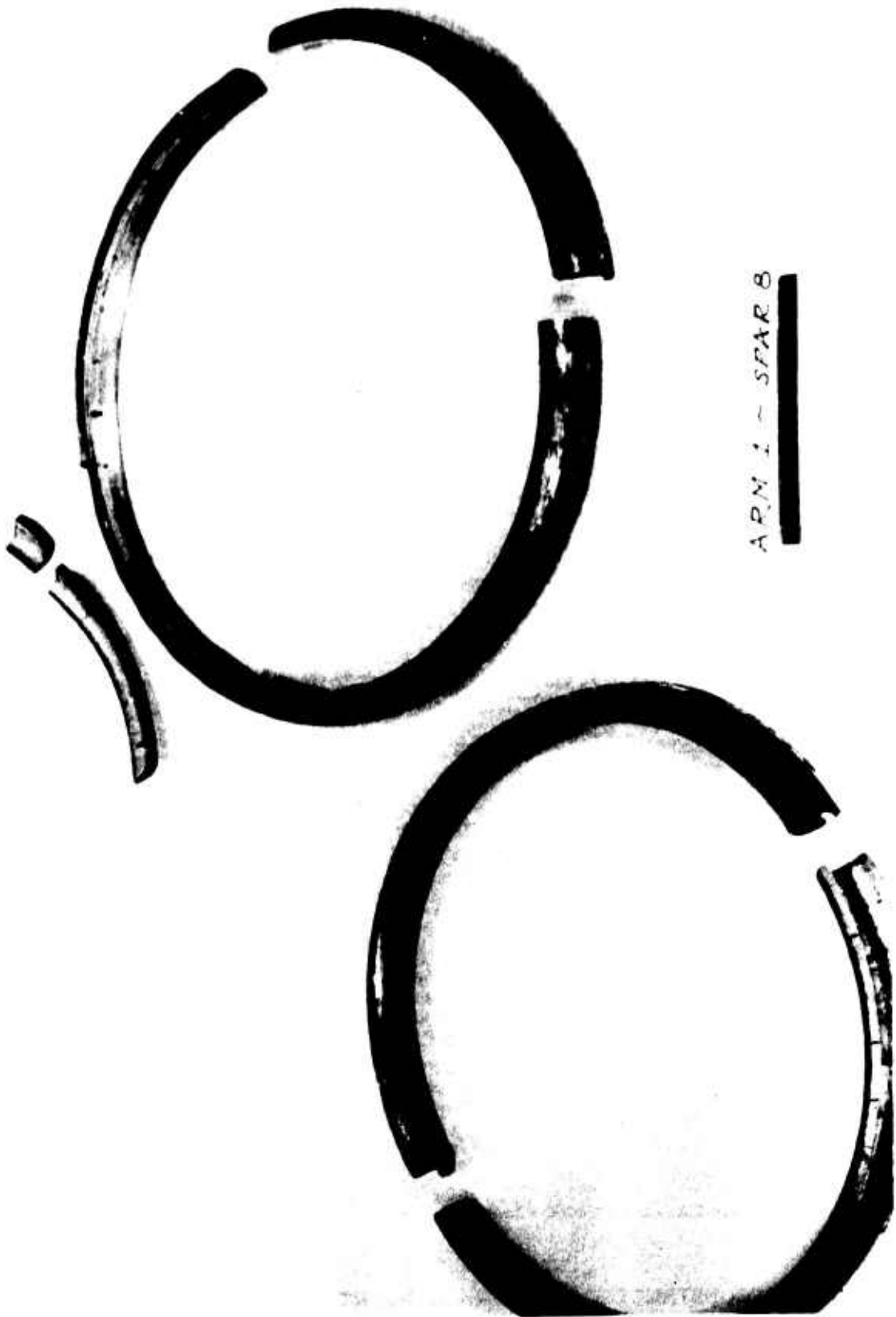
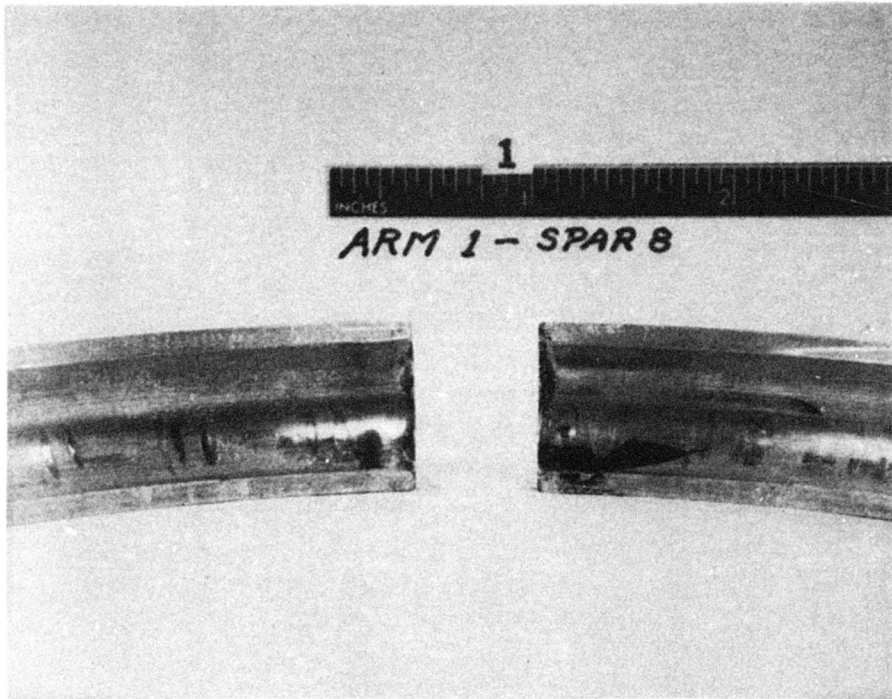
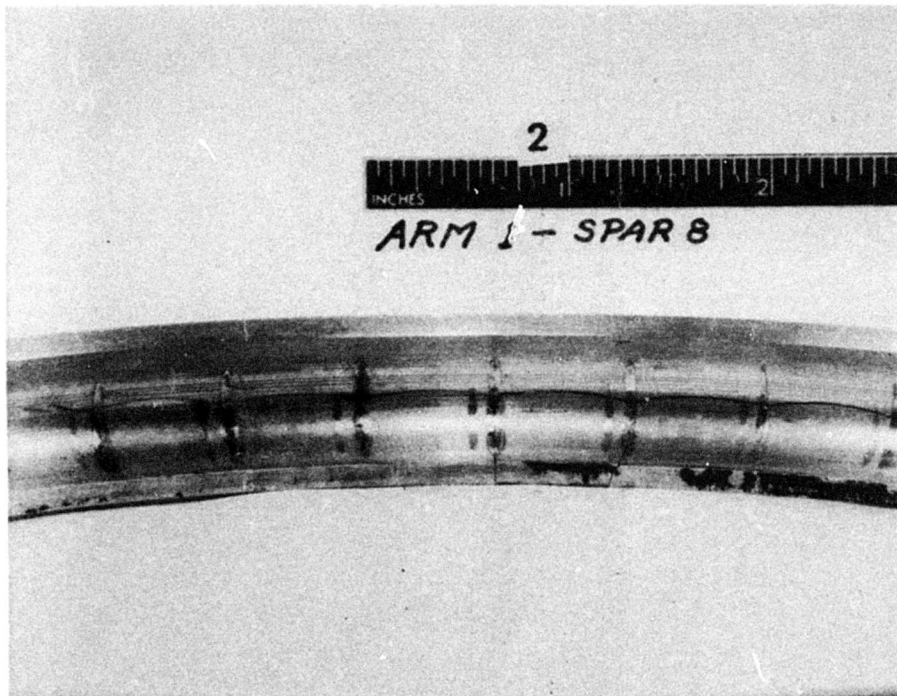


FIGURE 65. OUTER-RACE INSERT OF BARREL ARM NO. 1 AND INNER-RACE INSERT OF SPAR NO. 8

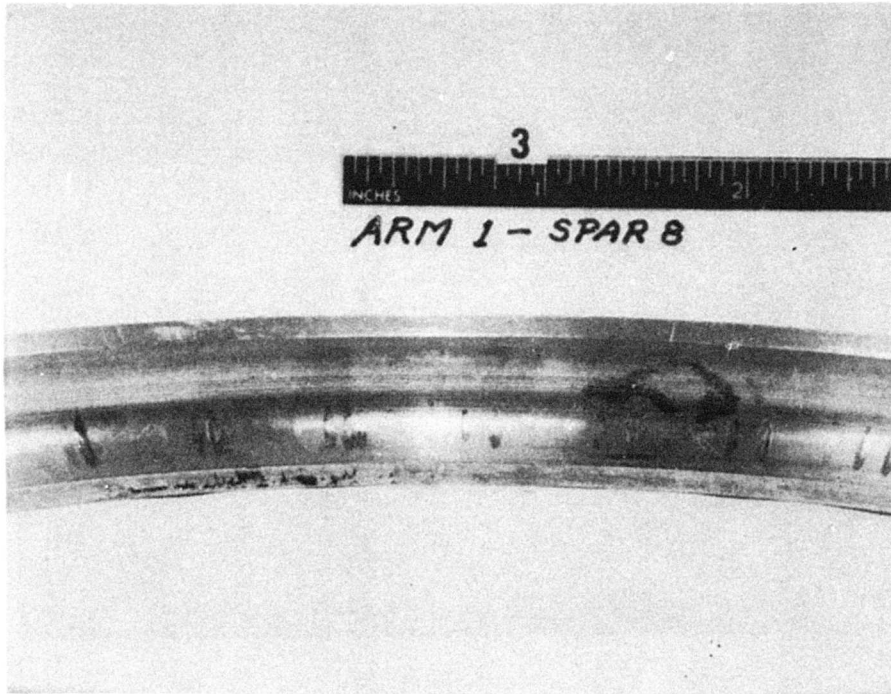


A

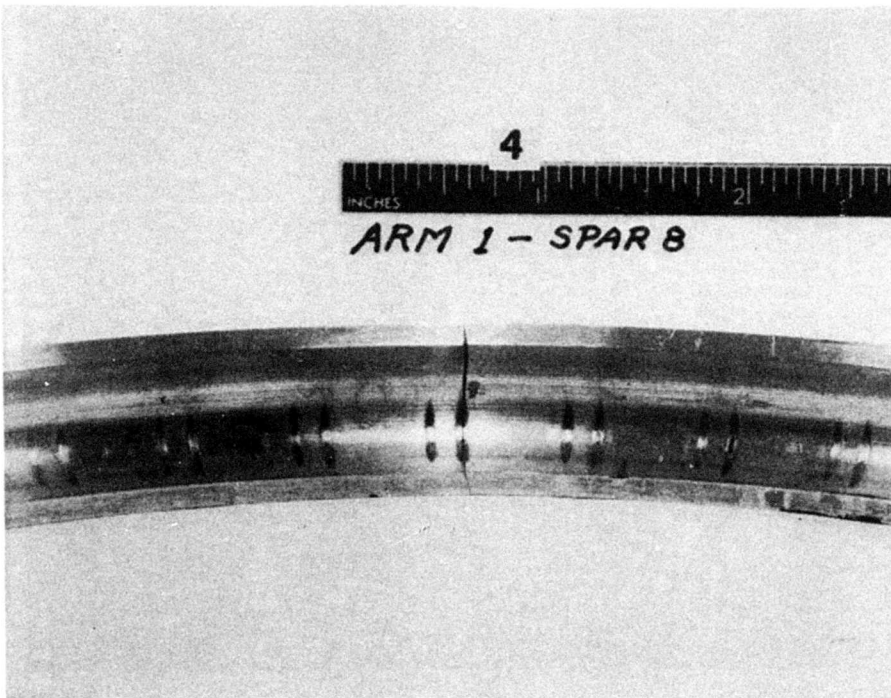


B

FIGURE 66. RECONSTRUCTED OUTER-RACE INSERT OF BARREL ARM NUMBER 1

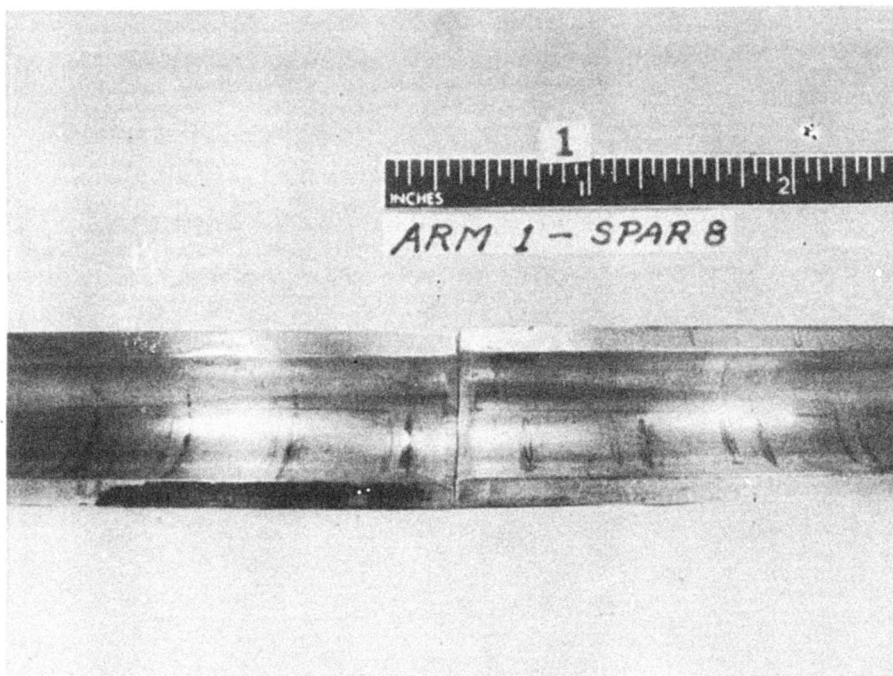


C

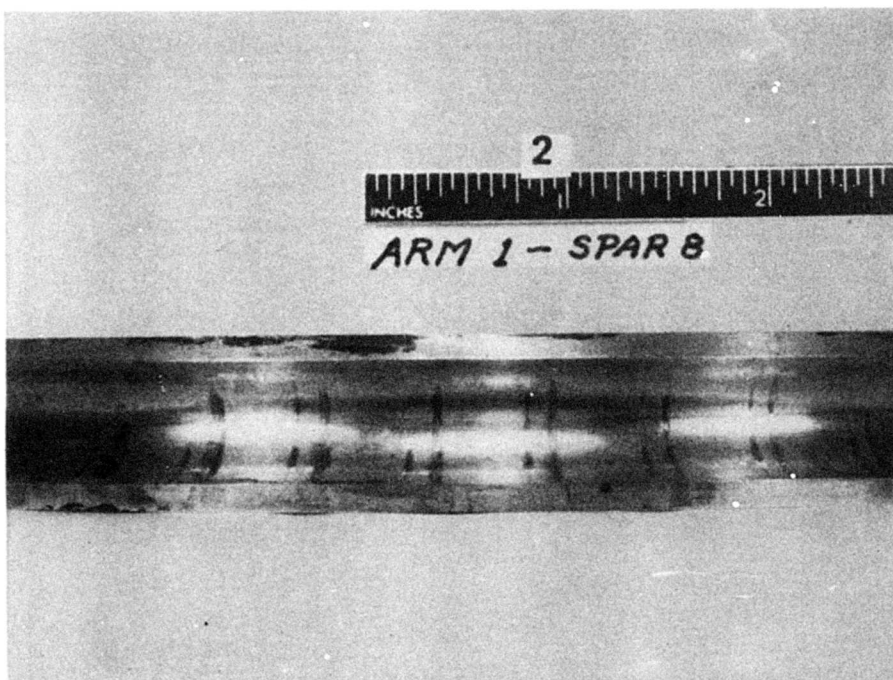


D

FIGURE 66. CONTINUED

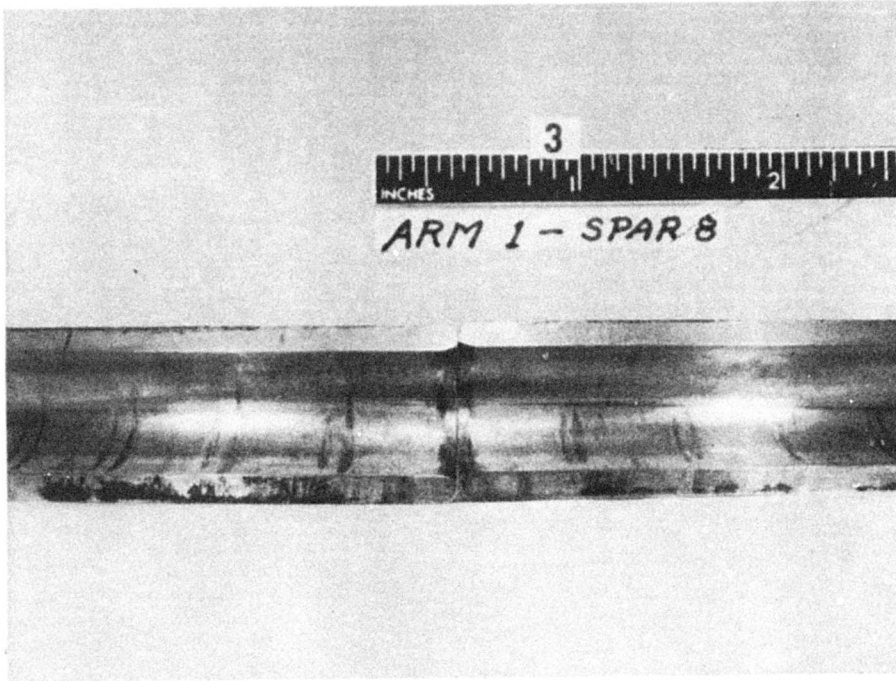


A

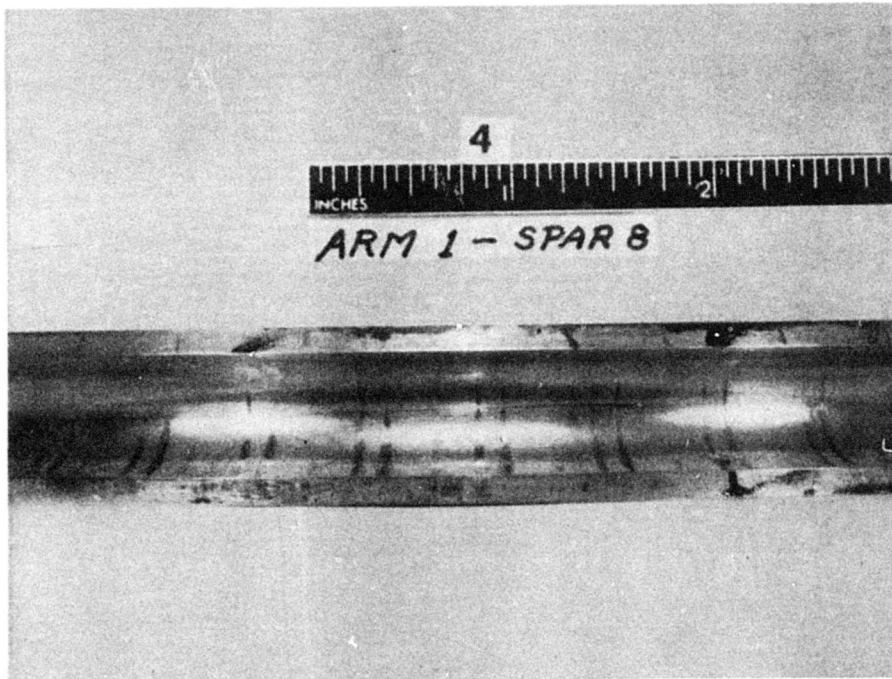


B

FIGURE 67. RECONSTRUCTED INNER-RACE INSERT OF SPAR NUMBER 8



C

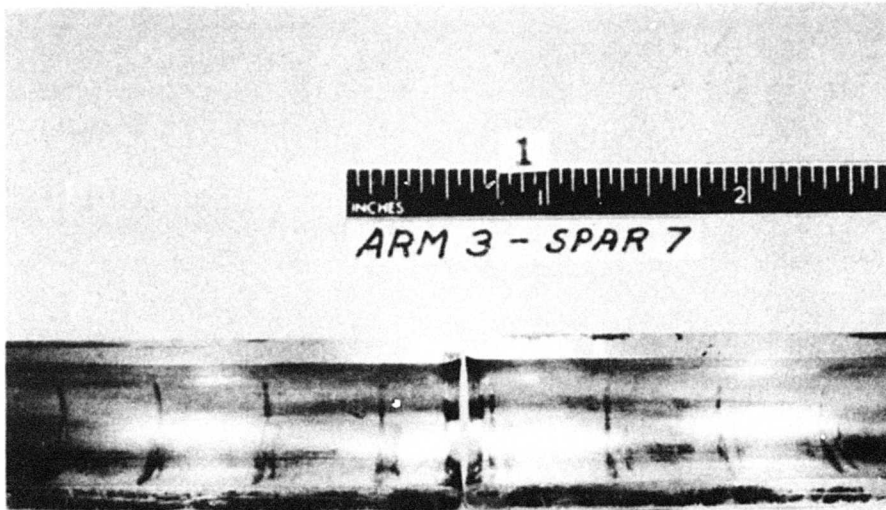


D

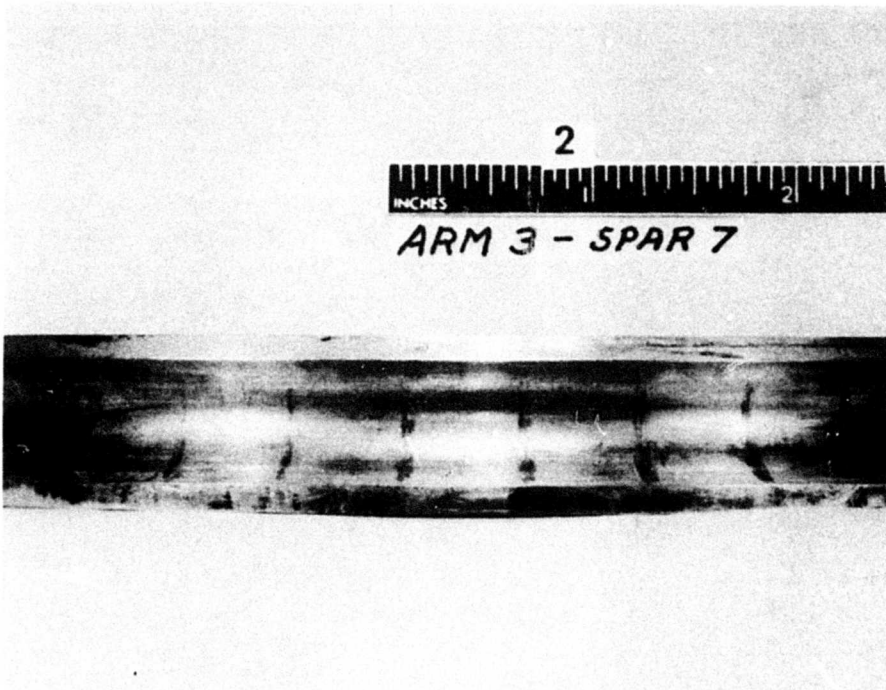
FIGURE 67. CONTINUED



FIGURE 68. OUTER-RACE INSERT OF BARREL ARM NO. 3 AND INNER-RACE INSERT OF SPAR NO. 7

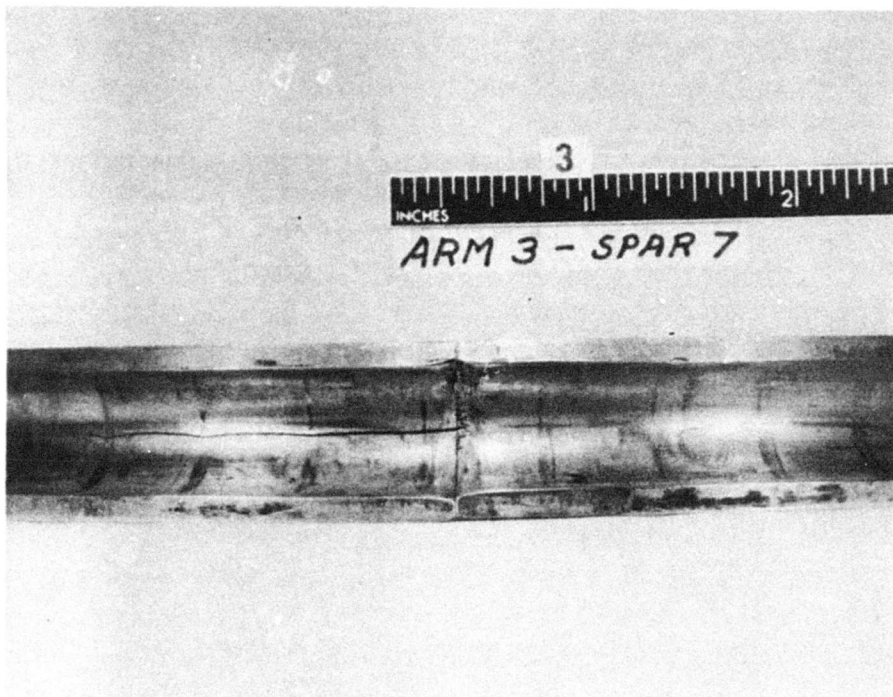


A

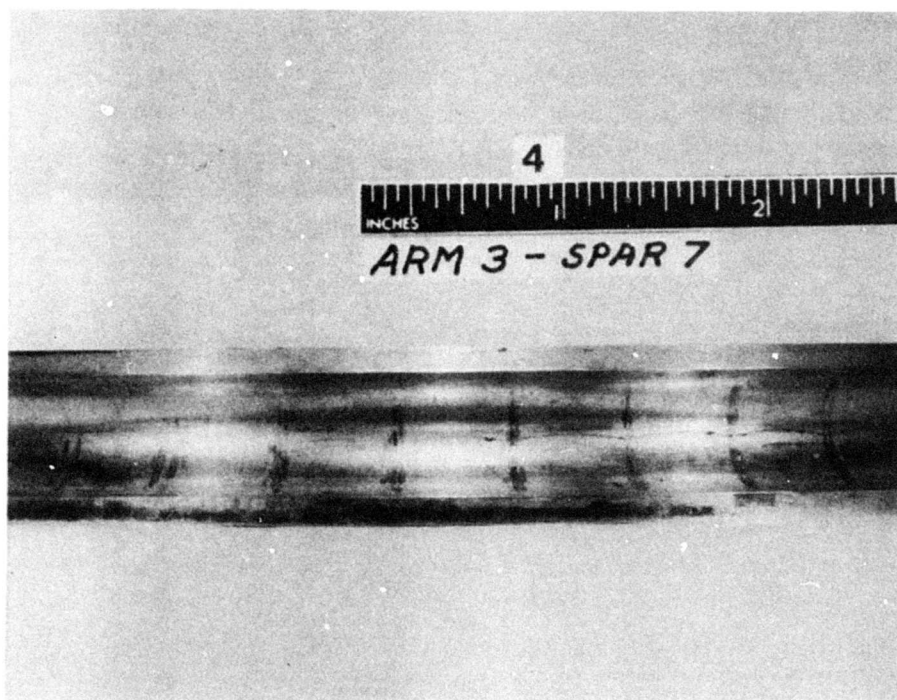


B

FIGURE 69. RECONSTRUCTED INNER-RACE INSERT OF SPAR NUMBER 7

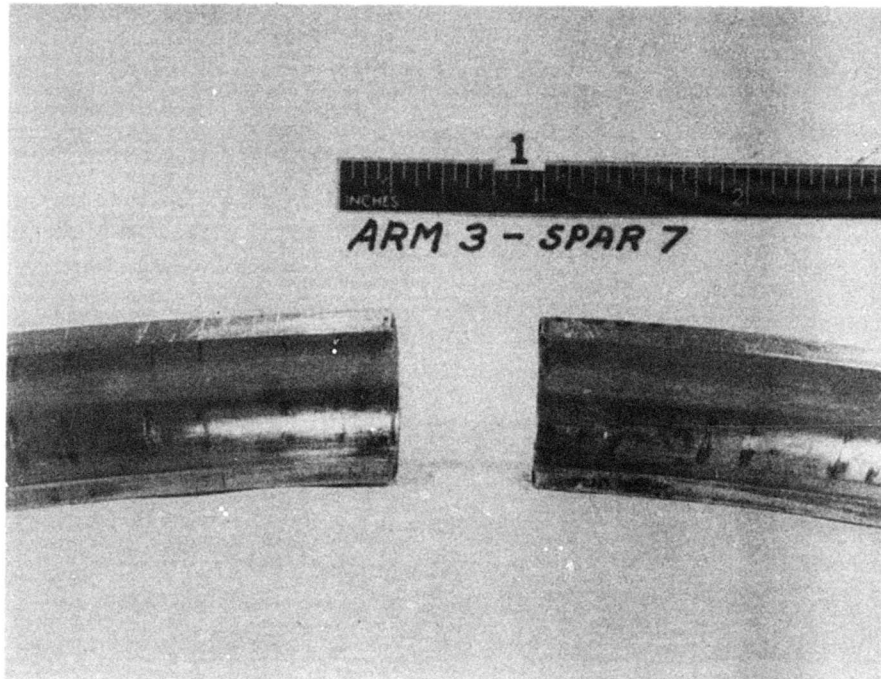


C

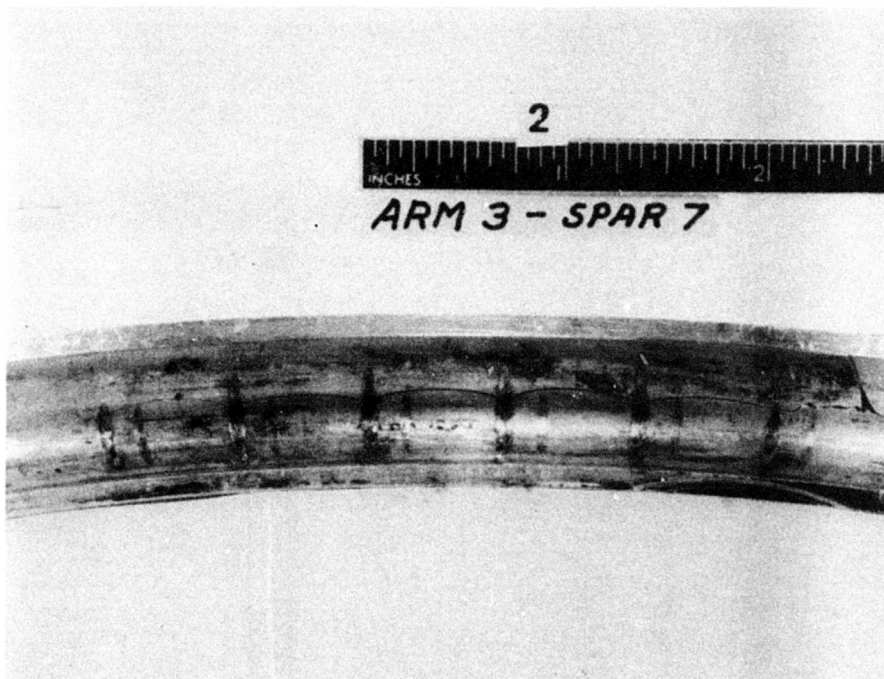


D

FIGURE 69. CONTINUED

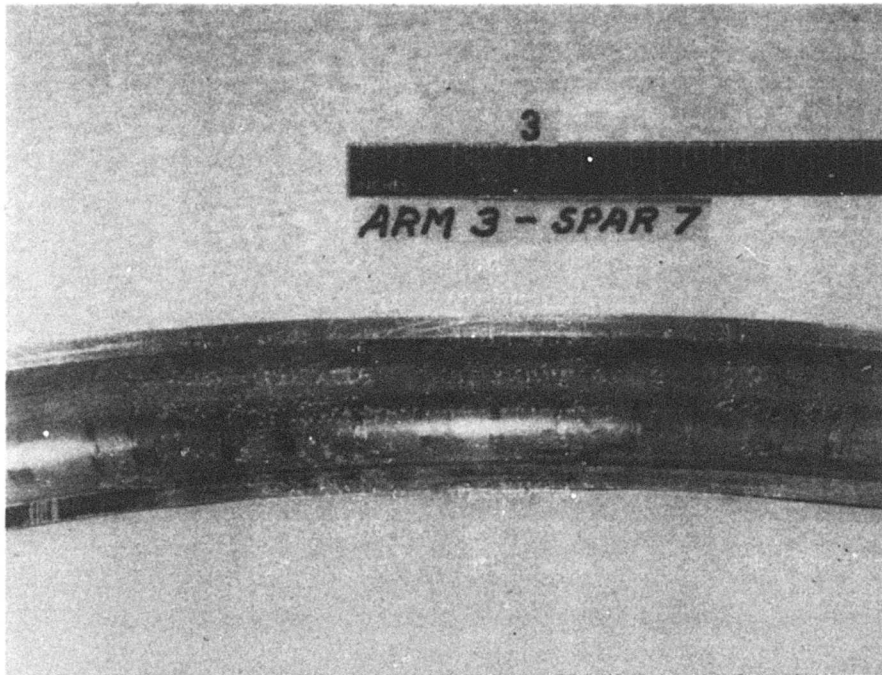


A

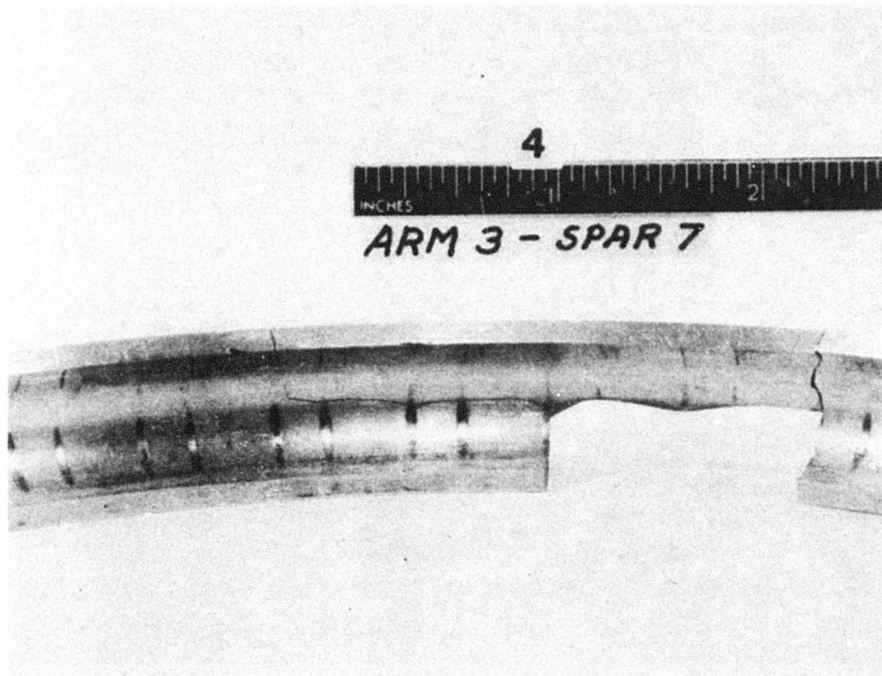


B

FIGURE 70. RECONSTRUCTED OUTER-RACE INSERT OF BARREL ARM NUMBER 3



C



D

FIGURE 70. CONTINUED

Material tests conducted on insert elements from the number two barrel arm revealed microstructure consisting of tempered martensite with uniform distributions of primary carbide. Spectrochemical analysis confirmed that these elements were made from the specified AISI 52100 material.

Examination showed the fractures to be fatigue in nature. The origins were located on the sides of the inserts that nest against the Gothic-arch grooves in the spars and barrel arms. The origins were in line with the apexes of the Gothic arches of the races where the races were not supported by the backup members. Figure 71 schematically illustrates the typical assembly.

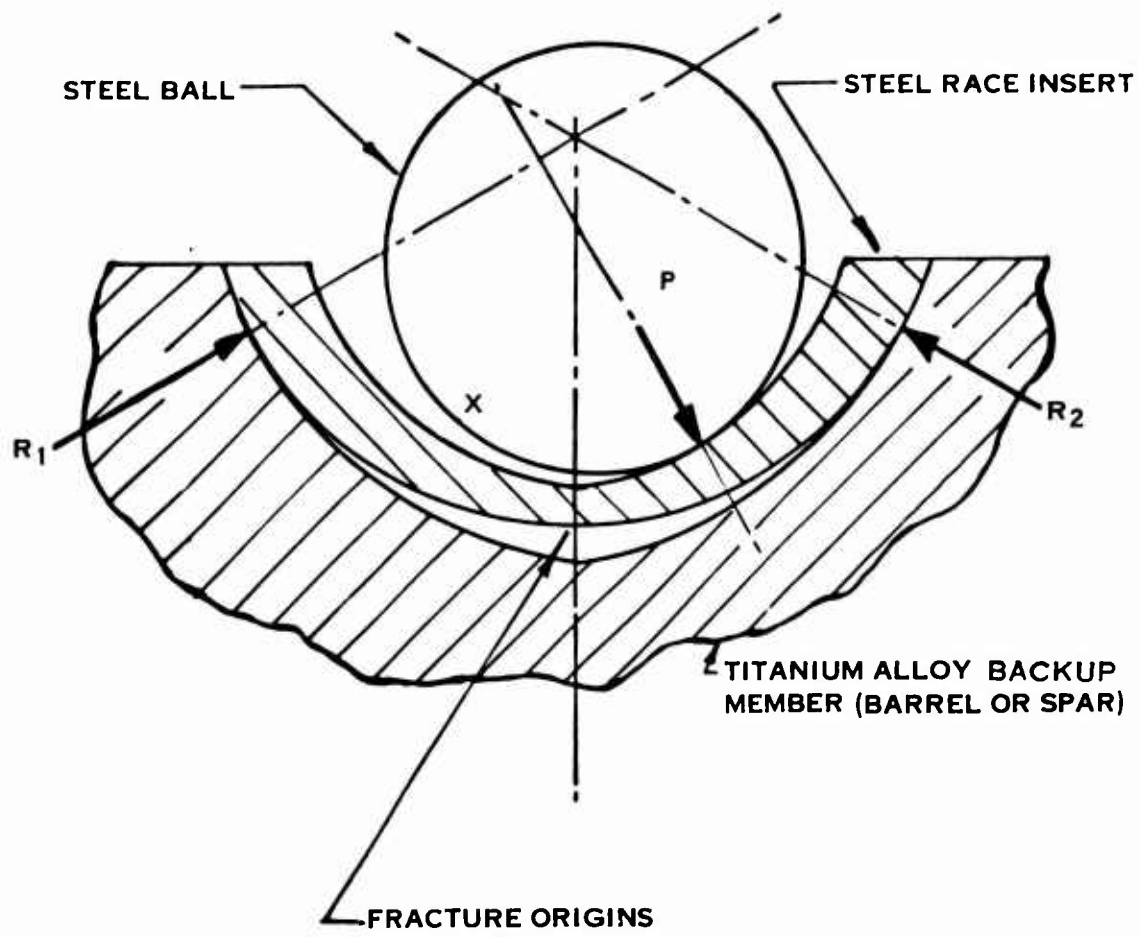
From the Figure, it can be seen that the arch of the backup member results in the reaction to the ball load being taken up in two points near the edges of the insert. The applied load hence develops tensile stresses on the back of the inserts where the fractures originated.

It was also noted that many of the crack origins were in material that had fretting damage. The adverse effect of fretting on the fatigue life of structures is well known; however, it may be that in this case, the fretting developed after the cracking occurred.

Depending on the tolerances of the insert radii and of the support member radii under deflection, ball contact is also possible on the other side of the race at point X in Figure 71. This type of behavior was evidenced by the ball contact patterns on the races where the impressions are coalescences of two distinct Hertzian contact patterns at the apex of the arch.

Analysis of the stresses associated with this tendency of the race insert to wrap around the ball indicated that stresses in excess of the material design allowable were experienced due to bending.

Prior to continuing the 3P-OOP fatigue test, at the next or second level, an overall assessment of the titanium propeller barrel program was conducted. The advisability of committing the remaining set of bearing race inserts to furthering the evaluation of the spar and bearing retention (3P-OOP) as opposed to establishing the structural integrity of the barrel tail shaft and arm regions (1P-OOP) was studied. Further, as the low-pressure bonding system employed for manufacture of the spars had not shown sufficient strength-to-weight benefits to achieve the estimated weight savings, it was concluded that no further Borsic aluminum work would be conducted.



P = BALL LOAD
 R₁ & R₂ = LOAD REACTIONS

FIGURE 71. SCHEMATIC OF GOTHIC-ARCH CONSTRUCTION

Fatigue Strength Investigation (FSI) 1P-OOP

As stated earlier the FSI determines structural characteristics and fatigue load capacity. The primary purpose of the 1P test was to subject the barrel tail shaft region to the complex loadings arising from out-of-plane vibratory bending moment and main support bearing reaction. A side benefit resulting from the 1P effort was that it increased the retention test samples.

As a result of the bearing-race insert-supply limitations just discussed, effort was next concentrated on modifications that would enhance the chances of completing two levels of 1P-OOP fatigue test. In lieu of manufacturing an additional Borsic aluminum spar, a set of three steel test bars that would have similar loading characteristics was designed and manufactured.

Modification of the race inserts involved circumferential separation of the Gothic arch at the apex in accordance with inner race modification SK89049 and outer race modification SK89050. See Figures 72 and 73, respectively. The inserts were cold worked all over by glass bead peening to improve the fatigue properties. In addition they were superficially plated with gold to improve resistance to fretting and to observe Hertzian patterns. Steel test bars in accordance with manufacturing drawing 761937 (see Figure 74) were fabricated. The Gothic-arch grooves in the bars were cold worked by glass bead peening. The above hardware, together with barrel number two, was utilized for this test.

The test assembly, in addition to the structural hardware used for support, contained the wedge mechanism discussed earlier to apply and maintain simulated centrifugal blade load. Strain gages located on the test bars were used to measure centrifugal load. The subsequent 1P-OOP fatigue evaluation was performed on a mechanical oscillator. Cam eccentric weights located at the outboard end of each test bar were adjusted to achieve the intended moment level on each arm. Phasing of these eccentric weights achieved the 1P loading. Bending moment was measured by the same test bar strain gaging. By determining moment distribution along each test bar, the desired shank moment could be set and controlled. The barrel cavity was filled with MIL-L-7808 lubricating oil. The 1P-OOP fatigue test setup is shown in Figure 75.

As discussed previously, the standard procedure for new designs is to initiate fatigue test at a level 20-30% below the design condition. As the result of the ESA, which indicated a conservative barrel design, it was concluded that no fractures would occur from testing at the first level. The procedure was thus modified to initiate testing at the continuous design condition shown in Table 4. After 134,000 of the planned ten million cycles, the test unit had to be disassembled to correct a deficiency in the test facility support structure which allowed in-plane rotation.

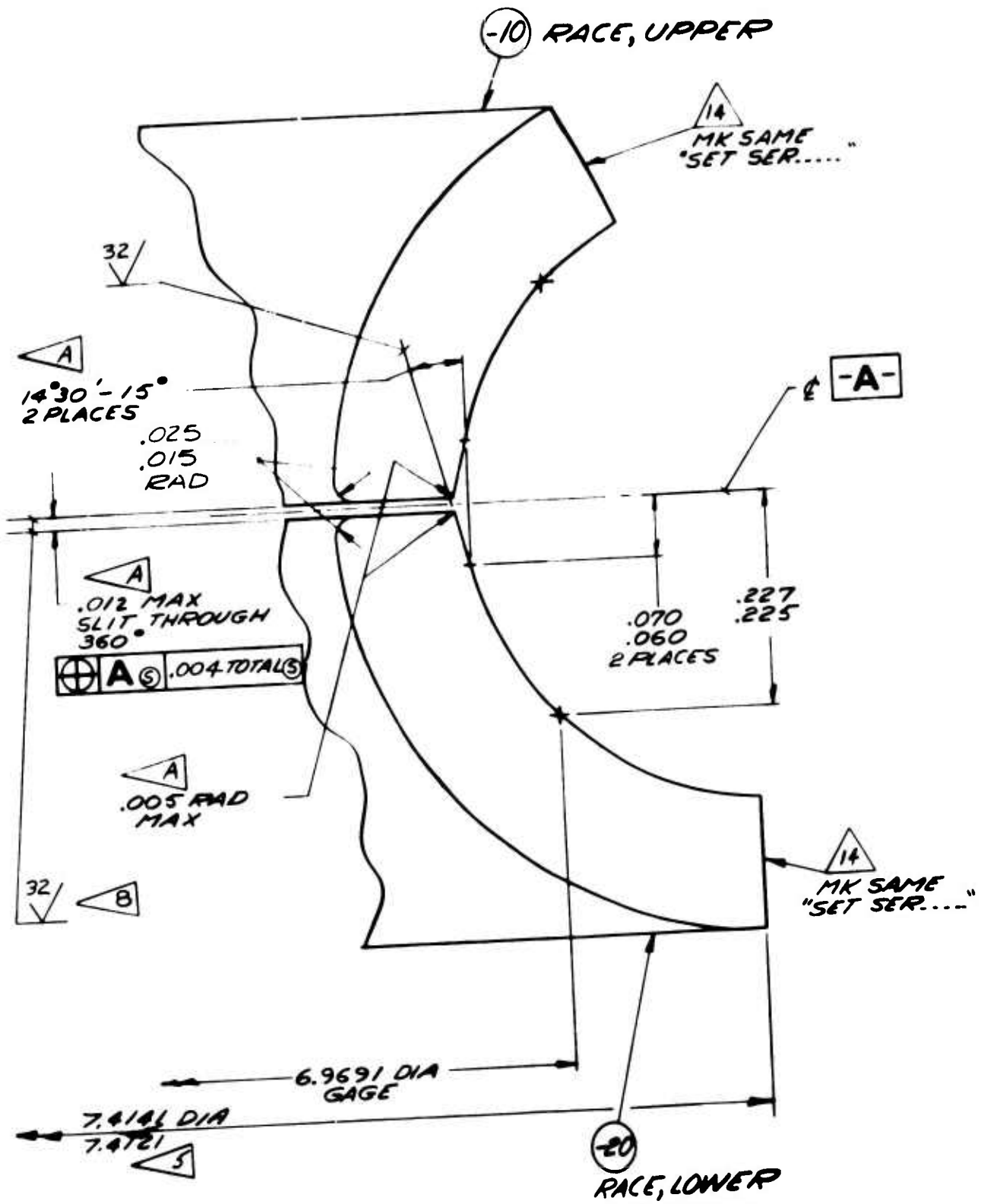


FIGURE 72. INNER-RACE INSERT REWORK DRAWING

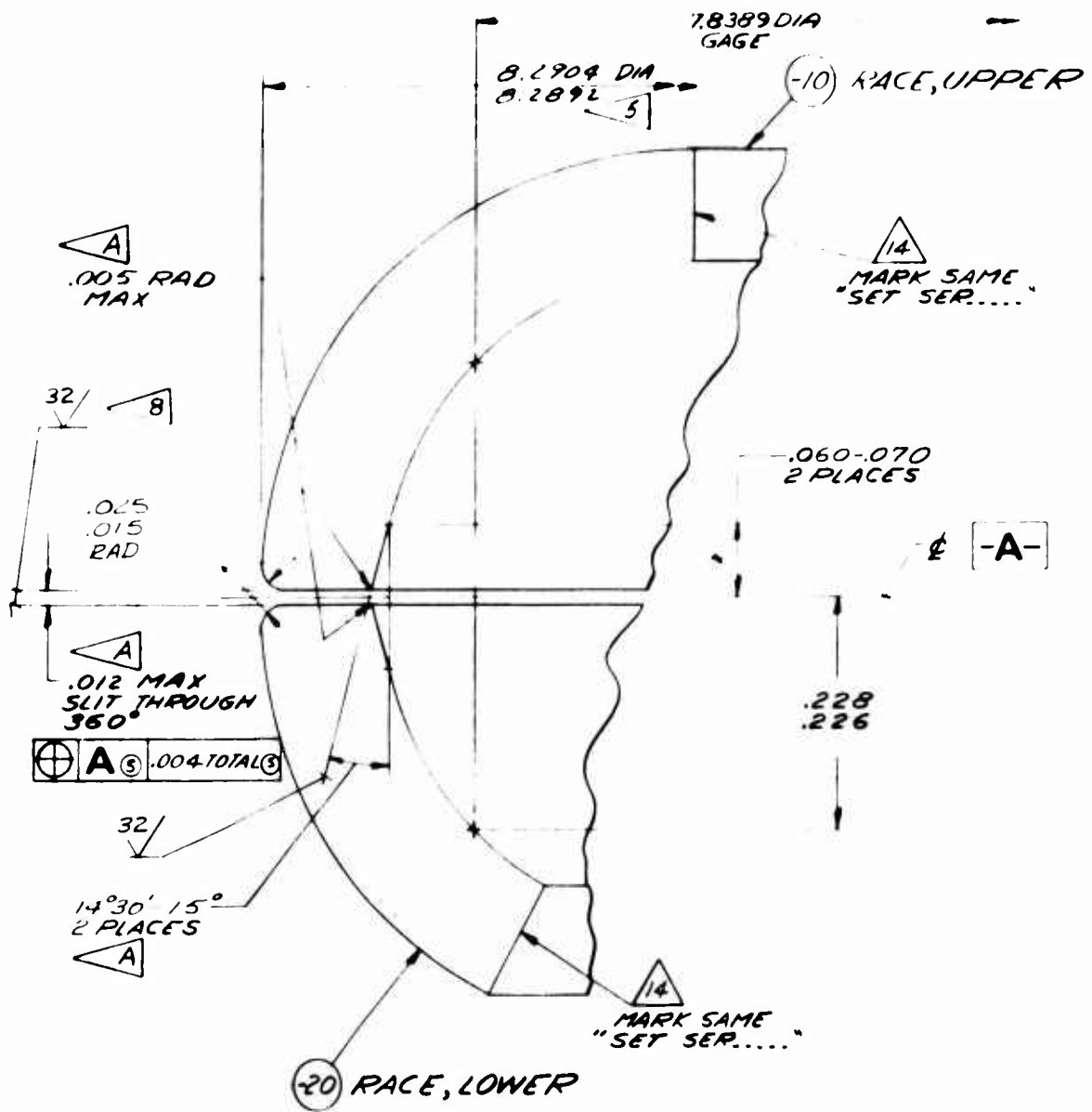


FIGURE 73. OUTER-RACE INSERT REWORK DRAWING

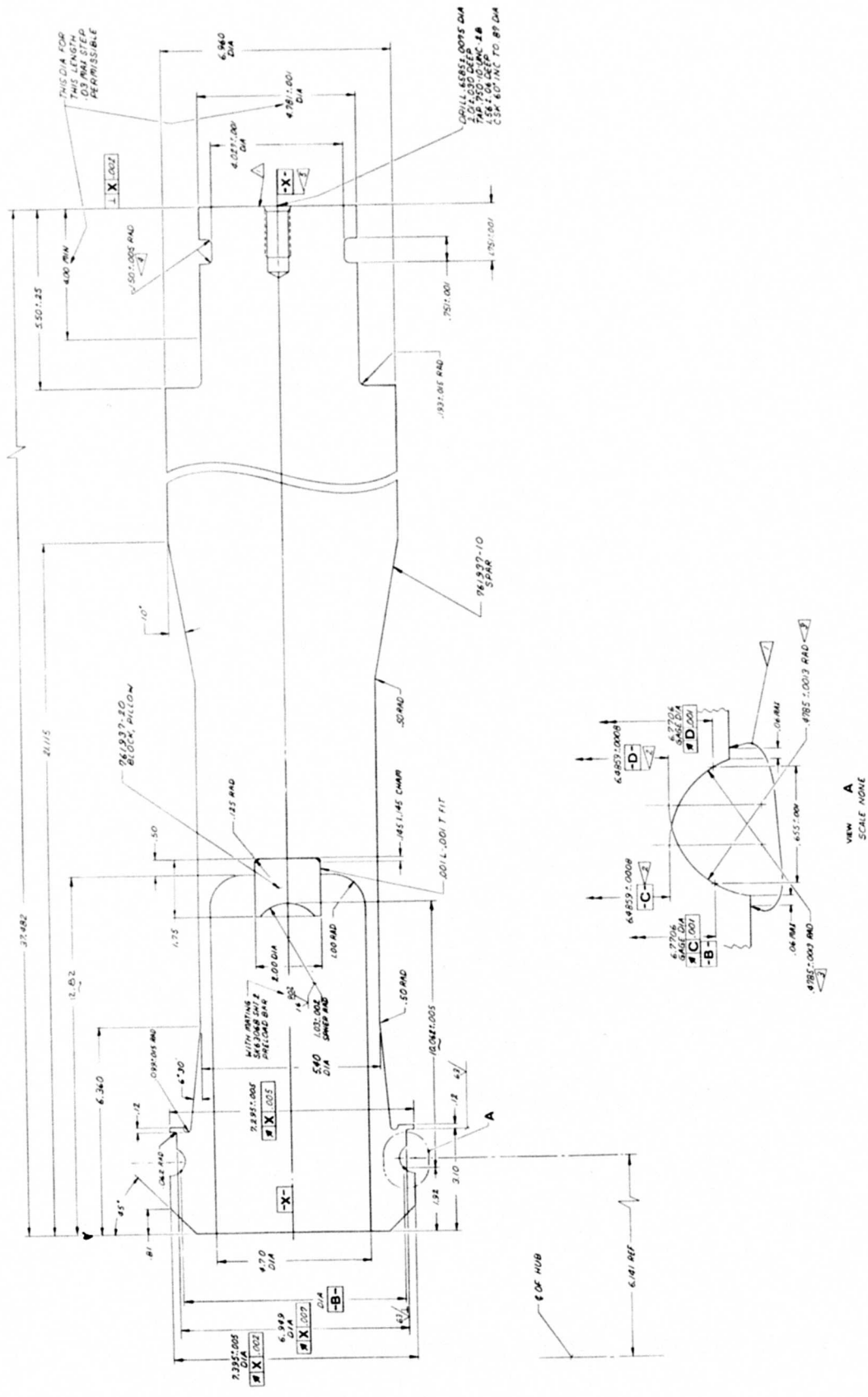


FIGURE 74. TEST BAR DETAIL DRAWING

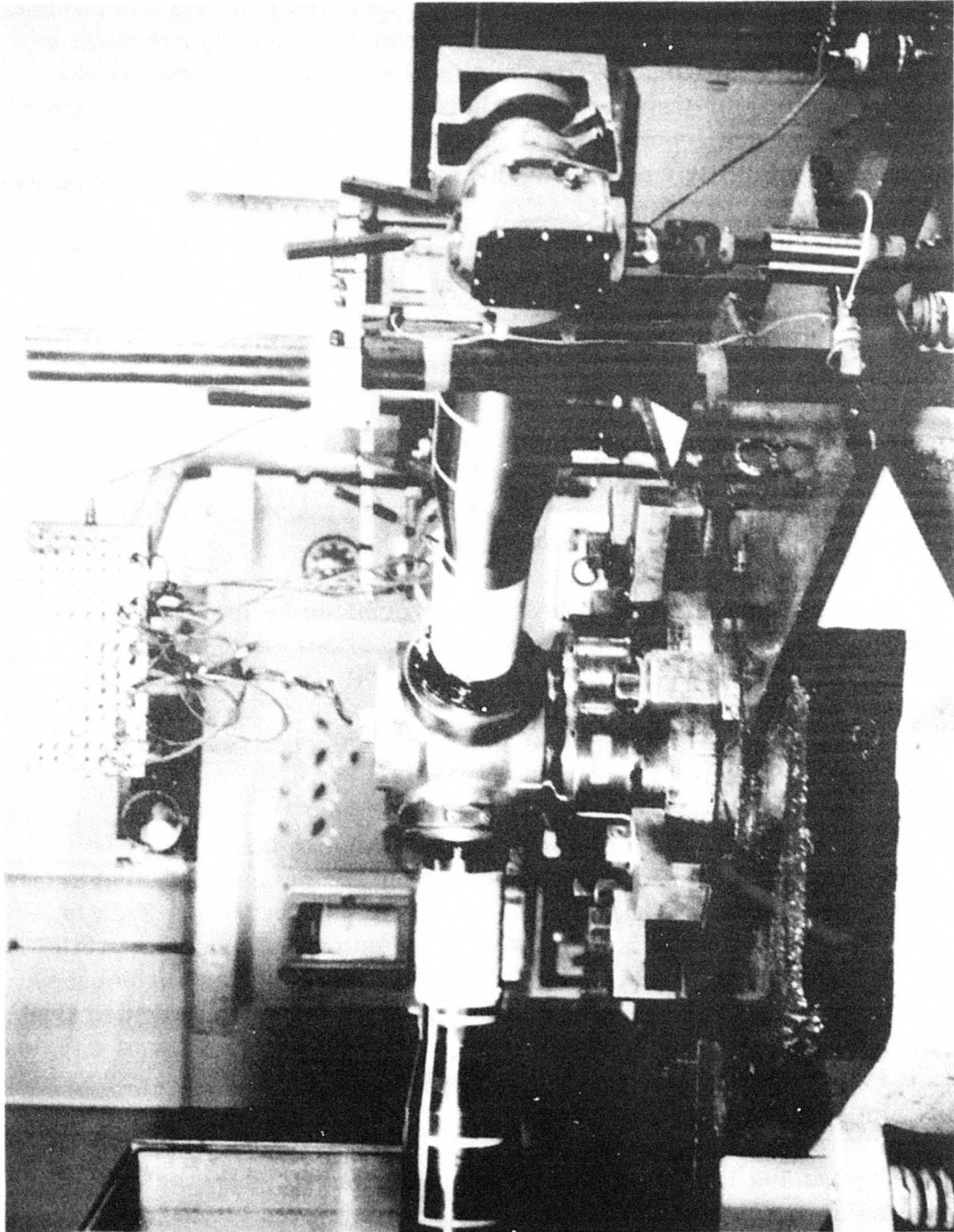


FIGURE 75. 1P OUT-OF-PLANE FATIGUE TEST SETUP

Minor modifications were incorporated to eliminate further rotation. After re-assembly and reloading, testing was resumed without incident. Following approximately one million cycles, the mechanical oscillator/test assembly began to operate erratically. Refinements in cam angle settings and load arm phasing did not correct the instability. At that time, the bending moment level was reduced to 50,000 inch-pounds and operation became satisfactory. The level was incrementally increased to 65,000 inch-pounds and operation remained stable. Approximately 210,000 cycles were accumulated during the investigation. As the previously experienced instability was no longer present, normal test was resumed.

Following the accumulation of 4.06 million cycles, one barrel arm had to be disassembled to stop excessive external oil leakage. Disassembly inspection confirmed the presence of a cut blade seal but, more significantly, revealed fractured inner and outer race inserts. Further disassembly of the remaining barrel arms revealed additional fractures.

Fluorescent penetrant inspection of the titanium barrel revealed no cracking or other structural damage. The retention area which was contacted by the steel race inserts was void of spalling damage. There were score marks noted in these areas resulting from contact of the edges of the fractured inserts.

The maximum stressed points of the barrel, as determined by the ESA, are plotted on the material modified Goodman diagram for the maximum load levels of the fatigue test; i. e., 50,000 inch-pounds shank moment (3P-OOP level) and 65,000 inch-pounds shank moment (1P-OOP level). See Figure 76. The points are below the modified Goodman diagram design stress curve, and hence fracture was not experienced at these levels.

The race inserts from all three arms were damaged, as can be seen in Figures 77 through 79. One section of the outer-race insert from the number 1 barrel arm position was fragmented into seven pieces by seven radial fractures. This is illustrated in Figure 77. The top row illustrates the outer-race inserts, while the bottom row illustrates the inner-race inserts. All of the radial fractures passed through ball impressions. The markings on the fracture surfaces indicated that the origins were located at the ball impressions. Figure 78a is a view of a typical fracture at a ball impression. Figure 78b shows the fracture surface. The inner-race inserts from this position were intact.

The top row of Figure 79a illustrates the outer-race inserts, while the bottom row illustrates the inner-race inserts from barrel arm two. From the number two barrel arm position, one of the outer-race inserts had two radial fractures, and a small section was broken away from one of the inner-race inserts. This is shown in Figure 79b and 79c, where a second crack, parallel to the fracture on the inner race insert, can be seen. Again, the fracture surfaces revealed that the origins were located at ball impressions.

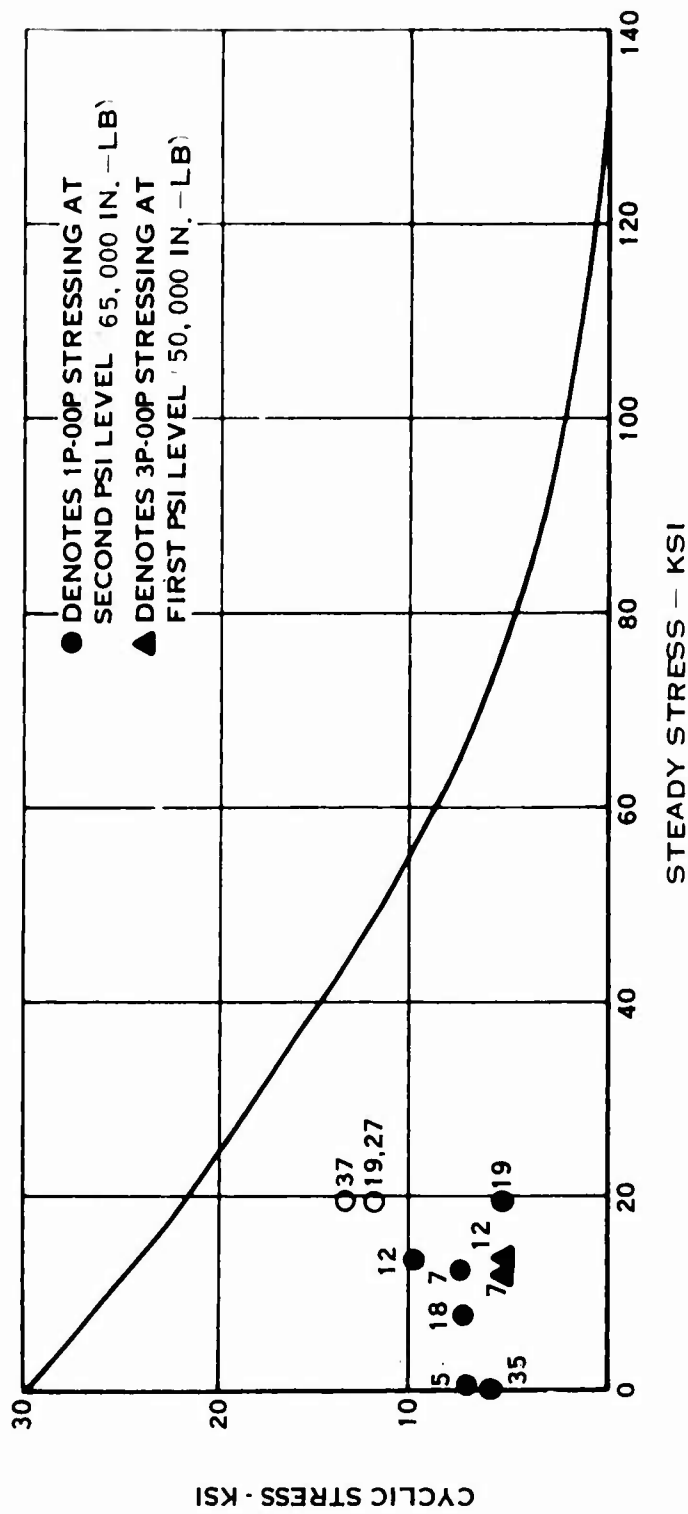


FIGURE 76. TITANIUM BARREL FATIGUE TEST RESULTS

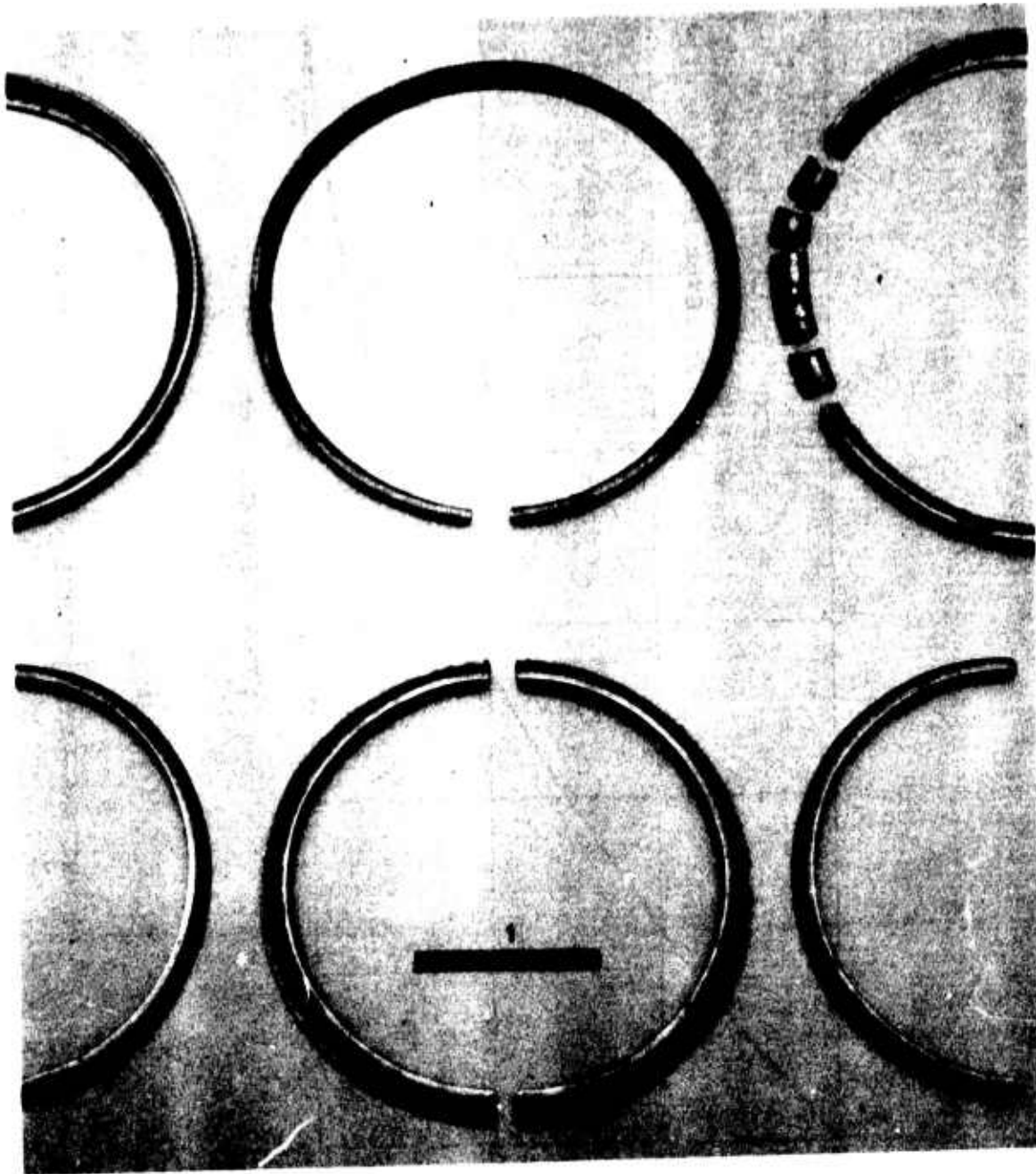
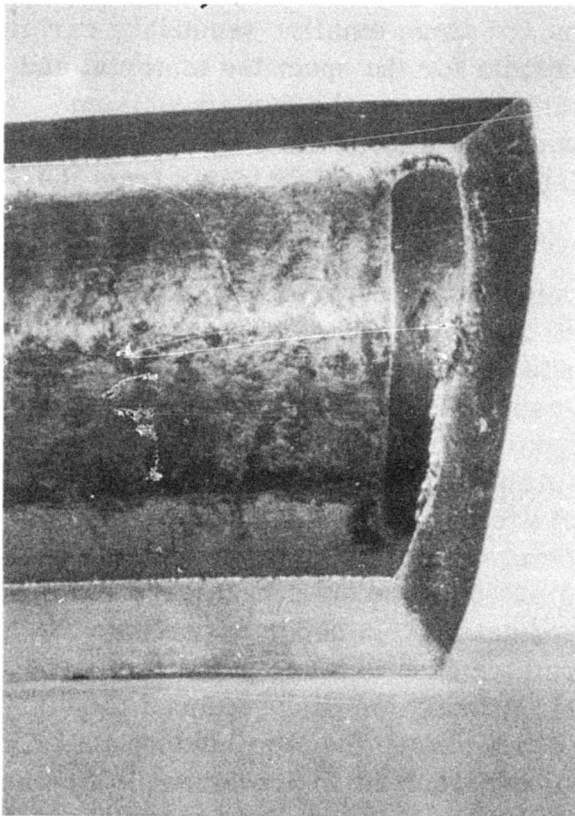
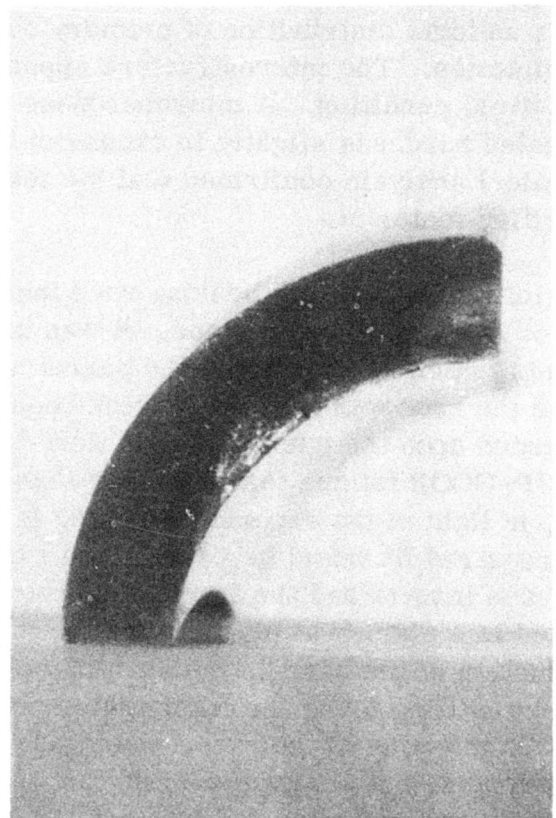


FIGURE 77. OUTER-RACE INSERT OF BARREL ARM 1 (TOP ROW)
AND INNER-RACE INSERT OF TEST BAR 1 (BOTTOM ROW)



X5 A



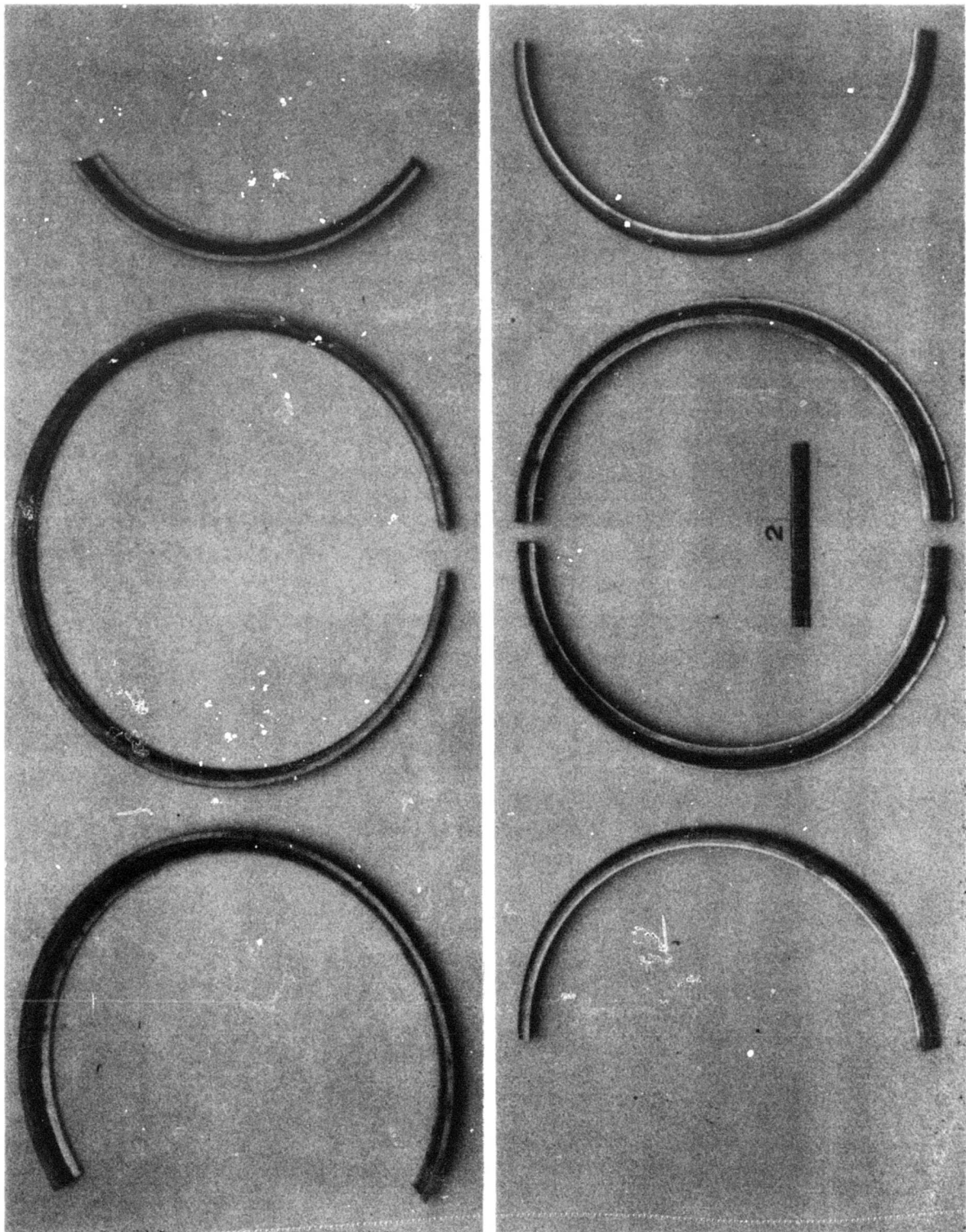
X5 B

FIGURE 78. INNER-RACE INSERT OF BARREL ARM 1

The third barrel arm position suffered damage to the inner race inserts. One pair had a single radial fracture through the approximate center of the semicircular arc. The other pair also had a radial crack in about the same location and also a circumferential fracture causing several small sections to break free. The overall view of the races is presented in Figure 80. The top row illustrates the outer-race inserts, while the bottom row illustrates the inner-race inserts. The surface of one of the circumferential cracks is shown in Figure 81. The relationship between the crack origin and the ball indentation is visible in this figure. The relationship between the fracture origins and the ball contact angle was determined by measurement of the damaged raceways. Fifteen origins, on outer-race segments, were found to lie between 41 and 70 degrees. Three origins on the inner-race segments were found to lie between 31 and 64 degrees.

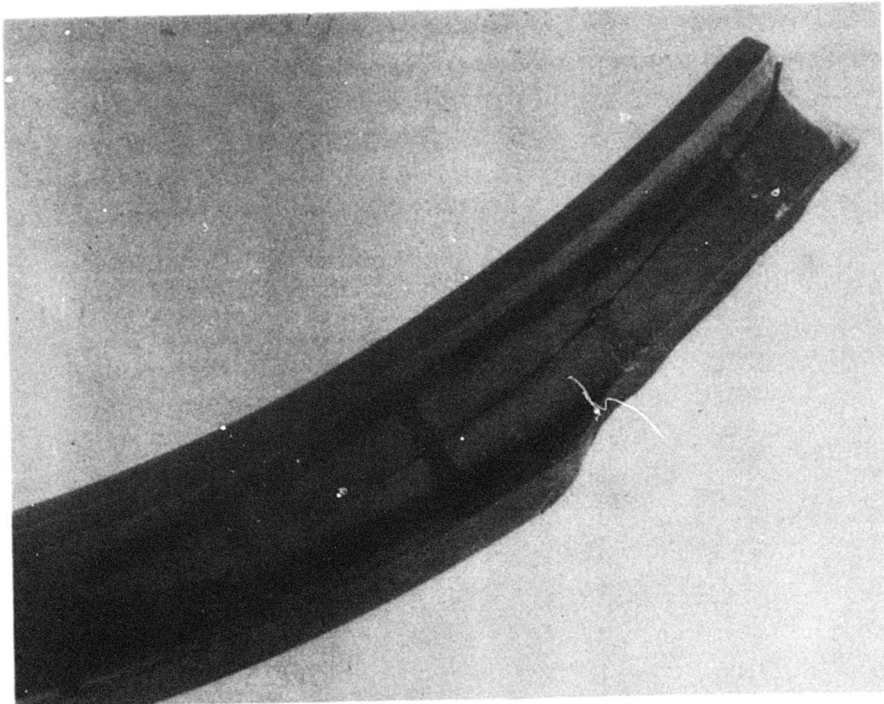
A microsection was taken through one of the sections, and the structure is shown in Figure 81b. The structure consisted of a tempered martensitic matrix which had a uniform distribution of primary carbides and some smaller secondary carbide precipitates. The microstructure appeared normal for the specified material and heat-treat condition. A microhardness evaluation taken on the same specimen revealed hardness slightly in excess of the specified range of Rc 58-62. Spectrochemical analysis confirmed that the tested race section was fabricated from the specified material.

The initial Gothic-arch bearing-race insert configuration covered and included an arc of 150° , in a radial plane. It was intended that this hardened steel race would fit into matching grooves in the barrel and blade retention. The fit was critical since the race was made only thick enough to carry the local ball contact loads and depended upon the surrounding material to support gross loading. The results of the 3P-OOOP fatigue test indicated that the anticipated fit had not been achieved and, in light of the experience gained in manufacturing the test hardware, that the required fit would be very difficult to achieve. The fretting on the outside of the race inserts and the fractures, which originated on the outside surface and propagated in a diametral plane, were the major indicators. In order to continue the evaluation of the barrel, the race inserts were reworked to a two piece configuration by slitting along the diametral plane. This rework obviously reduced the section modulus of the race, making it more dependent on the surrounding material for support, but analysis showed that the resulting inherent improvement in fit was sufficiently compensating and lowered the stresses on the outer surface of the races. In recognition of the fretting, the outer surfaces were also peened and gold plated.



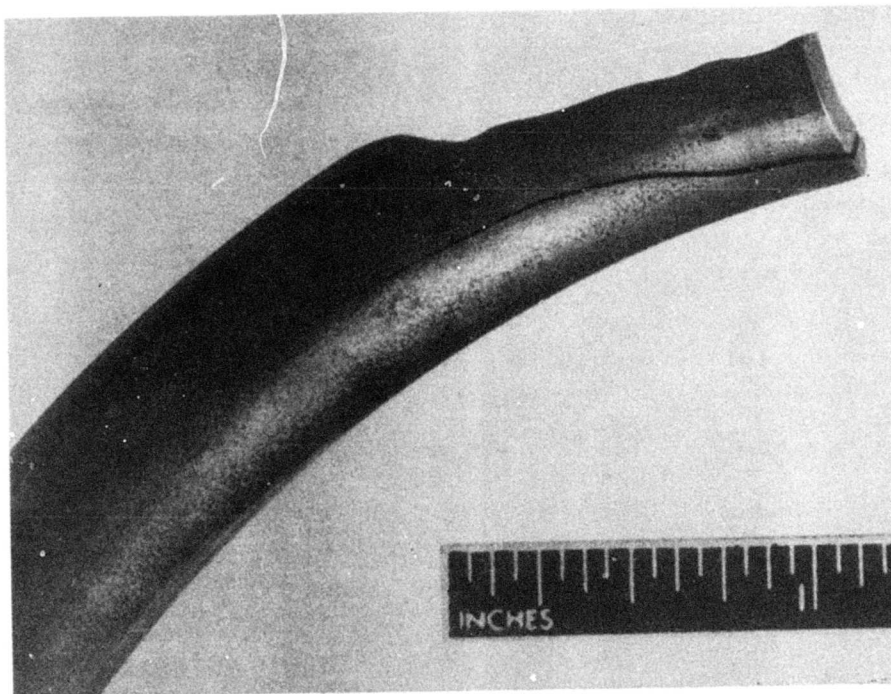
A

FIGURE 79. OUTER-RACE INSERT OF BARREL ARM 2 (TOP ROW)
AND INNER-RACE INSERT OF TEST BAR 2 (BOTTOM ROW)



B

X5



C

X5

FIGURE 79. CONTINUED

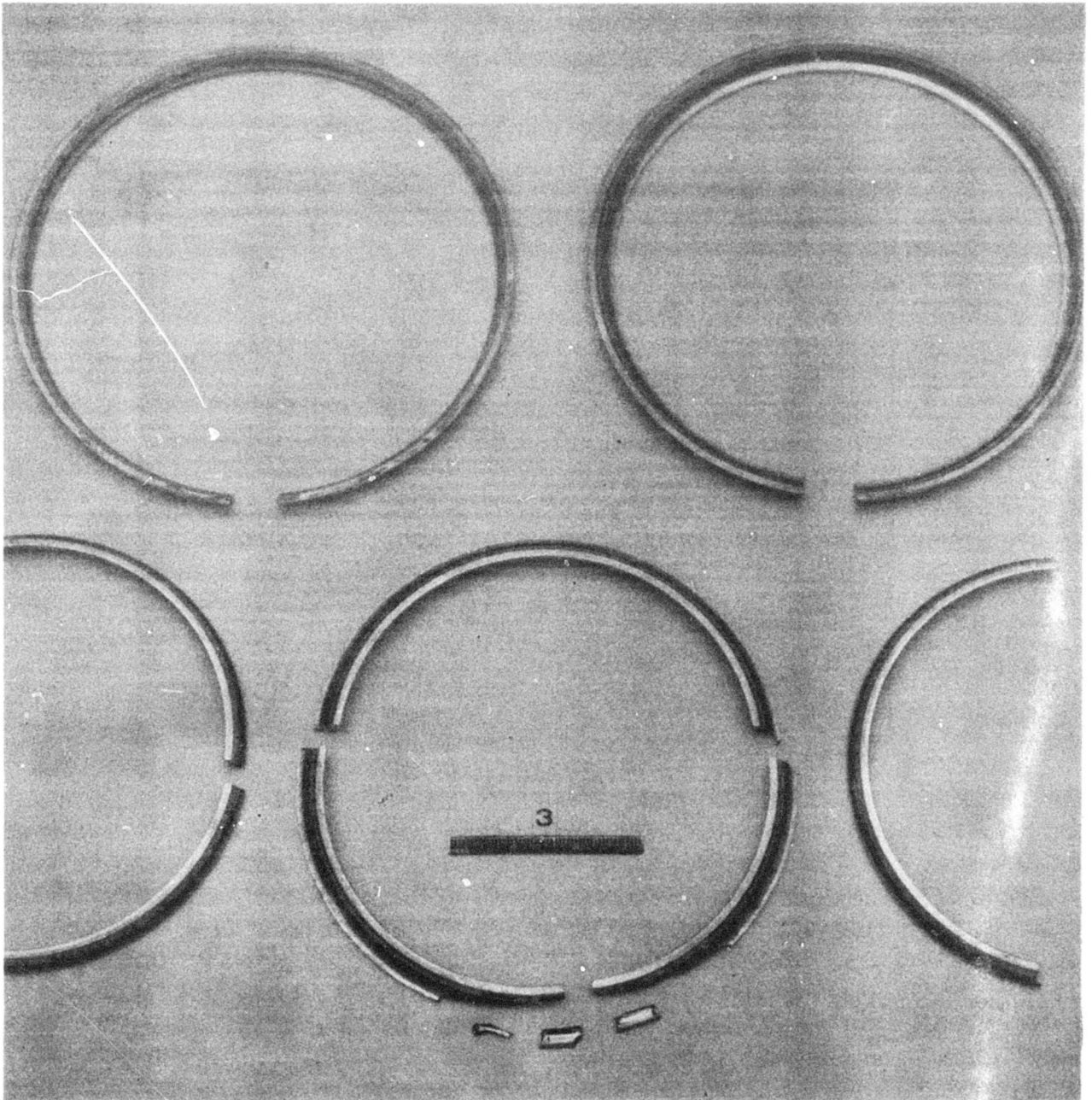
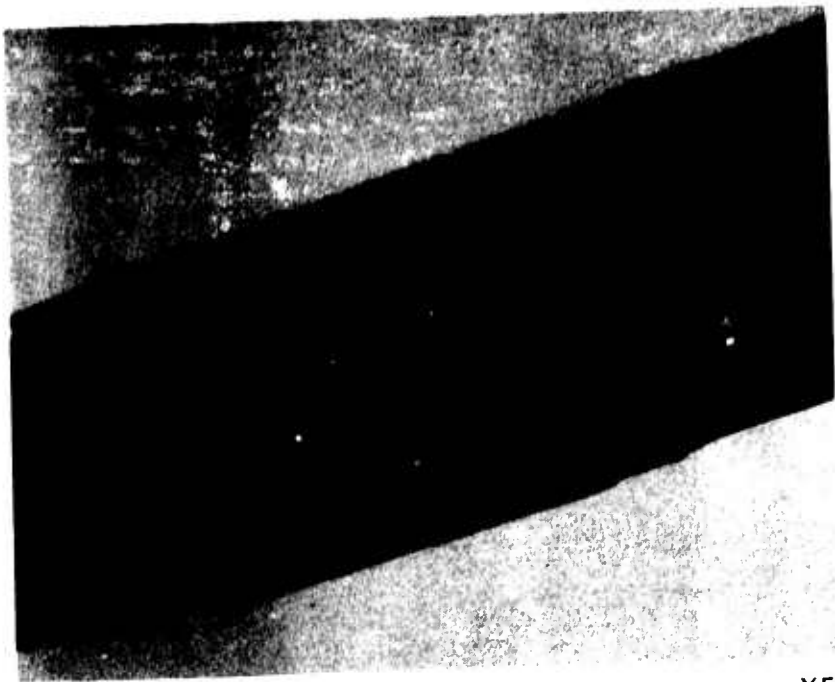


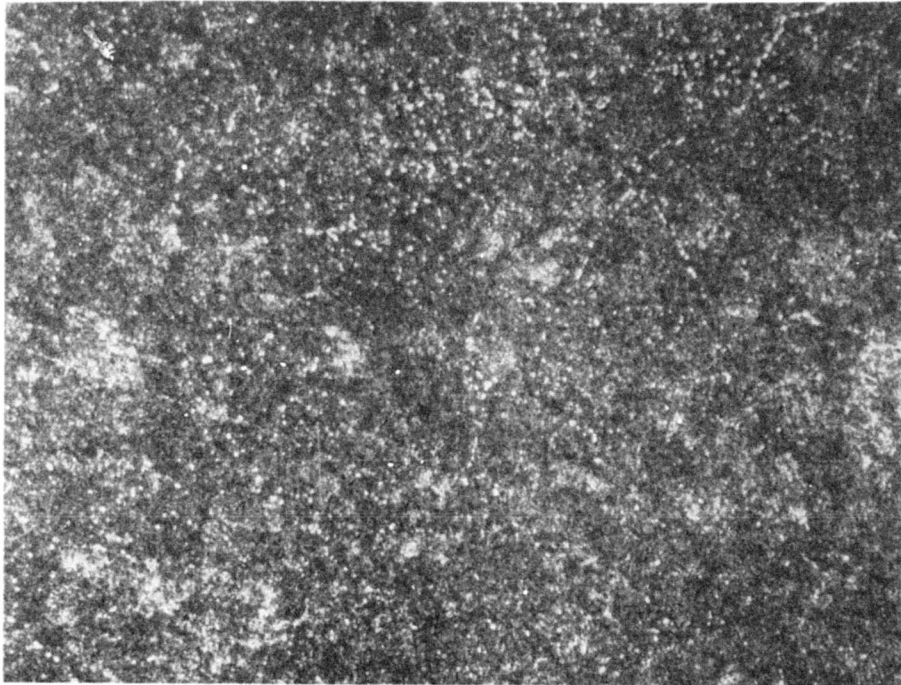
FIGURE 80. OUTER-RACE INSERTS OF BARREL ARM 3 (TOP ROW)
AND INNER-RACE INSERTS OF TEST BAR 3 (BOTTOM ROW)



A

X5

FIGURE 81. INNER-RACE INSERT OF BARREL ARM 3



B

X400

FIGURE 81. TYPICAL MICROSTRUCTURE OF BARREL ARM 3 INSERTS

As discussed earlier, the races were found fractured after 4.06 million cycles of 1P-OOP fatigue test. The examination indicated that the fractures were fatigue in nature and originated in the raceways at ball impressions. The multiple fracture origins were located at angles between 31 and 70 degrees. This behavior is in contrast to that observed on the race inserts used in the 3P-OOP test, where fractures originated on the back sides of the raceways. In that case, stress analysis indicated that secondary bending stresses could produce a fatigue overstress situation. Splitting the race inserts through the apexes lowered these bending stresses to below design limits. The 1P-OOP test results indicate the validity of the stress-strength analysis, as no cracks with origins on the back side of any insert were produced.

After examining the 1P-OOP races and reviewing both the initial stress calculations and those done preceding the rework, the following retention configuration changes would be considered in any future design:

1. Larger diameter balls to reduce the Hertz stress at the ball/race contact point.
2. Larger pitch diameter races to maintain the number of balls and the load per ball.

The revised race configuration would increase the race thickness in the critical 45-degree contact area, increase race section modulus, and provide positive race support and location on the constant diameter section.

BEARING DESIGN

The tail shaft of a typical propeller barrel extends into a gear case and is directly driven through a splined joint. The tail shaft usually is cantilevered in two radial roller bearings arranged to react bending moments and an angular contact ball bearing to react thrust. The advanced technology propeller tail shaft bearing assembly design is unique, in that it employs a single large-diameter small-cross-section duplex-tapered roller bearing to react these loads. The tapered roller bearing has the potential to carry heavier radial and thrust loads per pound of weight than any other type of bearing. The contact angle of this bearing assembly is large, nearly 50 degrees when compared to 15 to 20 degrees for a conventional bearing, in order to keep moment reactions low and thereby permit a small cross section. The physical installation involves a press fit on the barrel tail shaft and a clearance fit in the simulated gearbox housing. Outer-race rotation is prevented by three

equally spaced circumferential keys grounded to the housing. A tail shaft nut pre-loads the bearing assembly by taking up the internal clearance across the inner races to slightly over the maximum operating load as well as insures that the bearing components do not separate under the maximum moment. The bearing assembly is defined by Hamilton Standard drawing U738945. See Figure 82. The bearing assembly key statistics are listed in Table 18.

TABLE 18. BEARING CHARACTERISTICS	
Inside Diameter	10.625-10.626 inches
Outside Diameter	12.750-12.751 inches
Pitch Diameter	11.560 inches
Roller Diameter	0.3996 inch nominal
Roller Width	0.500 inch
Roller Number per Race	69
Roller Crown Radius	38.25 inches nominal
Width	2.00-2.03 inches
Contact Angle	48 degrees 31 minutes
Speed	1160 rpm

Figure 83 is an exploded view of the bearing assembly showing the forward and aft inner race and roller assemblies, the outer race, and the preload spacer. Figure 84 is an exploded view of the test assembly and includes the simulated tail shaft, bearing housing, assembled bearing, miscellaneous seals, locknut, and lockcup.

BEARING TEST

The bearing assembly test program involved the following four facets:

1. **Stiffness** - As this bearing is a large-diameter small-cross-section design, stiffness characteristics were established by evaluating the influence of external nonlinear loadings.
2. **Lubrication** - The influence of oil flow rate on bearing performance was determined by recording temperature profiles under controlled operating conditions.

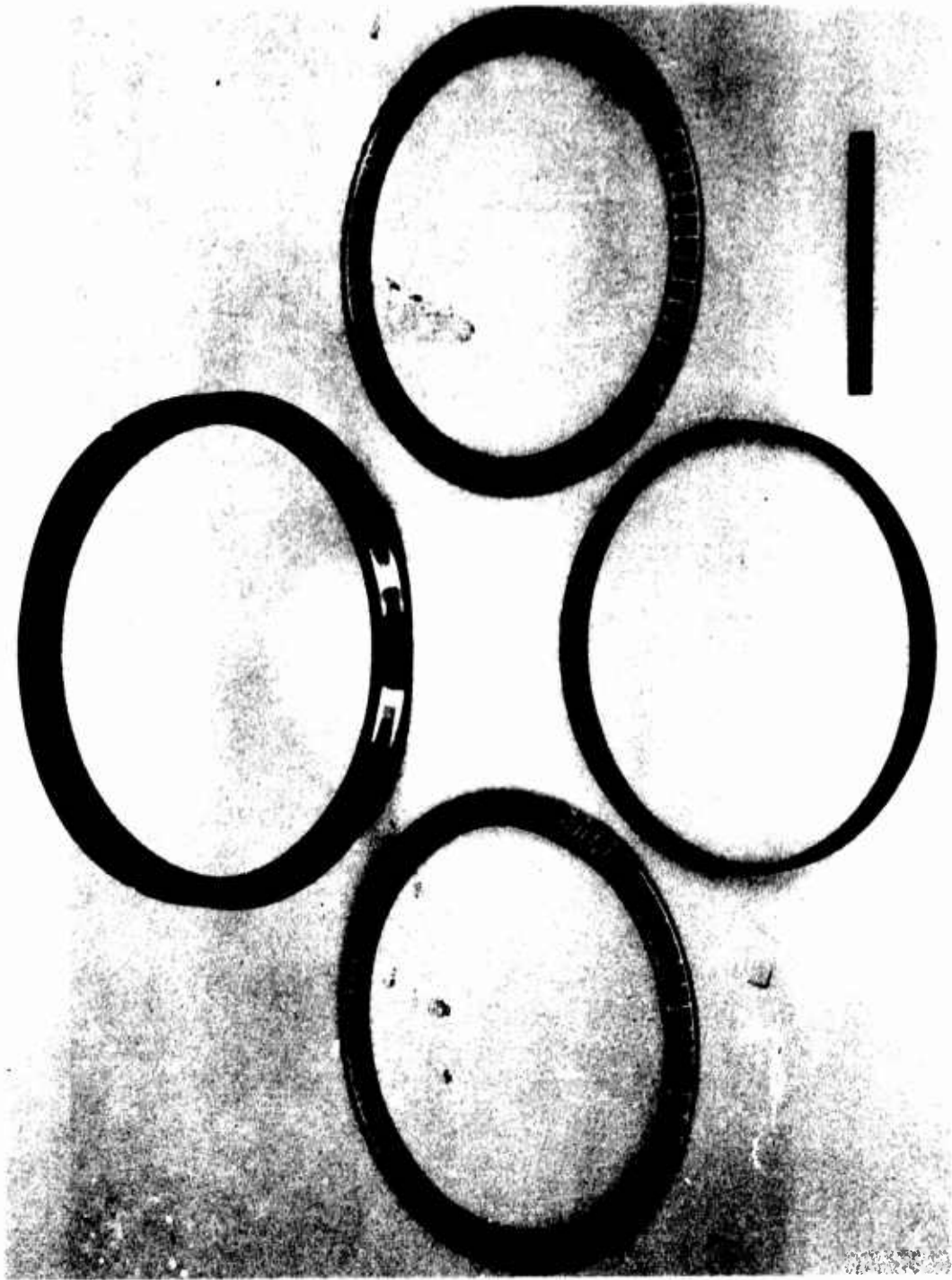


FIGURE 83. EXPLODED VIEW OF BEARING ASSEMBLY

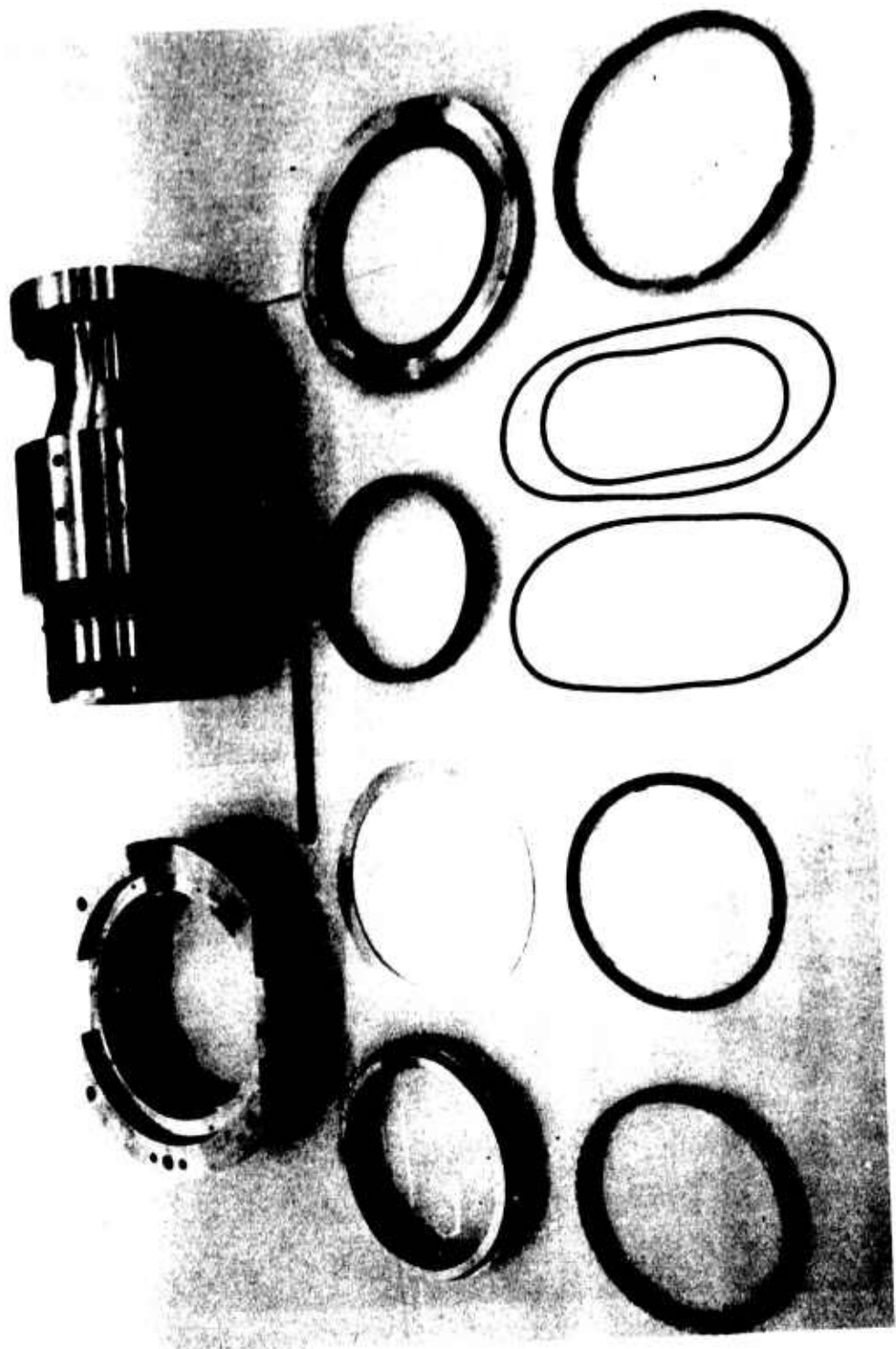


FIGURE 84. EXPLODED VIEW OF BEARING TEST CONFIGURATION

3. **Structural Integrity** - The anticipated service life of the bearing was established by operating to accelerated load schedules for periods equivalent to the calculated B-10 life.
4. **Interrupted Lubrication** - The effect of a lubrication system failure was established by operating with only residual oil/air mist.

Stiffness

The purpose of this static phase of the test program was to measure bearing stiffness in order to provide a basis for predicting the natural frequency of the propeller system employing duplex tapered roller bearings. Bearing number one was used in this test.

Loading conditions involved thrust levels from 2000 to 6000 pounds, bending moments from 30,000 to 75,000 inch-pounds, and deadweights from 300 to 1000 pounds. Bearing deflections were measured at discrete locations for varying load increments.

From the data obtained, it was evident that the system stiffness had a low sensitivity to moment and thrust loads. The system stiffness of 176.6×10^6 inch-pounds/radian obtained by test compares favorably with the calculated value of 163×10^6 inch-pounds/radian. This calculated value was based on stiffnesses of 627×10^6 inch-pounds/radian and 221×10^6 inch-pounds/radian for the bearing and barrel tail shaft, respectively.

Lubrication

The purpose of this test phase was to confirm adequacy of the specified lubricating oil flow and bearing preload as determined by design calculation. In this design, lubricating oil is pressure fed to the center of the simulated propeller barrel tail shaft and then centrifugally supplied to the test bearing by means of three 0.125-inch-diameter equally spaced holes. Six unequally spaced radial passages were incorporated in the test fixture that housed the bearing, to collect and drain expended oil by means of gravity. Temperature instrumentation consisted of a group of four equally spaced spring-loaded thermocouples arrayed about the stationary bearing outer race. This was supplemented by a series of temperature sensing tabs. Each tab having four heat-sensitive spots which turned black upon attainment of the particular level that it was designed to indicate. The tabs were affixed to the rotating inner race with a noninsulating adhesive compatible with MIL-L-7808 oil. The normal test

procedure employed for dynamic operation consisted of manually pressurizing the lubricating system to assure a minimum flow above the design rated condition of 1.6 quarts/minute, followed by pressurization of the two bending moment and two thrust hydraulic cylinders, and then the initiation of rotation, up to the required speed. After the required speed was attained, the cylinder pressure levels and flow were refined as necessary. Figure 85 is an overall view of the test facility with the test unit installed. Number one bearing was employed for the test.

Operating conditions involved thrust levels from zero to 3,260 pounds, bending moments from 2,820 to 80,000 inch-pounds, and the maximum design speed of 1160 rpm. Oil flows of from 1.75 quarts/minute to 3.25 quarts/minute were evaluated with 2,250 pounds bearing preload. The bearing was to run until either outer race temperature stabilized or 265° F was achieved.

The temperature differential between the inner and outer races ranged from 13° F when run with only the bearing preload and no thrust or bending moment, to a maximum of 40° F with the preload, 3,260 pounds of thrust and 80,000 inch-pounds of bending moment applied. These values compared favorably with the bearing manufacturer's recommendation of 50° F for maximum differential operating temperature. The temperature differential between the inlet lubricating oil and the outlet scavenging oil was 29° F at the high end of the flow range and 47° F at the low end. Outlet oil temperature confirmed bearing outer-race temperature and generally operated from 1° to 3° F higher. Approximately 14.3 hours of test time were accumulated during this evaluation.

At this time, a complete nondestructive disassembly inspection was conducted by the bearing manufacturer. Both raceways of the inner and outer races were found to be in excellent condition with no discernible wear on the thrust reacting inner-race flange. Both cages displayed some wear on the sides of the roller pockets toward the toe end. One cage felt tight; i. e., the cage-to-roller fit was minimal, and it displayed the greatest wear of the two cages. The rollers exhibited circumferential scratches which were not considered to be significant. No roller wear could be discerned by measurements. One roller did exhibit evidence of overheating. As a result, corrective action was instituted before testing resumed. The cages were stripped of silver plating, reworked to provide additional roller clearance, and replated. In addition, the rollers were burnish tumbled and the overheated roller replaced with one of matching size. The remaining bearings in the program, numbers two and three, were similarly reworked.

Structural Integrity

The purpose of this phase of the program was to demonstrate, by test, that the predicted bearing life could be met or exceeded. No bearing gives unlimited service. If it is effectively protected from environmental distress and is well lubricated, the

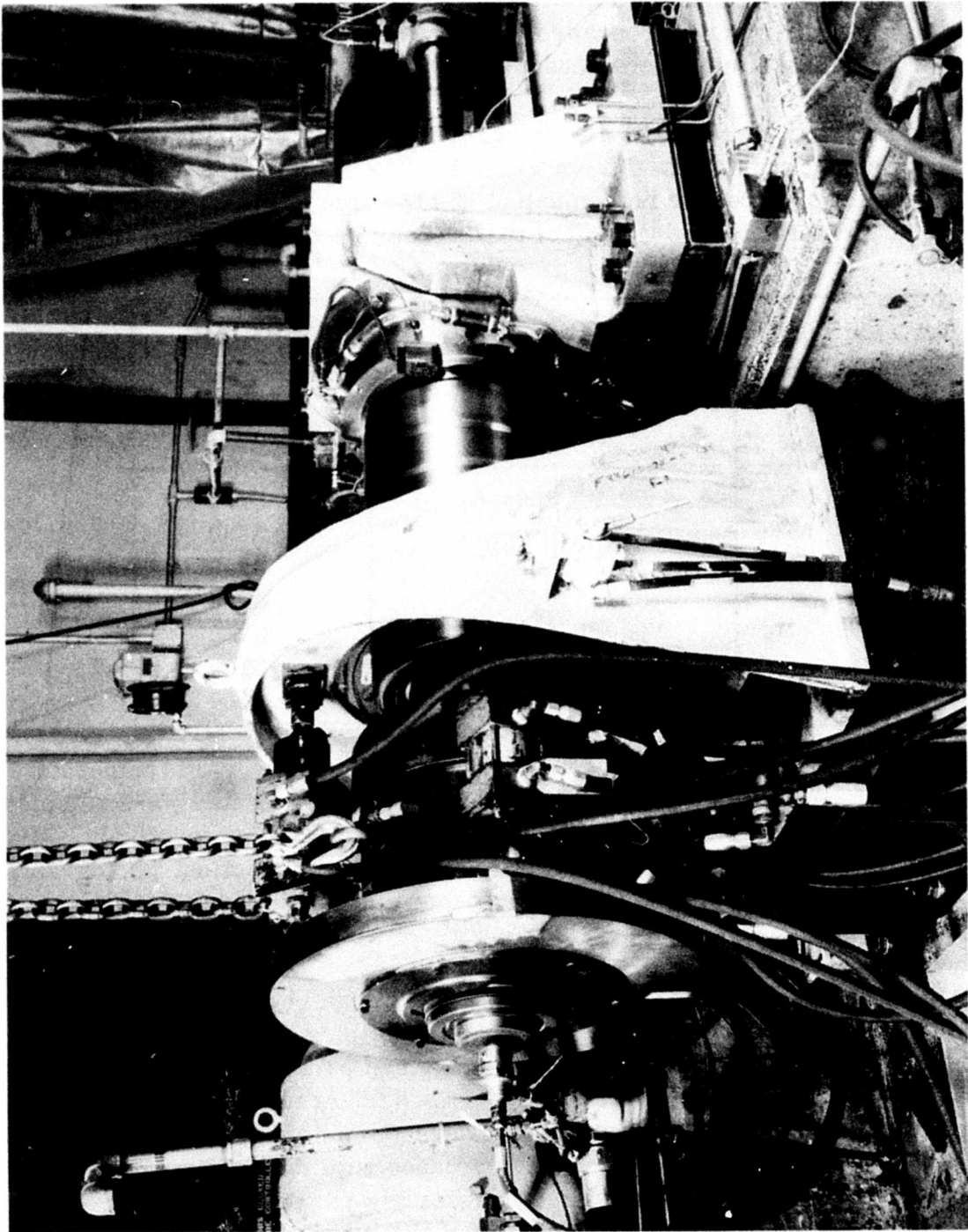


FIGURE 85. BEARING ENDURANCE TEST SETUP

cause of damage is reduced to fatigue of the material due to repeated stress application. The effect of this fatigue is a flaking which starts as a crack and develops into a spalled area. Historically, life is defined as that number of hours reached or exceeded by 90% of all bearings of a given group. For the purpose of this test the Timken spall size criterion of 0.1 square inch was chosen for terminating test. Three distinct endurance tests were conducted in the program.

The first test involved operation of a bearing, number one, in accordance with a 10-hour mission spectrum derived from Table 5. The spectrum is shown below in Table 19. Operating speed was held constant at 1160 rpm, as was flow at 1.6 quarts/minute. It was intended that 50 of the 10-hour spectrums would be accumulated.

TABLE 19. ENDURANCE TEST SPECTRUM		
Time (min.)	Bending Moment (in.-lb)	Thrust (lb)
63	32,300	3260
2	114,000	3260
82	39,000	3260
2	114,000	3260
77	45,400	3260
4	63,400	3260
370	80,600	3260

Tables 20, 21 and 22 record the test conditions and results; i. e., oil temperatures and average outer bearing race temperature. The cycles presented were selected at random and are the fifth, fifteenth and twenty-fourth cycles, respectively. Disassemblies were scheduled at regular intervals for visual inspection, photographic documentation and nondestructive fluorescent penetrant inspection. The first such inspection was conducted after 58 hours of endurance operation. The abnormal cage wear which was evident after the prior 14.3 hours of miscellaneous operation was not present at this inspection, indicating that the cage rework had alleviated the problem. No distress was evident on either the rollers or the inner race ribs. Figure 86 shows the typical appearance of the cage and rollers. Another disassembly inspection was conducted after an additional 62.8 hours and the condition of the bearing appeared unchanged. This phase of endurance testing was halted after 271.3 hours, 251.8 hours of which was in accordance with the spectrum and 19.5 hours of miscellaneous testing. The final disassembly inspection confirmed that there was no noticeable change in the condition of the bearing since the post-lubrication test modifications made prior to commencing the first endurance test.

TABLE 20. ENDURANCE TEST - CYCLE NO. 5						
Time (hr)	Thrust (lb)	Bending Moment (in. -lb)	Lubricating Flow (qt/min)	Inlet Temp. (° F)	Temp. Rise (° F)	Average Outer-Race Temp. (° F)
48.8	3260	32,300	3.6	124	20	142
50.2	3260	39,000	3.6	132	20	148
51.5	3260	45,400	3.6	137	19	152
51.5	3260	63,400	3.6	137	20	152
54.0	3260	80,600	3.6	142	19	157
54.3	3260	80,600	3.2	85	41	122
54.5	3260	114,000	3.2	98	34	129
58.0	3260	80,600	3.6	134	20	151

TABLE 21. ENDURANCE TEST - CYCLE NO. 15						
Time (hr)	Thrust (lb)	Bending Moment (in. -lb)	Lubricating Flow (qt/min)	Inlet Temp. (° F)	Temp. Rise (° F)	Average Outer-Race Temp. (° F)
141.8	3260	32,300	3.6	199	-15	180
143.2	3260	39,000	3.6	199	-23	170
143.2	3260	114,000	3.6	200	-22	170
144.5	3260	45,400	3.6	198	-12	180
144.5	3260	63,400	3.6	192	-6	181
150.3	3260	80,600	4.6	198	-12	182
150.8	3260	80,600	4.6	194	-45	163

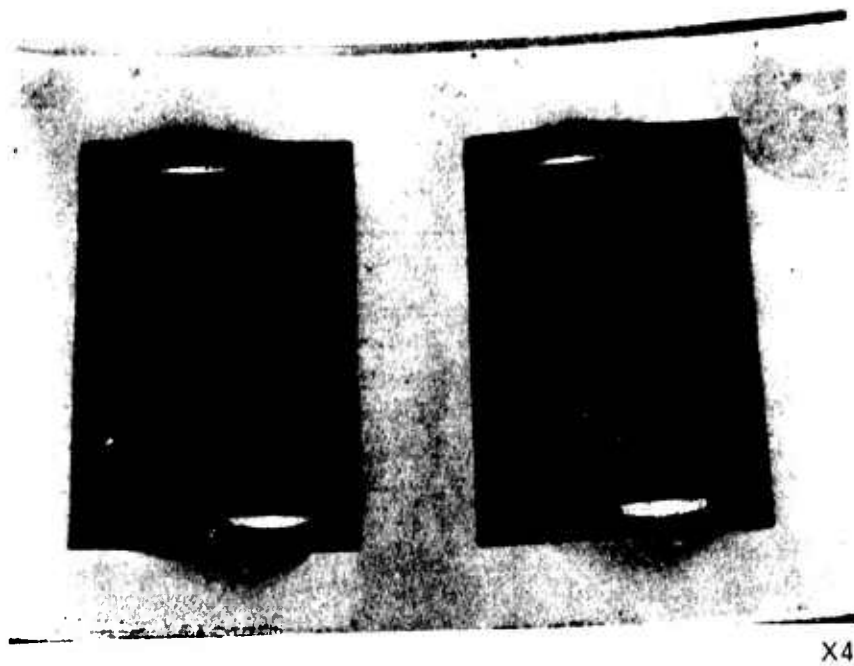


FIGURE 86. INNER RACE AND ROLLER ASSEMBLY OF BEARING NUMBER 1

TABLE 22. ENDURANCE TEST - CYCLE NO. 24						
Time (hr)	Thrust (lb)	Bending Moment (in. -lb)	Lubricating Flow (qt/min)	Inlet Temp (°F)	Temp Rise (°F)	Average Outer-Race Temp. (°F)
231.5	3260	32,300	4.0	198	-17	177
	3260	114,000	4.0	198	-16	177
233.0	3260	39,000	4.0	196	-16	178
234.3	3260	45,400	4.0	186	-34	145
	3260	63,400	4.0	181	-25	147
240.5	3260	80,600	4.0	200	-14	183

As a result of the excellent condition of the bearing, the test format was modified to alleviate some of the scheduled interim load levels. The bearing was then incrementally loaded in accordance with a further accelerated schedule to the analytically determined maximum capacity for a duration equivalent to the calculated B-10 life. The test spectrum for the accelerated phase of the test is shown in Table 23.

TABLE 23. ACCELERATED ENDURANCE TEST SPECTRUM - FIRST		
Time (hr)	Bending Moment (in. -lb)	Thrust (lb)
8	80,600	3260
8	80,600	6000
8	80,600	8000
8	95,000	3260
8	110,000	3260
16	125,000	3260
8	80,600	3260
56+	130,000	3260

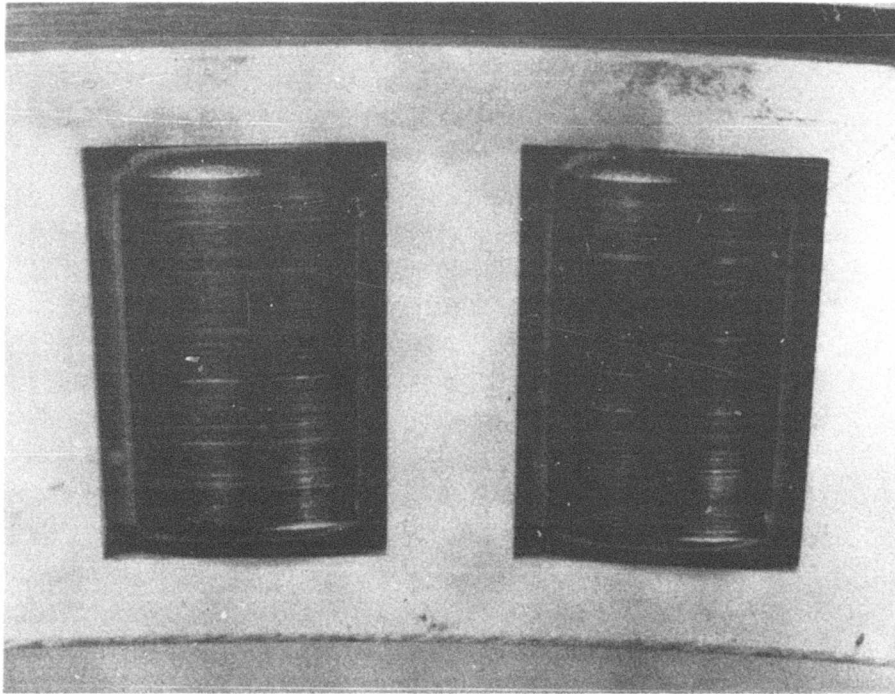
This second spectrum, when coupled with the first spectrum, analytically established a B-10 life of 368.2 hours. Inlet oil temperature was allowed to vary freely. The duration of test was to be an additional 250 hours or failure, whichever occurred first. Partial and complete disassemblies were again conducted at scheduled intervals for visual inspections, photographic documentation, fluorescent penetrant inspections, and dimensional checks. The test procedure was the same as during the earlier endurance test.

Table 24 summarizes the test conditions and test results; i. e., oil temperatures and the average outer race temperature.

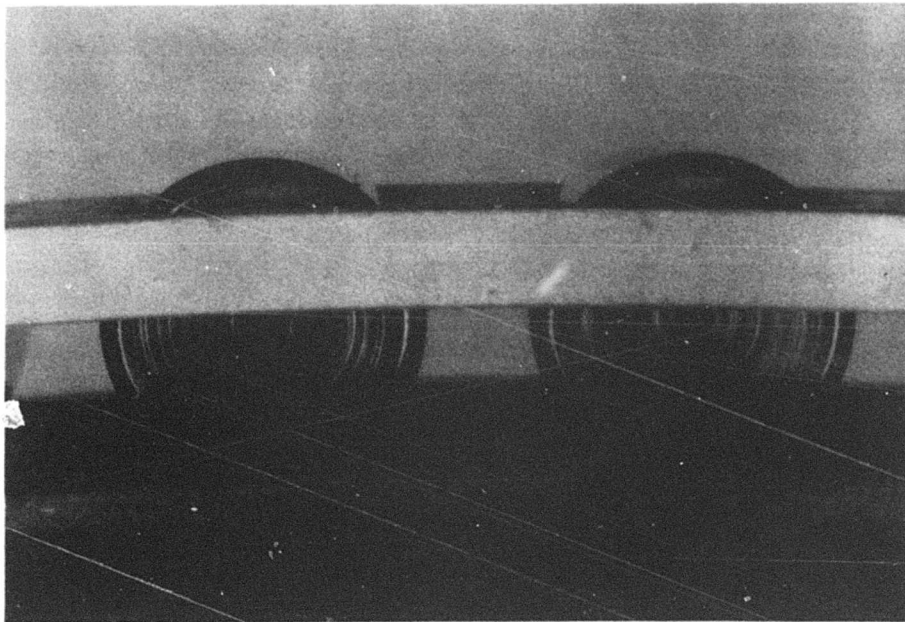
TABLE 24. ACCELERATED ENDURANCE TEST RESULTS - FIRST						
Time Endurance (hr)	Thrust (lb)	Bending Moment (in. -lb)	Lubricating Oil			Average Outer Race Temperature (° F)
			Lubricating Flow (qt/min)	Inlet Temp. (° F)	Temp. Rise (° F)	
254.3	3260	80,600	3.5	128	24	149
255.3	3260	80,600	3.0	137	25	158
256.3	3260	80,600	2.5	137	28	161
257.8	3260	80,600	2.0	120	39	156
260.6	3260	80,600	1.6	129	39	165
268.6	6000	80,600	1.6	129	42	168
276.2	8000	80,600	1.6	126	44	167
284.2	3260	95,000	1.6	130	41	169
292.2	3260	110,000	1.6	130	41	171
308.2	3260	125,000	1.6	135	43	176
316.3	3260	80,600	1.6	134	36	170
		142,000				
368.6	3260	130,000	1.6	135	41	176

The forward shaft seal and retainer plate was removed at 276.2, 292.2, 316.3, 327.8, 340.3, and 357.1 hours for visual inspection of the roller end faces and cage conditions. No significant changes were noted except for slight scratching of the roller faces after reacting the maximum thrust condition of 8000 pounds. At 308.2 hours, the test unit was disassembled for a routine visual inspection. The overall appearance of the bearing was excellent. Particular attention was given to the roller faces and the inner-race thrust reacting rib. The condition of the inner race and roller assemblies, numbers 1A and 1B, is documented by Figures 87 and 88, which are views looking at the two most highly polished roller bodies in each assembly.

After a total time of 388.1 hours - 368.6 hours in accordance with the test plan and 19.5 hours of miscellaneous operation - testing was halted by abnormal vibration. Prior operating experience had shown normal operation to be approximately one mil (double amplitude). There was no indication of abnormal outlet oil or outer race temperatures and no detection of magnetic particles. Visual inspection of the bearing indicated an area of spalling in the forward inner race (1A) and showed one of the 60 rollers to be heavily grooved at the toe end. See the left-hand roller in Figure 89.

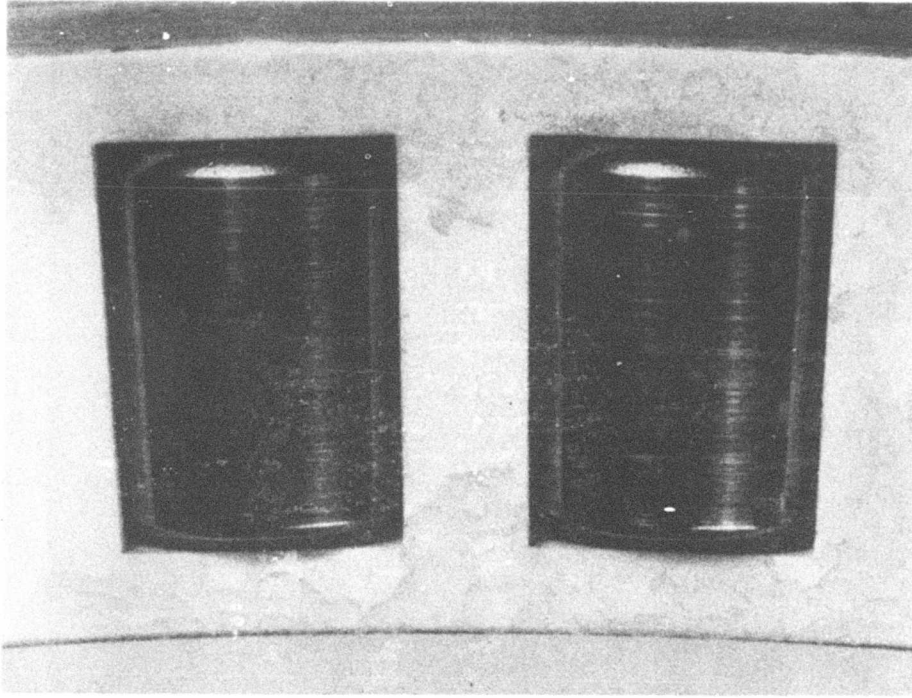


X4

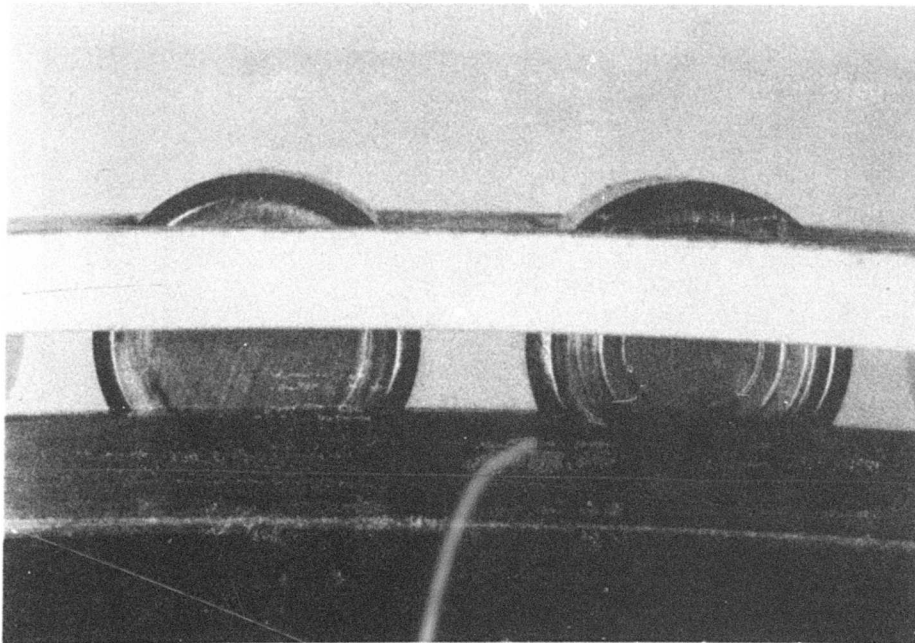


X4

FIGURE 87. INNER RACE AND ROLLER ASSEMBLY
OF BEARING NUMBER 1, SIDE 1A

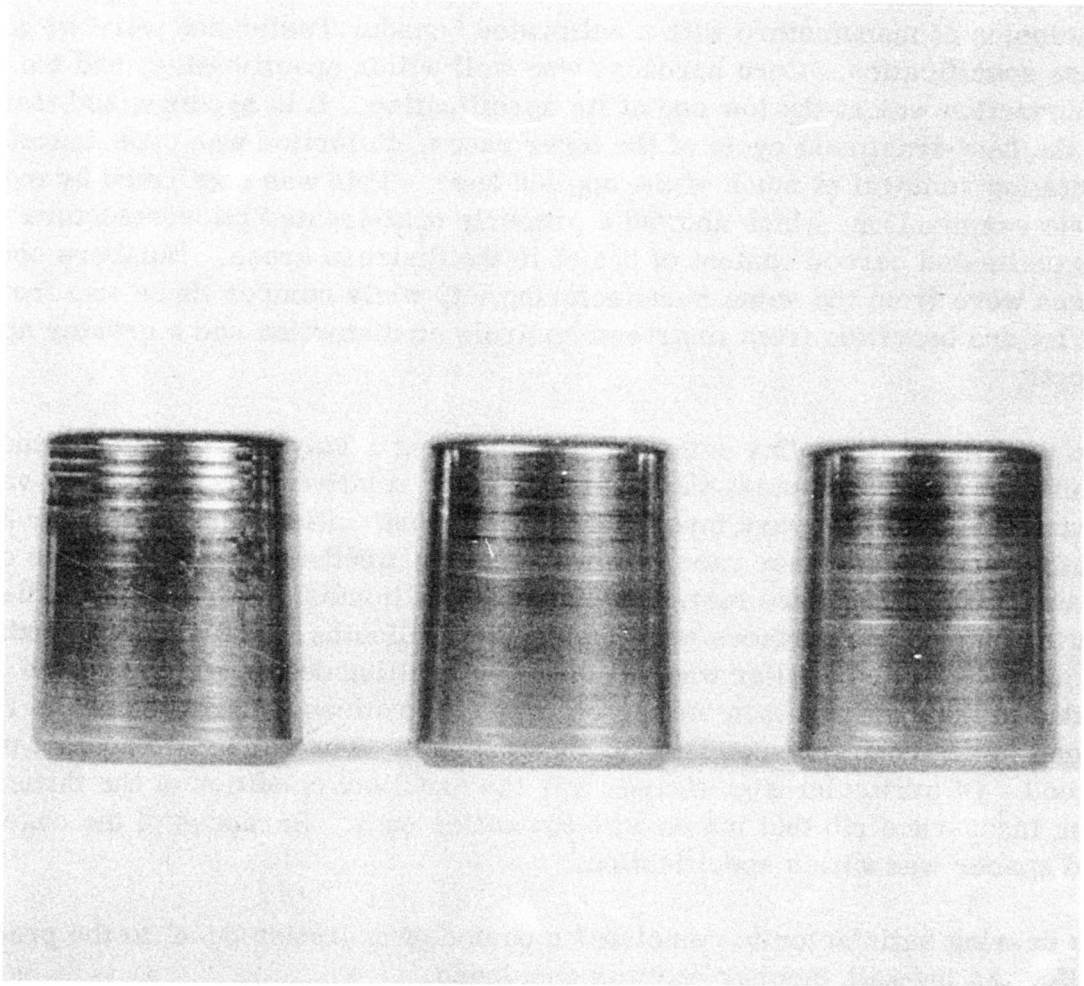


X4



X4

FIGURE 88. INNER RACE AND ROLLER ASSEMBLY
OF BEARING NUMBER 1, SIDE 1B



X4

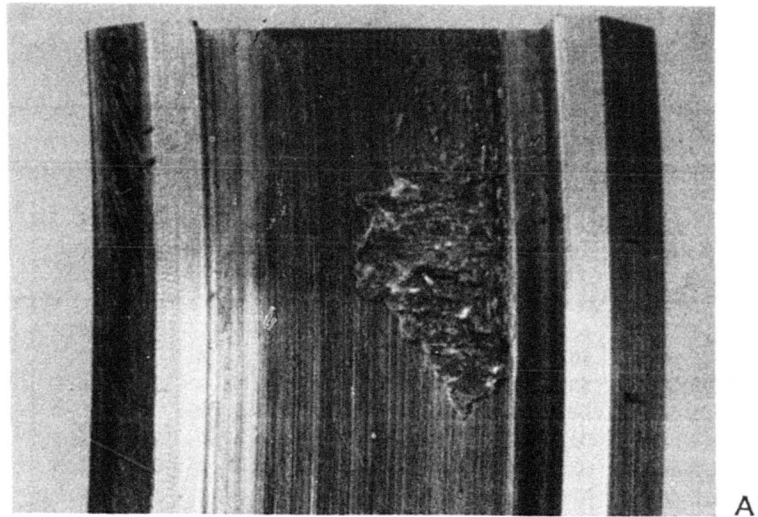
FIGURE 89. ROLLERS OF BEARING NUMBER 1, SIDE 1A,
SHOWING GROOVED CONDITION

The bearing was completely disassembled by the bearing manufacturer and subjected to detailed macro and micro examinations. The disassembly revealed three inner-race (1A) spalled areas, the axial location of which corresponds to the analytically predicted location of highest Hertzian contact stress. Sections were cut from these areas and macrophotographed. Figure 90 shows these areas. Five additional samples were taken from the same race as shown in Table 25 for microhardness and metallographic tests. One random sample each was taken from the other inner race (1B) and the common outer race. Table 25 shows the hardness gradients of the carburized sections, the core hardness, and depth of case for the inner and outer races. Hardness traverses of the inner races averaged 2.5 points below the drawing specification of RC60 minimum. The inner races had been inspected at the conclusion of manufacture with a calibrated Sonodur Tester and were within hardness specification. Core hardness was well within specification, and the depth of carburization was at the low end of its specification. It is hypothesized that during the heat-treatment cycle of the inner races, distortion was experienced, necessitating removal of much of the applied case. This was confirmed by metallographic examination, which showed a properly heat-treated microstructure with an estimated carbon content of 0.60% in the distress areas. Numbers one and two races were from the same manufacturing lot, while number three was from a second lot and benefited from improved controls on distortion and a greater applied case depth.

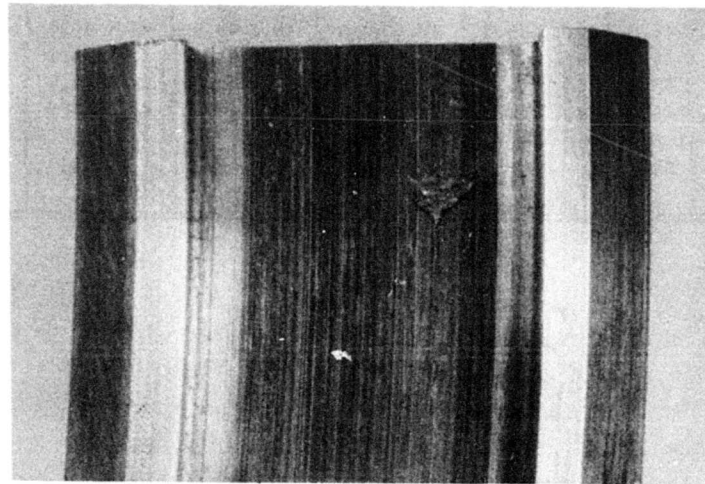
Surface profiles of the roller paths were made using a Talysurf Tester. Although no significant wear was noted, the inner races had relatively gross peak-to-valley discontinuities. The forward inner race (1A) discontinuities were just under 2000 millionths, and the aft inner race (1B) was 1000 millionths. A similar trace of an as-manufactured inner race measured under 50 millionths. The discontinuities of the mating outer-race surfaces were under 100 millionths. The grooved condition of the one roller cited earlier was attributed to spalling debris which became embedded in the cage and then abrasively wore the rollers. Hardness of the rollers was found to be above the specified RC 60 minimum. The roller end contact patterns were good. Of particular significance was the excellent condition of the thrust reacting inner-race rib that mates with the roller ends. Hardness of the cage and preload spacer was within specification.

As this bearing satisfactorily completed a period of operation equal to the predicted B-10 life, testing with number one was concluded.

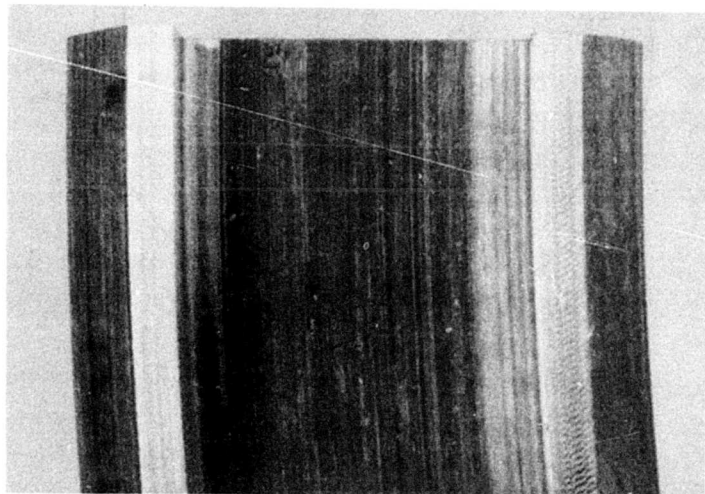
The final structural test program was conducted under still more stringent accelerated test conditions. Based on laboratory test data on fatigue failures, it is virtually impossible to precisely predict the life of an individual bearing because of no repeatability of failures. Even when tested under controlled conditions of the same



A



B

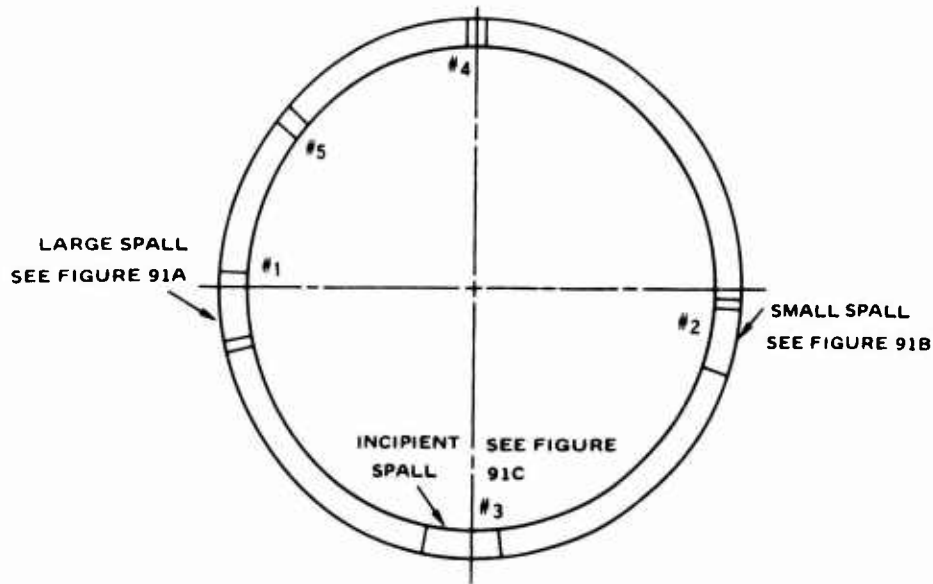


C

X4

FIGURE 90. INNER RACE OF BEARING NUMBER 1, SIDE 1A

TABLE 25. HARDNESS TRAVERSES								
Depth From Surface (in.)	Location 1	Location 2	Location 3	Location 4	Location 5	Serial Number 1B	Mating Surface to 1A	Mating Surface to 1B
0.002	56.8 56.8	57.2 57.2	55.6 56.4	58.2 58.6	58.0 58.4	58.4 57.6	60.9 71.4	61.4 60.9
0.004	56.8 56.8	57.5 57.2	56.0 56.4	58.2 58.6	58.0 58.8	57.6 57.6	60.7 60.9	61.4 60.9
0.006	56.8 56.0	57.2 57.2	56.4 56.4	58.2 58.6	57.2 58.4	57.6 56.4	59.6 59.2	60.9 60.5
0.008	-- 56.4	56.4 56.4	56.0 55.6	57.4 57.4	56.8 58.2	56.4 55.6	58.4 58.6	59.5 59.6
0.010	55.4 56.4	55.6 56.4	54.8 55.6	56.8 56.4	56.4 57.0	55.4 54.8	57.2 58.4	58.8 58.4
0.014	-- 54.6	55.2 54.8	53.5 53.5	55.2 55.6	55.6 55.2	53.5 52.5	56.2 56.0	56.8 56.4
0.018	-- 52.5	53.2 53.5	52.5 52.8	53.5 54.4	53.6 54.0	51.8 50.7	54.8 54.4	55.2 55.2
0.022	51.6 50.0	52.2 51.8	50.8 51.0	52.3 53.5	51.8 53.4	50.0 49.3	53.2 53.5	53.5 53.2
0.026	-- 49.3	52.2 50.5	49.5 49.6	51.6 52.2	50.7 51.8	48.8 47.4	51.1 51.5	52.2 51.8
0.030	48.3 48.3	49.6 48.6	48.3 48.3	49.6 50.4	49.1 49.6	47.4 46.7	49.1 49.8	50.0 49.3
0.034	-- 46.8	47.9 47.2	47.2 46.8	47.9 48.6	46.8 48.6	45.1 45.1	47.4 48.1	47.9 47.9
0.038	-- 44.9	46.5 45.6	45.6 45.6	46.0 47.2	44.8 46.8	44.5 44.9	46.8 46.6	46.8 46.8
0.042	44.9 44.9	45.5 44.9	44.9 45.1	44.9 45.1	44.4 44.8	44.5 44.5	44.9 44.9	44.9 44.9
Core	42.0	41.6	--	41.6	--	41.6	41.6	41.6
Case Depth	0.024	0.028	0.025	0.030	0.029	0.021	0.029	0.029



load and speed, it must be recognized that there will be a variation in life. Further, it is rare that two bearings are manufactured with identical dimensional or metallurgical characteristics. It can then be said, with respect to accelerated testing, that a single test producing bearing damage may not be significant. Two or more tests, however, producing similar results, increase the statistical confidence level. On this basis, a further endurance test, using serial number three bearing, was undertaken in lieu of the contaminated lubrication test. The manufacturing history of this particular bearing was such that it was considered as being representative of future production. See Figures 91 and 92 for the as-manufactured appearance.

This second accelerated endurance test involved continuous operation at the final test point of the previous schedule; i. e., bending moment was 130,000 inch-pounds, thrust 3,260 pounds, speed 1,160 rpm, and lubricating flow 1.6 quarts/minute. These conditions analytically established a B-10 life of 67.7 hours.

The test procedure was the same as for the earlier accelerated endurance test. Inlet temperature was again allowed to vary freely. The duration of test was scheduled for 75 hours or failure, whichever occurred first. Partial disassemblies were again scheduled at regular intervals as well as a final complete bearing disassembly by the manufacturer at the conclusion of the test. Table 26 summarizes the test conditions and test results; i. e., oil temperatures and average outer-race temperature.

TABLE 26. ACCELERATED ENDURANCE TEST SPECTRUM AND RESULTS - SECOND						
Time (hr)	Thrust (lb)	Bending Moment (in. -lb)	Lubricating Flow (qt/min)	Inlet Temp. (°F)	Temp. Rise (°F)	Average Outer-Race Temp. (°F)
1	3260	130,000	1.6	132	61	191
5	3260	130,000	1.6	136	64	197
10	3260	130,000	1.6	138	57	193
20	3260	130,000	1.6	140	50	189
40	3260	130,000	1.6	134	40	173
60	3260	130,000	1.6	138	40	178
75.2	3260	130,000	1.6	136	37	160

The incremental data presented in Table 26 was selected at random. The forward shaft seal and retainer plate was removed at 13.3, 36.3, and 59.5 hours to allow visual inspection of the condition of the roller faces and the cage. No significant wear was detected at any of the three inspections.

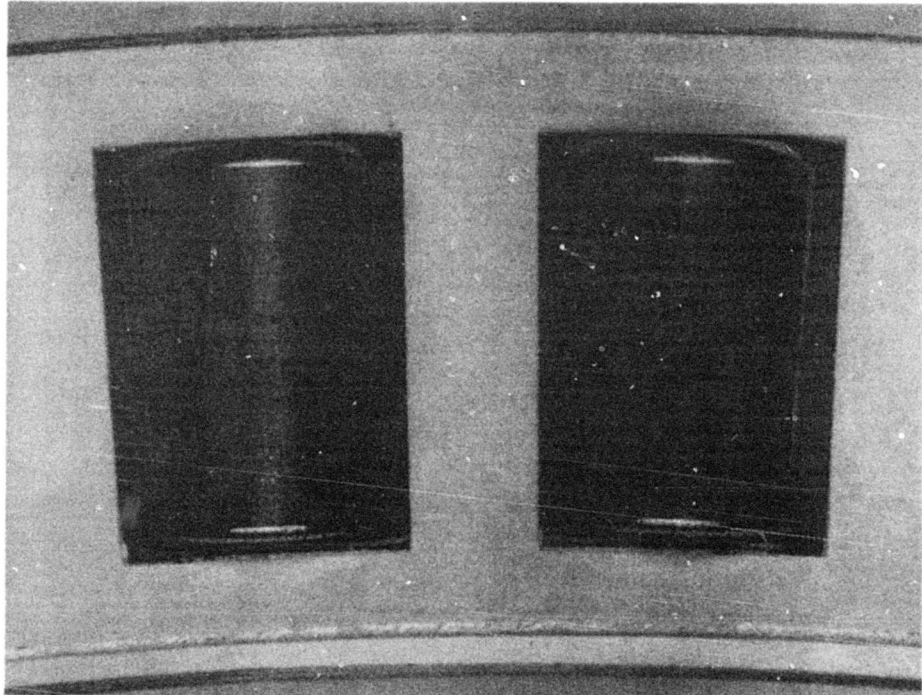
At a total time of 79.5 hours - 75.2 hours in accordance with the plan and 4.3 hours of miscellaneous operation - the test was concluded as planned. Visually, the bearing was satisfactory except for what appeared to be a moderate loss of silver plating from the aft cage (3B). The bearing was then completely disassembled by the manufacturer and subjected to nondestructive surface inspection.

All of the bearing components appeared to be in excellent condition except for one side of the common outer race. Both inner races (3A and 3B) appeared to still be in the as-manufactured condition, with little or no marking present and no sign of any heat or scuffing being generated at the thrust reacting rib. The appearance of the rollers was equally good. Figures 93 and 94 are views looking at the most highly polished number 3A forward (thrust) and serial number 3B aft roller bodies, respectively. The cage pockets showed signs of normal roller contact and feathered silver plating. The initial observation of a moderate loss of silver, made at the time of disassembly, was not substantiated by the detailed disassembly.

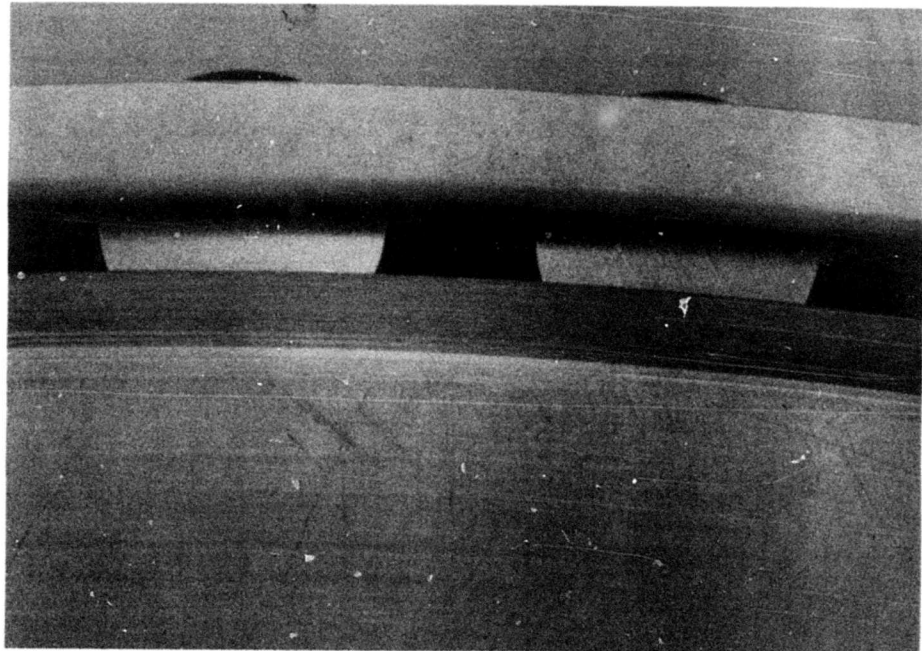
While the aft side of the common outer race (3B) was, as indicated, in excellent condition, the forward (thrust) side exhibited an area of minor, extremely fine grain spalling. The area in question was approximately 4.0 inches in length and 0.1 inch in width, and oriented in the plane of moment load application. Figure 95 is a view of the area in question, while Figure 96, taken at a magnification of four, focuses on the area of maximum damage. The manufacturer considered the quantity of lubricant used during the test to be sufficient, as there was no evidence of overheating.

From the manufacturer's experience, this type of fine spalling usually indicates marginal lubricant viscosity. However, it is believed that this phenomenon resulted from continuous operation at a single high load level without benefit of periodic excursions to lower load levels. The rate of propagation of this condition is not determinate, and as it had not yet produced damage sufficient to terminate useful life, the bearing is considered to be capable of further endurance operation.

The objective of this phase of the test program was considered to be completed, as 75 hours were successfully accumulated, vs. the E-10 life of 67.7 hours, and the post-test inspection results were satisfactory.

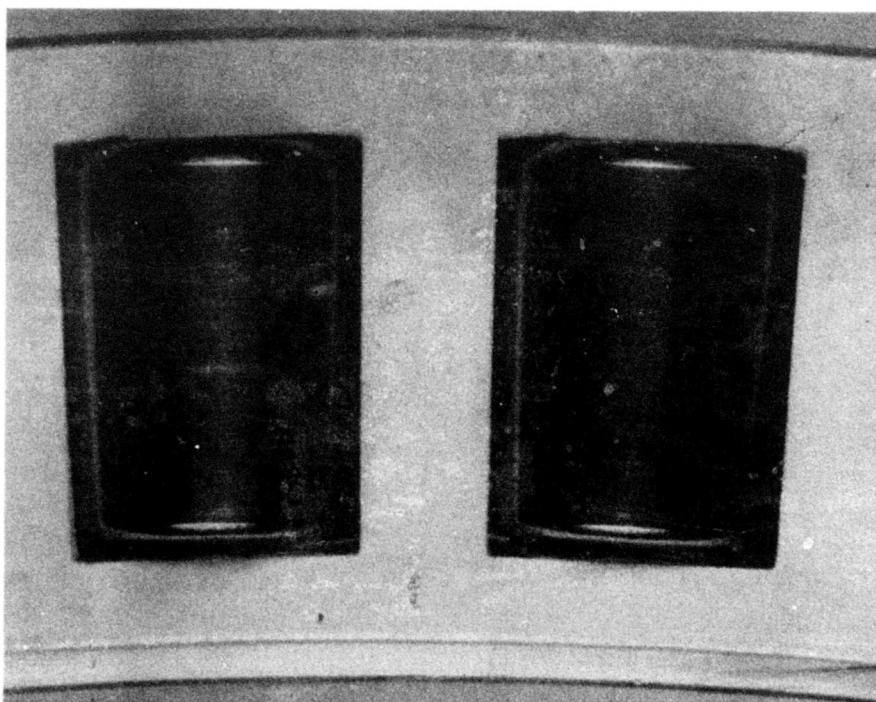


X4

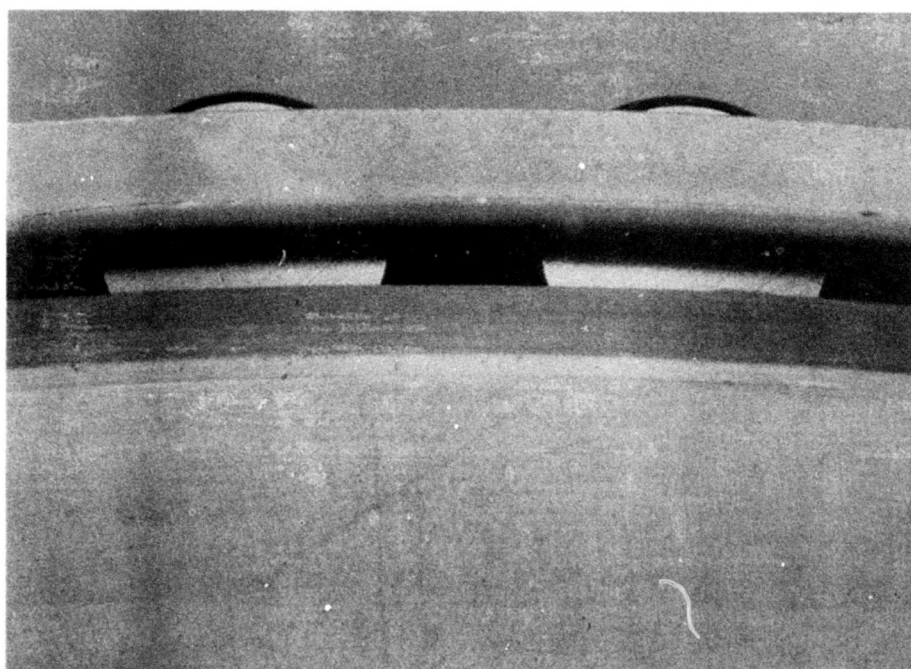


X4

FIGURE 91. INNER RACE AND ROLLER ASSEMBLY
OF BEARING NUMBER 3, SIDE 3A

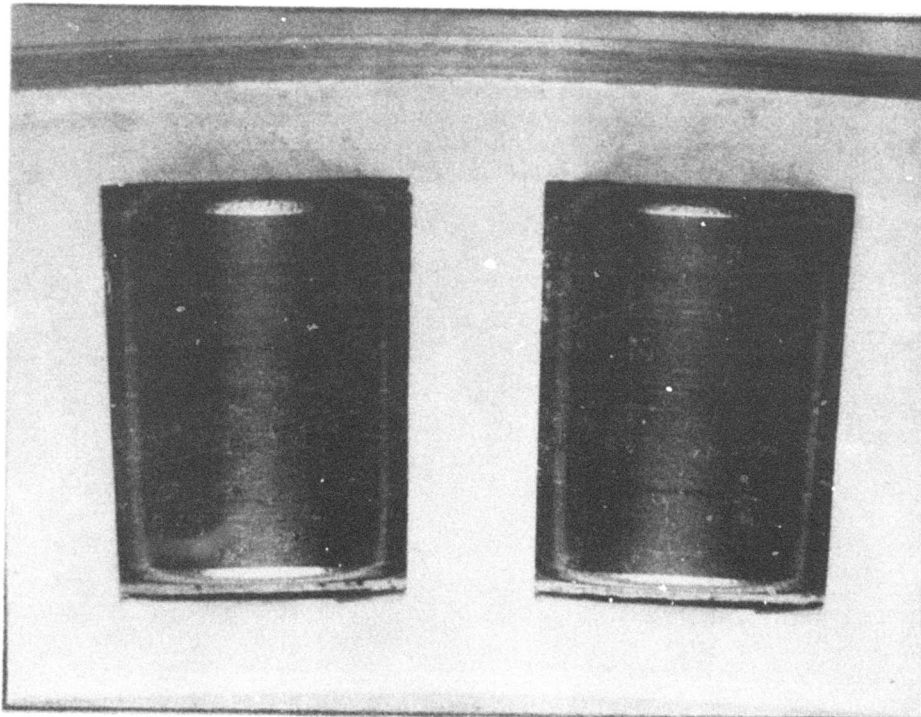


X4

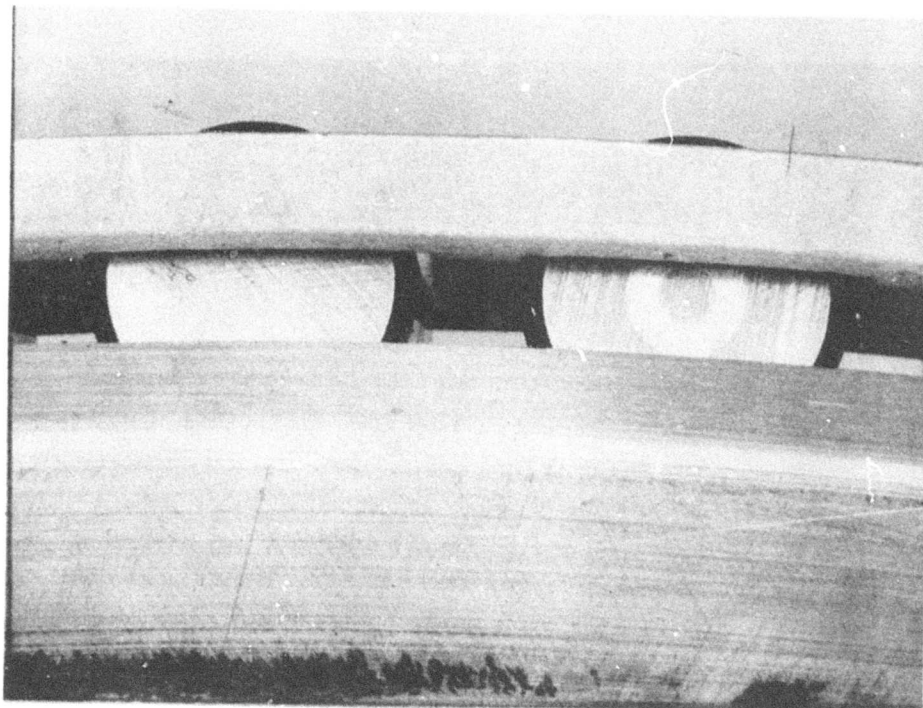


X4

FIGURE 92. INNER RACE AND ROLLER ASSEMBLY
OF BEARING NUMBER 3, SIDE 3B

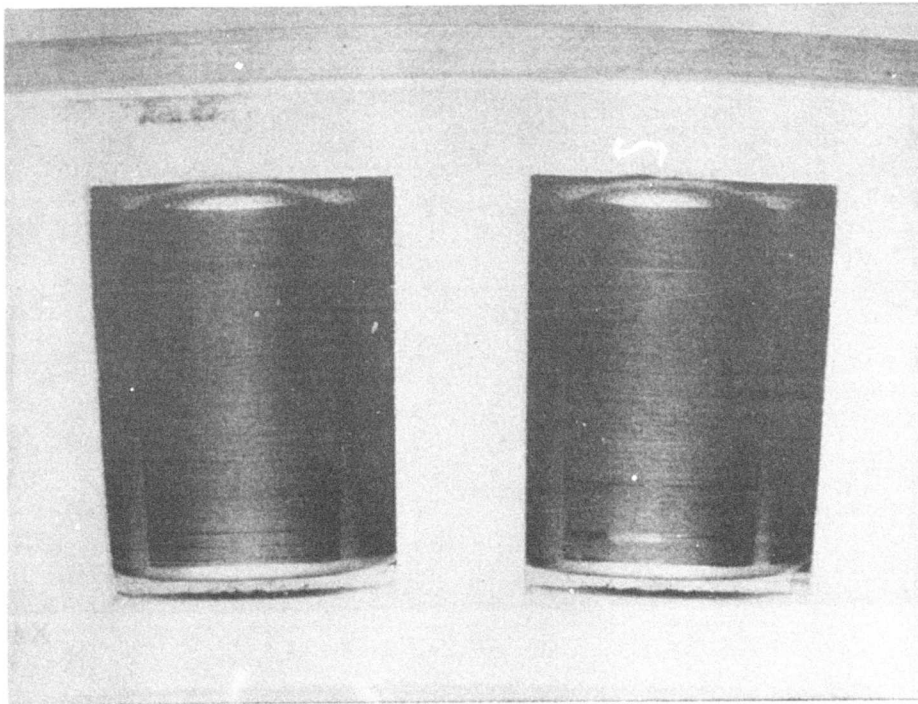


X4

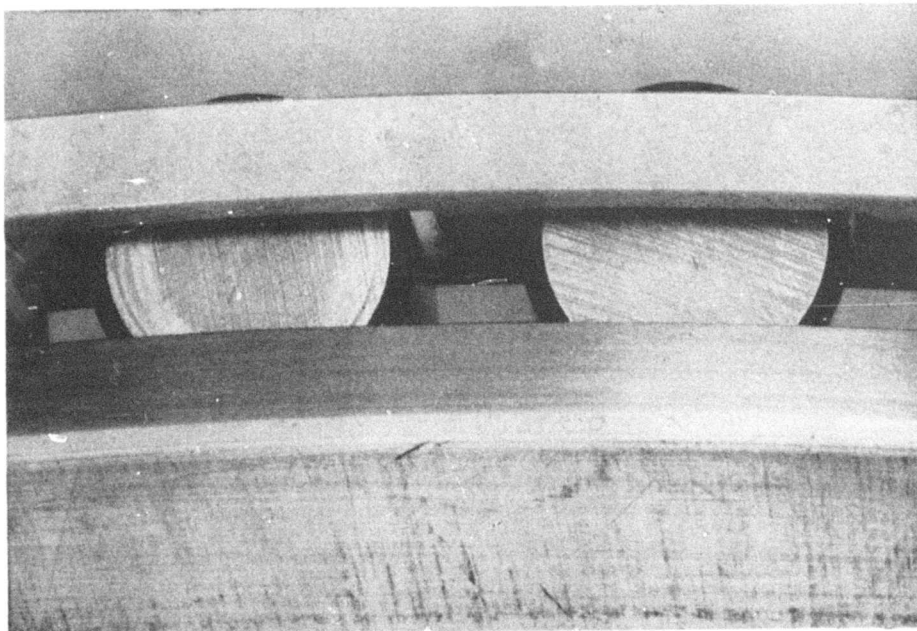


X4

FIGURE 93. INNER RACE AND ROLLER ASSEMBLY
OF BEARING NUMBER 3, SIDE 3A



X4

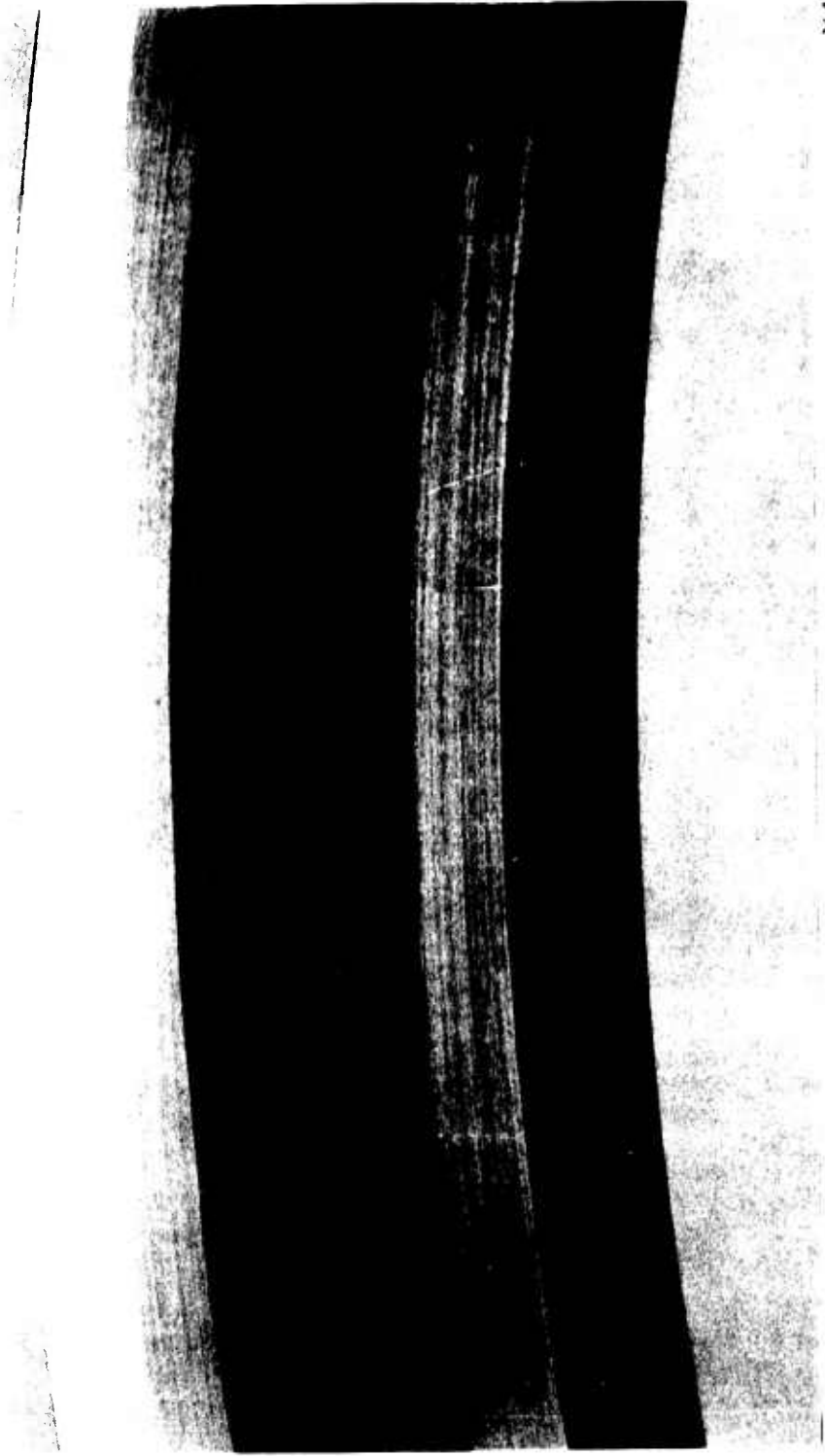


X4

FIGURE 94. INNER RACE AND ROLLER ASSEMBLY
OF BEARING NUMBER 3, SIDE 3B



FIGURE 95. OUTER RACE OF BEARING NUMBER 3, SIDE 3A



X4

FIGURE 96. OUTER RACE OF BEARING NUMBER 3, SIDE 3B

Interrupted Lubrication

Design of transmission housings normally involves the use of castings. Execution of the casting design involves the provision of supporting structure for shafting and mounting of associated bearings and shaft seals. Inherent in this construction are pockets which tend to retain oil in close proximity to the bearing. In the design of the bearing test fixture, the position of the two lowest scavenge oil gravity drain holes were arranged to retain expended oil to a level approximating the bearing pitch diameter.

The bearing was to be operated at the maximum shaft speed of 1160 rpm, the mean effective continuous thrust of 3260 pounds, and a bending moment of 26,000 inch-pounds. The initial step in the test procedure was to operate at the rated lubricating flow of 1.6 quarts/minute until race temperature stabilized, as measured at the four equally spaced thermocouple locations on the stationary outer race. Then, after the temperature stabilized, the inlet flow was to be terminated while gravity drain scavenging was maintained. Flow interruption was to be accomplished by shutting down the supply pump and allowing the oil within the simulated barrel tail shaft to be centrifuged. The test was scheduled for 4 hours of operation or until the outer race temperature reached 300°F, whichever occurred first. Number two bearing was used for this evaluation.

Prior to initiating test, a total of 5.3 hours of operation was accumulated. This operation involved checkout of the installation, bearing run-in, and temperature stabilization.

Run number one attempted to record the 4 hours of continuous operation but ultimately involved only 42 minutes of operation. The average stabilized outer-race temperature at the start of the run, prior to interrupting flow, was 158°F. The observed race temperature after 12 minutes was 277°F. At 12 minutes 20 seconds, an automatic overtemperature shutdown was precipitated by one of the commercial test facility bearings, used to support test facility shafting, having exceeded its present 250°F limit. The shutdown meter was reset to 350°F, and all test conditions were restored within 55 seconds. Race temperature decayed during this momentary interruption and continued to do so until a temperature of 226°F was reached at the 42-minute mark. It was necessary to stop the test at this time due to an emergency requiring the test operator.

Subsequently, after accumulating an additional 1.0 hour to reestablish a stabilized temperature, run number two recorded 3 hours 18 minutes of operation, thereby completing the 4-hour test objective. The peak race temperature during this run was 202°F, which was reached after 40 minutes. It remained constant until the 75-minute mark, at which time a gradual cool-down to 192°F occurred between this time and the 3-hour 18-minute shutdown mark. Total bearing time at this point was 10.3 hours.

Disassembly inspection revealed, with the exception of single scratches on several rollers at their toe ends, a very satisfactory condition. The scratches were attributed to a bit of unknown debris becoming imbedded in the cage and then abrasively wearing the roller.

A post-test static measurement of the unexpended oil in the forward cavity, between the bearing and the adjacent shaft seal, revealed 3.5 ounces to be present. A similar measurement of the aft cavity revealed an additional 4.0 ounces. On this basis, it was assumed that during interrupted flow operation, the bearing was lubricated and cooled by 7.5 ounces of oil. This quantity of oil floods the bearing to approximately its pitch diameter.

Although the bearing had completed its 4-hour requirement, followed by the satisfactory visual inspection, a judgment to further explore the bearing's capability was made. Because of the previous acceptable operation with 7.5 ounces of oil, run number three explored positive lubricating flows as far below the design rated condition as permitted by the available flow-measuring equipment and interrupted flow for increasing bending moments. Thrust was maintained at the mean effective continuous level.

After 1.0 hour of operation with a positive flow of 1.6 quarts/minute, a thrust of 3260 pounds and a bending moment of 26,000 inch-pounds, the flow was reduced by 0.6 quart/minute. Race temperature peaked at 155°F, or a 7°F rise above stabilized operation, after 6 minutes. A further reduction of 0.4 quart/minute, or a total of 0.6 quart/minute, yielded a 12°F total rise after 50 minutes. Total bearing time was 13.2 hours. Flow was then interrupted, and a peak temperature of 256 F was achieved after 17 minutes. After the race temperature was reduced to 155 F by resuming the design rated condition, a bending moment of 36,000 inch-pounds was applied and the flow interrupted. A peak of 231°F was achieved after 39 minutes. Total time was 15.9 hours.

As recorded earlier, the operating procedure was to flow the design rated condition until the outer-race temperature stabilized, and then to shut down the supply pump. The external test fixture scavenge drain lines required to return oil to the lubricating system sump remained in the system in order that positive flow could be readily resumed. The orientation of the two lowest drain lines caused some residual oil to accumulate. During dynamic operation, this oil appeared to pulsate, indicating a degree of entrapped air.

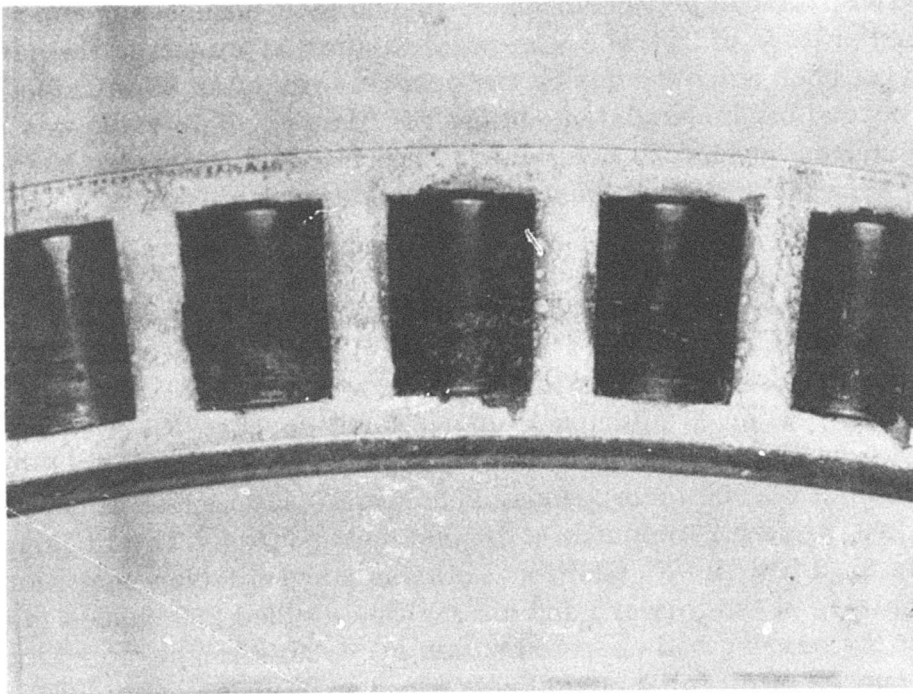
Run number four evaluated the possible effect of the scavenge drain line back pressure on the bearing environment at a still higher moment of 46,000 inch-pounds. The race reached 218°F after 52 minutes of operating with interrupted flow. At this point, the test unit was momentarily shut down, and the two drain lines were

removed in order to vent the bearing environment directly to ambient conditions and to measure the amount of oil being purged when operation was initiated from zero flow. The previous test condition of 46,000 inch-pounds was repeated, and a bearing temperature of 214.5°F was reached after 31 minutes, the same temperature having been achieved during the previous run after 35 minutes. However, 9 ounces of purged oil accumulated outside the fixture. This value was inconsistent with the 7.5 ounces heretofore mentioned. The fact that excessive bearing temperature was not being experienced indicated that additional oil was still present within the bearing environment.

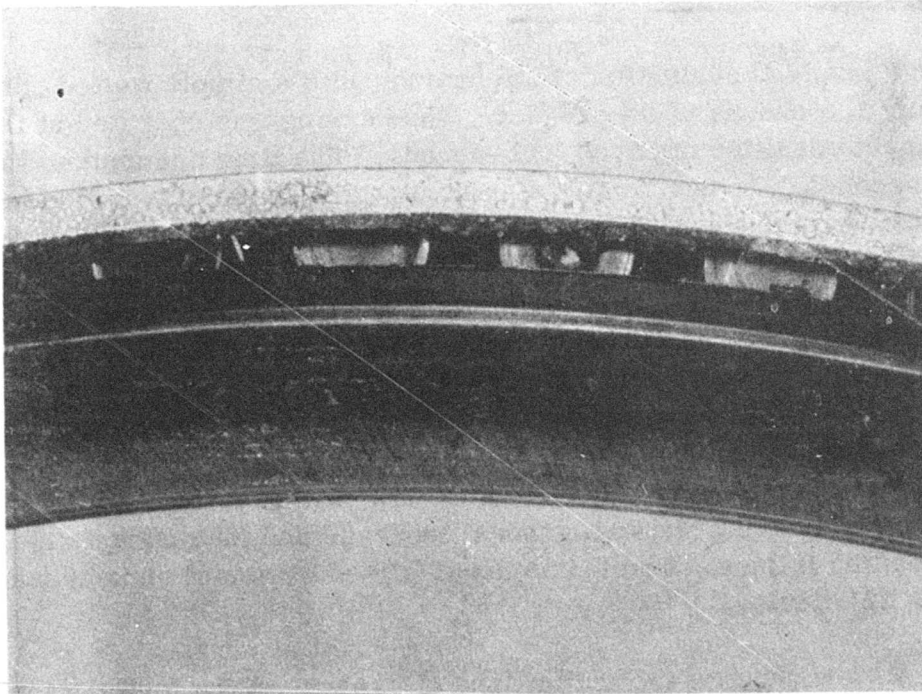
Run number 5 explored the effect of further increases in moment loading, while at a constant thrust of 3,260 pounds. The spectrum included the range from 26,000 inch-pounds to 76,000 inch-pounds in 10,000 inch-pound increments. Temperature stabilized at 187°F after 37 minutes at 26,000 inch-pounds, 195°F after 20 minutes at 36,000 inch-pounds, 199°F after 20 minutes at 46,000 inch-pounds, 203.5°F after 40 minutes at 56,000 inch-pounds, 206°F after 30 minutes at 66,000 inch-pounds, and 203°F after 27 minutes at 76,000 inch-pounds. Total bearing time at this point was 21.3 hours. No additional oil was purged during operation. Post-test static draining of the forward and aft cavities yielded 2.0 ounces in each. This indicated that the bearing had operated within acceptable temperature limits with as little as 4.0 ounces of oil for a period of 2.8 hours. Disassembly inspection revealed no visual change from the 10.3-hour condition reported at the end of run number two.

Run number 6 involved evaluation of the bearing with a simply wetted condition; i. e., approximately 1.5 ounces of oil present. The bearing was operated at the original bending moment condition of 26,000 inch-pounds. The time accumulated was 7 minutes 20 seconds. Approximately 2 minutes were accumulated in establishing the test parameters of speed, bending moment and thrust. During this period, race temperature rose from 71°F to 75.5°F. After 3 minutes, temperature rose to 79°F; after 4 minutes, 85°F; after 5 minutes, 91°F; after 6 minutes, 107°F; after 7 minutes, 215°F; and at the 7-minute 20-second mark, approximately 300°F. At that time, shutdown was initiated. Operation was not prolonged in the region of 300°F because of the possible consequence of rendering the titanium simulated propeller tail-shaft unusable. Two minutes and 40 seconds after shutdown, race temperature had decreased to 200°F. These temperatures indicate that the failure of a nonlubricated bearing shows a gradual increase and then abrupt rise in the few seconds preceding failure. Total time accumulated on serial number two bearing was 21 hours 22 minutes.

Figure 97 is a view showing the major area of damage on the forward inner race (2A). Surface scaling and scoring of the roller is in evidence, as is blistering of the cage silver plating. Figure 98 is a similar view of the aft inner race, showing

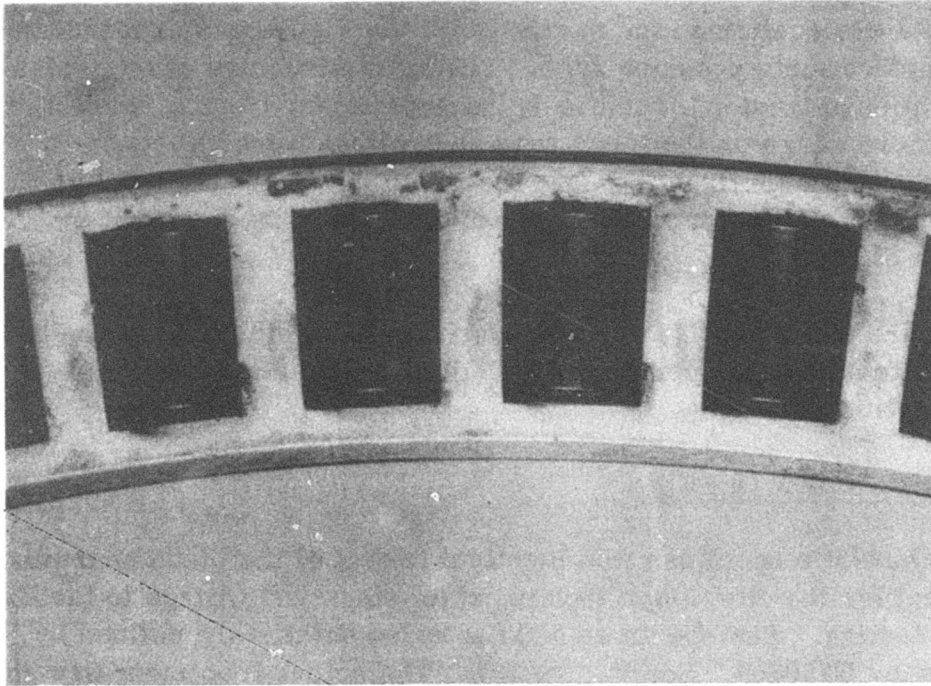


X2

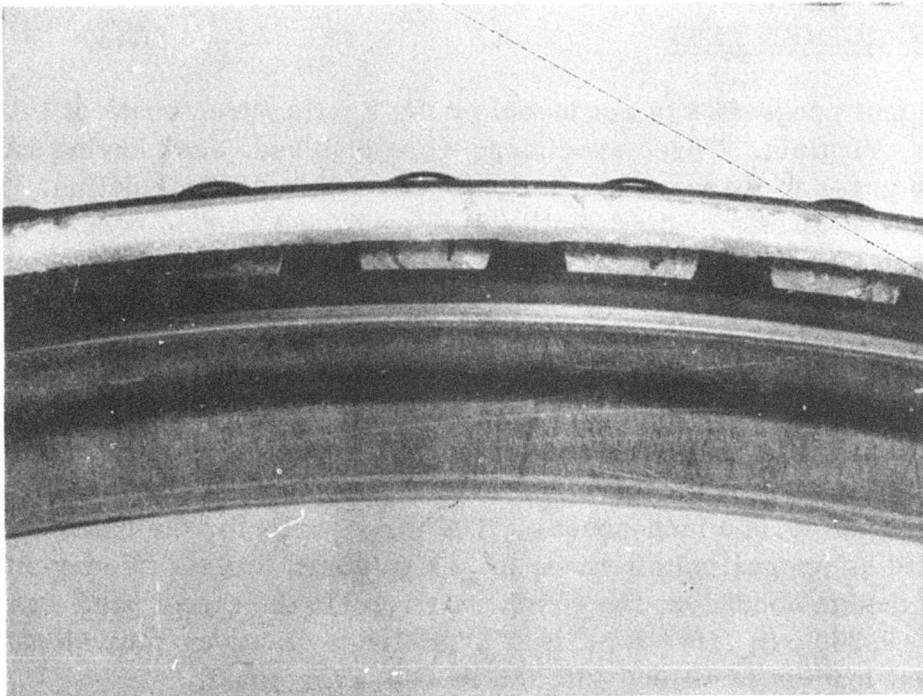


X2

FIGURE 97. INNER RACE AND ROLLER ASSEMBLY
OF BEARING NUMBER 2, SIDE 2A



X2



X2

FIGURE 98. INNER RACE AND ROLLER ASSEMBLY
OF BEARING NUMBER 2, SIDE 2B

considerably less damage (2B). Figure 99 shows the forward (2A) and aft (2B) sides of the common outer race. Discoloration associated with overheating is visible on both surfaces. Metallographic examination of the forward inner race and several rollers confirmed the overheating. In Figure 100a rehardening of the inner-race contact surface can be seen. The microstructure of the typical roller showed normal heat-treated structure in the undamaged areas. See Figure 100b. Microhardness readings on the inner race and rollers were as low as R_C^{33} . As these readings were significantly below the R_C 60 minimum required on the surface of the inner race and throughout the rollers, the local temperature was probably in excess of $1000^\circ F$.

This phase of the test program was considered to be completed, as the bearing demonstrated its ability to operate for a limited period after loss of its pressurized lubricating oil supply.

BALLISTIC SPECIMEN DESIGN

Design of the ballistic specimen was identical to that of the blade spar discussed earlier, except for the addition of several steel rings and fittings to facilitate low cycle fatigue testing. The specimen and the added details are defined by Hamilton Standard drawing U750764. See Figure 101. The actual specimens are shown ready for shipment in Figure 102.

BALLISTIC SPECIMEN TEST

The ballistic test program was conducted by the Eustis Directorate of USAAMRDL at Ft. Eustis, Virginia. Three specimens were involved, each having four equally spaced strain gages to measure elongation in the longitudinal direction. The test sequence involved tensile loading, ballistic impact, and tension-tension cycling until fracture. The cycle ceiling was established on the basis of the number equivalent to 50 minutes of flight operation following ballistic damage.

In order to establish a corollary between the Hamilton Standard out-of-plane fatigue test procedure and the USAAMRDL in-plane tension-tension fatigue test procedure, the following rationale was employed. As cited earlier, the spar continuous design condition is a centrifugal load of 45,000 pounds and a vibratory bending moment of 65,000 inch-pounds. The target area for the ballistic strikes was designated as approximately three inches outboard of the titanium outer support. At the design condition, the resultant stress in the target area was calculated to be $12,000 \pm 9,300$ psi. On the basis of this stress state, an equivalent ballistic specimen axial loading of $45,000 \pm 35,135$ lb was determined.

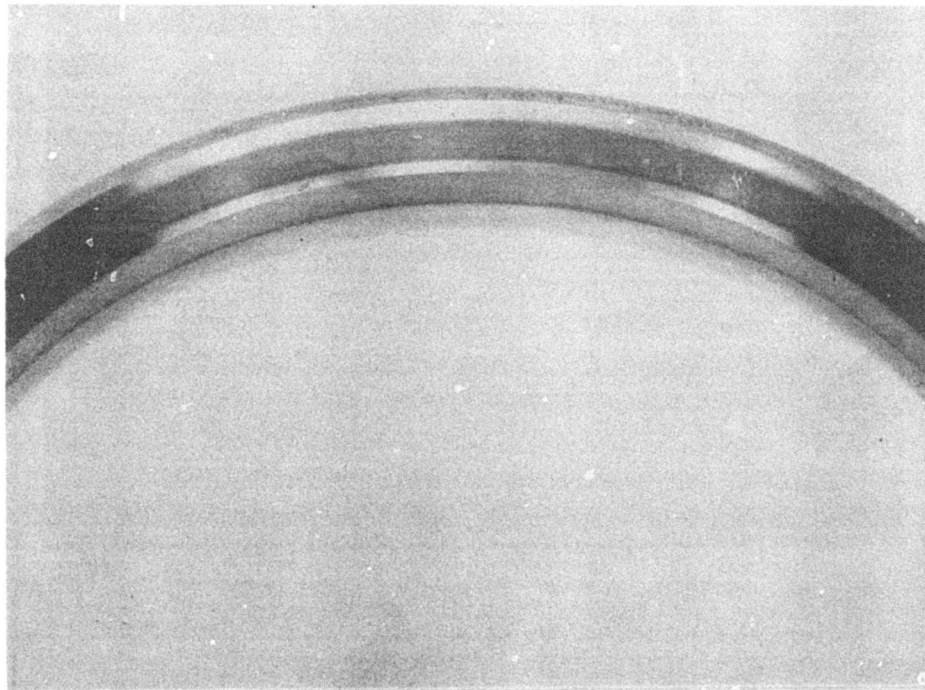
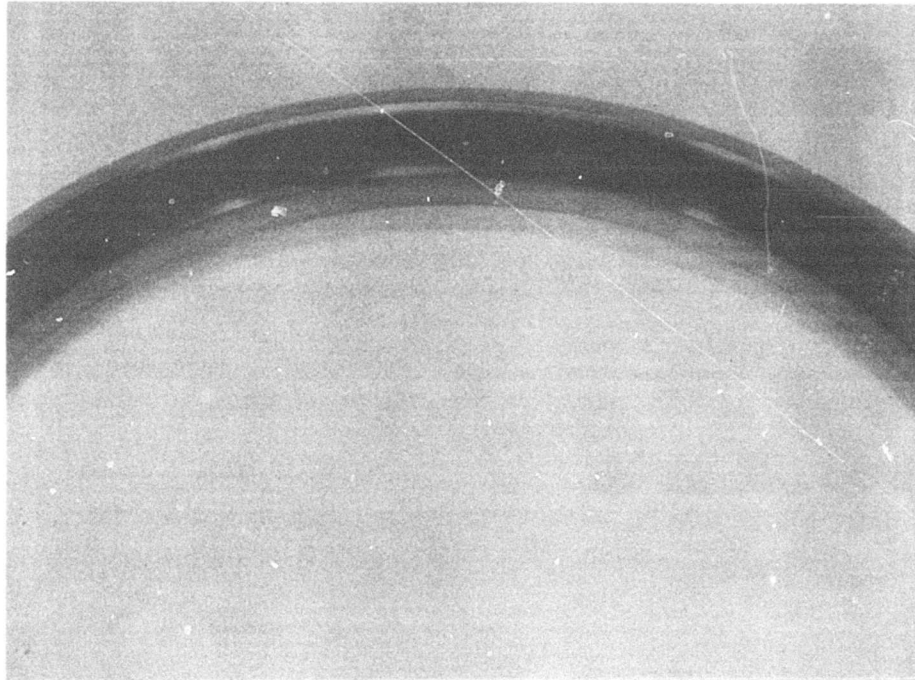
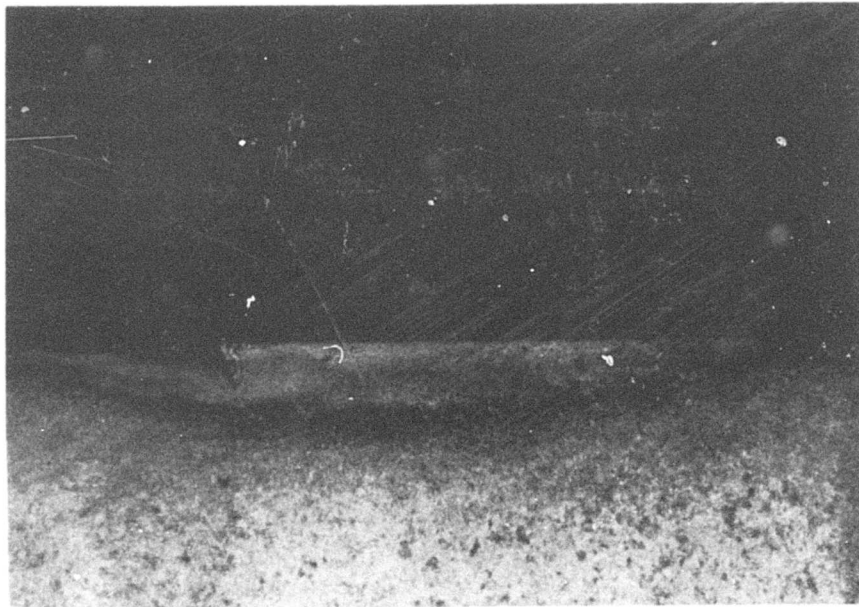
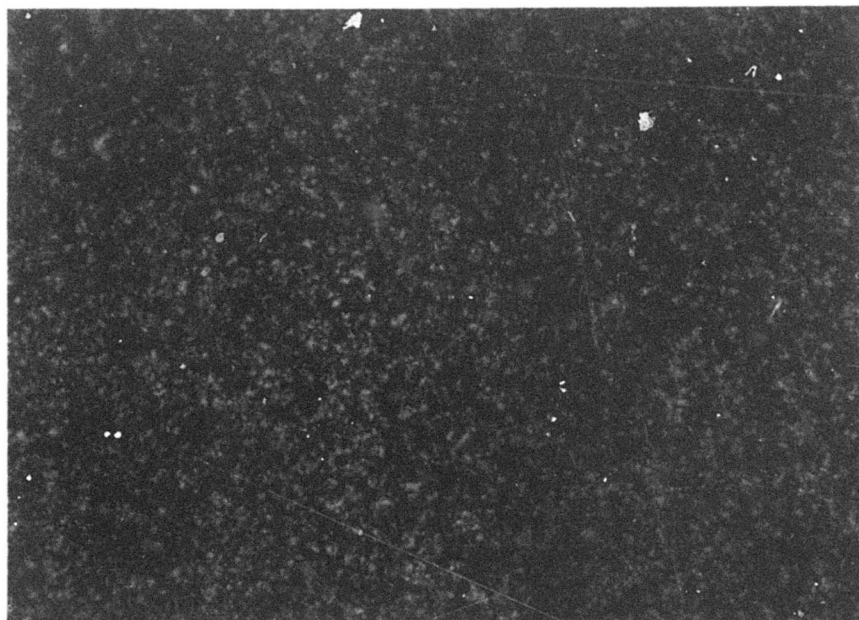


FIGURE 99. OUTER RACE OF BEARING NUMBER 2, SIDES 2A AND 2B



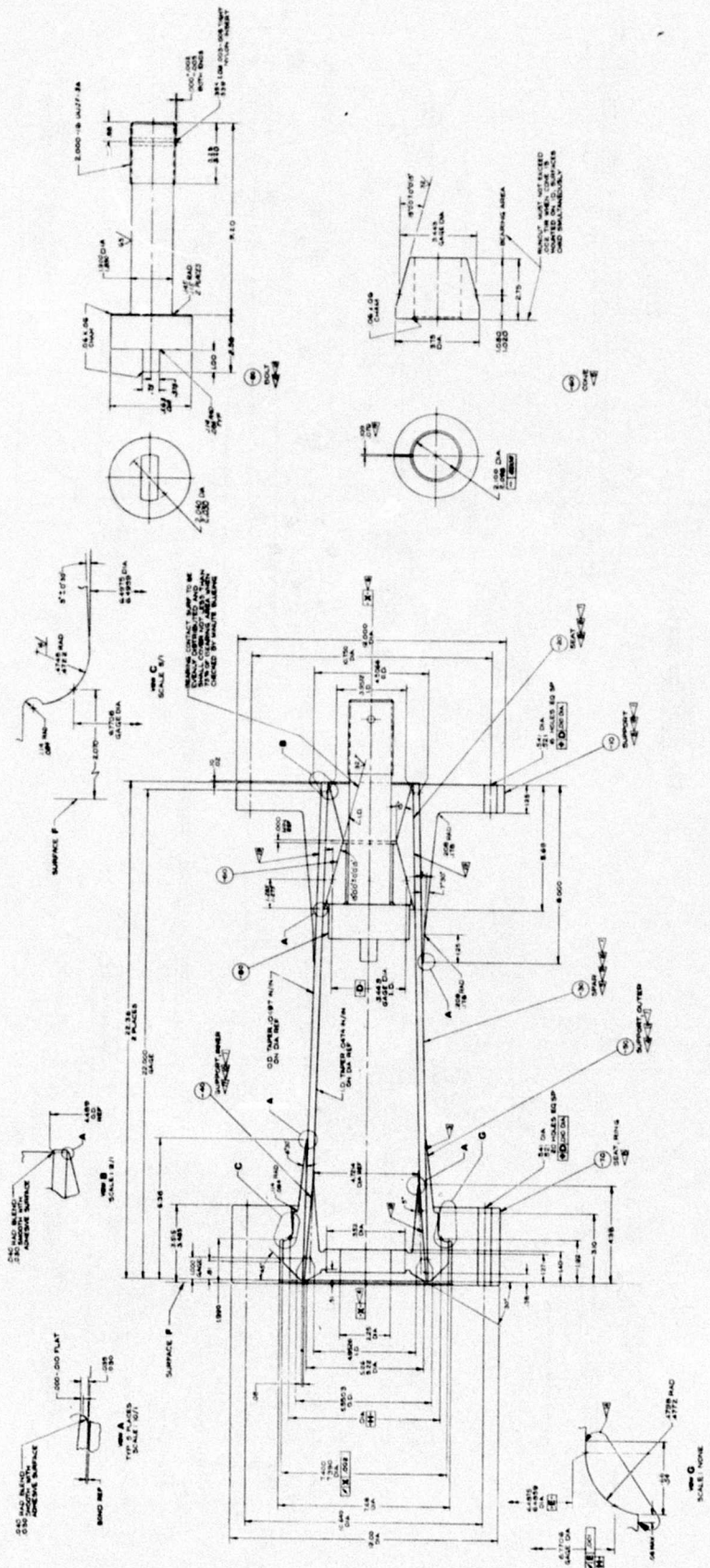
A



B

X500

FIGURE 100. TYPICAL MICROSTRUCTURE OF INNER RACE AND ROLLERS



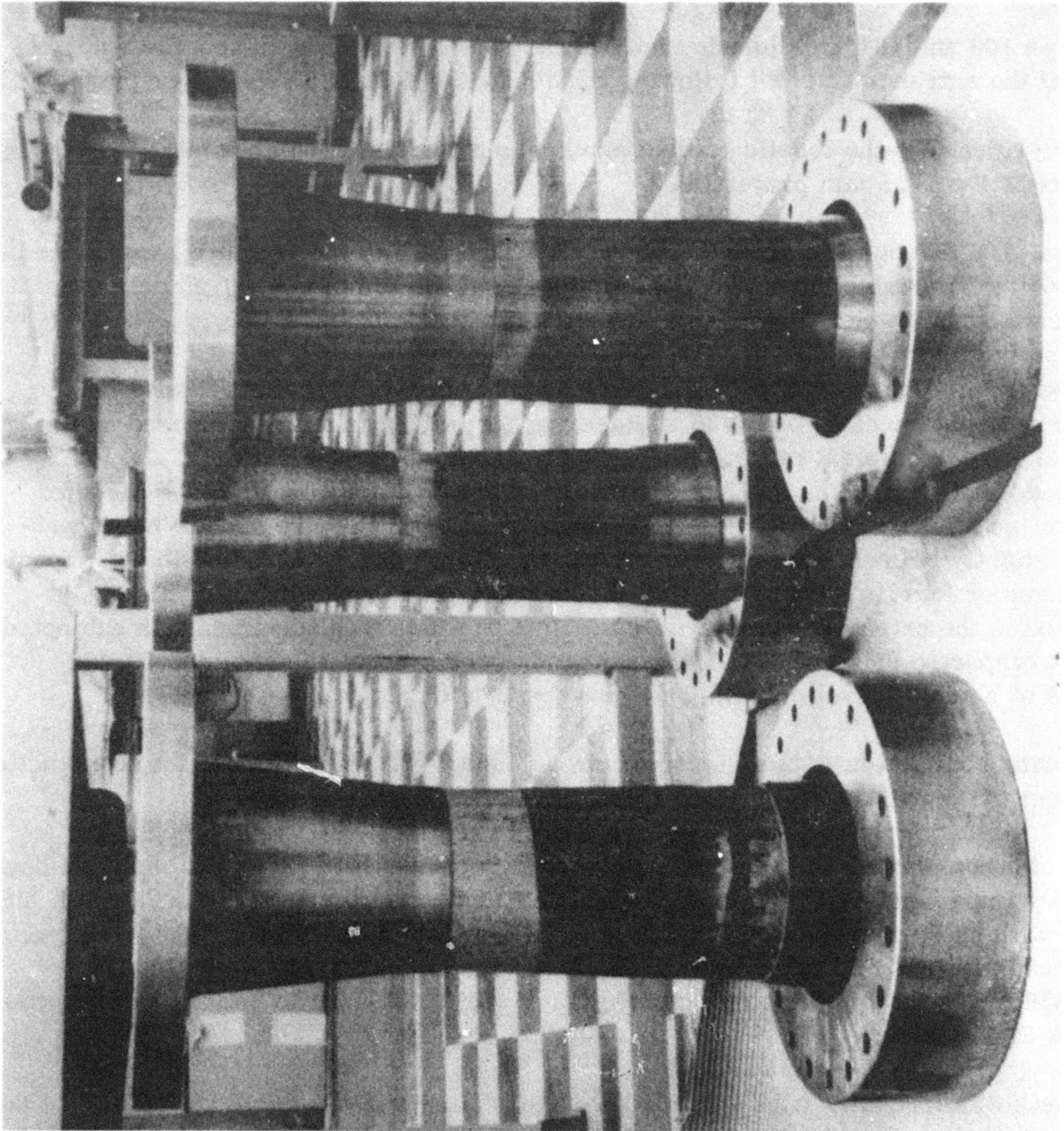


FIGURE 102. BALLISTIC TEST SPECIMENS

The test history of each specimen is contained in Table 28. It should be noted that the calculated steady stresses shown in the table are based on gross section area; i. e., area losses due to the ballistic strikes were not taken into account, while cyclic stresses are based on the classical notch factor of 3.0 for a round hole in a flat plate.

Figures 103 and 104 are closeup views of the extent of damage to specimen number four at the entrance and exit following impact by the second 0.50-caliber projectile.

Figure 105 shows the tensile loading machine and specimen number one following impact by the 14.5 mm projectile.

Figures 106 through 111 show the circumferential path of the fracture experienced by specimen serial number two after sustaining three tumbled 0.30-06 caliber strikes and undergoing tension-tension fatigue tests.

Figure 112 is a presentation of the results for all Borsic aluminum test work; i. e., spars and specimens in terms of engineering stress. Again superimposed on the diagram are the typical infinite-life strength curves for sound material and for degraded material. The number of cycles for the fracture condition are included next to the fracture points. Specimen numbers one and two are seen to have fractured slightly below the average or typical strength line for degraded fibers. Specimen number four is seen to fall well below this typical strength line. This is attributed to the extensive number of test points to which this specimen was subjected and is supported by the fact that the specimen successfully accumulated 29,400 cycles at a stress level only slightly less than the typical strength line.

Following completion of test, one-half of each specimen was returned for examination by Hamilton Standard.

The retention portion of specimen number 4 was examined. This specimen had been initially impacted with a single 0.50-caliber round and, after some testing, was hit again with another round approximately 90° from the first strike. The fracture occurred after 38,900 axial load cycles at a calculated stress state of 10,830 ± 13,830 psi. The fracture path included only one of the four holes, as seen in profile in Figure 113.

The path was irregular with some longitudinal splitting and interply delamination at the bullet hole. This is illustrated in Figure 114. Figure 114a is an external view of the exit site, while Figure 114b shows the fracture surface and interply separation at the midpoint.

TABLE 27 BALLISTIC SPECIMEN TEST SPECTRUM AND RESULTS

Steady Load (lb)	Cyclic Load (lb)	Steady Stress (psi)	Cyclic Stress (psi)	Cycles	Comments
S/N 1					
32,500	0	8,700	0	none	Impacted with one 0.50 caliber round
32,500	11,500	8,700	9,210	29,400	runout
32,500	14,140	8,700	11,340	29,400	runout
32,500	18,000	8,700	14,400	29,400	runout
32,500	23,000	8,700	18,450	29,400	runout
45,000	17,500	12,000	14,010	29,400	runout
45,000	35,135	12,000	28,140	29,400	runout
65,000	35,135	17,400	28,140	29,400	runout
81,000	19,000	26,600	15,210	45,000	runout
0	106,700	0	85,500	1/4	successfully loaded
32,500	27,500	8,700	22,350	45,000	runout (test rig fracture)
45,000	0	12,000	0	none	Impacted with second 0.5 caliber round 90° from first shot
16,250	5,750	4,350	4,605	29,400	runout
32,500	5,750	8,700	4,605	29,400	runout
32,500	11,500	8,700	9,240	29,400	runout
40,600	17,250	10,830	13,830	28,900	fractured in spar
S/N 1					
45,000	0	11,900	0	none	Impacted with one 14.5 mm round
45,000	17,600	11,900	13,950	35,000	runout
45,000	35,200	11,900	27,900	35,000	runout
45,000	44,000	11,900	35,950	35,000	runout
67,500	17,600	17,900	13,950	35,000	runout
67,500	32,500	17,900	28,800	34,000	fractured in spar
S/N 2					
45,000	0	11,900	0	none	Impacted with three consecutive .30-06 rounds
11,250	8,800	3,000	7,050	35,000	runout
15,000	11,700	4,010	9,390	35,000	runout
22,500	17,600	6,020	14,100	35,000	runout
30,000	23,500	8,030	18,840	35,000	runout
37,700	26,400	10,100	21,180	35,000	runout
45,000	35,000	12,000	28,050	1,180	fractured in spar

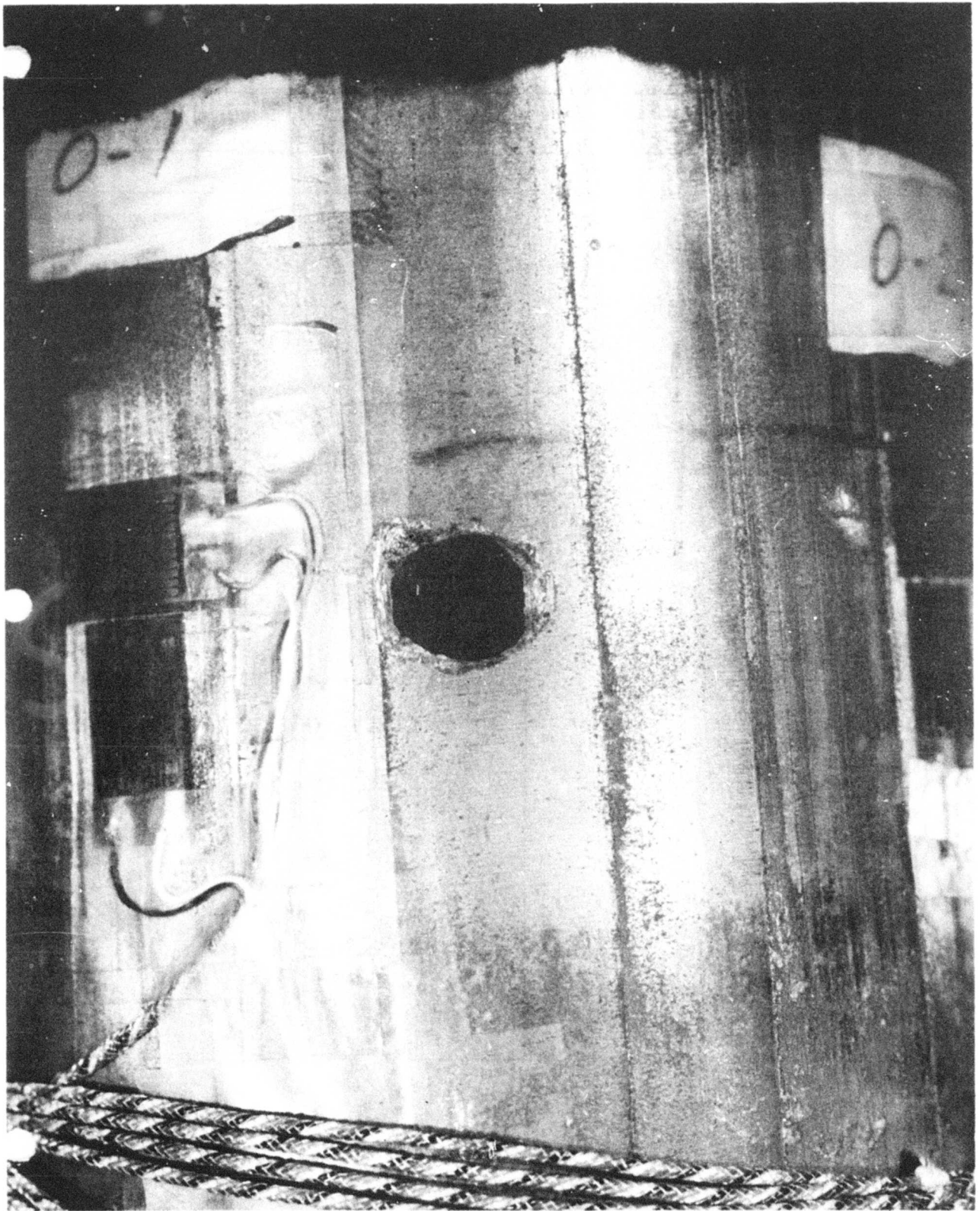


FIGURE 103. ENTRANCE DAMAGE TO BALLISTIC SPECIMEN NUMBER 4,
0.50 CALIBER PROJECTILE

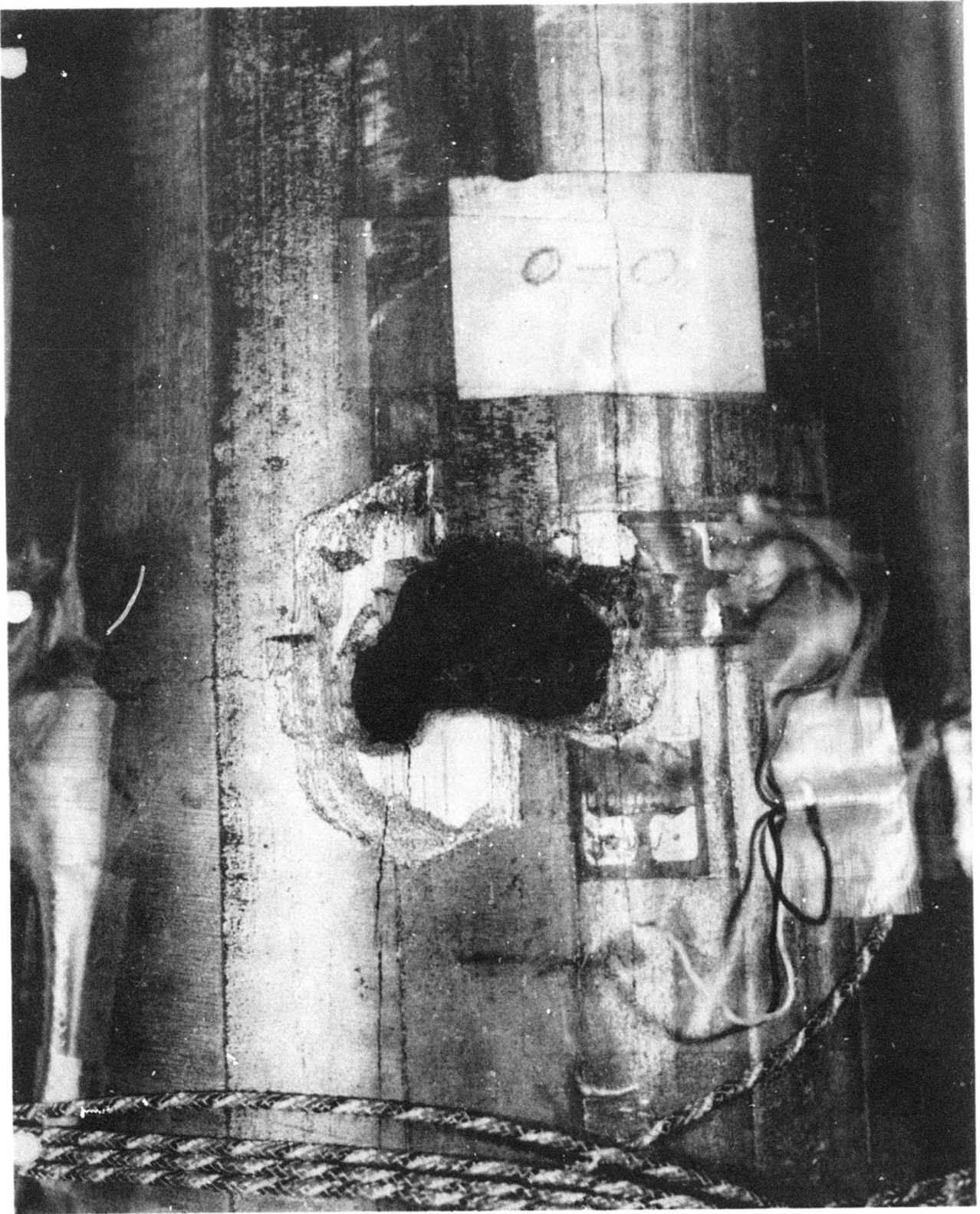


FIGURE 104. EXIT DAMAGE TO BALLISTIC SPECIMEN NUMBER 4,
0.50 CALIBER PROJECTILE

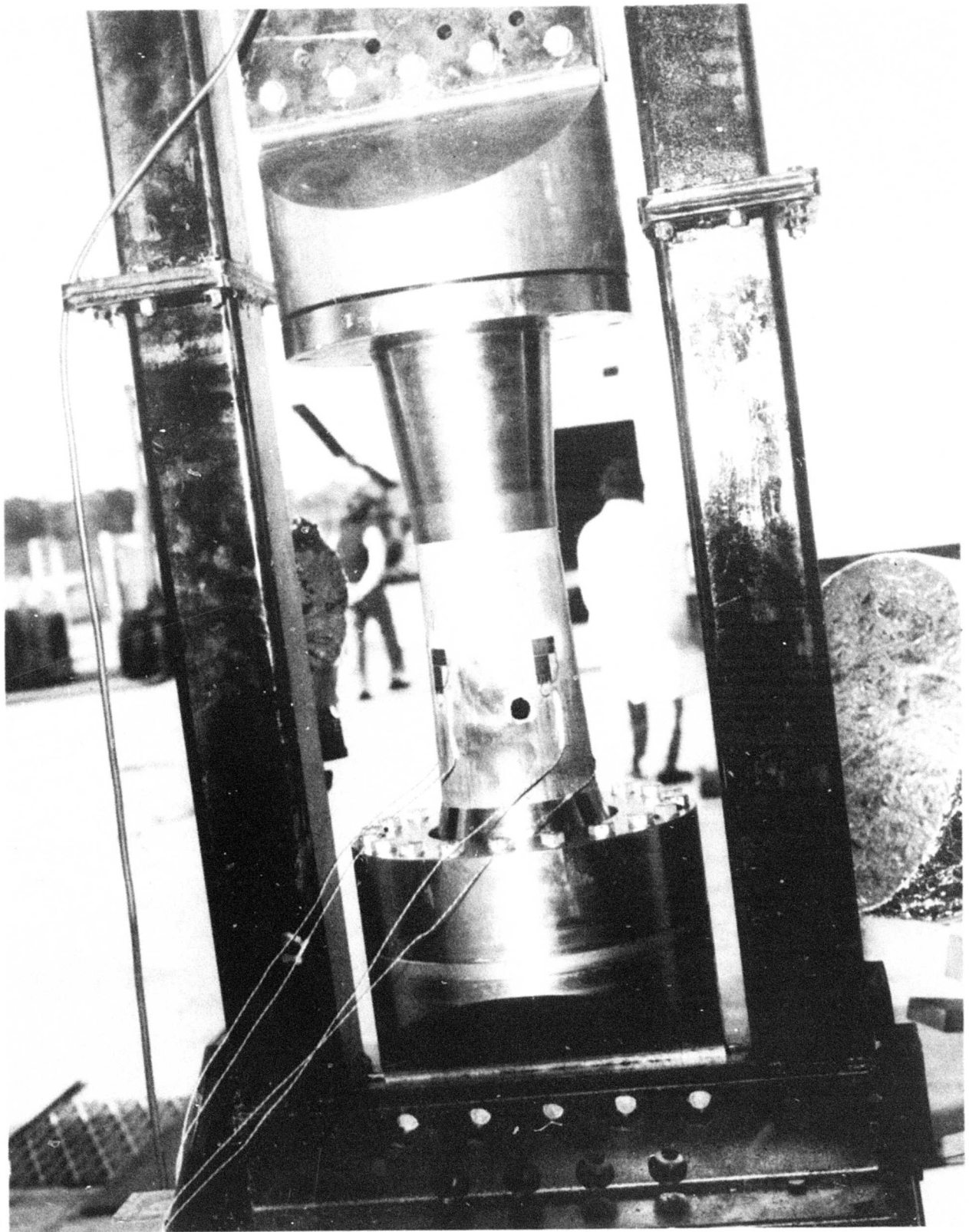


FIGURE 105. TENSILE LOADING MACHINE WITH SPECIMEN NUMBER 1
FOLLOWING IMPACT BY 14,5 MM PROJECTILE

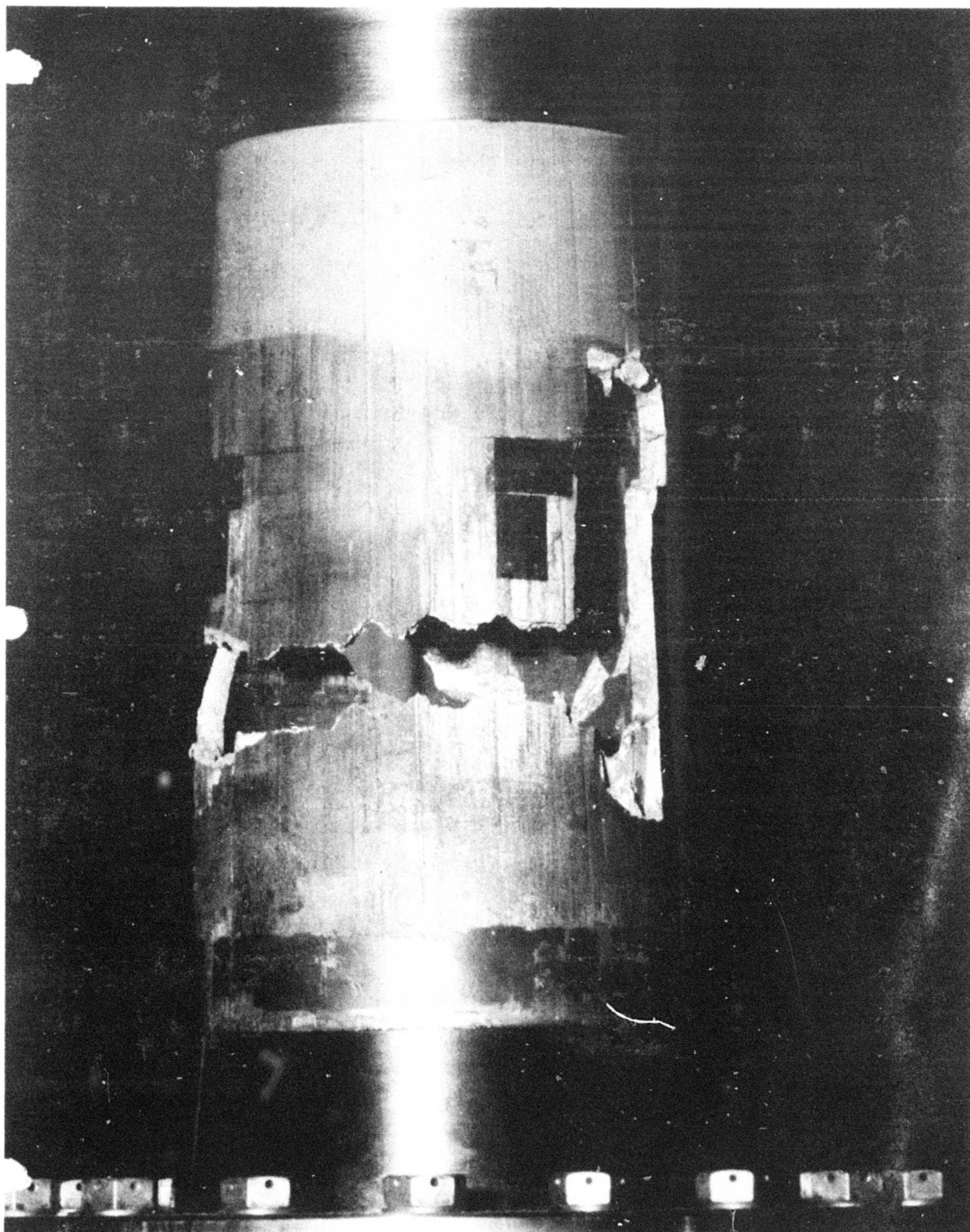


FIGURE 106. BALLISTIC SPECIMEN NUMBER 2 FATIGUE TEST FRACTURE, 0° TO 120° OF REVOLUTION

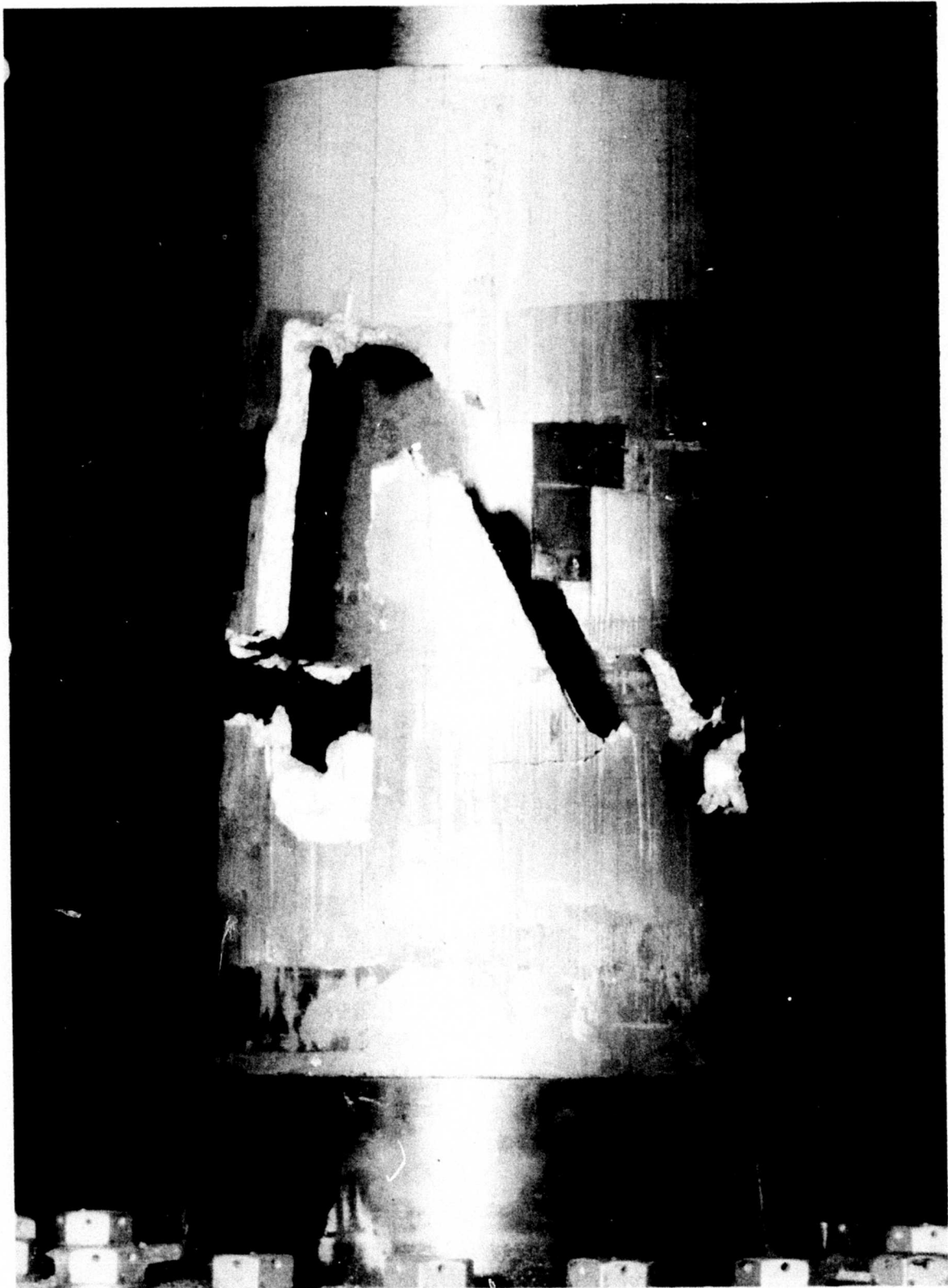


FIGURE 107. BALLISTIC SPECIMEN NUMBER 2 FATIGUE TEST FRACTURE,
90° TO 210° OF REVOLUTION

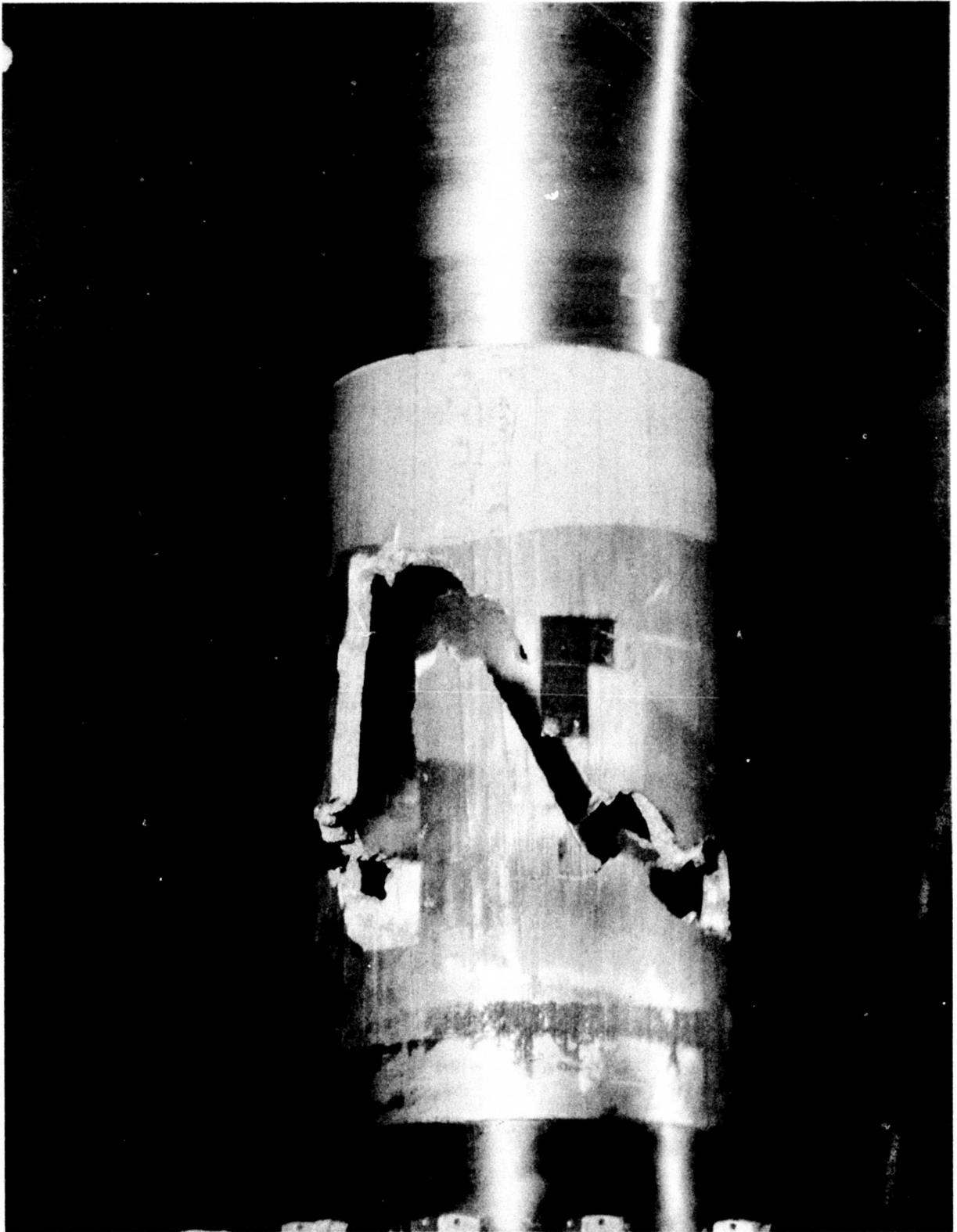


FIGURE 108. BALLISTIC SPECIMEN NUMBER 2 FATIGUE TEST FRACTURE, 100° TO 220° OF REVOLUTION

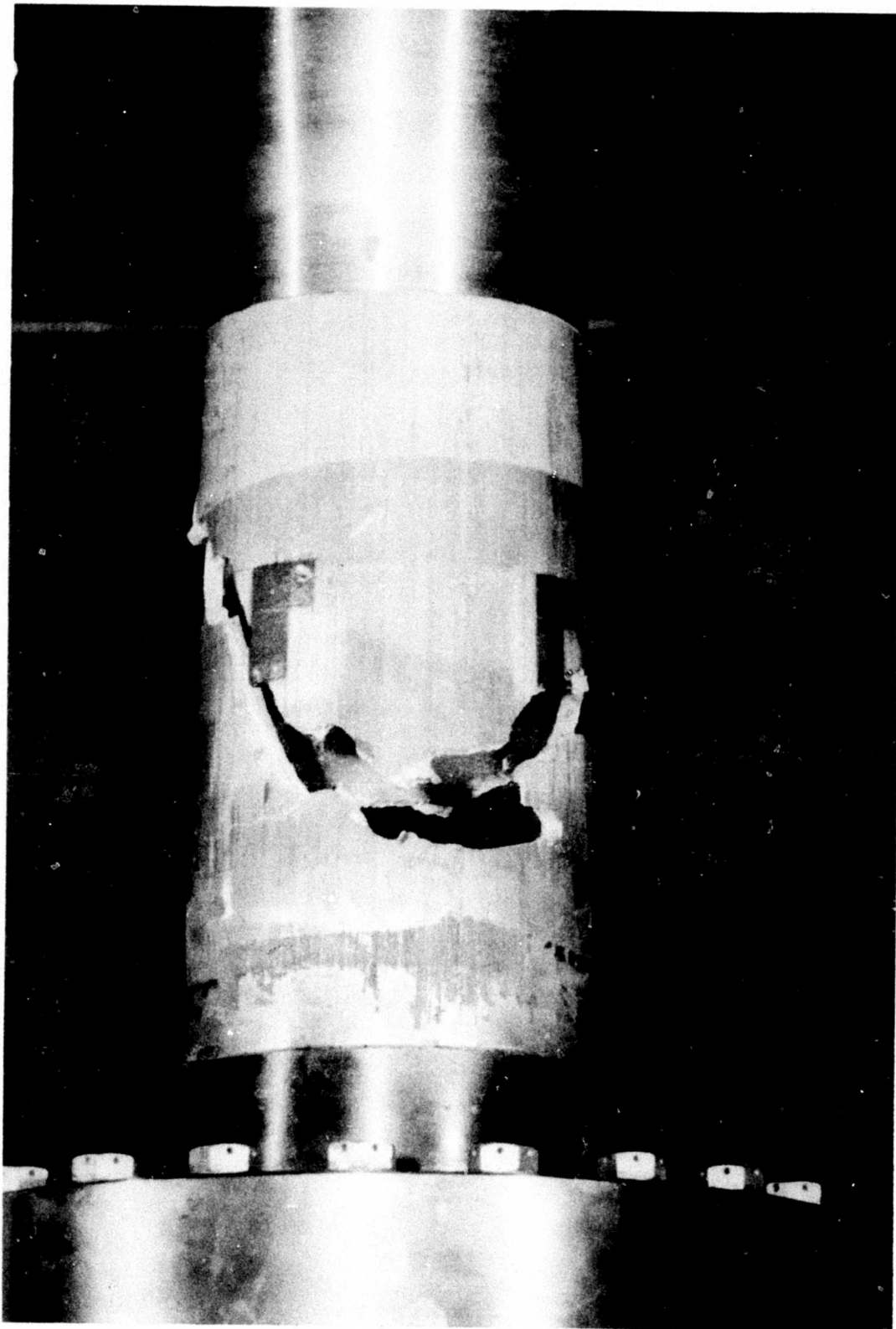
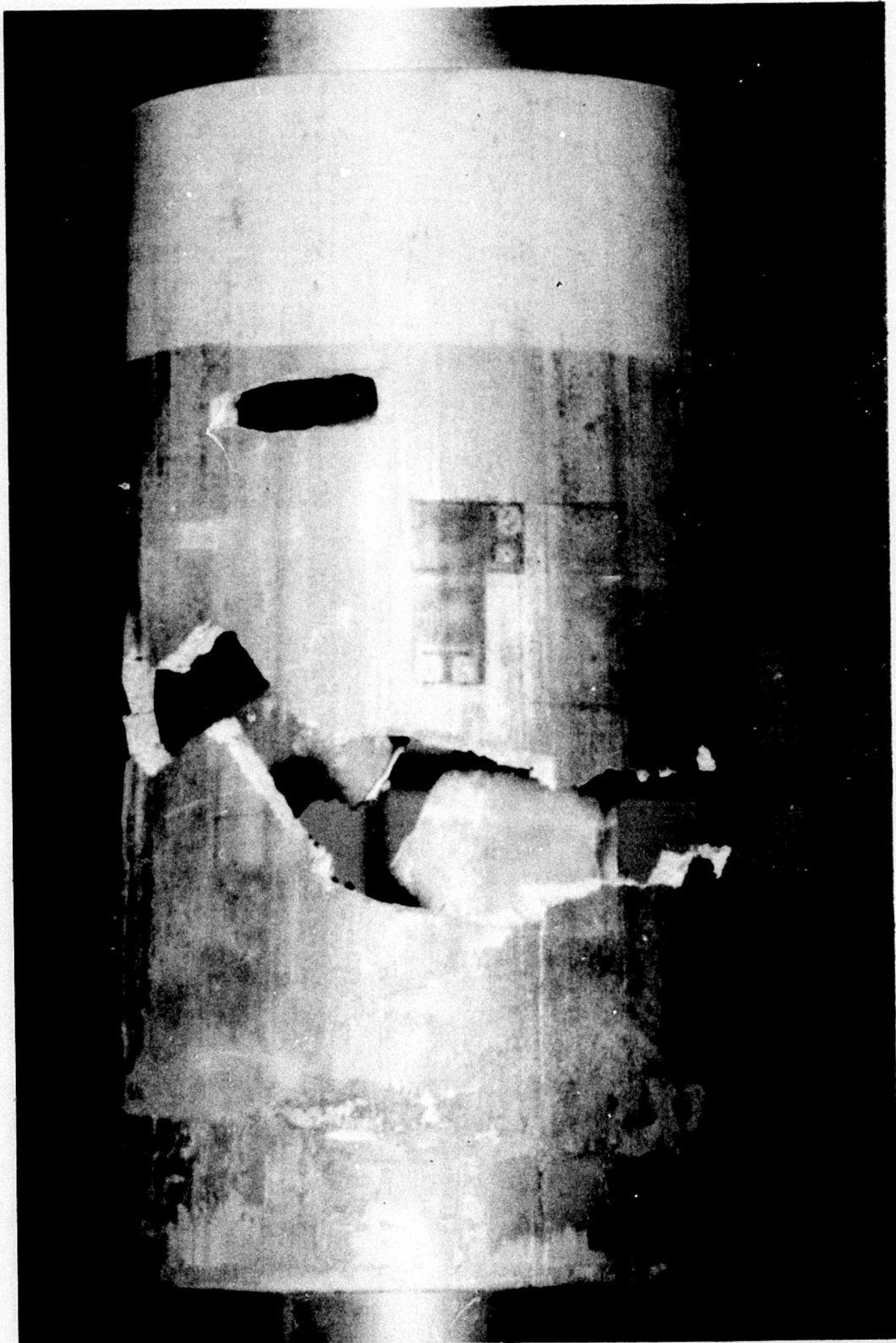


FIGURE 109. BALLISTIC SPECIMEN NUMBER 2 FATIGUE TEST FRACTURE, 160° TO 210° OF REVOLUTION



FIGURE 110. BALLISTIC SPECIMEN NUMBER 2 FATIGUE TEST FRACTURE, 180° TO 300° OF REVOLUTION



**FIGURE 111. BALLISTIC SPECIMEN NUMBER 2 FATIGUE TEST
FRACTURE, 280° TO 45° OF REVOLUTION**

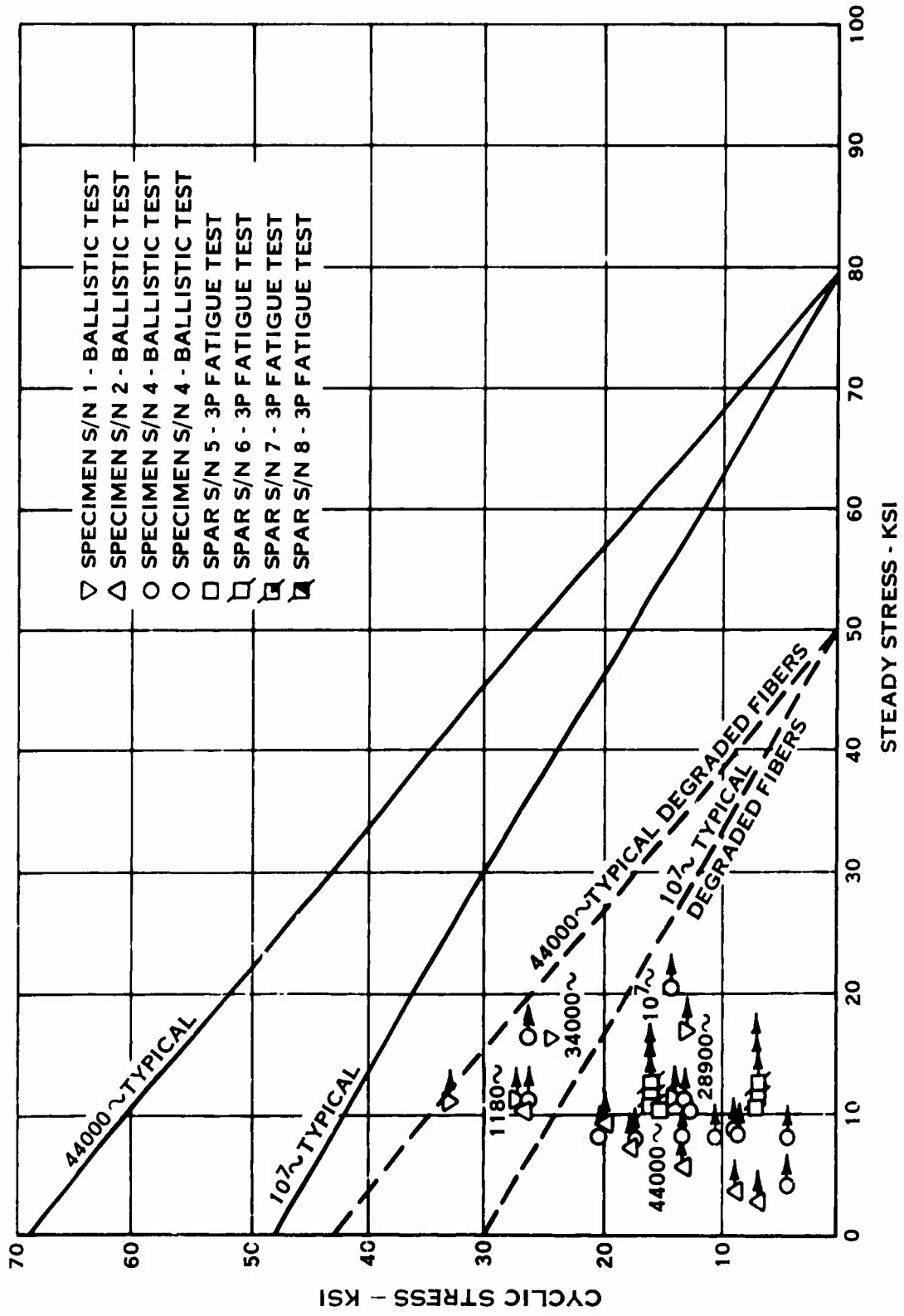


FIGURE 112. BORSIC ALUMINUM FATIGUE TEST RESULTS

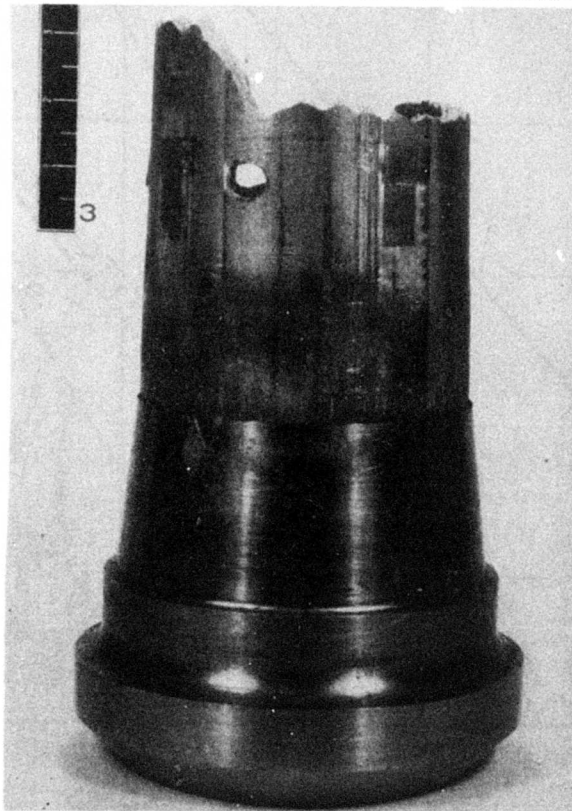
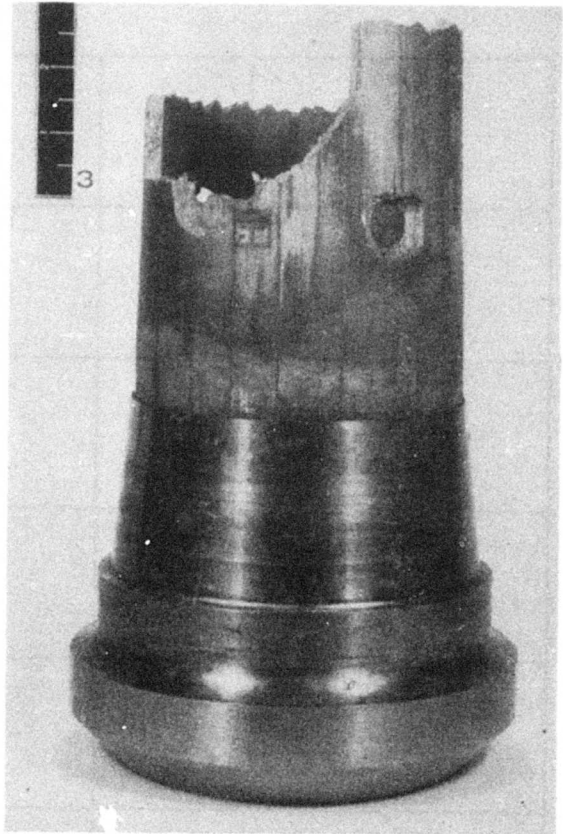
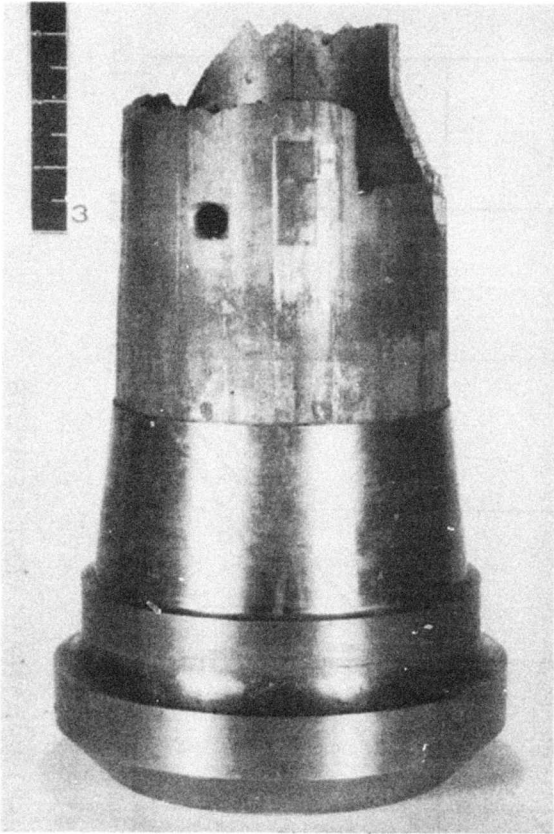
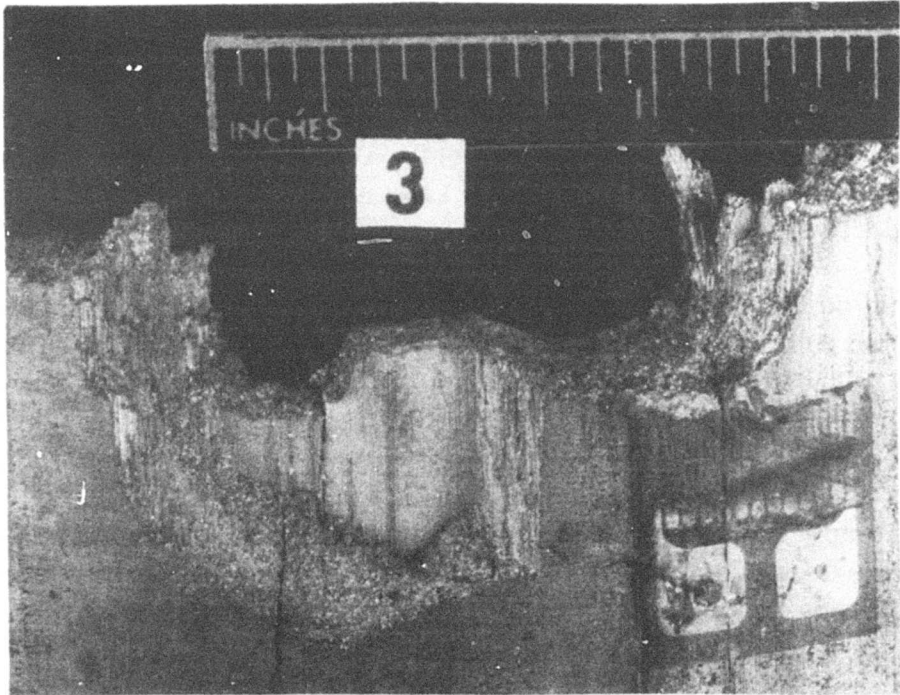
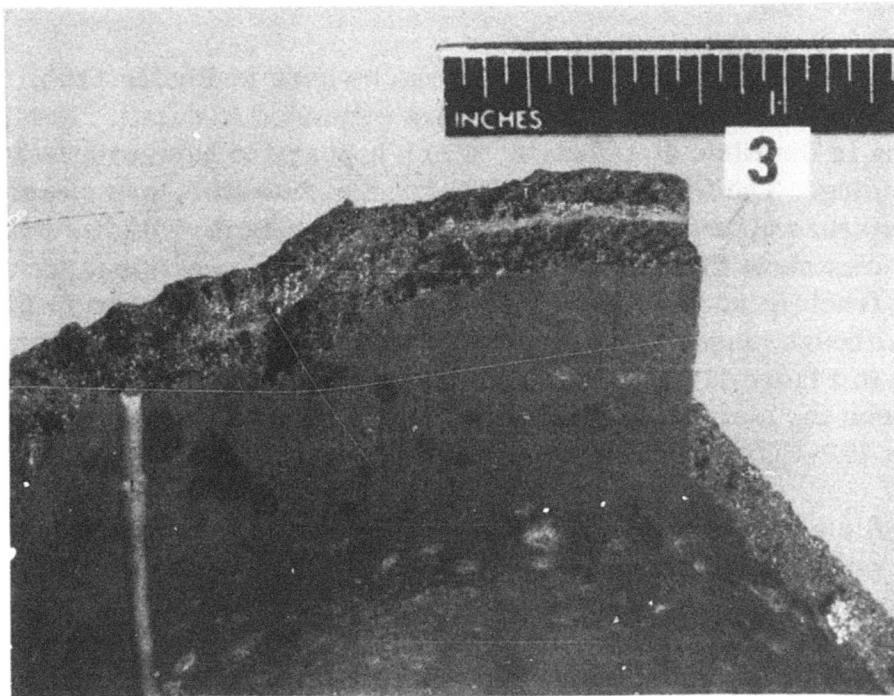


FIGURE 113. RETENTION SECTION OF BALLISTIC SPECIMEN NUMBER 4



A



B

FIGURE 114. EXIT DAMAGE TO BALLISTIC SPECIMEN NUMBER 4

The outboard portion of specimen serial number one was examined. It had been impacted with a single 14.5 mm round and fractured after 34,000 axial load cycles at a calculated stress state of $17900 \pm 28,800$ psi. The fracture path included both holes and had an irregular contour. Interply and longitudinal cracking representative of fiber-to-matrix splitting was evident. The damage to this specimen is presented in Figures 115 and 116. Figures 116a and 116b are external and internal views, respectively, of the impact site.

The retention portion of specimen number two was examined. This specimen had been subjected to three consecutive .30-06 rounds and had fractured after 1180 $\pm 28,050$ psi. The fracture passed through two holes and was very irregular. The fractured specimen is presented in Figure 117.

Close views of two of the points of impact area shown in Figure 118. Again, considerable interply delamination had occurred in the area of impact. Figures 118a and 118b are external and internal views, respectively, of the impact site. Figure 118c is an internal impact view, while 118d is an external view at a second impact site.

Sections of the fracture surfaces of each specimen were examined by means of a scanning electron microscope. Sections near a hole of specimen number one are shown in Figure 119.

Interply splitting near the mid-thickness can be seen in Figure 119b. The numbers on Figures 119a and 119b indicate the areas examined in detail. Notable in these fractographs is the fiber distribution, which appears to have relatively uniform interply spacing. The fibers on a particular ply, however, are closely packed, and in some areas appears to be touching their neighbors. Higher magnifications of the fractures show that the fibers generally have edge origins; see Figure 119f. The matrix fracture surface is largely ductile rupture, as shown in Figures 119c and 119d, although closely spaced parallel ridges, suggestive of fatigue striations, are evident in Figure 119g. There was no evidence of the massive chemical reaction between the matrix and the boron of the fibers as was present on spar serial number five (3P-OOP fatigue test).

Metallographic sections were prepared from each of the specimens at the ballistic penetration points, and the results of specimen numbers one and four are presented in Figures 120a through h.

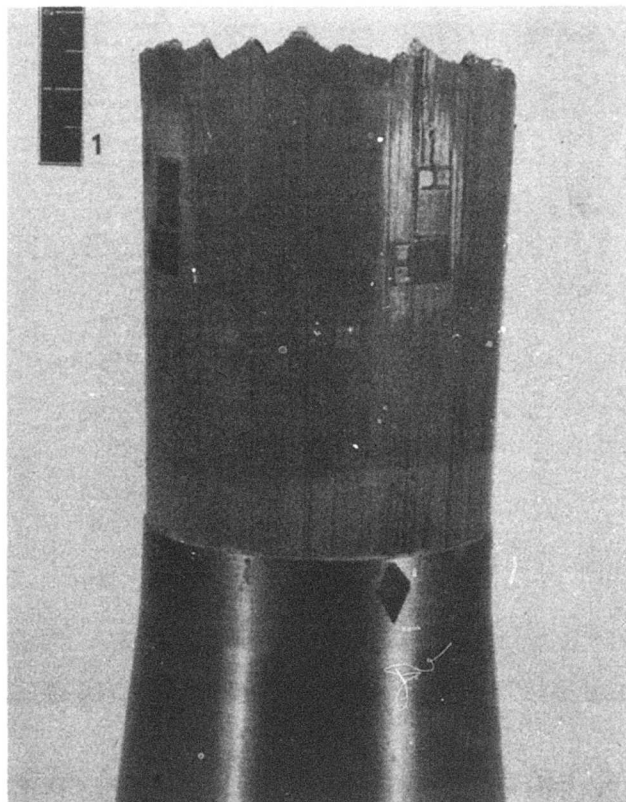
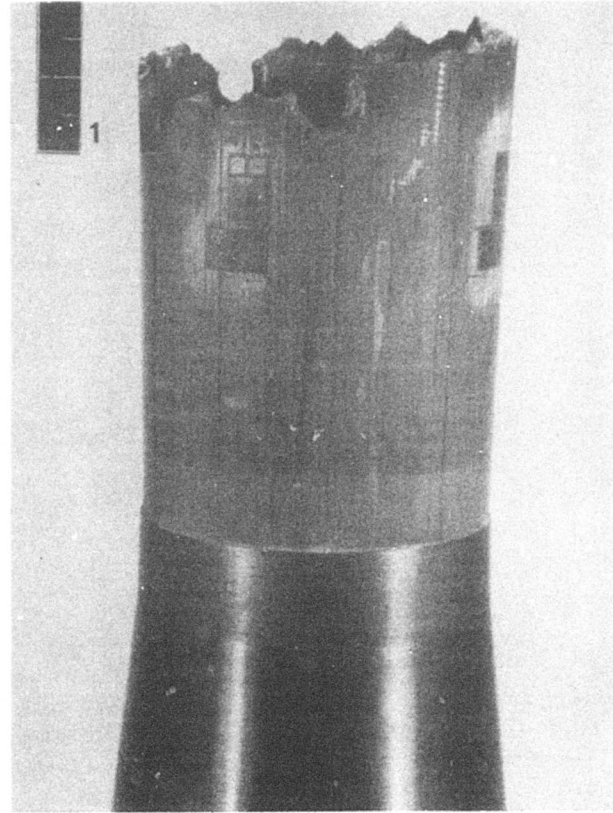
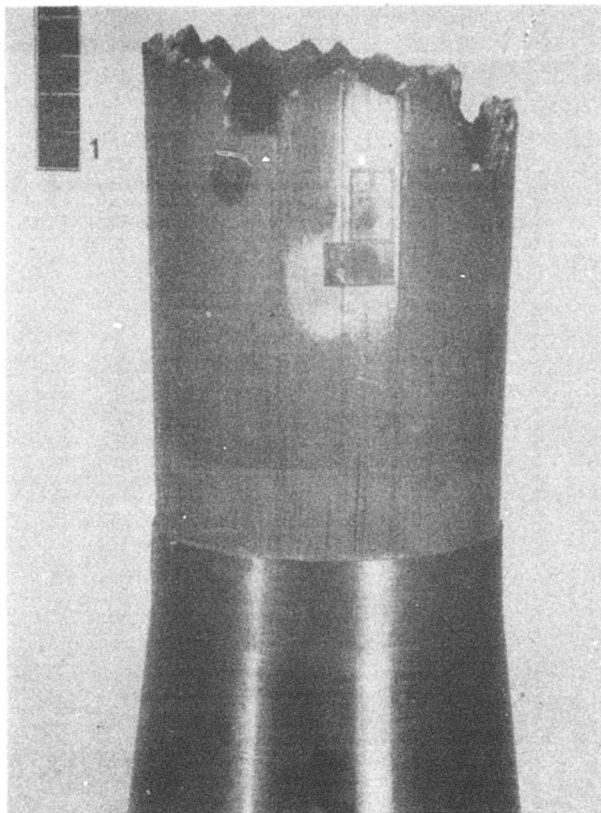
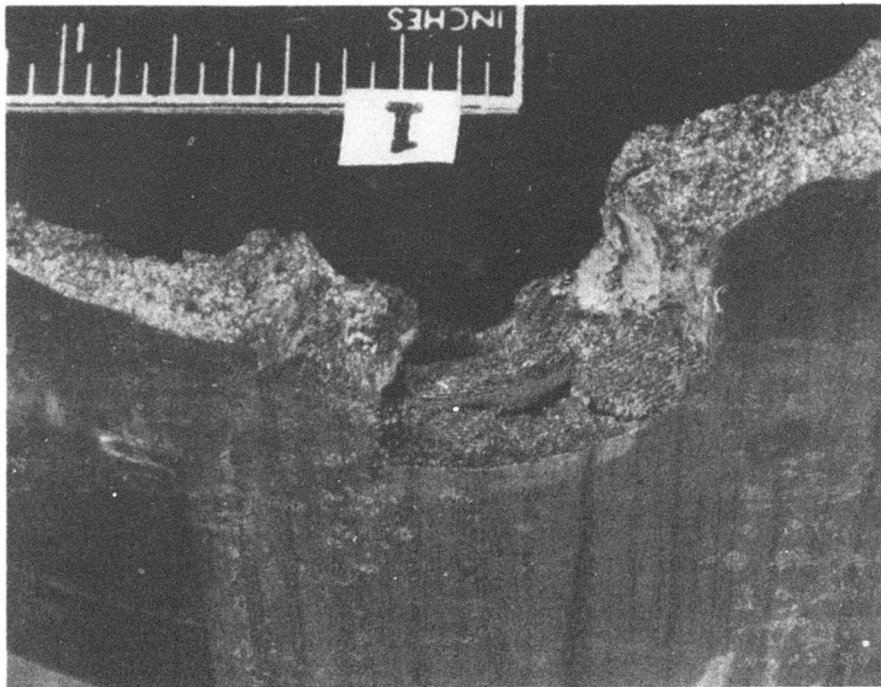
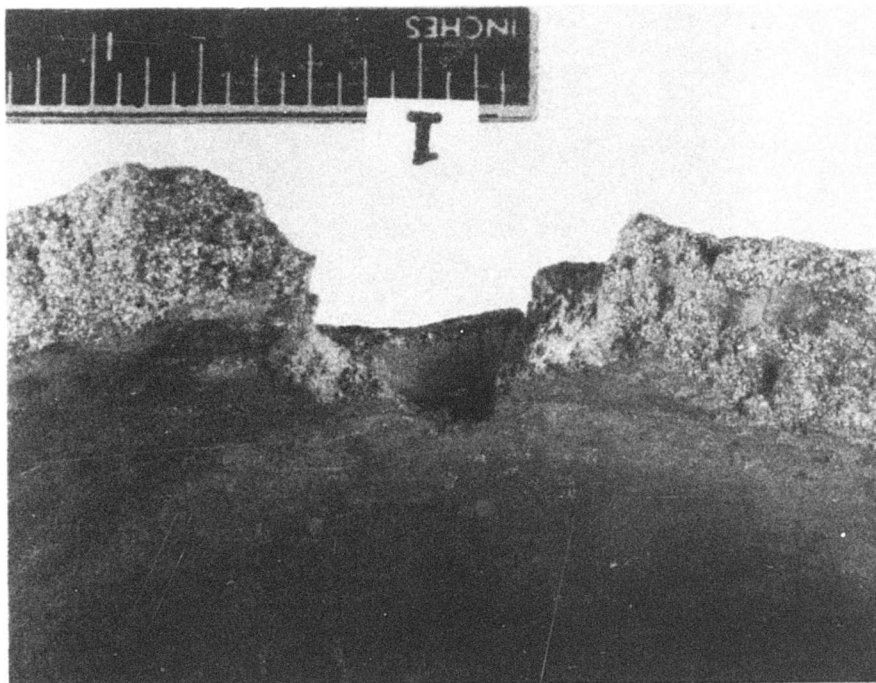


FIGURE 115. OUTBOARD SECTION OF BALLISTIC SPECIMEN NUMBER 1



A



B

FIGURE 116. EXIT DAMAGE TO BALLISTIC SPECIMEN NUMBER 1

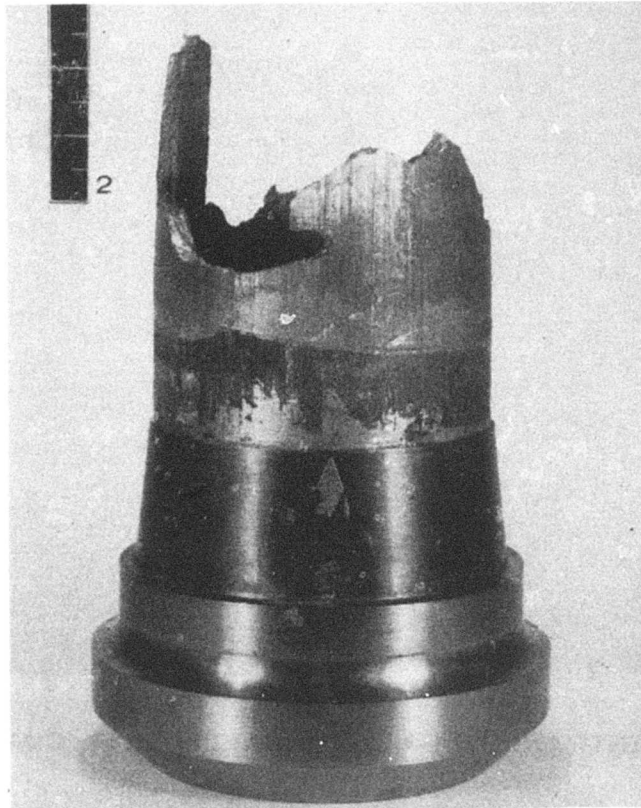
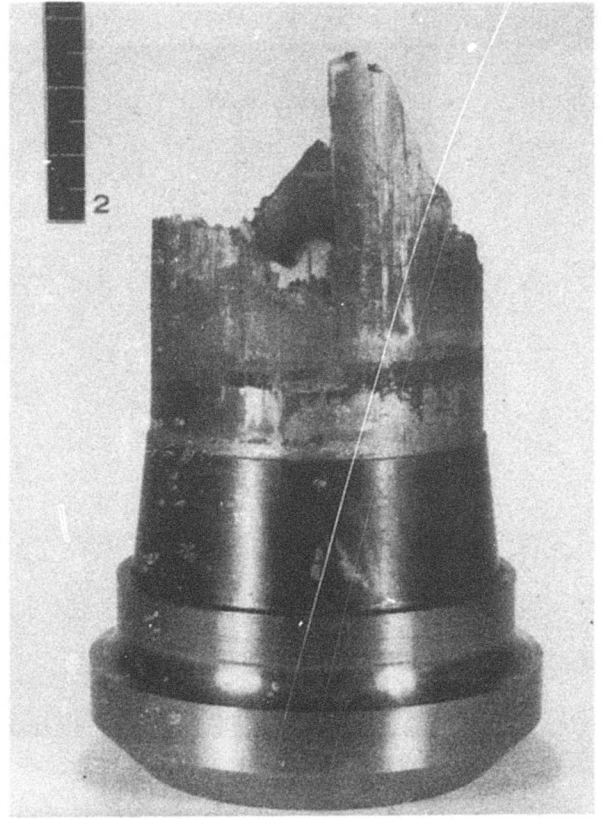
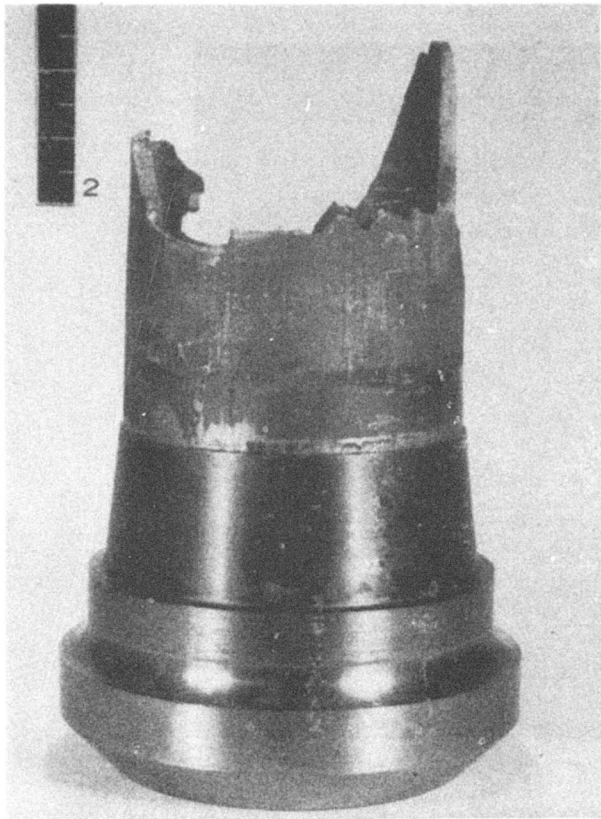
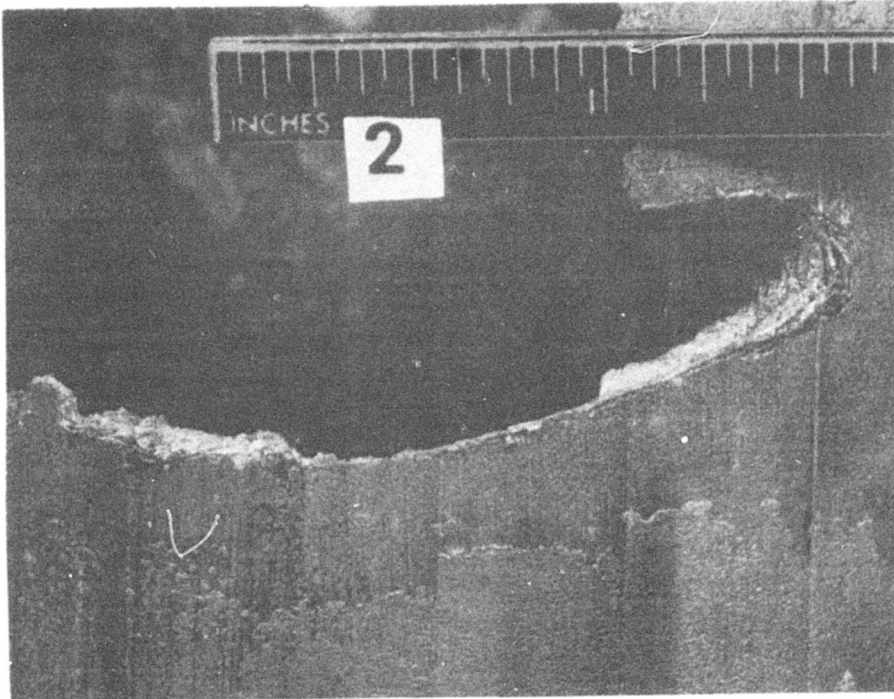
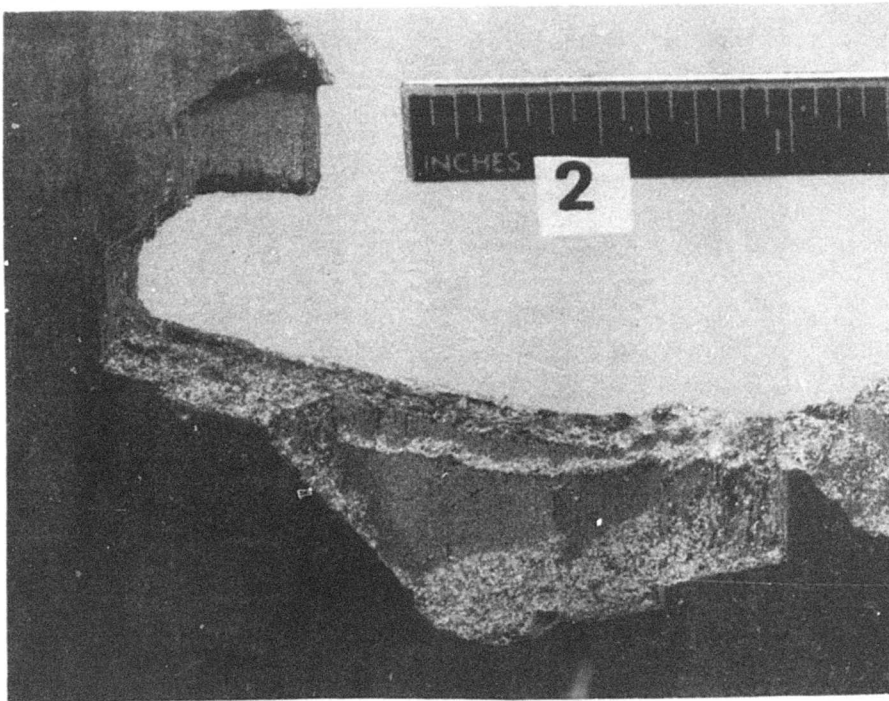


FIGURE 117. RETENTION SECTION OF BALLISTIC SPECIMEN NUMBER 2

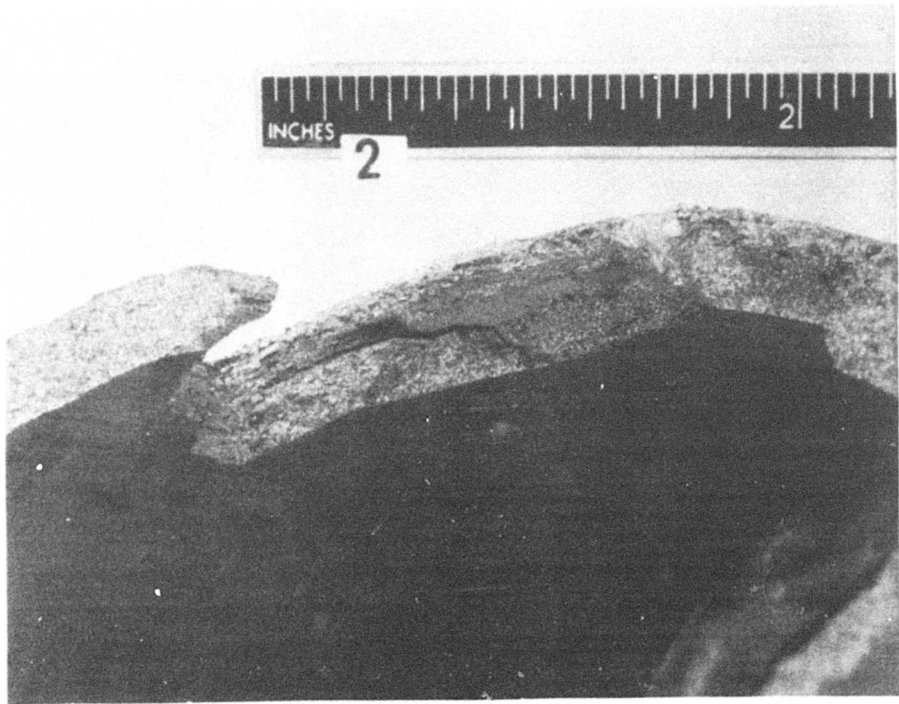


A



B

FIGURE 118. ENTRANCE DAMAGE TO BALLISTIC SPECIMEN NUMBER 2

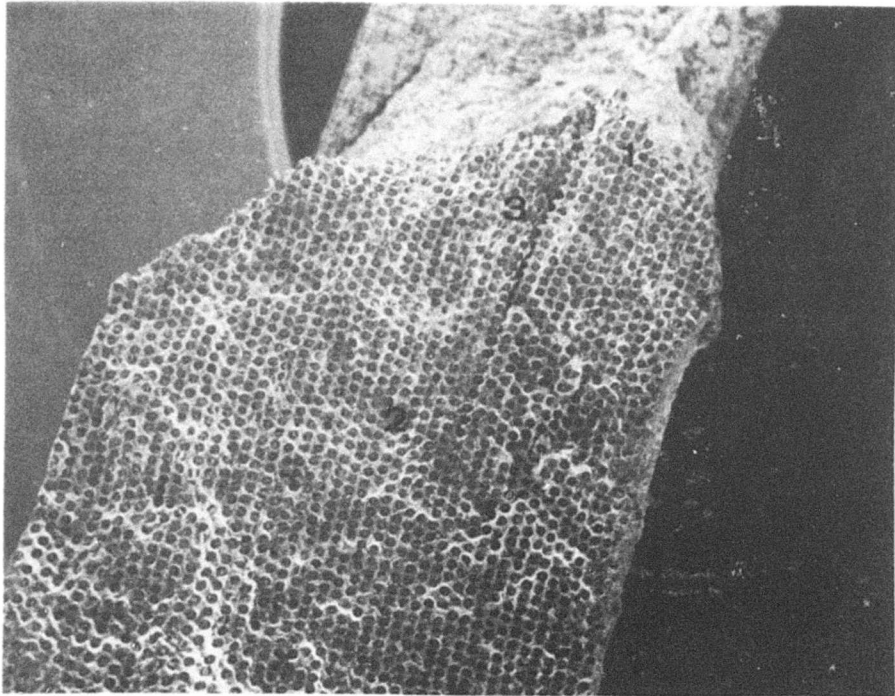


C

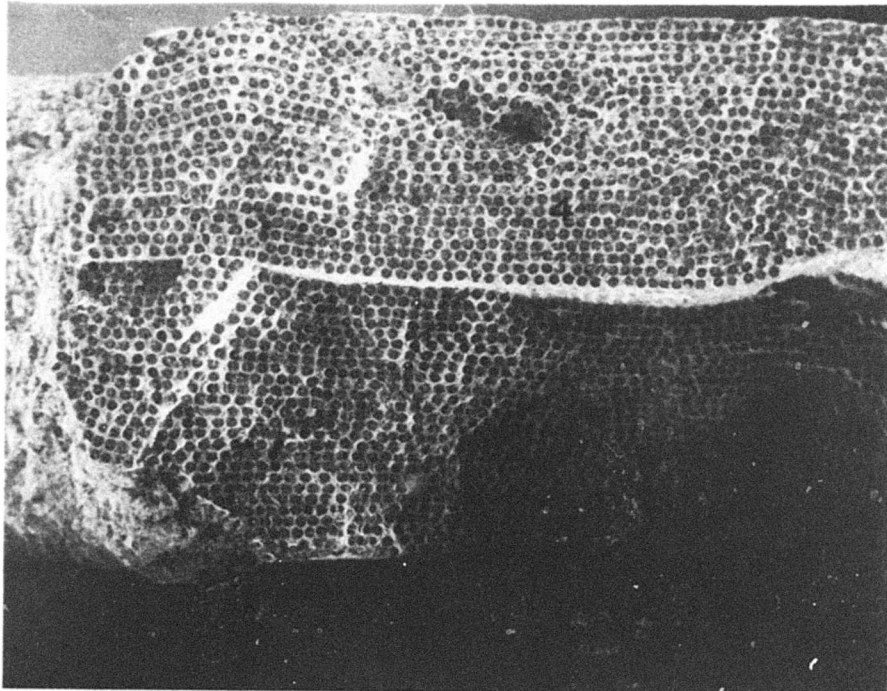


D

FIGURE 118. CONTINUED

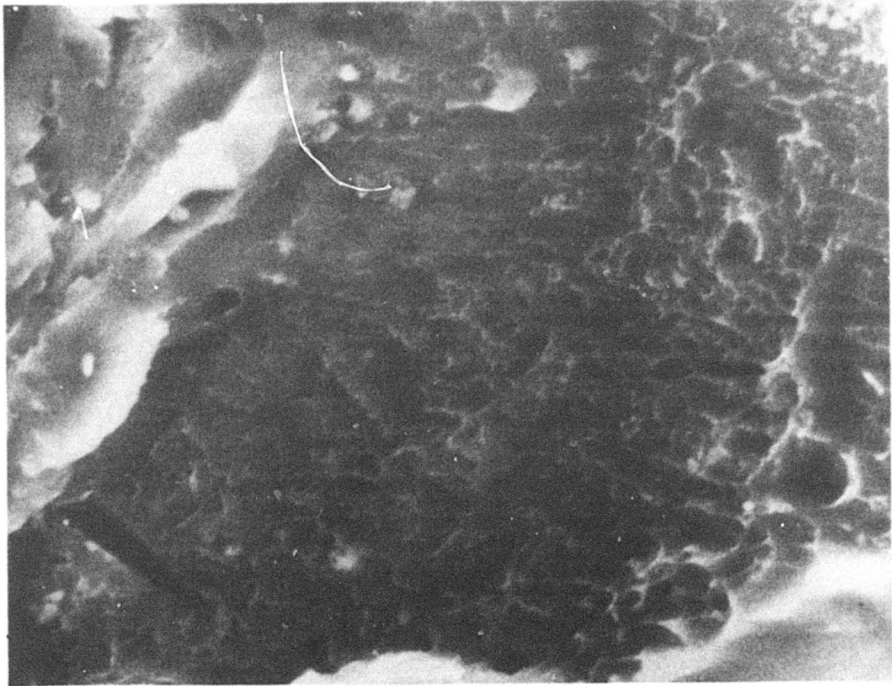


A
X10



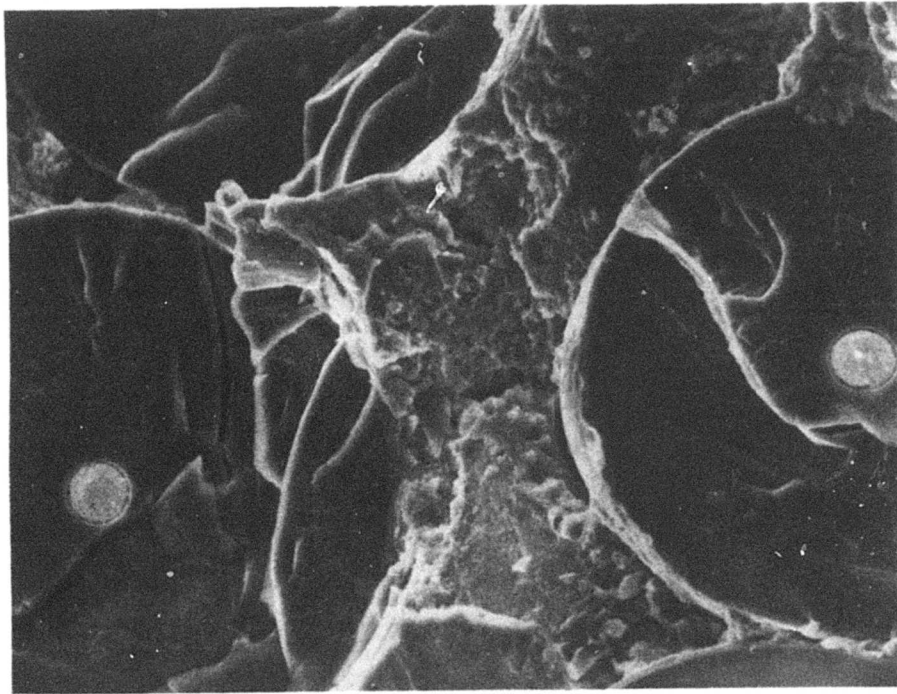
B
X10

FIGURE 119. SCANNING ELECTRON MICROSCOPE FRACTOGRAPHS OF BALLISTIC SPECIMEN NUMBER 1



C

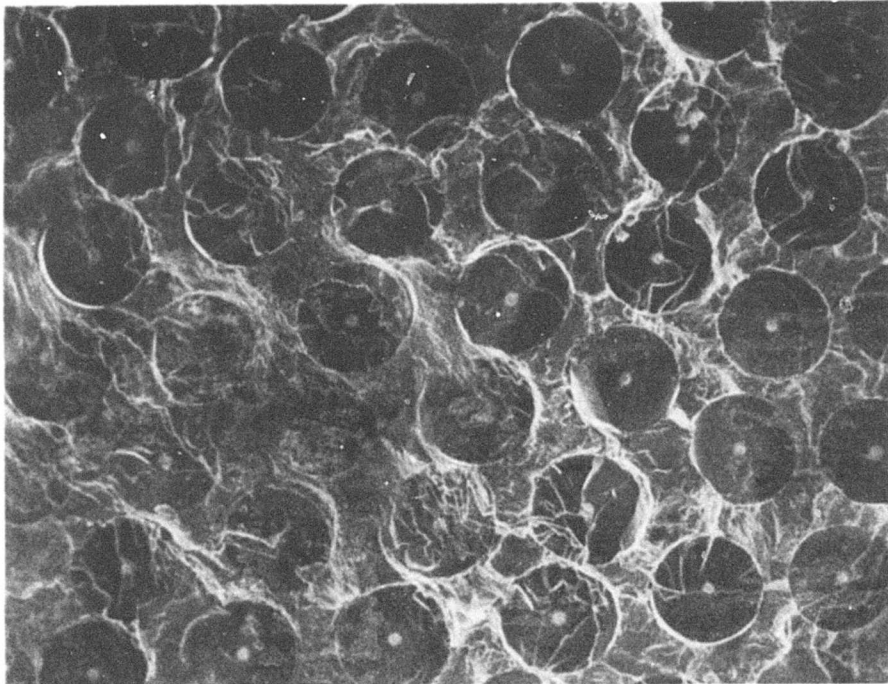
X2500



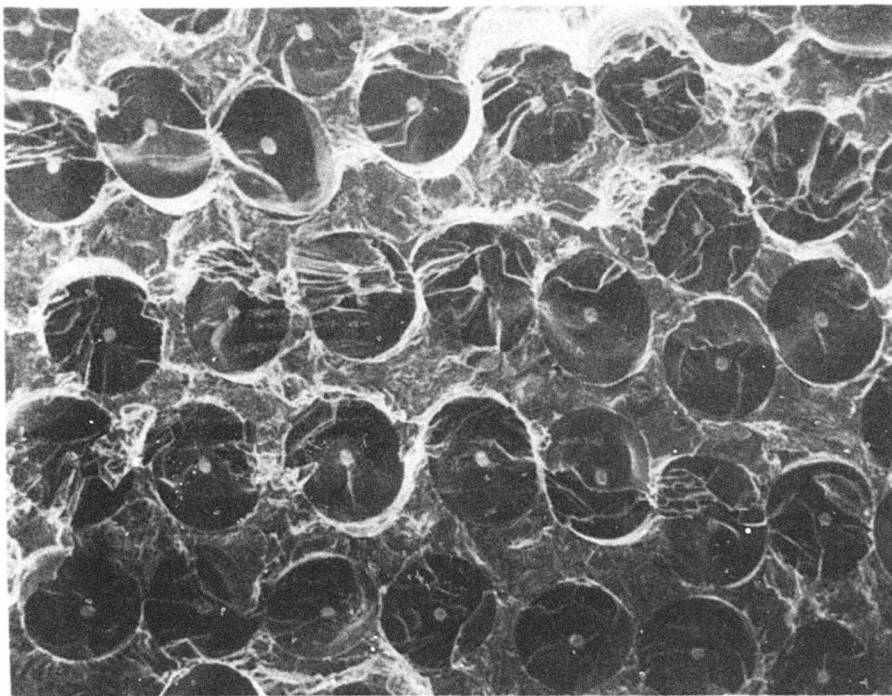
D

X500

FIGURE 119. CONTINUED

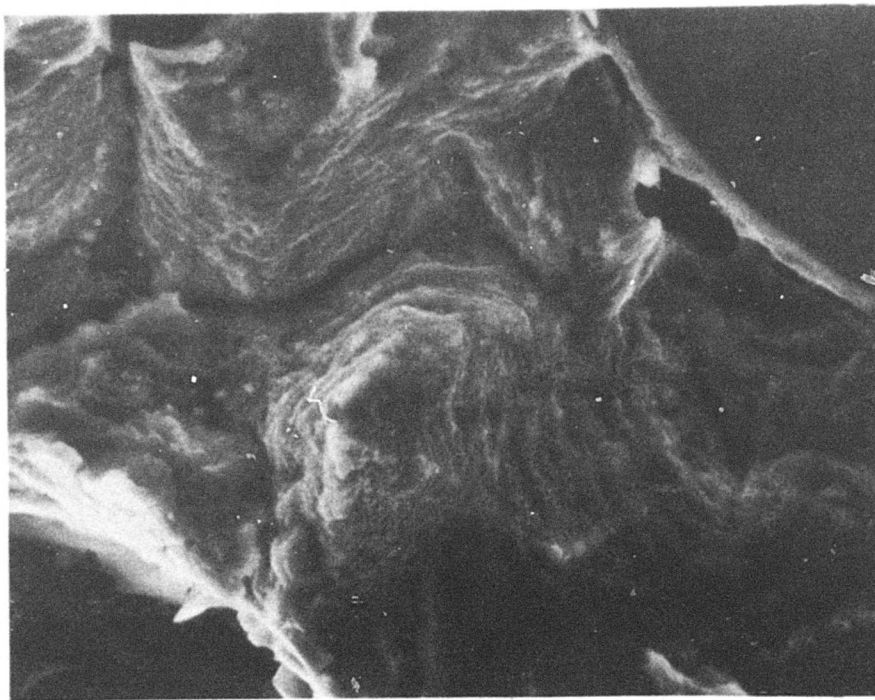


E



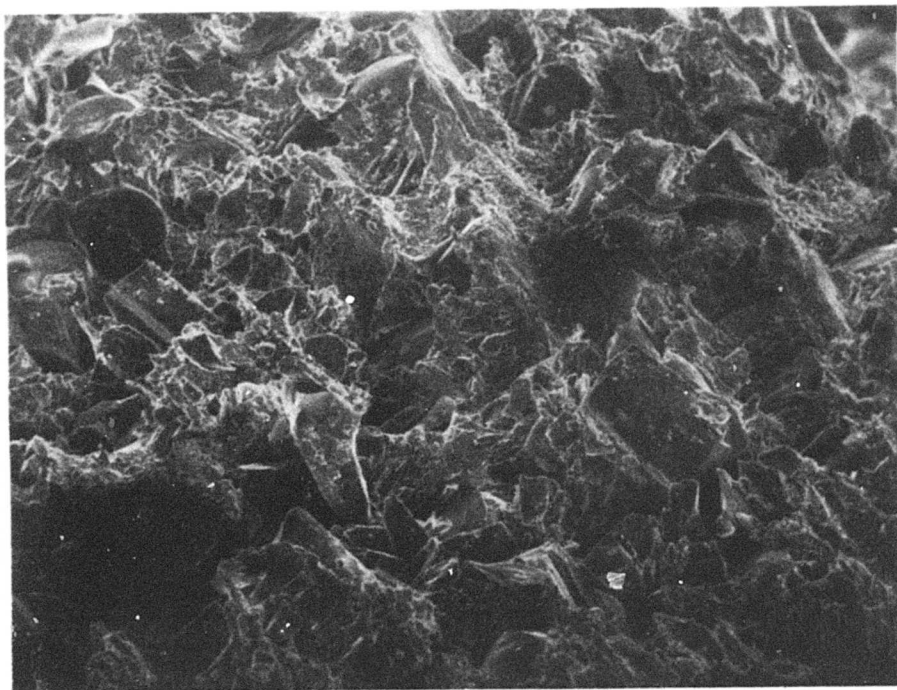
F

FIGURE 119. CONTINUED



X2500

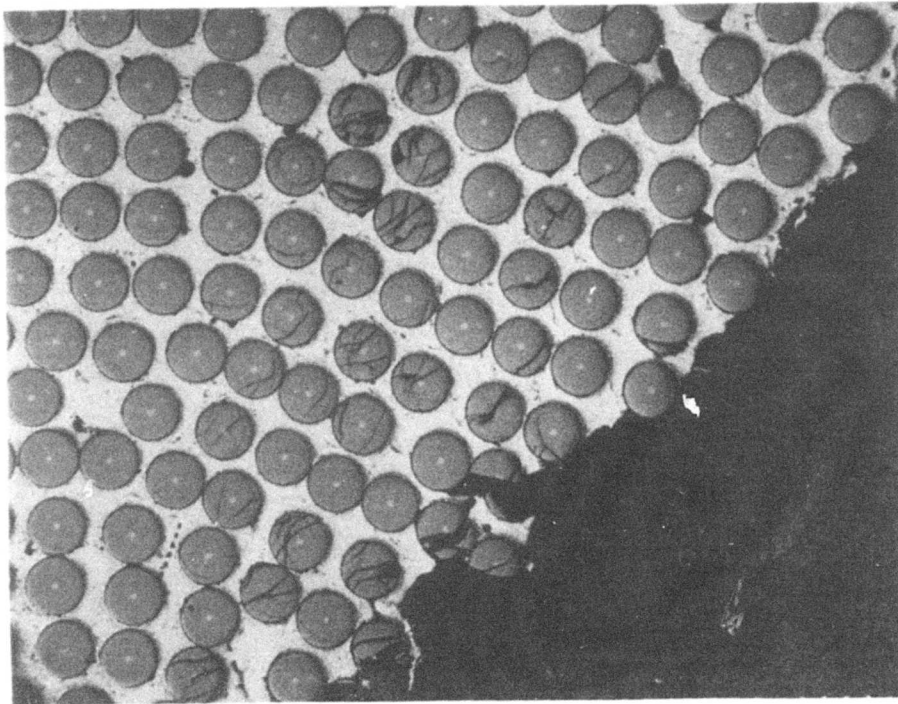
G



X100

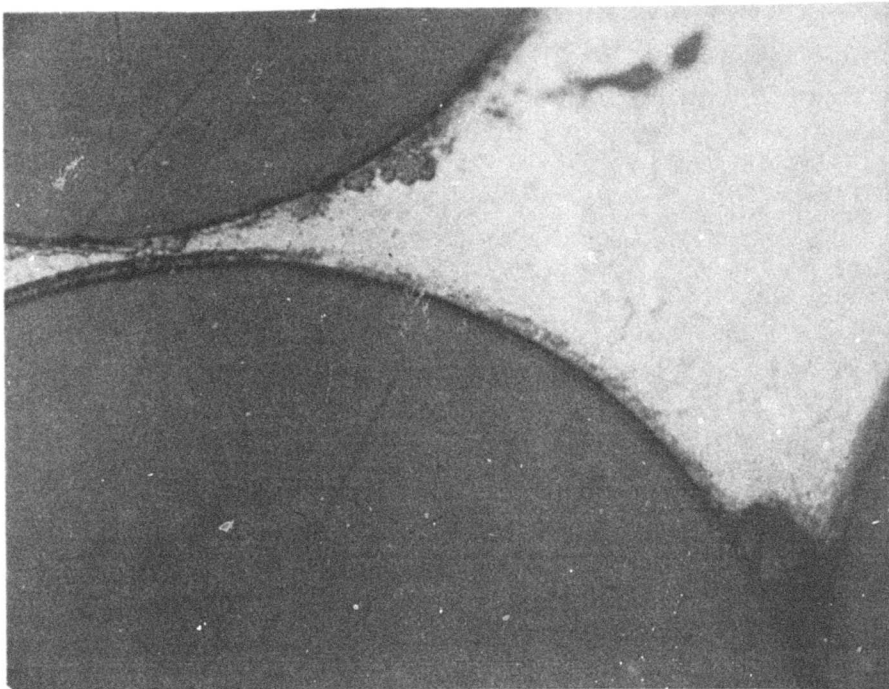
H

FIGURE 119. CONTINUED



A

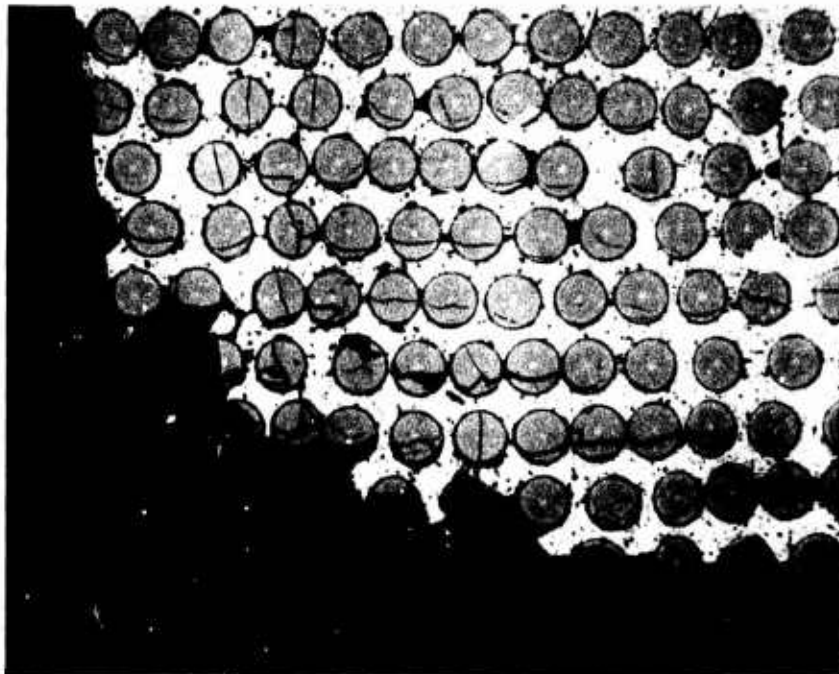
X50



B

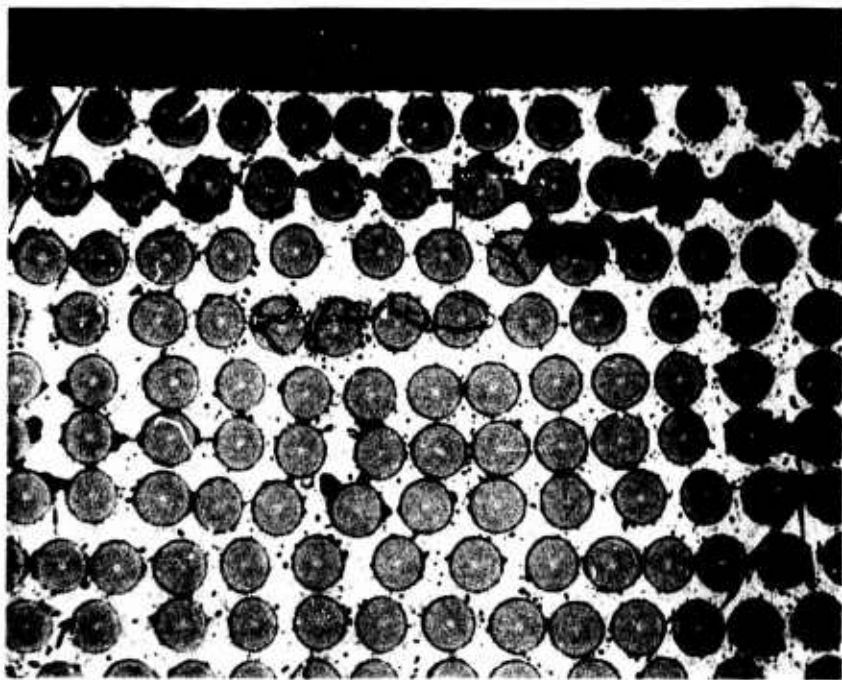
X1000

FIGURE 120. METALLOGRAPHIC SECTIONS OF BALLISTIC SPECIMENS
NUMBERS 1 AND 4



C

X50



D

X50

FIGURE 120. CONTINUED

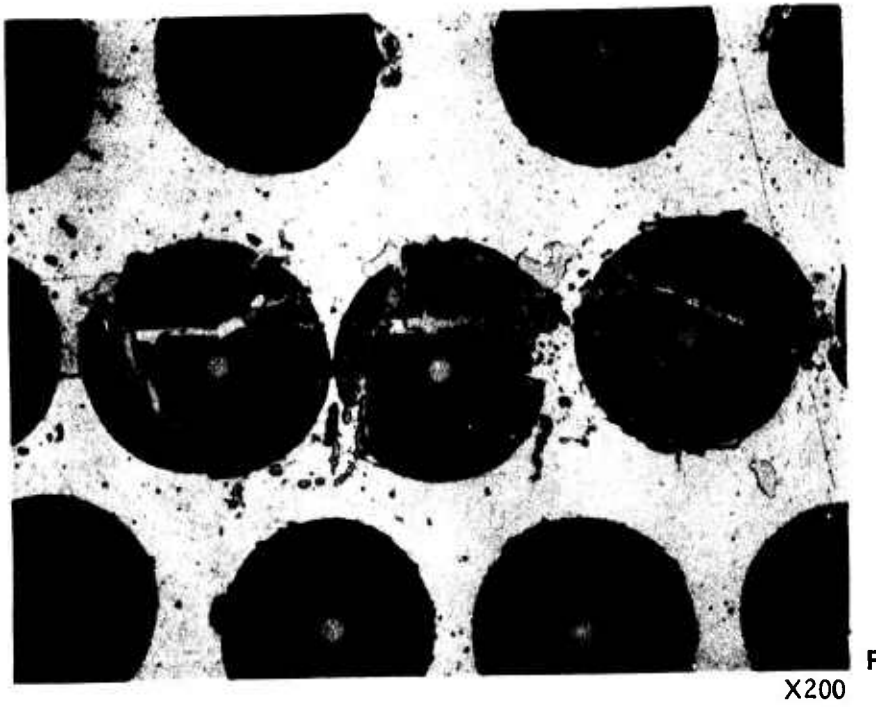
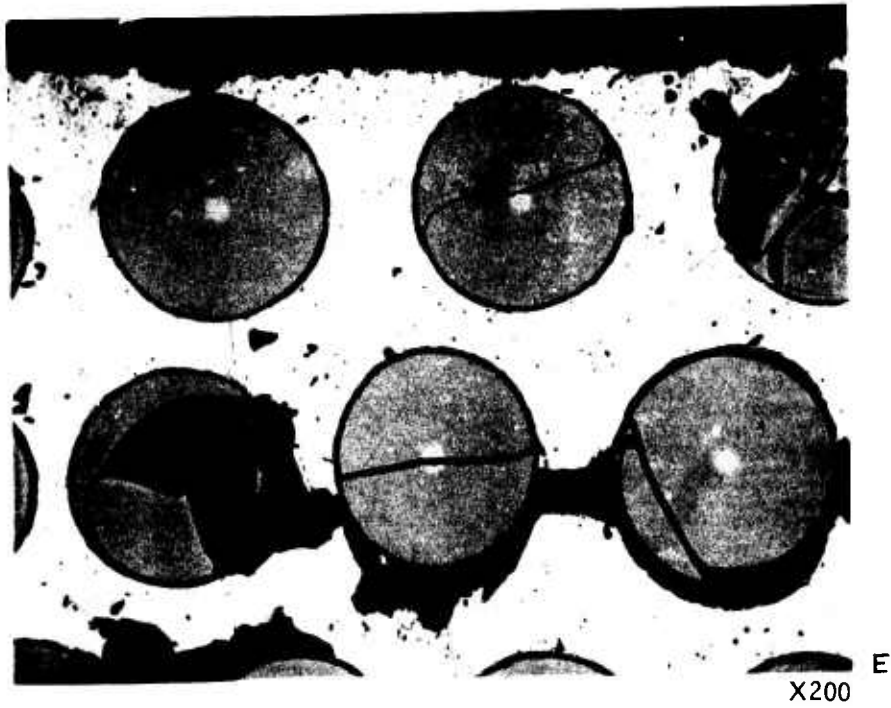
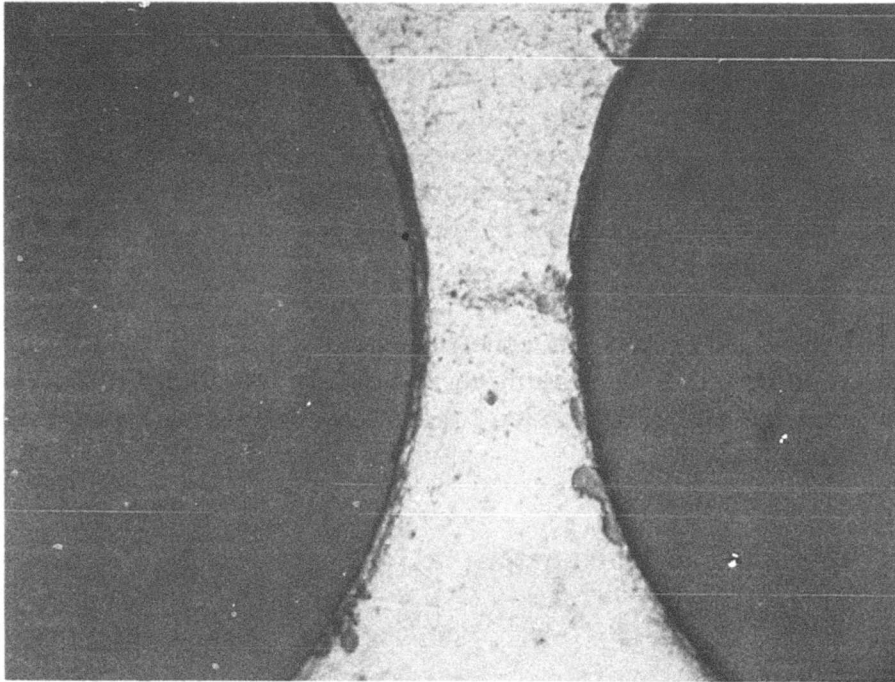
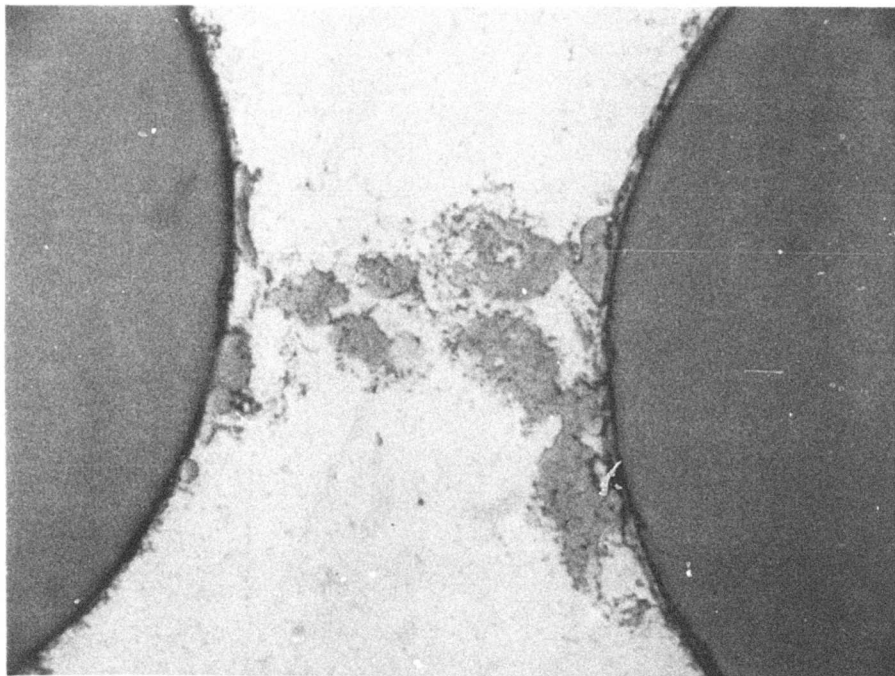


FIGURE 120. CONTINUED



G

X1000



H

X1000

FIGURE 120. CONTINUED

In these areas, longitudinal splitting of the fibers had occurred, as well as separation of the composite at the fiber/matrix interface. See Figures 120a, c, d and e. In one area of specimen serial number four, four fibers were found with longitudinal splits which had evidently occurred either prior to or during the compaction process as the spaces between fiber fragments were filled with aluminum alloy matrix. See Figure 120f. In these particular fibers, extensive aluminum/boron reaction had occurred. In general, there was a concentration of silicon-rich phases surrounding the fibers, suggesting a diffusion of some silicon from the fiber coating outward into the matrix and therefore raising the possibility of some fiber damage. See Figures 120b, g, and h.

Groups of fibers were extracted from the matrix of each specimen from both the mid-span section outboard of the retention and either from within the retention braze joint or from the outboard bonded joint. The individual strengths are given in Tables 28 through 33.

TABLE 28. TENSILE STRENGTH OF FIBERS FROM
 BONDED AREA OF SPECIMEN
 NUMBER 1

Strength Distribution (ksi)	Number of Samples	Residual Composite Strength (ksi)
under 101	1	
101-120	0	119
12-140	4	133
141-160	12	133
161-180	5	140
181-200	5	146
201-220	1	159
221-240	2	168
241-260	1	179
261-280	5	179
281-300	2	186
301-320	8	173
321-340	9	153
341-360	14	112
361-380	14	65
381-400	11	24
401-420	6	0
Average strength,		$\bar{X} = 294,000$ psi
Standard deviation,		$\sigma = 94,000$ psi
Sample size,		$n = 100$

TABLE 29. TENSILE STRENGTHS OF FIBERS FROM
OUTBOARD OF BRAZED AREA OF
SPECIMEN NUMBER 1

Strength Distribution (ksi)	Number of Samples	Residual Composite Strength (ksi)
under 100	3	
101-120	1	115
121-140	1	133
141-160	2	149
161-180	3	162
181-200	5	170
201-220	5	176
221-240	10	168
241-260	11	154
261-280	14	126
281-300	15	90
301-320	13	55
321-340	14	10
340-360	2	4
360-460	0	5
460-480	1	0
Average strength, $\bar{X} = 265,000$ psi		
Standard deviation, $\sigma = 63,000$ psi		
Sample size, $n = 100$		

**TABLE 30. TENSILE STRENGTHS OF FIBERS FROM
BRAZED AREA OF SPECIMEN
NUMBER 2**

Strength Distribution (ksi)	Number of Samples	Residual Composite Strength (ksi)
under 101	3	
101-120	8	107
121-140	6	116
141-160	11	115
161-180	6	119
181-200	12	108
201-220	7	104
221-240	2	108
241-260	0	117
261-280	3	118
281-300	3	117
301-320	0	115
321-340	7	109
341-360	14	65
361-380	8	38
381-400	7	12
401-420	3	0
Average strength, $X = 247,000$ psi		
Standard deviation, $\sigma = 103,000$ psi		
Sample size, $n = 100$		

**TABLE 31. TENSILE STRENGTHS OF FIBERS FROM
OUTBOARD OF BRAZED AREA OF
SPECIMEN NUMBER 2**

Strength Distribution (ksi)	Number of Samples	Residual Composite Strength (ksi)
under 101	1	
101-120	0	119
121-140	2	136
141-160	5	147
161-180	5	157
181-200	2	170
201-220	7	172
221-240	8	168
241-260	19	133
261-280	16	98
281-300	22	39
301-320	10	10
321-340	1	7
341-360	1	4
361-460	0	4
461-480	1	0
Average strength, $X = 253,000$ psi		
Standard deviation, $\sigma = 55,000$ psi		
Sample size, $n = 100$		

**TABLE 32. TENSILE STRENGTHS OF FIBERS FROM
BRAZED AREA OF SPECIMEN
NUMBER 4**

Strength Distribution (ksi)	Number of Samples	Residual Composite Strength (ksi)
under 101	2	
101-120	1	116
121-140	2	133
141-160	1	150
161-180	0	169
181-200	4	180
201-220	5	187
221-240	15	168
241-260	9	159
261-280	22	109
281-300	17	66
301-320	12	32
321-340	7	10
341-360	3	0
Average strength, $X = 263,000$ psi		
Standard deviation, $\sigma = 54,000$ psi		
Sample size, $n = 100$		

TABLE 33. TENSILE STRENGTHS OF FIBERS FROM
OUTBOARD OF BRAZED AREA OF
SPECIMEN NUMBER 4

Strength Distribution (ksi)	Number of Samples	Residual Composite Strength (ksi)
under 101	1	
101-120	3	115
121-140	3	130
141-160	5	141
161-180	3	153
181-200	0	170
201-220	0	187
221-240	3	197
241-260	3	205
261-280	7	202
281-300	19	159
301-320	18	112
321-340	17	61
341-360	12	22
361-380	3	12
381-400	1	8
401-420	1	4
421-440	0	5
441-460	1	0
Average strength,		$X = 286,000$ psi
Standard deviation,		$\sigma = 74,000$ psi
Sample size,		$n = 100$

Table 34 summarizes the results and compares these results to those generated previously during the investigation of spar serial number five (3P-OOP fatigue test). The similarity between mechanical properties indicates that the ballistic specimens and the fatigue test spar had essentially the same degree of degradation.

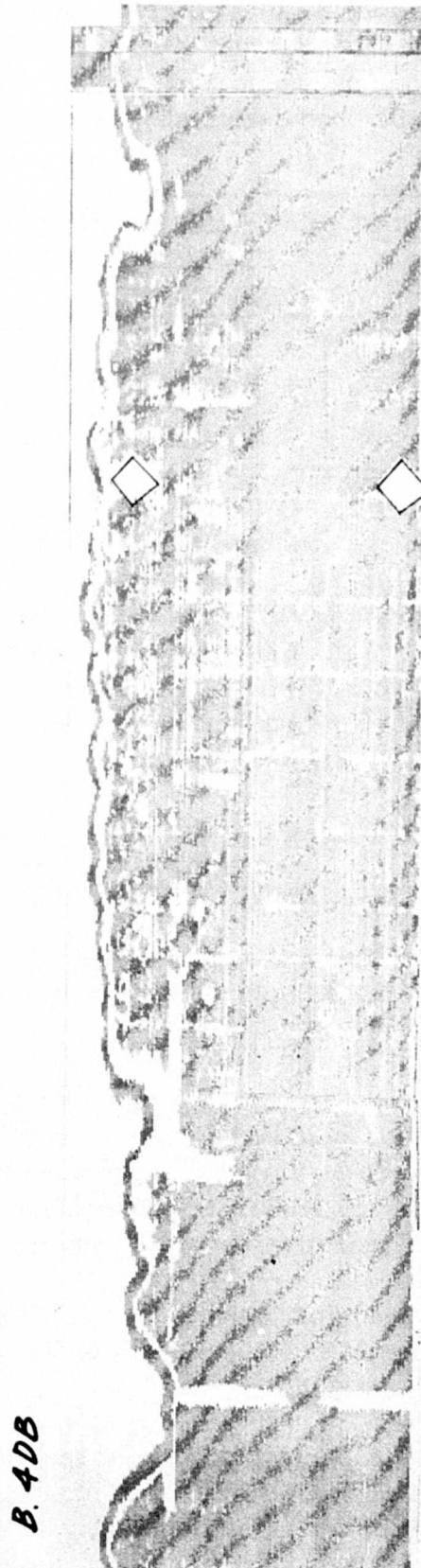
TABLE 34. TENSILE STRENGTHS OF EXTRACTED FIBERS FROM ALL SPARS AND SPECIMENS					
Serial Number	Test Description	Fiber Location	Average UTS (ksi)	Deviation (ksi)	Dry Bundle Strength (ksi)
1	Ballistics	Outboard Moment Arm	265	63	176
			294	94	186
2	Ballistics	Outboard Retention	253	55	172
			247	103	118
4	Ballistics	Outboard Retention	286	74	205
			263	54	187
5	Fatigue	Outboard Retention	226	37	162
			294	66	224

Ultrasonic or C-scan inspections of the areas at or near the points of ballistic impact on specimens numbers four, one, and two are recorded in Figures 121, 122, 123, respectively.

The black areas indicate dense composite, relatively free of cracks, voids and inclusions, and the white indicates defective areas. From past experience, 4 Db scans are considered to be the most representative of the true condition of a spar or specimen. Figure 121 illustrates the section of specimen number four between the ending of the external titanium collar and the fracture.

The top edge of the scan corresponds to where the specimen fractured after fatigue testing. Based on the 4 Db scan, 90-95% of the cross section contained no significant defects.

Figure 122 shows a comparable section of specimen number one. Based on the 4 Db scan, this spar is more porous than number four. An estimated 85% of the cross section contained detectable defects.



SETTINGS:
FREQUENCY: 2 1/4 MHZ
SENSITIVITY: 3
TRANSDUCER: 3/4"
PULSE LENGTH: MINIMUM

REJECT: 9 O'CLOCK
CLIPPER: 5
tone: 9
PRINT: POSITIVE
DATE: 5/9/74

FIGURE 121. ULTRASONIC INSPECTION OF RETENTION SECTION OF BALLISTIC SPECIMEN NUMBER 4

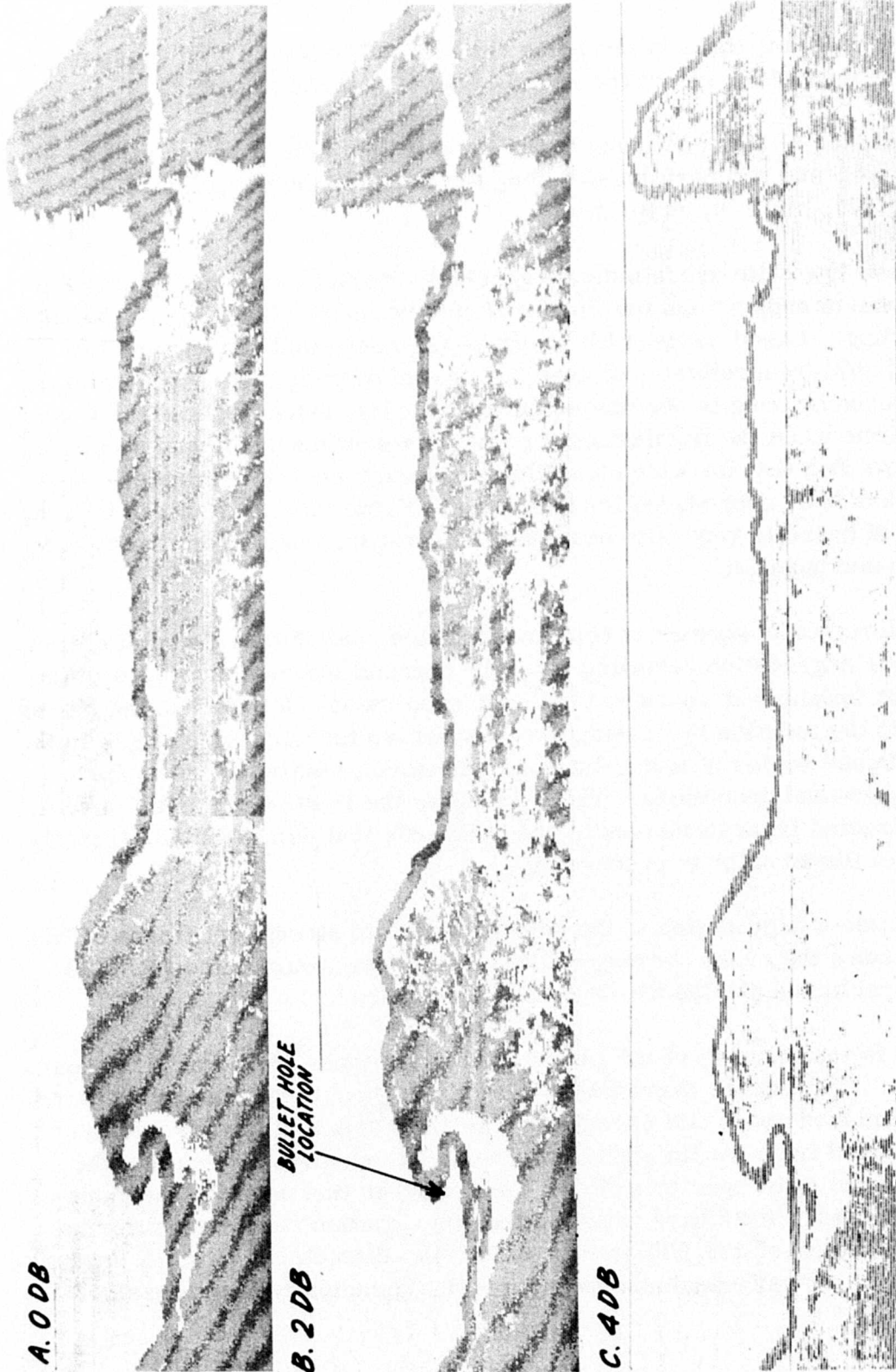


FIGURE 122. ULTRASONIC INSPECTION OF OUTBOARD SECTION OF BALLISTIC SPECIMEN NUMBER 1

Figure 123 shows a comparable section of specimen number two.

Looking at the 4 Db scan, three bullet holes can be readily seen. The cross section of this specimen shows that 40% of the area is free of detectable defects.

Ultrasonic inspection of the specimens in the area of the braze joint on specimens numbers four, one, and two performed during the manufacturing cycle are shown in Figures 124, 125, and 126, respectively.

In these C-scans, the white areas indicate generally sound braze bonding between the external titanium support and the Borsic aluminum spar. Black areas indicate poor braze bonding. Based on the 4 Db scans, specimens numbers one and two contain 35% and 30%, respectively, of generally sound brazing. No estimate of the percentage of sound brazing in specimen number four was made because the C-scan was taken at a time when the titanium collar was only semimachined and was of a greater thickness than that for which a calibration specimen was available. However, the scan has been reproduced for reference. From this scan, it can be said that the quality of braze is generally sound for the first inch back from the top edge of the titanium outer support.

A study was undertaken in support of this investigation, and it was aimed at defining the extent of fiber degradation resulting from the thermal process employed in the fabrication of the fatigue test spars and ballistic specimens. It explored the means of mitigating this degradation by varying process parameters and/or changes to the alloy system. In one series of tests, three panels were prepared in the same fashion as the spars and specimens. Table 35 shows the results of tensile tests of the fibers extracted from these panels and compares that data with the strength of the same lot of fibers prior to processing.

The results indicate a degradation in the average ultimate strength of fibers of 35%. The table also shows the grand average of the tensile data accumulated from the three ballistic specimens and the 3P-OOP fatigue test spar.

Included as well is the strength of the fibers used in the tapes from which the spars were fabricated. The average degradation in strength from virgin fibers to fibers extracted from finished spars and specimens was 42%, only slightly greater than the degradation found from the finished test panels. It can also be seen that the initial strength of the spar/specimen fibers was less than that used for the panels. However, in both cases, the fibers satisfied the specification requirement for an average tensile strength of 400,000 psi for 0.0057-in. -diameter fibers. It appears that the relatively low spar/specimen strength is due principally to processing.

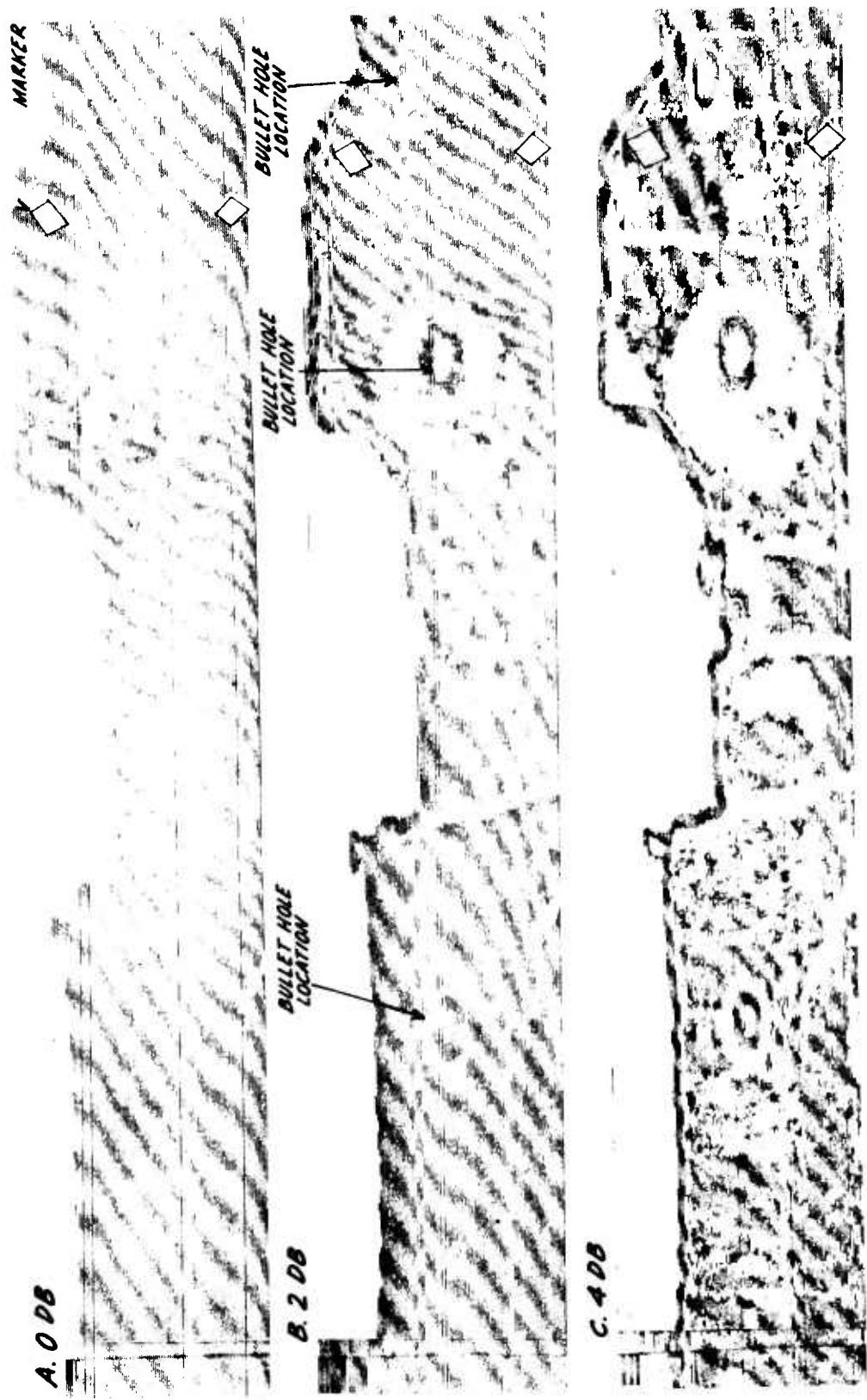


FIGURE 123. ULTRASONIC INSPECTION OF RETENTION SECTION OF BALLISTIC SPECIMEN NUMBER 2



OTHER SETTINGS
FREQUENCY: 10 MHZ
TRANSDUCER: 3/8
PULSE LENGTH: MINIMUM
REJECT: 8 O'CLOCK
*SENSITIVITY: .6 * 10*

CLIPPER: 8
tone: 4
PRINT: NEGATIVE
DATES: 4/22/73, 4/23/73

FIGURE 124. IN-PROCESS ULTRASONIC INSPECTION OF BALLISTIC SPECIMEN NUMBER 4

A. TOP (Ti-6AL-4V TAPERED)
SENSITIVITY: 6 x 10



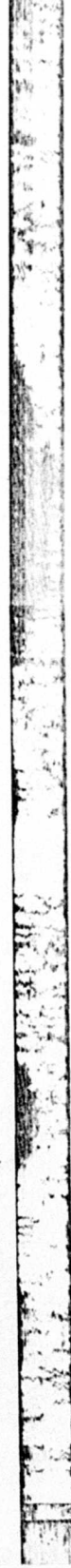
B. BOTTOM
(1) SENSITIVITY: 1.2 x 10



(2) SENSITIVITY: 1.4 x 10



(3) SENSITIVITY: 1.6 x 10

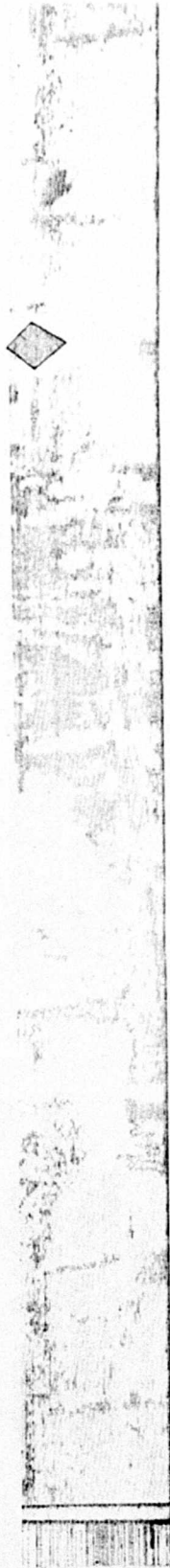


OTHER SETTINGS:
FREQUENCY: 10 MHz
TRANSDUCER: 3/8"
PULSE LENGTH: MINIMUM
REJECT: 8 O'CLOCK

CLIPPER: 8
TONE: 4
PRINT: NEGATIVE
DATES: 4/22/73, 4/23/73

FIGURE 125. IN-PROCESS ULTRASONIC INSPECTION OF BALLISTIC SPECIMEN NUMBER 1

A. TOP (Ti-6Al-4V TAPERED)
SENSITIVITY: .6 x 10



B. BOTTOM
(1) SENSITIVITY: 1.2 x 10



(2) SENSITIVITY: 1.4 x 10



(3) SENSITIVITY: 1.6 x 10



OTHER SETTINGS:
FREQUENCY: 10 MHz
TRANSDUCER: 3/8
PULSE LENGTH: MINIMUM
REFLECT: 8 O'CLOCK

CLIPPER: 8
TONE: 4
PRINT: NEGATIVE
DATES: 4/22/73, 4/22/73

FIGURE 126. IN-PROCESS ULTRASONIC INSPECTION OF BALLISTIC SPECIMEN NUMBER 2

TABLE 35. EXTRACTED FIBER TENSILE STRENGTHS

Material Tested	Fabrication Parameters			Composite Fiber Data				Fiber Used in Tape	
	Time above 1070° F minutes	Peak Temperature (° F)	Time at Peak Temperature minutes	Sample Size	Average UTS (ksi)	(ksi)	Dry Bundle Strength	Sample Size	Average Ultimate Tensile Strength (ksi)
Specimens and Spars	120	1120	30	1000	264	63	180	247	460
Panel 1094	125	1100	65	100	338	59	239	20	520
Panel 1097	121	1100	65	100	336	76	236	20	515
Panel 101098	126	1105	60	100	330	68	243	20	515

In summary, examination of the ballistic specimens showed that the fractures were generally chordal in orientation, and in most cases the fractures passed through the ballistic penetration points. When the holes were located at different stations, the connecting fracture surfaces contained longitudinal splits. In all cases, some interply delaminations were noted, and these features appear to be associated with the penetration sites. It is probable that this splitting took place at impact and was not part of the fatigue fracture process. Further, the fibers generally had edge origins, and the aluminum alloy matrix showed evidence of ductile overstress rupture. In some areas, the matrix had closely spaced features suggestive of fatigue striations. The fracture surfaces were generally flat, and the appearance suggests that the cracks grew through the matrix and rapidly across the fibers. Most of the matrix fracture was ductile dimpling. It was reported by USAAMRDL that the specimens ruptured quickly, with no indication of cracking up to the final separation. The fibers, therefore, were apparently ineffective in retarding crack propagation. Mechanical tests performed on fibers extracted from the ballistic specimens indicated that the fibers were defective and essentially the same as those from the fatigue test spar. It was noted earlier that the microstructure of spar serial number five confirmed fiber degradation by showing evidence of a severe matrix/fiber chemical reaction. Such an extent of reaction was not seen in the ballistic specimens, but some evidence of reaction was present. It is possible that the degree of reaction sufficient to impair fiber strength need not be obvious upon metallographic examination.

As all three ballistic test specimens were judged to have ably demonstrated the ability to operate for a limited period following ballistic damage, this phase of the test was thus concluded.

CONCLUSIONS

Based on the results obtained from this program, the following conclusions were reached:

SPAR

- A low-pressure bonding process was successfully developed to fabricate large-diameter, thick-wall Borsic aluminum spars.
- Braze bonding of titanium alloy to Borsic aluminum produced satisfactory joints.
- During fatigue test, spar fracture occurred at the fiber-matrix interface and involved fibers significantly degraded due to chemical interaction between the fibers and the matrix.
- Analysis showed the fiber degradation to be a result of the relatively long period of time at elevated temperature required by the material system and tooling configuration.
- The selected low-pressure fabrication process does not show sufficient strength-to-weight benefits to achieve the objective of a significant weight reduction.
- The ballistic impact test demonstrated that a Borsic aluminum spar would have sufficient damage tolerance to enable a 30-minute flyback after multiple hits of up to 14.5 mm.

BARREL

- The ability to produce complex shaped barrel forgings, with flat plate section fatigue properties, was demonstrated by 35 samples from one forging.
- Experimental stress analysis demonstrated a conservative design capable of achieving the objective of a 38-pound configuration.
- The Gothic-arch retention fractured prematurely during fatigue test, thereby precluding full evaluation of the barrel.
- Analysis of the Gothic-arch bearing indicated that further redesign was required to produce sufficient structural integrity.

BEARING

- Structural integrity was demonstrated to be commensurate with anticipated service life, as two samples exceeded the B-10 life prediction.
- The ability to operate after loss of positive lubrication flow was demonstrated, as one bearing operated for over 15 hours without benefit of pressurized flow of oil.
- This concept can be incorporated in future advanced technology propeller systems.

RECOMMENDATIONS

As a consequence of the results obtained during this investigation, further work is recommended in the following areas:

- Design and fabricate an increased capacity retention insert configuration for the titanium barrel concept.
- Conduct fatigue testing of the barrel and retention to establish the structural limitations of these components.
- Alternate process cycles, boron aluminum material systems, and improved tooling should be investigated as a means to improve the structural capacity of the blade spar.
- Full-scale spars should be fabricated and metallurgically inspected to confirm the absence of chemical attack on the boron fibers.
- The full-scale spars should be evaluated by fatigue test.

LITERATURE CITED

1. Toth, I. J., and Shimmin, K. K., "Fatigue and Fracture of Metal-Matrix Composites", Proceedings of the Air Force Conference on Fatigue and Fracture of Aircraft Structures and Material, AFFDL-TR-70-144, December, 1969.
2. Varholak, E. M., Advanced Technology V/STOL Propeller Retention System Investigation, Hamilton Standard Division, United Technologies Corporation, USAAMRDL Technical Report 71-39, U.S. Army Air Mobility Research and Development Laboratory, Fort Eustis, Virginia, January 1972.
3. Neffinger, N. A., Advanced Technology for Aircraft Propeller Shank, Barrel and Bearing-Final Stress Analysis Report, HSER 6079, Hamilton Standard Division, United Technologies Corporation, Windsor Locks, Connecticut, July 1972.

LIST OF SYMBOLS

ESA	Experimental stress analysis
FSI	Fatigue strength investigation
IP	In-plane loading
K_T	Stress concentration factor
K_{IC}	Critical stress intensity factor
n	Sample size
OOP	Out-of-plane loading
R	Stress ratio (minimum to maximum)
\bar{X}	Average strength
1P	Once per revolution bending load
3P	Three times per revolution bending load
σ	Standard deviation
B-10	Bearing life expectancy during which 90% of a given group of bearings will remain in service, hours